UNIVERSITY OF NOVA GORICA
GRADUATE SCHOOL

ULTRAFAST ELECTRON DYNAMICS IN CORRELATED SYSTEMS PROBED BY TIME-RESOLVED PHOTOEMISSION SPECTROSCOPY

DISSERTATION

Tanusree Saha

Mentor: Prof. Dr. Giovanni De Ninno

Nova Gorica, 2023

UNIVERZA V NOVI GORICI
FAKULTETA ZA PODIPLOMSKI ŠTUDIJ

PREUČEVANJE ULTRA HITRE DINAMIKE ELEKTRONOV V KORELIRANIH SISTEMIH S POMOČJO ČASOVNO LOČLJIVE FOTOEMISIJE

DISERTACIJA

Tanusree Saha

Mentor: Prof. Dr. Giovanni De Ninno

Nova Gorica, 2023

Acknowledgements

Firstly, I would like to express my sincere gratitude to my Ph.D. supervisor, Prof. Dr. Giovanni De Ninno, for his invaluable supervision, support, encouragement and tutelage during the course of my doctoral study in his group, Laboratory of Quantum Optics (LKO). I would like to offer my special thanks to Dr. Primož Rebernik Ribič for his insightful comments and suggestions at every stage of the research activity. I am deeply grateful to Prof. Kalobaran Maiti (Tata Institute of Fundamental Research, India) for his extensive collaborations in the course of my Ph.D. work. I could not have undertaken this journey without the generous support from Štipendije Ad futura, who financed my studies at the Graduate School (Physics), University of Nova Gorica (UNG). I would like to express my deepest appreciation to the company, HQGraphene, who have continued to provide us with high quality samples required for the experiments. Thanks to E. Nicolini and G. Bortoletto at Elettra Sincrotrone (Italy) for characterization of the samples using Laue diffraction. I am incredibly thankful to the referees for the careful and insightful review of my thesis and their comments, which helped to improve its readability significantly.

I would like to extend my sincere thanks to Dr. Barbara Ressel for her treasured support during the experiments, which was really influential in developing my skills with the pump-probe experimental setup. Many thanks to my fellow group members at LKO - Dr. Ganesh Adhikary, Dr. Jurij Urbančič, Dr. Matija Stupar, Dr. Alberto Simoncig, Dr. Alessandra Ciavardini, Dr. Federico Galdenzi and Arun Ravindran, for their cooperation and technical assistance during the lab activities. I had the great opportunity of working with theoreticians, Dr. Arindam Pramanik from Tata Institute of Fundamental Research (India), Dr. Denis Golež and Dr. Jernej Mravlje from Jožef Stefan Institute (Slovenia), and beamline scientists at Elettra Sincrotrone (Italy), Dr. Luca Petaccia and Giovanni De Santo. I am also thankful to our physics department at UNG and the professors for offering different courses that broadened my knowlegde of the ongoing research in various fields. I am grateful to my friends and colleagues for a cherished time spent together in the social gatherings.

Words cannot express my gratitude to Zipporah, Shima and Akansha for all the entertainment and Friday get-togethers at our apartment. I would like to express my deepest regards and respect for our landlady, Mrs. Marjetka Bogataj, who made my stay very smooth and comfortable in Slovenia. An exceptional thanks to my dearest Bhargabi who has been firmly there all along as a friend. Finally, this endeavor would not have been possible without the support of my family - Maa, Baba, Arindam, Mashi, Mesho, Sourav, Boro Pishi, Choto Pishi. Their belief in me over these years has kept my motivation high during the course of my study and research.

This thesis is dedicated to my mother, Mrs. Jhuma Saha, my father, Mr. Prasanta Kumar Saha, and my friend, Dr. Arindam Pramanik. Without their affection, encouragement, patience and moral support, the thesis would not have been possible. My parents' high regard for education has been a great source of inspiration and strength for me. Arindam has been my teacher and guardian, and our scientific discussions over the years have greatly influenced my research perspectives. It is all with GOD's GRACE.

Publications

Publications in the framework of the thesis

- **Tanusree Saha**, Denis Golež, Giovanni De Ninno, Jernej Mravlje, Yuta Murakami, Barbara Ressel, Matija Stupar, and Primož Rebernik Ribič, "Photoinduced phase transition and associated time scales in the excitonic insulator Ta_2NiSe_5." *Physical Review B* **103**, 144304 (2021).
- **Tanusree Saha**, Luca Petaccia, Barbara Ressel, Primož Rebernik Ribič, Giovanni Di Santo, Wenjuan Zhao, and Giovanni De Ninno, "Electronic band structure in pristine and sulfur-doped Ta_2NiSe_5." *Physical Review B* **106**, 075148 (2022).
- **Tanusree Saha**, Arindam Pramanik, Barbara Ressel, Alessandra Ciavardini, Federico Galdenzi, Arun Ravindran, Primož Rebernik Ribič, and Giovanni De Ninno, "Uncovering the nature of transient and metastable non-equilibrium phases in 1*T*-TaS_2." (under review in *Physical Review B*)
ArXiv link: *https://doi.org/10.48550/arXiv.2301.05895*
- Ganesh Adhikary, **Tanusree Saha**, Primož Rebernik Ribič, Matija Stupar, Barbara Ressel, Jurij Urbančič, Giovanni De Ninno, A. Thamizhavel and Kalobaran Maiti, "Orbital selective dynamics in Fe pnictides triggered by polarized pump pulse excitations." *Europhysics Letters* **136**, 17002 (2021).

Publications on other topics

- Alberto Simoncig, Matija Stupar, Barbara Ressel, **Tanusree Saha**, Primoz Rebernik Ribic, and Giovanni De Ninno, "Dissecting Mott and charge-density wave dynamics in the photoinduced phase of 1*T*-TaS_2." *Physical Review B* **103**, 155120 (2021).
- Ram Prakash Pandeya, Anup Pradhan Sakhya, Sawani Datta, **Tanusree Saha**, Giovanni De Ninno, Rajib Mondal, C. Schlueter, A. Gloskovskii, Paolo Moras, Matteo Jugovac, Carlo Carbone, A. Thamizhavel, and Kalobaran Maiti, "Emergence of well-screened states in a superconducting material of the $CaFe_2As_2$ family." *Physical Review B* **104**, 094508 (2021).
- Ram Prakash Pandeya, Sawani Datta, Anup Pradhan Sakhya, **Tanusree Saha**, Giovanni De Ninno, Rajib Mondal, Paolo Moras, Matteo Jugovac, Carlo Carbone, A Thamizhavel, and Kalobaran Maiti, "Doping induced band renormalization in 122-type Fe-based superconductor." *Journal of Physics: Conference Series* **2164**, 012004 (2022).

Abstract

Complex systems in condensed matter are characterized by strong coupling between different degrees of freedom constituting a solid. In materials described by many-body physics, these interactions may lead to the formation of new ground states such as excitonic insulators, Mott insulators, and charge and spin density waves. However, the inherent complexity in such materials poses a challenge to identifying the dominant interactions governing these phases using equilibrium studies. Owing to the distinct timescales associated with the elementary interactions, such complexities can be readily addressed in the non-equilibrium regime. Additionally, these materials might also show the emergence of new, metastable "hidden" phases under non-equilibrium. The thesis investigates the ultrafast timescales of fundamental interactions in candidate systems by employing time-and angle-resolved photoemission spectroscopy in the femtosecond time domain. **In the (supposed) excitonic insulator model system Ta_2NiSe_5, the timescale of band gap closure and the dependence of rise time (of the photoemission signal) on the photoexcitation strength point to a predominantly electronic origin of the band gap at the Fermi level.** The charge density wave (CDW) - Mott insulator $1T$-TaS_2 undergoes photoinduced phase transition to two different phases. The initial one is a transient phase which resembles the systems's high temperature equilibrium phase, followed by a long-lived "hidden" phase with a different CDW amplitude and is primarily driven by the CDW lattice order. For the spin density wave system $CaFe_2As_2$ where multiple bands contribute in the formation of Fermi surfaces, selective photoexcitation was used to disentangle the role played by different electron orbitals. By varying the polarization of photoexcitation pulses, it is observed that d_{xz}/d_{yz} orbitals primarily contribute **to** the magnetic ordering while the d_{xy} orbitals have dominant role in the structural order. The findings of the present study provide deeper perspectives on the underlying interactions in complex ground phases of matter, therefore, initiating further experimental and theoretical studies on such materials.

Keywords: complex systems, charge density wave, excitonic insulator, metastable phase, Mott insulator, non-equilibrium, spin density wave, timescales, time- and angle-resolved photoemission, ultrafast dynamics

Povzetek

Za kompleksne sisteme v kondenzirani snovi je značilna močna sklopitev med različnimi prostostnimi stopnjami, ki to snov tvorijo. V materialih, ki jih opisuje fizika več teles, lahko takšne interakcije vodijo v nastanek novih osnovnih stanj, kot so ekscitonski in Mottovi izolatorji ter valovi gostote naboja in spina. Zaradi zapletene narave takšnih sistemov lahko z ravnovesnimi študijami le stežka prepoznamo prevladujoče interakcije v omenjenih fazah. Po drugi strani pa lahko zaradi prisotnosti različnih karakterističnih časovnih skal kompleksne materiale lažje obravnavamo z nerovnovesnimi tehnikami. Poleg tega lahko v neravnovesju v omenjenih materialih pride do pojava novih, metastabilnih t.i. skritih stanj. V disertaciji smo raziskali ultra hitre časovne skale osnovnih interakcij v omenjenih sistemih z uporabo femtosekundne kotno ločljive fotoemisijske spektroskopije. V (domnevnem) ekscitonskem izolatorju Ta_2NiSe_5 karakteristični čas, v katerem se zapre energijska vrzel, ter odvisnost karakterističnega časa dviga fotoemisijskega signala od jakosti svetlobnega vzbujanja kažeta na to, da je energijska vrzel v omenjenem materialu elektronskega izvora. V Mottovem izolatorju 1T-TaS_2, v katerem so prisotni valovi gostote naboja (ang. charge density wave - CDW) pride pri fotovzbujanju do prehoda v različne neravnovesne faze in sicer najprej v neravnovesno stanje, ki je podobno visoko temperaturnem ravnovesnem stanju in nato v dolgoživo "skrito" stanje z manjšo CDW amplitudo, pri čemer je gonilna sila teh prehodov kristalni red CDW. V vzorcih $CaFe_2As_2$, za katere so značilni valovi gostote spina in kjer več energijskih pasov prispeva k nastanku Fermijeve površine, smo s selektivnim fotovzbujanjem ugotavljali kakšna je vloga različnih orbital. S spreminjanjem polarizacije vzbujevalnih sunkov smo opazili, da dxz/dyz orbitale primarno prispevajo k magnetnemu urejanju, medtem ko imajo dxy orbitale glavno vlogo v strukturnem redu. Ugotovitve te študije ponujajo nov vpogled v temeljne interakcije v kompleksnih materialih in predstavljajo osnovo za nadaljnje eksperimentalne in teoretične raziskave.

Ključne besede: kompleksni sistemi, val gostote naboja, ekscitonski izolator, metastabilna faza, Mottov izolator, neravnovesje, val gostote spina, časovne skale, časovno in kotno ločljiva fotoemisija, ultrahitra dinamika

List of Figures

List of Abbreviations

ARPES	Angle-resolved photoemission spectroscopy
BCS	Bardeen–Cooper–Schrieffer
BEC	Bose–Einstein condensate
CB	Conduction band
CDW	Charge density wave
CG	Classical geometry
EDC	Energy distribution curve
e-e	electron-electron
EI	Excitonic insulator
e-mag	electron-magnon
e-ph	electron-phonon
fs	femtosecond
FWHM	Full width at half-maximum
FELs	Free-electron lasers
HHG	High harmonic generation
IR	Infra-red
LEED	Low-energy electron diffraction
LHB	Lower Hubbard band
MDC	Momentum distribution curve
OPA	Optical parametric amplifier
OPG	Off-plane geometry
PLD	Periodic lattice distortion
PES	Photoemission spectroscopy
SDW	Spin density wave

STM	Scanning tunnelling microscopy
trARPES	Time- and angle-resolved photoemission spectroscopy
UHB	Upper Hubbard band
UHV	Ultra-high vacuum
UV	Ultra-violet
VB	Valence band
XUV	Extreme ultra-violet
1D	One-dimensional
2D	Two-dimensional

Introduction

Conventional band theory based on non-interacting or weakly interacting electron systems distinguishes metals, semiconductors, and insulators [1, 2, 3, 4, 5]. Although this approach has been successful in many respects, one is confronted with a many-body problem in certain materials. Such materials are characterized by strong interactions between various microscopic components of a solid, such as charge, spin and lattice. Solids may undergo phase transitions to intriguing ground states, namely, charge and spin density waves (CDW, SDW) [6], Mott insulators [7, 8], excitonic insulators [9], superconductors [10], etc. These transitions can be achieved by varying external parameters such as temperature [11], pressure [12], or chemical doping [8, 13]. Extensive experimental and theoretical studies performed in equilibrium resulted in a microscopic understanding of these materials. However, identifying the dominant interaction leading to such ground states is not straightforward and here comes the necessity of a non-equilibrium approach to investigate their interplay. The most common experimental approach to delve into the non-equilibrium regime of matter is by combining two ultrashort pulses: a pump-pulse excites the system from its state of equilibrium, and a time-delayed probe-pulse follows the temporal dynamics leading the system back towards its fundamental state [14, 15, 16]. Several pump-probe techniques have been implemented, including time-resolved photoemission and optical spectroscopy, time-resolved electron and X-ray diffraction, etc. [17]. The advancement in the generation of ultrashort pulses have made it possible to observe these processes on the femtosecond (10^{-15} secs) [18] time scale. Apart from providing information on the lifetime of the energy states along different relaxation pathways, the efficacy of this technique lies in its ability to temporally discriminate the various microscopic interactions based on their characteristic timescales [15, 19]. In particular, owing to their distinct timescales, one can dissect electron-electron from electron-lattice interactions and coherent from incoherent phononic processes. The non-equilibrium dynamics, therefore, can offer new insights into the origin of different equilibrium phases in condensed matter systems.

Materials whose physical properties are governed by multiple microscopic interactions may undergo destruction of the charge and lattice ordering of the ground state under non-equilibrium conditions [20, 21]. The collapse of the ground state raises a few central questions: what are the timescales of collapse? On which timescale is the ground state ordering restored? What are the properties of transient non-equilibrium phases? Do these phases correspond to any of the equilibrium phases? If not, what is the origin of such novel phases and which microscopic interactions govern them? Regarding this, photoinduced phase transitions, melting times of energy gaps and the emergence of metastable phases have been some of the active research topics in

recent times. In many-body complex systems, the timescales of gap quenching are a fingerprint of the underlying interactions which have a predominant role in gap formation. In Mott insulators, the quenching is extremely fast, and the timescale is set by the electronic hopping time given by the bandwidth [22, 23]. The Peierls-CDW materials exhibit quenching times that are comparable to the timescales of the slower, lattice-driven processes [24, 25]. For excitonic insulators, carrier screening time, given by the plasma frequency, determines the characteristic timescale [21]. In the context of quenching dynamics, time- and angle-resolved photoemission spectroscopy (trARPES) is ideal amongst all the available pump-probe techniques, since it can map the electronic band structure (energy vs momentum) and Fermi surfaces in the ultrafast time domain. More interestingly, tuning some experimental parameters, such as the polarization of the pump/probe pulses, pump fluence, etc., can unravel some important and unknown electronic properties of materials. Polarization-dependent studies can readily disentangle the contributions of different electron orbitals, which is crucial when the electronic properties arise from multiple bands constituting the Fermi surface [26]. Non-equilibrium phase transitions and persistent hidden phases are some phenomena [24, 27] that might occur under the effect of high photoexcitation strength (pump fluence) in solid-state systems.

Now that we have provided a preliminary idea of some of the intriguing aspects of different ordered phases as well as of the great allure of non-equilibrium methods (trARPES for the present study) in identifying them, we will move towards the aim of the current dissertation. Although a very large amount of equilibrium and non-equilibrium studies have been performed on excitonic insulators (EI), Mott insulators, CDW and SDW systems, some gaps remain in the knowledge of these materials. In complex systems, there has been a minimal emphasis on the ordering of charge and lattice degrees of freedom in the non-equilibrium transient phase(s). Furthermore, most studies have focussed on the initial stages of the dynamics, i.e., on the collapse of electronic and lattice order. Much less attention has been paid to the dynamics leading the system back to the ground state. For prototypical excitonic insulators, melting of the energy gap on structural timescales has raised questions on the predominant nature of the ground state. Moreover, the excitation density dependence of the timescales is also controversial. In Fe-based systems (pnictides, for example), the parent compounds exhibit phase transition to the SDW ground state, accompanied by a structural transition. The underlying complexity in these systems is that their Fermi surfaces comprise multiple energy bands. Such complex physics can be reliably revisited in the time domain to decouple the role of different orbitals by exploiting the different polarizations of the pulses. The above open questions have been addressed in the thesis, and for the intended work, prominent examples have been chosen: Ta_2NiSe_5 (Excitonic insulator), 1T-TaS_2 (CDW-Mott insulator), $CaFe_2As_2$ (SDW multiband system). The answers to the above questions lie in the characteristic timescales of electron-electron and electron-lattice interactions for the investigated systems. In the scope of this thesis, the objective of the non-

equilibrium studies is to identify the timescales associated with the dynamics of different spectroscopic features, which could be achieved at the current temporal resolution of the employed trARPES equipment. In equilibrium, phase transitions in materials whose physics is governed by various interactions can be achieved by chemical doping. Here, we have shed light on the effect of chemical doping and the dimensionality aspects in the layered compound Ta_2NiSe_5 under equilibrium using (static) ARPES. Since every model has its intricacies, a combined study of different models by exploiting static and time-resolved ARPES provides a broad view of the response of an ordered phase to external perturbations. The organization of the thesis is as follows:

PART I An overview of the historical background of different models of solid-state systems within the framework of the thesis, followed by a description of the experimental techniques and the employed experimental setup, is provided in the first part of the thesis, consisting of Chapters 1 and 2.

- **Chapter 1.** In this chapter, we describe some intriguing ground states of matter, such as excitonic insulators, Mott insulators, and charge and spin density waves. We also discuss the methodology of ARPES and time-resolved ARPES techniques that are used to study these materials. In addition, the different timescales of microscopic elementary processes in solids and the ultrafast carrier dynamics in semiconductors after photoexcitation are briefly reviewed.

- **Chapter 2.** The time-resolved ARPES experiments were carried out at the CITIUS beamline, consisting of a laser system delivering femtosecond light pulses, high-harmonic generation setup, an ultra-high vacuum (UHV) equipment and a hemispherical electron analyzer. This chapter begins with a description of ultrashort light pulses, followed by the principle of high harmonic generation. Then, we provide an overview of the relevant experimental setup for time-resolved ARPES at CITIUS and briefly discuss the preparation of a time-resolved experiment.

PART II The second part of the thesis consists of Chapters 3, 4, 5, and 6, where we present the obtained results in the selected model systems. In the following, the studies on each investigated compound are presented in a nutshell.

- **Chapter 3. Effects of doping on the equilibrium band structure and the dimensionality of Ta_2NiSe_5**

  In this chapter, we present an angle-resolved photoemission study of the electronic band structure of Ta_2NiSe_5, as well as its evolution upon Sulfur-doping. Our experimental data show that while the excitonic insulating phase is still preserved at a S-doping level of 25%, such a phase is heavily suppressed when there is a substantial amount, $\sim 50\%$,

of Sulfur-doping at liquid nitrogen temperatures. Moreover, our photon energy-dependent measurements reveal a clear three dimensionality of the electronic structure, both in Ta_2NiSe_5 and $Ta_2Ni(Se_{1-x}S_x)_5$ ($x = 0.25, 0.50$) compounds.

- **Chapter 4. Non-equilibrium electron dynamics in Ta_2NiSe_5**

  In this chapter, we investigate the non-equilibrium electronic structure and characteristic timescales in a candidate excitonic insulator, Ta_2NiSe_5, using time- and angle-resolved photoemission spectroscopy. Following a strong photoexcitation, the band gap closes transiently within 100 fs, i.e., on a timescale faster than the typical lattice vibrational period. Furthermore, we find that the characteristic time associated with the rise of the photoemission intensity above the Fermi energy decreases with increasing excitation strength, while the relaxation time of the electron population towards equilibrium shows an opposite behavior. We argue that these experimental observations can be consistently explained by an excitonic origin of the band gap in the material. The excitonic picture is supported by microscopic calculations based on the non-equilibrium Green's function formalism for an interacting two-band system. We interpret the speedup of the rise time with fluence in terms of an enhanced scattering probability between photoexcited electrons and excitons, leading to an initially faster decay of the order parameter. We show that the inclusion of electron-phonon coupling at a semiclassical level changes only the quantitative aspects of the proposed dynamics, while the qualitative features remain the same.

- **Chapter 5. Distinct characterization of the transient and metastable non-equilibrium phases in 1T-TaS_2**

  In this chapter, we probe the photoinduced transient phase and the recovery dynamics of the ground state in a complex material: the CDW-Mott insulator 1T-TaS_2, by exploiting femtosecond trARPES. We reveal striking similarities between the band structures of the transient phase, where the Mott electronic order and CDW lattice order are suppressed, and the (equilibrium) structurally undistorted metallic phase. Following the transient phase, we find that the restoration of the Mott and CDW ordering begins around the same time. This highlights that the Mott transition is tied to the CDW structural distortion, although earlier studies have shown that the collapse of Mott and CDW phases are decoupled from each other. Interestingly, as the suppressed order starts to recover, a long-lived metastable phase emerges before the material recovers to the ground state. Our results demonstrate that it is the CDW lattice order that drives the material into this metastable phase, which is indeed a commensurate CDW-Mott insulating phase but with a smaller CDW amplitude. Moreover, we find that the long-lived state emerges only under strong photoexcitation and has no evidence when the photoexcitation strength is weak.

- **Chapter 6. Orbital selective electron dynamics in $CaFe_2As_2$**

  In this chapter, we study the electron dynamics in $CaFe_2As_2$, an Fe-based compound exhibiting SDW ground state by employing time-resolved ARPES. The Fermi surface of this material consists of three hole pockets (α, β and γ) around the Γ-point and two electron pockets around the X-point, with the hole pockets having d_{xy}, d_{yz} and d_{zx} orbital symmetries. The β band constituted by d_{xz}/d_{yz} orbitals exhibits a gap across the magnetic phase transition. We discover that tuning the polarization of pump pulses can induce orbital selective photoexcitation of electrons. More specifically, while s-polarized light excites the states of the three hole bands, p-polarized light excites electrons essentially from α and β bands - which are responsible for magnetic order. Interestingly, within the magnetically ordered phase, the excitation due to the p-polarized pump pulses occurs at a time scale of 50 fs, which is significantly faster than the excitation induced by s-polarized light (200 fs). These results suggest that the relaxation of different ordered phases occurs at different timescales and this method of selective excitations can be used to disentangle complexity in multiband systems.

Finally, in **Chapter 7**, we summarize the core findings of our study and provide perspectives for future research work in the investigated materials and other complex systems.

References

[1] H. Bethe, "Theorie der Beugung von Elektronen an Kristallen." *Annalen der Physik* **87**, 55 (1928).

[2] A. Sommerfield, "Zur Elektronentheorie der Metalle auf Grund der Fermischen Statistik." *Zeitschrift für Physik* **47**, 1 (1928).

[3] F. Bloch, "Bemerkung zur Elektronentheorie des Ferromagnetismus und der elektrischen Leitfähigkeit." *Zeitschrift für Physik* **57**, 545 (1929).

[4] A. H. Wilson, "The theory of electronic semi-conductors." *Proceedings of the Royal Society London A* **133**, 458 (1931).

[5] A. H. Wilson, "The theory of electronic semi-conductors." *Proceedings of the Royal Society London A* **134**, 277 (1931).

[6] G. Grüner, "Density Waves In Solids (1st edition)." CRC Press, 1994.

[7] N. F. Mott, "Metal-Insulator Transition." *Reviews of Modern Physics* **40**, 677 (1968).

[8] M. Imada, A. Fujimori, and Y. Tokura, "Metal-insulator transitions." *Reviews of Modern Physics* **70**, 1039 (1998).

[9] R. S. Knox, "Theory of Excitons." Academic Press, New York and London, 1963.

[10] J. Bardeen, L. N. Cooper, and J. R. Schrieffer, "Microscopic Theory of Superconductivity." *Physical Review* **106**, 162 (1957).

[11] A. Zimmers, L. Aigouy, M. Mortier, A. Sharoni, Siming Wang, K. G. West, J. G. Ramirez, and I. K. Schuller, "Role of Thermal Heating on the Voltage Induced Insulator-Metal Transition in VO_2." *Physical Review Letters* **110**, 056601 (2013).

[12] P. A. Cox, "The electronic structure and chemistry of solids." Oxford University Press, 1987.

[13] D. Jérome, T. M. Rice and W. Kohn, "Excitonic insulator". *Physical Review* **158**, 462 (1967).

[14] D. J. Hilton, R. P. Prasankumar, S. A. Trugman, A. J. Taylor and A. D. Averitt, "On Photo-Induced Phenomena in Complex Materials: Probing Quasiparticle Dynamics using Infrared and Far-Infrared Pulses." *Journal of the Physical Society of Japan* **75**, 011006 (2006).

[15] U. Bovensiepen and P. S. Kirchmann, "Elementary relaxation processes investigated by femtosecond photoelectron spectroscopy of two-dimensional materials." *Laser and Photonics Reviews* **6**, 589 (2012).

[16] R. J. D. Miller, "Femtosecond crystallography with ultrabright electrons and x-rays: capturing chemistry in action." *Science*, **343**, 1108 (2014).

[17] D. J. Hilton, "Ultrafast Pump–Probe Spectroscopy: Optical techniques for solid state materials characterization." edited by R. P. Prasankumar A. J. Taylor. CRC Press - Taylor and Francis Group (2012).

[18] M. L. M. Balistreri, *et al.*, "Tracking femtosecond laser pulses in space and time." *Science* **295**, 1080 (2001).

[19] U. Bovensiepen, H. Petek and M. Wolf, "Dynamics in Solid States Surfaces and Interfaces." Volume 1, Current Developments, Wiley-VCH, Weinheim (2010).

[20] H. Ichikawa *et al.*, "Transient photoinduced hidden phase in a manganite." *Nature Materials* **10**, 101 (2011).

[21] T. Rohwer *et al.*, "Collapse of long-range charge order tracked by time-resolved photoemission at high momenta." *Nature* **471**, 490 (2011).

[22] S. Wall *et al.*, "Quantum interference between charge excitation paths in a solid-state Mott insulator." *Nature Physics* **7**, 114 (2011).

[23] B. Moritz, T. P. Devereaux, and J. K. Freericks, "Time-resolved photoemission of correlated electrons driven out of equilibrium." *Physical Review B* **81**, 165112 (2010).

[24] A. Tomeljak, H. Schäfer, D. Städter, M. Beyer, K. Biljakovic and J. Demsar, "Dynamics of Photoinduced Charge-Density-Wave to Metal Phase Transition in $K_{0.3}MoO_3$." *Physical Review Letters* **102**, 066404 (2009).

[25] F. Schmitt *et al.*, "Transient Electronic Structure and Melting of a Charge Density Wave in $TbTe_3$." *Science* **321**, 1649 (2008).

[26] G. Adhikary, B. Ressel, M. Stupar, P. R. Ribič, J. Urbančič, G. D. Ninno, D. Krizmancic, A. Thamizhavel, and K. Maiti, "Orbital-dependent electron dynamics in Fe-pnictide superconductors." *Physical Review B* **98**, 205142 (2018).

[27] I. Vaskivskyi, J. Gospodaric, S. Brazovskii, D. Svetin, P. Sutar, E. Goreshnik, I. A. Mihailovic, T. Mertelj, and D. Mihailovic, "Controlling the metal-to-insulator relaxation of the metastable hidden quantum state in 1*T*-TaS_2." *Science Advances* **1**, e1500168 (2015).

Contents

1 Overview of the relevant scientific background

This chapter begins with a description of the different classes of materials investigated in the thesis work, followed by brief introduction to the spectroscopic methods that have been used to study the material properties. Then, the various microscopic elementary processes in solids and the ultrafast phenomena induced in semiconductors by photoexcitation is shortly presented. Such a presentation will serve as a basis for understanding the dynamics of the charge carriers and the lattice in a solid.

1.1 Some intriguing ground states of matter

The discovery and understanding of new phases of matter arising from interactions between multiple microscopic degrees of freedom is one of the primary goals of condensed matter physics and provides fundamental hints for manufacturing new electronic devices. Such phases are classified on the basis of dominant interactions amongst the degrees of freedom. Some of the distinct, well-defined models are *Mott insulators* [1], characterized by the localization of electrons at the atomic sites due to strong repulsive Coulomb interaction, *excitonic insulators* [2], arising from the attractive electron-hole Coulomb interaction, and *Peierls insulators* [3], resulting from electron–phonon interactions, where a periodic lattice distortion drives the formation of a charge density wave (CDW). Besides these, other ground states include conventional *band insulators*, which are well explained by the nearly-free electron band theory, *Anderson insulators*, arising from electron–impurity interactions, and *topological insulators* [4], which have an energy gap for the bulk electronic states but have gapless conducting surface states due to band inversion, as a result of spin-orbital coupling.

1.1.1 Excitonic insulators

In this intriguing insulating phase, predicted decades ago [2, 5, 6], bosonic particles determine the physical properties of the system instead of electrons. An excitonic insulator (EI) is a many-body ground state which is realized in narrow-band gap materials. These can be semiconductors, where the conduction and valence bands are separated by a small energy gap ($E_G > 0$), or semimetals, where the two bands have a small overlap in energy ($E_G < 0$). In these systems, the attractive electron-hole Coulomb interaction may lead to a spontaneous formation of bosonic strongly-bound pairs of electrons and holes,

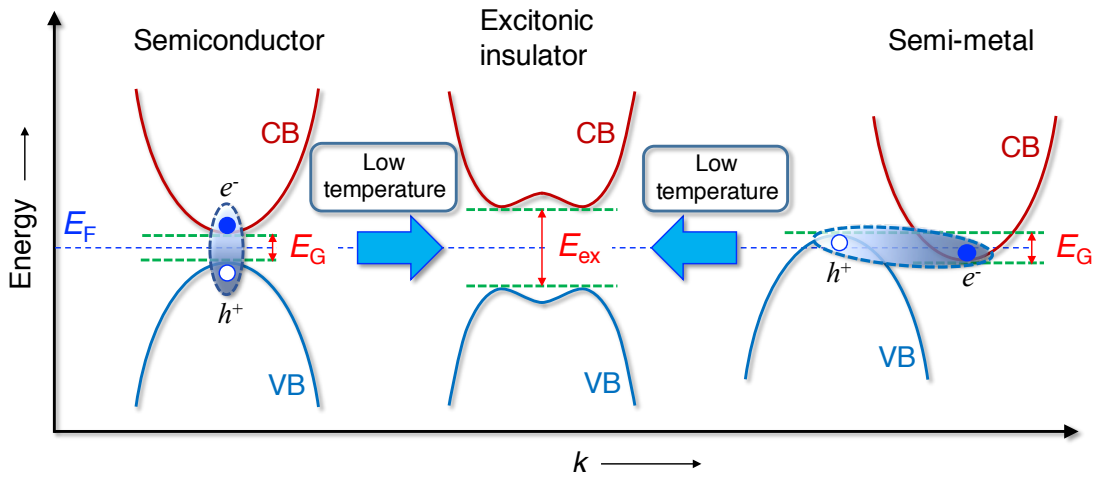

Figure 1.1: Schematics of the transition into the excitonic insulator state from a narrow energy gap (overlap) semiconducting (semi-metallic) state. A characteristic band flattening occurs if the exciton binding energy exceeds $\mid E_G \mid$, which is a pre-requisite for the spontaneous formation of excitons, thus leading to a larger energy gap $E_{ex} = E_G + E_B$. The filled (open) circles indicate electrons e^- (holes h^+), VB and CB are the valence and conduction bands, respectively, E_F is the Fermi level and k is the wavevector.

namely, excitons, and hence give rise to an unconventional insulating ground state. Such a state is characterized by a band gap corresponding to the exciton binding energy E_B. The transition from semi-metallic/semiconducting state into the EI state is illustrated in Figure 1.1. The exciton-binding energy is given by [6],

$$E_B = \frac{1}{2}\left(\frac{\mu^*}{m_e}\right)\left(\frac{1}{\epsilon^2}\right) \tag{1.1}$$

in Rydberg units. Here, μ^* is the reduced effective mass of electron and hole, m_e is the rest mass of an electron and ϵ is the dielectric constant of the material. The pre-requisite for the spontaneous formation of excitons is $E_B > \mid E_G \mid$ and the excitonic state will be most stable in a zero band gap material ($E_G = 0$). The spontaneous formation of excitons is suppressed with increasing values of $\mid E_G \mid$, which also leads to a decrease of the EI transition temperature T_C. As $\mid E_G \mid$ is increased such that it is comparable to or larger than the exciton binding energy, i.e., when $\mid E_G \mid \gtrsim E_B$, the excitonic phase becomes increasingly unstable against the semiconducting/semimetallic ground state. This is schematically represented in the EI phase diagram in Figure 1.2. There are two possible means of varying the band gap, i.e., by chemical substitution or applying physical pressure.

Since E_G is usually significantly larger than E_B in semiconductors and insulators preventing spontaneous formation of excitons, the search for potential excitonic insulators began focussing on materials with nearly zero band gap [7] or nearly zero band overlap. In the late 1960s, two main groups of materials were suggested for the realization of an EI ground state: divalent

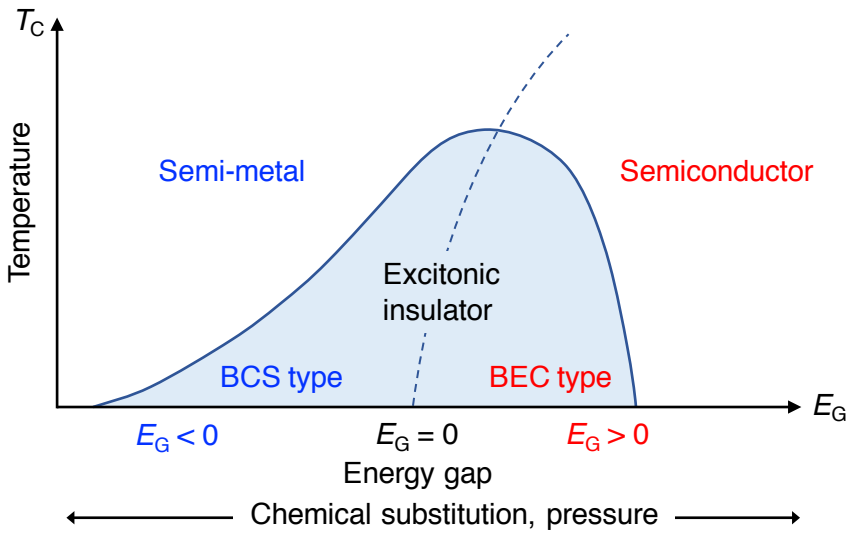

Figure 1.2: Modified from Ref. [8]. Schematic T_C vs. E_G phase diagram of an excitonic insulator (blue region): The dashed line indicates the crossover from semi-metallic to semiconducting behaviour. The energy gap E_G can be controlled by external parameters such as chemical substitution (doping) or pressure.

metals and 'group V' semi-metals and related alloys. In some narrow band gap materials, the exciton binding energy is very small making it almost impossible to observe the EI phase [9]. A way to realize EI phase in such materials is by quantum confinement, in which large Coulomb interactions can enhance E_B [10] and thus overcome E_G.

The EI phase has been identified in a number of materials, such as $TiSe_2$ [11, 12], Ta_2NiSe_5 [13], $TmSe_{1-x}Te_x$ [14], InAs/GaSb quantum wells [15], etc. Heat capacity measurements showed that the phase transition in some of these materials is strongly influenced by lattice and spin degrees of freedom [16, 17]. In semi-metals, formation of excitons leads to the opening of a band gap at the Fermi level as well as a modulation of charge density in real space, which are also characteristics of the Peierls phase (electron-lattice interaction). This makes it difficult to determine the origin of the insulating phase since the dominant interaction is not easily identified. An example of such a candidate excitonic insulator is 1T-$TiSe_2$ [18, 19]. To distinguish between the Peierls and EI phases in such candidates, it is crucial to know the electron-phonon coupling strength in the target material. The smaller the value of the coupling constant, the smaller is the periodic lattice distortion (PLD). In that case, an occurrence of the CDW phase will rule out the PLD scenario and unambiguously identify the EI phase. An example of such a semi-metallic system is Sb [20].

The stabilization of an EI ground state may involve broken lattice symmetries: translational symmetry is destroyed if the excitons are formed in an indirect band gap material [21], while breaking of point-group symmetry occurs in other cases [22]. There are different regimes in the phase diagram of an excitonic insulator [6, 23, 24], namely, the BCS regime, which captures

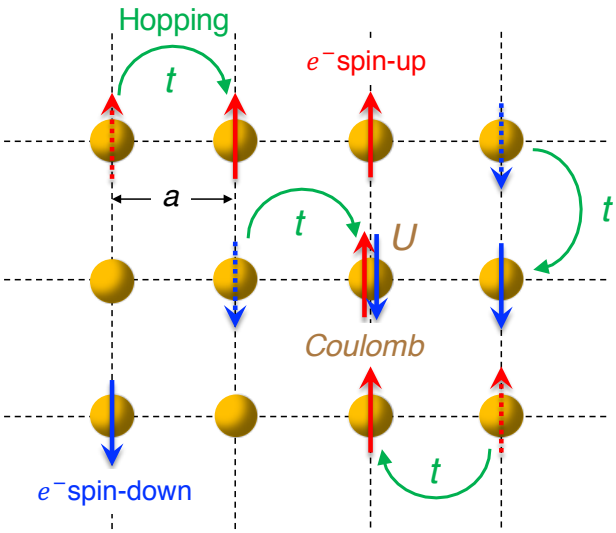

Figure 1.3: Modified from Ref. [37]. A schematic of the Hubbard model: electrons hop from one lattice site to the other with a hopping amplitude t and the Coulomb repulsion energy between the electrons occupying the same lattice site is denoted by "U". Red and blue arrows correspond to electrons with spin-up and spin-down, respectively, yellow spheres denote the atoms, a is the interatomic distance.

the phase transition from a semi-metal to EI, and the BEC regime, explaining the transition for a narrow-gap semiconductor [see Figure 1.2]. Formation of a gap below T_C has been experimentally observed in electrical transport [25] and optical [26] measurements, and an anomalous flattened dispersion of the hole-like valence band is considered as a fingerprint of the EI phase, see Figure 1.1.

1.1.2 Mott-Hubbard insulators

The early classification of solid-state systems into metals and insulators is based on the filling of electronic bands, and this description holds within the framework of non-interacting or weakly interacting electron systems. In the non-interacting electron theory, periodicity of the lattice structure inside a crystal is responsible for the formation of band structure. The basic distinction between metals and insulators was established during the early development of quantum mechanics [27, 28, 29]. Although the band picture was successful in many respects, several transition-metal oxides with a partially filled d-electron band, that were expected to be metallic, did not fulfill the theoretical prediction and were reported to be insulators. A typical example of such a material is nickel oxide NiO [30]. The importance of electron interactions in solids was brought forward by Mott and Peierls [31], who proposed that strong Coulomb repulsion between electrons (electron-electron correlations) could be the origin of the insulating behavior in compounds having a partially filled band near E_F. Mott took the first important steps [32, 33, 34, 35] towards understanding how electron-electron correlations could explain the insulating state, and we call this state the Mott insulator. The outcome of electron cor-

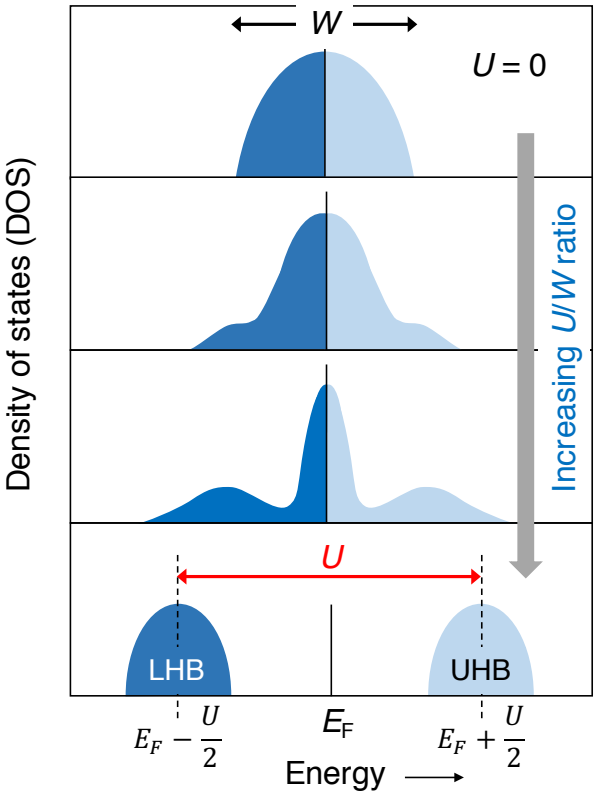

Figure 1.4: Modified from Ref. [36]. Evolution of the density of states with "U/W" ratio for a half-filled band at Fermi level E_F. "U" stands for Coulomb repulsion energy, "W" is the bandwidth, LHB and UHB are the lower and upper Hubbard bands, respectively.

relations can be understood by slowly bringing together a large number of monovalent metallic atoms [37]. Each atom contributes one electron, which can move in the periodic lattice formed by the ion cores and is subjected to the Coulomb repulsion by other electrons. The possibility of electrons moving from one lattice site to the other depends on the distance between the atoms. During electron hopping between different sites, the presence of two electrons at the same lattice site will cause intra-site Coulomb repulsion between those electrons. In such a situation, there is an energy cost to be paid by the initially delocalized electrons due to on-site Coulomb interaction. If the interatomic distance is increased above its equilibrium value, the overlap between the outermost atomic orbitals will be smaller, leading to a narrow valence band. For very large interatomic distances, the overlap between the orbitals is minimal, and the hopping of the electrons among the lattice sites becomes difficult with the given kinetic energy. The intra-site Coulomb repulsion becomes dominant, and hence the repulsive energy cost exceeds the (kinetic) energy gain of the electron, leading to the localization of electrons at the lattice sites. This occurs above a critical interatomic distance, and the system becomes a Mott insulator, which cannot be described within the framework of the nearly-free electron band theory of solids.

The most widely used theoretical model to understand Mott physics is the Hubbard model [38, 39], schematically shown in Figure 1.3. This model is represented by a Hamiltonian [40] consisting of two terms:

$$H = -t\sum_{ij,\sigma} c^{\dagger}_{i,\sigma}c_{j,\sigma} + U\sum_{i} n_{i\uparrow}n_{i\downarrow} \tag{1.2}$$

where, $c^{\dagger}_{i,\sigma}$ and $c_{i,\sigma}$ are the creation and annhilation operators of an electron with spin σ at the i-th ion site, t is the hopping amplitude and is taken to be positive, U is the Coulomb repulsion energy, and $n_i = c^{\dagger}_i c_i$ is the number operator giving the occupancy at site i. The first term represents the kinetic energy defined by the hopping of electrons between different lattice sites in a solid and the second term is the electrostatic Coulomb repulsion between the electrons at the same lattice site. There is a competition between these two terms since the hopping term favours delocalization of electrons and the repulsion term favours electron localization at the lattice sites. According to the Hubbard model, the variables that determine the basic properties of correlated electron systems [41] are the ratio U/t (or U/W where W is the electron bandwidth determined from t), the temperature and the electron density n. For a half-filled band near E_F, the Mott insulating phase is realized in a solid for large distances between the atoms indicating the situation where $U \gg t$. On the other hand, for small interatomic distances where $U \ll t$, the solid with a half-filled band will behave as a metal. Hence, it is expected that there will be critical value of U/t for a metal-insulator transition to occur. Without any electron-electron interactions, the density of states reflects the situation of a metal with a single band across the Fermi level. However, in the Mott phase, on-site Coulomb repulsion among the electrons will split this single band into two bands, namely, the upper and lower Hubbard bands (UHB and LHB, respectively) [41, 42], separated by an energy gap $\Delta \approx U$. This is represented in Figure 1.4.

Mott insulators represent a large class of materials with half-filled d or f orbitals, which are supposed to be metallic according to conventional band theory, but are found to be insulating in nature [43, 44, 45]. Examples of such materials are MnO, mixed-valence systems such as, $La_{1-x}Sr_xMnO_3$ and Fe_3O_4, nuclear fuel materials UO_2 and Pu, some organic compounds, etc. Some of the well studied Mott insulators include Cr-doped V_2O_3, ternary chalcogenides ($GaMo_4S_8$, $GaTa_4Se_8$), high T_c cuprates and the dichalcogenide 1T-TaS_2 [37]. A first order phase transition from a high conductivity phase to a high resistivity phase is a common feature in all these systems. Mott transition can be controlled by external parameters such as pressure, which is able to tune the hopping amplitude t, and chemical doping which can change the Coulomb repulsion energy U [44]. Despite the success of the Hubbard model in describing the Mott transition in several compounds, a complete understanding of the interplay between different ordered phases, for example, charge density wave state coexisting with the Mott phase, requires effects due to electron-electron and electron-phonon interactions to be distinguished [46]. This is possible by monitoring the dynamics of the material under non-

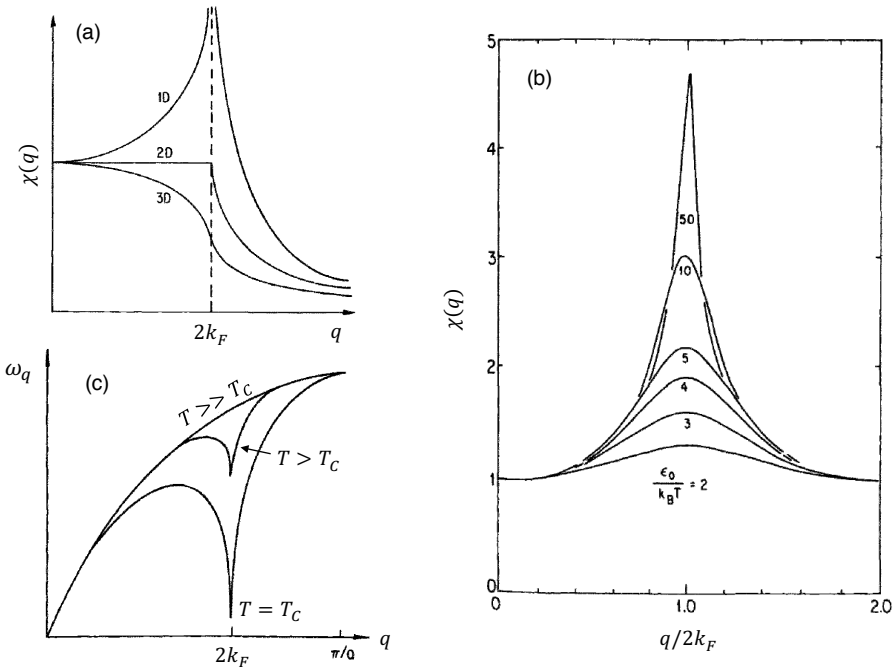

Figure 1.5: Taken from Ref. [54]. (a) Dependence of the Lindhard response function $\chi(q)$ on dimensionality. (b) The response function of a 1D electron gas at different temperatures. (c) Phonon dispersion relation of a 1D metal at different temperatures, T_C is the CDW transition temperature.

equilibrium conditions [47].

1.1.3 Charge and Spin density waves

One of the consequences of reduced dimensionality of the electronic structure in metals is the formation of broken symmetry states, known as density waves, brought about by electron-phonon or by electron-electron interactions. The resulting ground state consists of a periodic spatial variation of the charge density or spin density, leading to the charge density wave (CDW) and the spin density wave (SDW) states, respectively, below a critical temperature T_C. The existence of charge density waves was first proposed by Fröhlich in 1954 [48] and by Peierls in 1955 [3, 49], while spin density waves were postulated by Overhauser in 1962 [50, 51]. Experimental evidence for these ground states was found much later, when materials with a linear chain structure and metallic properties were discovered and investigated.

The following provides a general description of the density waves in solids. For a time independent potential $\phi(\mathbf{r})$ acting on an electron gas ($\mathbf{q}$ is the wave vector),

$$\phi(\mathbf{r}) = \int \phi(\mathbf{q}) e^{i\mathbf{q}\cdot\mathbf{r}} d\mathbf{q} \tag{1.3}$$

the rearrangement of the charge density is expressed in terms of an induced

charge $\rho^{ind}(\mathbf{r})$.

$$\rho^{ind}(\mathbf{r}) = \int \rho^{ind}(\mathbf{q}) e^{i\mathbf{q}\cdot\mathbf{r}} d\mathbf{q} \tag{1.4}$$

The response of the electron gas is usually treated within the framework of linear response theory [52], such that

$$\rho^{ind}(\mathbf{q}) = \chi(\mathbf{q})\phi(\mathbf{q}) \tag{1.5}$$

where $\chi(\mathbf{q})$ is the Lindhard response function that defines the stability of the electron system [53]. In d dimensions, it is given by [54],

$$\chi(\mathbf{q}) = \int \frac{d\mathbf{k}}{(2\pi)^d} \frac{f_{\mathbf{k}} - f_{\mathbf{k+q}}}{\epsilon_{\mathbf{k}} - \epsilon_{\mathbf{k+q}}} \tag{1.6}$$

where, $f_{\mathbf{k}} = f(\epsilon_{\mathbf{k}})$ is the Fermi function. For a one-dimensional electron gas, the response function takes the following form [54]:

$$\chi(q) = -e^2 n(\epsilon_F) ln \left| \frac{q + 2k_F}{q - 2k_F} \right| \tag{1.7}$$

where $n(\epsilon_F)$ is the density of states at the Fermi level per spin direction and k_F is the Fermi wavevector. In one dimension, the response function diverges at $q = 2k_F$, as can be followed from Equation 1.7 and is shown in Figure 1.5(a), leading to a divergent charge redistribution. This suggests that at $T = 0$, the electron gas is unstable with respect to the formation of a periodically varying electron charge or electron spin density with wavelength $\lambda_0 = \pi/k_F$, which may be commensurate (λ_0/a is a rational number) or incommensurate (λ_0/a is irrational) with the underlying lattice (a being the lattice constant). The divergence of the response function comes from the particular topology of the Fermi surface called FS nesting, where large segments of the FS can be connected by a single wave vector $\mathbf{q}$. In Equation 1.6, the most significant contribution to the integral comes from pairs of electronic states for which $\epsilon_k = \epsilon_{k+q}$. Since the FS of a 1D electron gas consists of two points, $+k_F$ and $-k_F$, there is perfect FS nesting at $q = 2k_F$. In higher dimensions, perfect nesting is no longer possible leading to the removal of singularity at $q = 2k_F$ [see Figure 1.5(a)]. However, for highly anisotropic metals with $t_b/t_a \to 0$, $t_c/t_a \to 0$, perfect nesting may be obtained. Here, t is the hopping amplitude and a, b, c are the lattice constants. For a finite temperature $T > 0$,

$$\chi(2k_F, T) = -e^2 n(\epsilon_F) ln \frac{1.14\epsilon_0}{k_B T} \tag{1.8}$$

where ϵ_0 is an arbitrary cutoff which is usually chosen to be equal to Fermi energy ϵ_F. According to Equation 1.8, $\chi(2k_F)$ has a logarithmic divergence as $T \to 0$. Such a behaviour indicates the formation of density waves in solids at low temperatures and the transition temperature T_C is given by

$$k_B T_C = 1.14\epsilon_0 exp\left(\frac{-1}{g n(\epsilon_F)}\right) \tag{1.9}$$

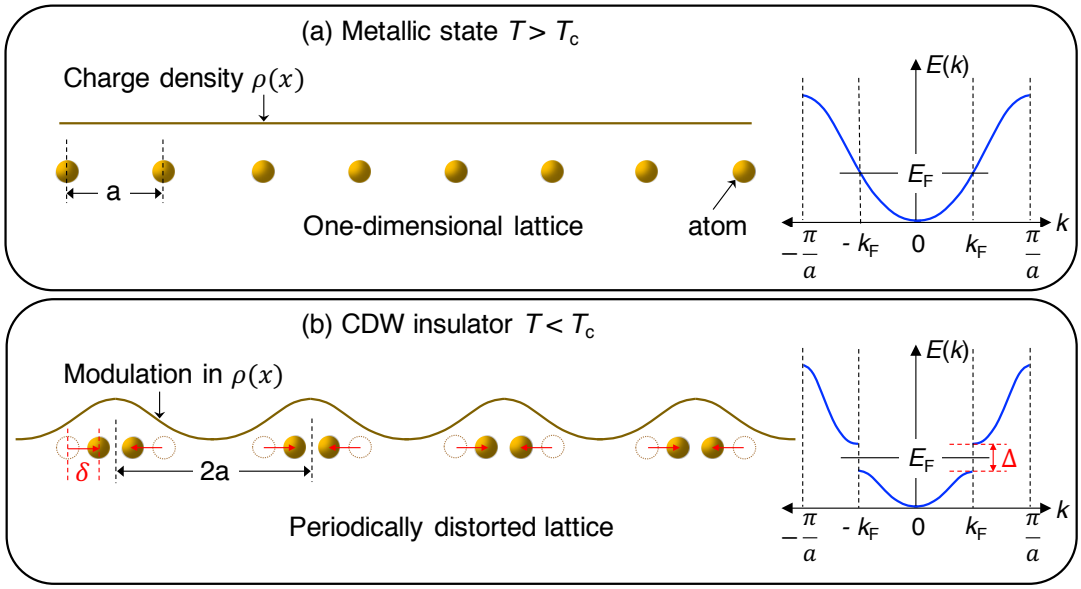

Figure 1.6: (a) A one-dimensional lattice of periodicity a and charge density $\rho(x)$ in its metallic state, at $T > T_C$ and its corresponding nearly-free electron E versus k band structure at half-filling up to k_F (Fermi wavevector) (b) For a distortion δ, the lattice periodicity changes from a to $2a$ driving a periodic modulation of the charge density. The new Brillouin zone boundary appears at $k_F = \pm\pi/2a$, leading to the opening of an energy gap Δ at the Fermi level E_F at $T < T_C$.

where g is a coupling constant which is independent of the wave vector. The temperature dependence of the response function is shown in Figure 1.5(b).

In the case of charge density waves, a consequence of electron-phonon interaction is the renormalization of phonon frequencies, ω_q. For a 1D electron gas, $\chi(q,T)$ has its maximum at $q = 2k_F$. With decreasing temperature, the renormalized phonon frequency $\omega_{ren,2k_F} \rightarrow 0$ and this defines the transition temperature (Equation 1.9 with g as the electron-phonon coupling constant) when a "frozen-in" lattice distortion occurs, known as the Kohn anomaly [55, 56] as shown in Figure 1.5(c). This identifies a second-order phase transition from a metallic state to a CDW state. The renormalization of the phonon frequencies also occurs in higher dimensions, however the reduction of the phonon frequencies is less significant. The electronic band structure is also strongly modified by the formation of charge density waves. Take a 1D system consisting of a linear chain of N atoms, where the nearest neighbour distance is a and the highest occupied energy band is half-filled [57]. For a finite lattice distortion δ shown in Figure 1.6, let the change in real space periodicity be from a to $2a$, which results in a reduction of the size of the Brillouin zone. An energy gap Δ, in the nearly-free electron band picture, opens up at the Fermi level E_F at the new BZ boundaries, $k = k_F = \pm\pi/2a$, turning the material into an insulator. A schematic of the formation of charge density wave in a 1D metal is shown in Figure 1.6. To experimentally confirm the features associated with a CDW state, transport measurements, scanning tunnelling microscopy (STM) and spectroscopy, inelastic neutron scattering

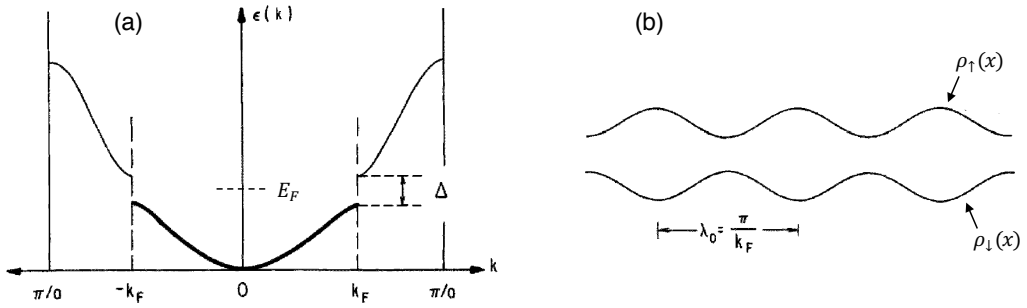

Figure 1.7: Taken from Ref. [54]. (a) Formation of an energy gap and (b) charge density modulation for the two spin subbands in the SDW ground state.

techniques can be utilized to determine the wavelength of the charge modulation, the temperature dependence of the Kohn anomaly in the phonon spectrum, etc.

For spin density waves, a consequence of the interaction between electrons with opposite spin is an enhanced magnetic susceptibility, $\chi_M(q) = f\,[\chi(q)]$, under an externally applied magnetic field [54]. This enhancement is most important for perturbations with $q = 2k_F$ because the maximum of $\chi(q,T)$ lies at this wave vector. $\chi_M(2k_F,T)$ continues to increase with decrease in temperature and has a divergence at T_C, which sets the temperature of phase transition from metallic to SDW state. The SDW state is characterized by the opening of a gap at the Fermi level [see Figure 1.7(a)] in both spin subbands, resulting in a metal-insulator transition. The ground state has a well defined magnetic response, similar to that of an antiferromagnet. A spin density wave can be viewed as two charge density waves, one for the "spin-up (↑)" and one for the "spin-down (↓)" subbands as shown in Figure 1.7(b). The charge density wave modulations in 1D are given by

$$\rho_\uparrow(x) = \rho_0(x) + S_0\cos(2k_Fx + \phi) \tag{1.10}$$

$$\rho_\downarrow(x) = \rho_0(x) + S_0\cos(2k_Fx + \phi + \pi) \tag{1.11}$$

where, $\rho_0(x)$ is the charge distribution (obtained from Bloch theorem) in the absence of density waves and S_0 is the amplitude of the CDWs. The resulting spin density variation is given by $\rho_\uparrow(x) - \rho_\downarrow(x) = 2S_0\cos(2k_Fx + \phi)$ with no modulation in the charge distribution $\rho_0(x)$. Both the spin rotational and translational symmetries are broken in the spin density wave state whereas, in CDW ground state, only the translational symmetry is lost. Transport and magnetic measurements are generally used to evaluate the essential characteristics of the SDW ground state.

A large number of organic and inorganic solids have crystal structures in which the underlying lattice exhibits a linear chain-like structure. Some of the well known CDW materials [54] are mixed valence Platinum chain compounds, transition metal chalcogenides ($NbSe_3$, TaS_3), transition metal oxides ($A_{0.3}MoO_3$ where A = K, Rb or Tl), organic charge-transfer system

TTF-TCNQ [58, 59], etc. In cuprate superconductors such as $Bi_2Sr_2CaCu_2O_{8+\delta}$ (Bi2212), $YBa_2Cu_3O_{6+x}$ (YBCO), different charge ordering phenomena have been reported [60, 61] but suprisingly, periodic lattice distortion is not the driving force behind the formation of CDW phase in these materials. This pointed towards the crucial role of electron correlations in the formation of CDW phase in cuprates [62]. The well known examples of SDWs include Chromium and Bechgaard's salt $(TMTSF)_2PF_6$ [63]. The parent compounds of many Fe-based superconductors ($CaFe_2As_2$, $EuFe_2As_2$, etc.) also display spin density wave transition.

1.2 Photoemission spectroscopy

Photoemission (or photoelectron) spectroscopy, also known as PES, is a general term that refers to all those techniques based on the application of the photoelectric effect originally observed by Hertz [64] and later explained as a manifestation of the quantum nature of light by Einstein [65]. The development of PES as an analytical tool dates back as far as 1956 and is largely attributable to Kai Siegbahn [66], for his contribution to the development of high-resolution electron spectroscopy, and William L. Jolly, who pioneered core-level electron spectroscopy.

1.2.1 Fundamental description

When a sample is irradiated with photons having energy greater than its work function, Φ, electrons are ejected out of the sample and escape in different directions. Energy conservation gives:

$$E_{kin} = h\nu - \Phi - |E_B| \tag{1.12}$$

where E_{kin} is the kinetic energy of the photoemitted electron, $h\nu$ is the energy of the incident photon and E_B is the binding energy of the electron (referenced with respect to E_F). The energetics of the photoemission process is shown in Figure 1.8 where E_{kin} is given with respect to the vacuum level, E_{vac}. The electrons photoemitted out of the sample surface can be collected by a hemispherical analyser consisting of an electrostatic lens system and imaged onto the detector (its working principle is presented in Chapter 2). The geometry of a photoemission experiment is shown in Fig 1.9. The conventional setup for photoemission gives information about the density of states (DOS) of a solid shown in Figure. 1.8.

The PES spectrum comprises (1) different peaks, corresponding to different electronic energy levels and transitions, and (2) a non-uniform background originating from inelastically scattered photoelectrons inside the material called secondary photoelectrons. The peaks in the spectrum can have different origins such as, core levels, valence band, Auger transitions, satellites and energy loss peaks due to plasmons. Analysis of the energy and width of the peaks provides essential information on the lifetime of the photohole and

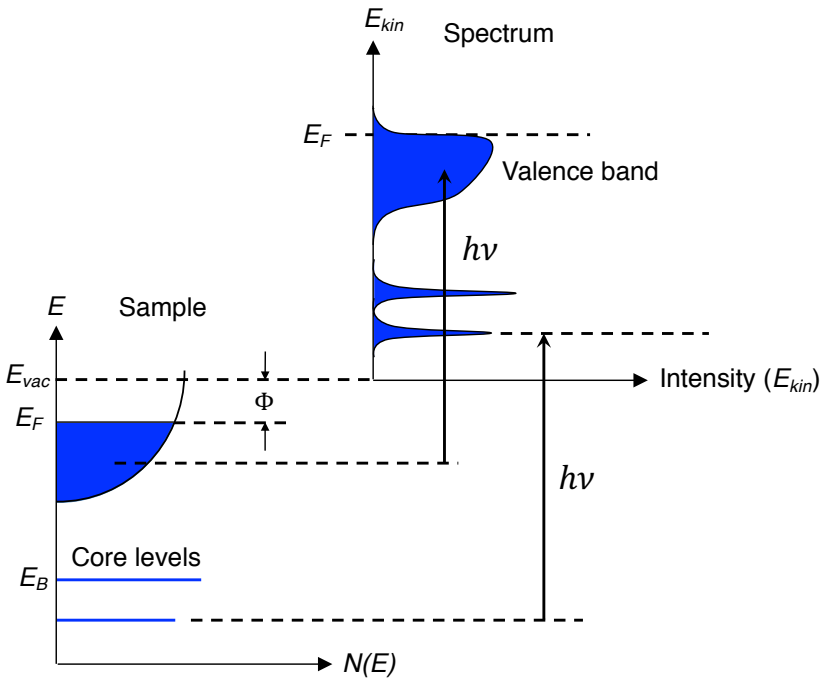

Figure 1.8: Modified from Ref. [67]. Energetics of the photoemission process: (right) The intensity of the photoemitted electrons measured as a function of the kinetic energy E_{kin} is expressed in terms of (left) the binding energy E_B for the electronic density of states inside the solid ($E_B = 0$ at E_F).

chemical properties of the atoms in the system. The core-level energy states are almost independent of momentum as the electrons occupying these states are localized electrons. The photoelectrons detected in valence band photoemission, are delocalized and their energy depends on the momentum. Such electrons can be photoemitted using photons in the energy range of ultraviolet and soft X-ray regime. The application of the photoemission process to the study of momentum-dependent electronic structure of solids is called angle-resolved photoelectron spectroscopy (ARPES). The short mean free path of electrons inside the solid makes PES surface sensitive. It is clear from the mean free path diagram in Figure 1.10 that only a thin layer, of a few Å, close to sample surface can be studied by PES. An extensive overview of literature on the subject is available in Refs. [68, 69].

1.2.2 Theoretical model

The photoemission process is usually treated by theory under the assumption of the independent-particle picture and of the sudden approximation, i.e., disregarding the many-body interactions as well as the relaxation of the system during photoemission itself. Within this approach, a simplified description of the process is given by the phenomenological 'three-step model', introduced by Berlung and Spicer in 1964 [70, 71, 72]: (1) Optical excitation of the electron in the bulk, (2) Travel of the excited electron to the surface, (3) Escape of the

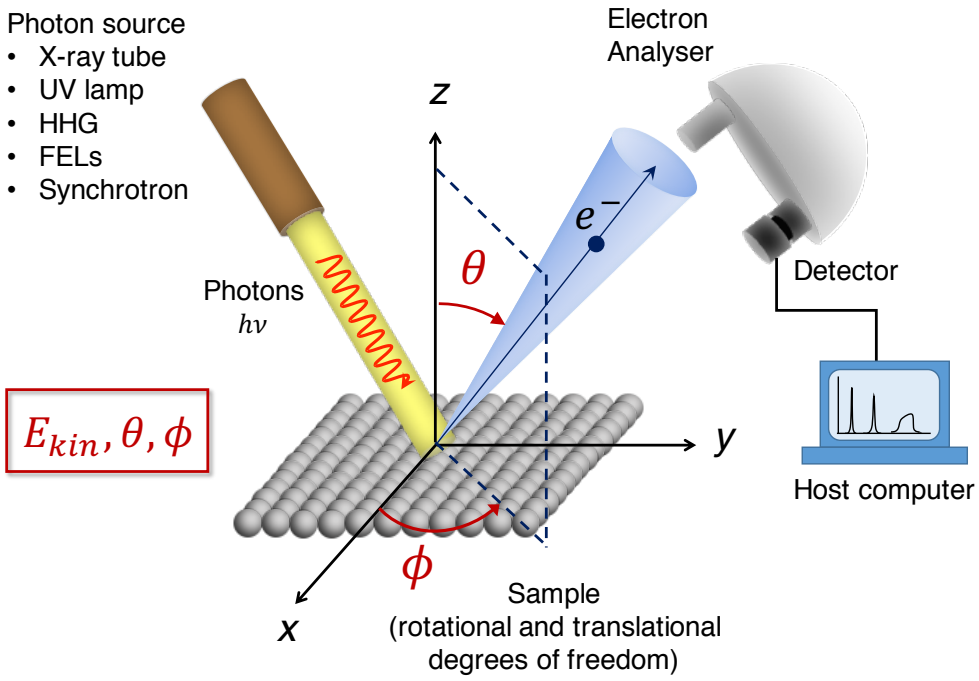

Figure 1.9: Geometry of a photoemission experiment: The different components of electron momentum are specified by the polar (θ) and azimuthal (ϕ) angles. The photo-emitted electrons are collected by an electron analyser and the detector measures the number of photoelectrons entering the analyzer slit as a function of E_{kin} and angle of emission θ.

photoelectron into vacuum. The transition probability w_{fi} for an optical excitation between the ground state $|\Psi_i\rangle$ to one of the possible final states $|\Psi_f\rangle$ can be approximated by Fermi's golden rule [68]:

$$w_{fi} = \frac{2\pi}{\hbar}|\langle\Psi_f|H_{int}|\Psi_i\rangle|^2\delta(E' - E^0 - h\nu) \tag{1.13}$$

where H_{int} is the perturbation Hamiltonian, E^0 and E' are the energies of the initial and final electronic states, respectively, and the incident photon energy is $h\nu$. The Hamiltonian of an electron in an electromagnetic field is,

$$\begin{aligned} H &= \frac{1}{2m}\left[\mathbf{p} + \frac{e}{c}\mathbf{A}(\mathbf{r})\right]^2 - e\phi_s + V(\mathbf{r}) \qquad (1.14)\\ &= \frac{p^2}{2m} - e\phi_s + \frac{e}{2mc}\left[\mathbf{A}(\mathbf{r})\cdot\mathbf{p} + \mathbf{p}\cdot\mathbf{A}(\mathbf{r})\right] + \frac{e^2}{2mc^2}|\mathbf{A}(\mathbf{r})|^2 + V(\mathbf{r}) \\ &= H_0 + H_{int} \\ H_0 &= \frac{p^2}{2m} + V(\mathbf{r}) \qquad (1.15) \end{aligned}$$

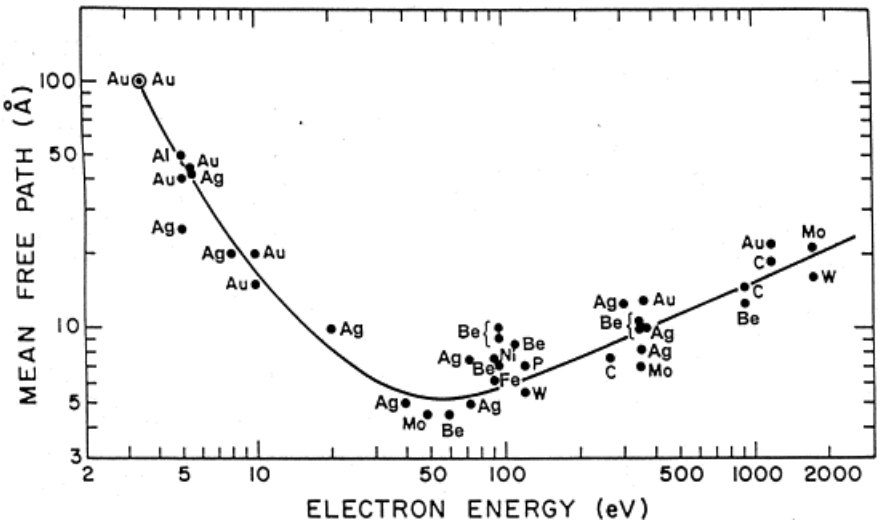

Figure 1.10: From [73]. Universal curve of the electron inelastic mean free path as a function of its kinetic energy. The dots indicate the mean free path for different elements.

where, H_0 is the unperturbed Hamiltonian, $\mathbf{p}, m, e$, are the momentum, mass, charge of an electron, respectively, and c is the speed of light in vacuum. $\mathbf{A}(\mathbf{r})$ and ϕ_s are the vector and scalar potentials of the incident electromagnetic field. The quadratic term ($\simeq \mathbf{A}^2$) can be neglected since it has considerable effect only in case of intense electromagnetic fields. Using the commutator relation $[\mathbf{p}, \mathbf{A}] = -i\hbar\nabla \cdot \mathbf{A}$, we get,

$$H_{int} = +\frac{e}{mc}(\mathbf{A}\cdot\mathbf{p}) + \frac{i\hbar e}{2mc}(\nabla\cdot\mathbf{A}) - e\phi_s \tag{1.16}$$

With the choice of Coulomb gauge, $\nabla \cdot \mathbf{A}$ can be set to zero. Since there are no sources present, ϕ_s can also be made zero. Hence,

$$H_{int} = +\frac{e}{mc}\mathbf{A}\cdot\mathbf{p} \tag{1.17}$$

Therefore, the transition probability takes the following form,

$$w_{fi} \propto \frac{2\pi}{\hbar}\left[|\langle\Psi_f|\mathbf{A}\cdot\mathbf{p}|\Psi_i\rangle|\right]^2 \delta(E' - E^0 - h\nu) \tag{1.18}$$

During its propagation towards the sample surface, the electron suffers inelastic collisions, giving rise to a continuous background in the photoemission spectrum, which is usually subtracted during data analysis. The electron originating at a depth z below the surface and at an angle θ with respect to the normal of the sample surface has to travel a distance $z/\cos\theta$ to reach the surface. Hence the photocurrent originating from a layer of thickness dz at a depth z is given by,

$$dI(z) \propto \exp(-z/\lambda\cos\theta)dz \tag{1.19}$$

where λ is the mean free path of the electron which depends on its kinetic energy, as can be seen from Figure 1.10. It shows that the shortest (< 5 Å)

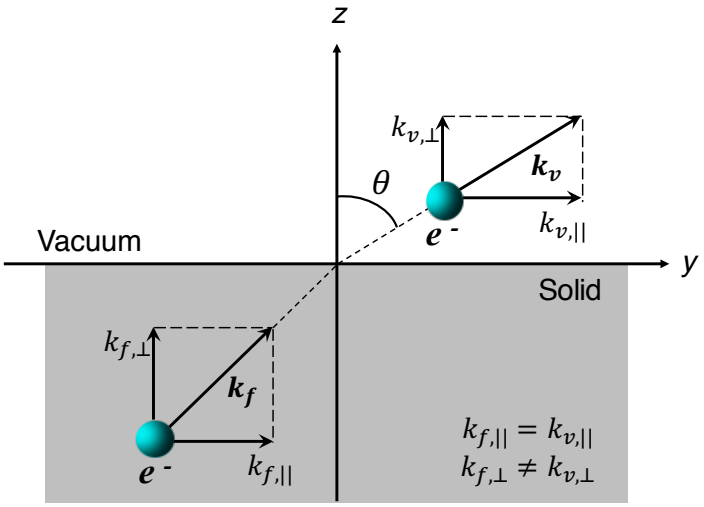

Figure 1.11: Schematic showing the conservation of wave vector during a photoemission process: As the electron is transmitted across the surface of the solid, only the component of momentum parallel to the surface, $\hbar k_{||}$, is conserved.

mean free path of an electron lies in the kinetic energy range of 40-100 eV, due to which ultra-violet photons are used to perform the most surface sensitive photoemission measurements. High photon energies of 5 keV or more are used to probe electrons coming from the bulk of the material, where the electron mean free path is approximately 40 Å or more [68, 74].

After the photoelectron has travelled to the sample surface, the escape of the electron into the vacuum is possible only when the kinetic energy associated with the perpendicular momentum component exceeds the sample's work function. Since the sample surface does not perturb the translational symmetry in the xy plane, the parallel momentum component is conserved but due to the abrupt change in potential along the z-axis, the perpendicular momentum component is not conserved across the sample surface [see Equations 1.20 and 1.21].

$$\left|\frac{\mathbf{p}_{v,||}}{\hbar}\right| = |\boldsymbol{k}_{v,||}| = |\boldsymbol{k}_{f,||}| \tag{1.20}$$

$$|\boldsymbol{k}_{v,\perp}| \neq |\boldsymbol{k}_{f,\perp}| \tag{1.21}$$

Here, $\mathbf{p}_v$ is the momentum of the electron in vacuum and $E_{kin} = \hbar^2|\boldsymbol{k}_v|^2/2m$. The conservation laws of momentum during a photoemission process are depicted in Figure 1.11.

For completeness, we mention that the quantum mechanical description of the photoemission process is given by the 'one-step' model [75]. According to this model, photon absorption, electron removal and its detection are treated as a single coherent process. The wave functions of the initial and final states must obey the appropriate boundary conditions at the surface of the solid and the conservation laws of energy and momentum. Though the outcomes

from this model offer more accuracy in some cases, due to its simplicity, the three-step model is more suitable for introductory purposes.

1.2.3 Angle-resolved photoemission

Angle-resolved photoemission spectroscopy (ARPES) is a highly advanced spectroscopic method that allows the direct experimental study of the energy band structure of solids. The kinematics of the photoemission process in a nearly-free electron model [67] is shown in Figure 1.12. The measured observables are the kinetic energy E_{kin} and the emission angle θ of the photoemitted electrons with respect to the sample normal. From these parameters, the wave vector or linear momentum $\boldsymbol{k}_v = \mathbf{p}/\hbar$ of the photoelectrons in vacuum is determined. Its modulus is given by:

$$k_v = |\boldsymbol{k}_v| = \sqrt{\frac{2mE_{kin}}{\hbar^2}} \tag{1.22}$$

For an electron photoemitted at an angle θ [see Figure 1.11], the components of momentum parallel ($||$) and perpendicular ($\perp$) to the sample surface are given by the following relations:

$$k_{v,||} = k_{v_y} = k_v \sin\theta \tag{1.23}$$

$$k_{v,\perp} = k_{v_z} = k_v \cos\theta \tag{1.24}$$

Starting from the observables defined by the experiment, the objective is to deduce the electronic dispersion relations $E(\boldsymbol{k})$ for the solid left behind, which means the relation between binding energy E_B and momentum $\boldsymbol{k}$ for the electrons propagating inside the solid. The energy conservation law relating the kinetic energy of the photoelectron to the binding energy of the state inside the solid is given by Equation 1.12.

The next step is to gain knowledge of $\boldsymbol{k}$ inside the crystal [76]. Due to the abrupt potential change along the z axis, the perpendicular component of momentum k_z is not conserved across the sample surface. Since the parallel component remains unchanged at the surface, conservation of momentum gives:

$$k_{f,||} = k_{v,||} = k_v \sin\theta \tag{1.25}$$

To determine the perpendicular component of momentum ($k_{f,\perp}$), one can adopt the dispersion relation for a nearly-free electron model. The dispersion relation for a Bloch state is:

$$E(\boldsymbol{k}) = -E_0 + \frac{\hbar^2 k^2}{2m} \tag{1.26}$$

where $E_0 > 0$ and denotes the bottom of the valence band in Figure 1.12 (E_0 and E_f are referenced to E_F, while E_{kin} is referenced to the vacuum level E_{vac}). Since the energy of the final state E_f is equal to $E_{kin} + \Phi$ (which follows from

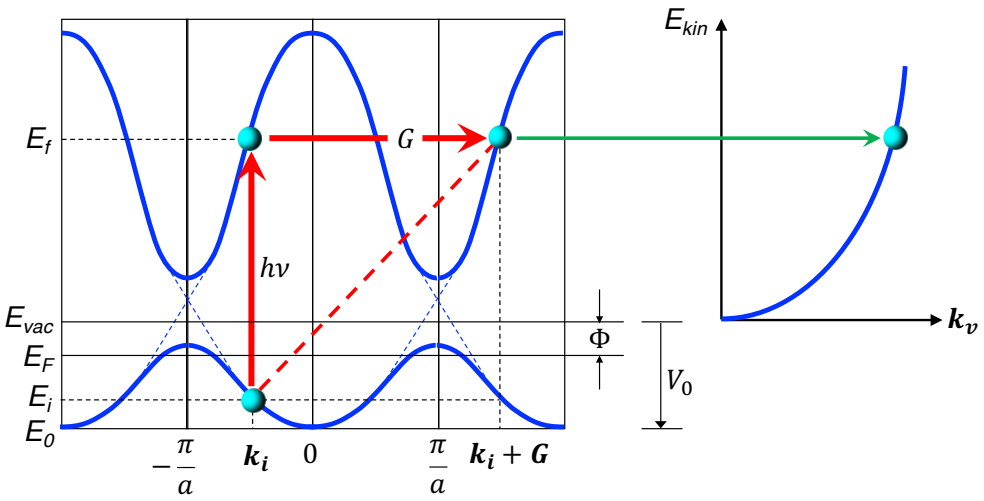

Figure 1.12: Modified from Ref. [67]. (Left) Schematic representation of the kinematics of the photoemission process for a nearly-free electron model. $\boldsymbol{G}$ is the reciprocal lattice vector, the blue circle denotes the electron. (Right) Free-electron final state in vacuum.

Figure 1.12) and $\hbar^2 k_{f,||}^2/2m = E_{kin}\sin^2\theta$ [according to Equations 1.22 and 1.25], one obtains the following relation for the perpendicular component:

$$k_{f,\perp} = \sqrt{\frac{2m}{\hbar^2}(E_{kin}\cos^2\theta + V_0)} \tag{1.27}$$

Here, $V_0 = \phi + E_0$ is defined as the inner potential [see Figure 1.12]. V_0 can be determined, theoretically, from band structure calculations or, experimentally, from the observed periodicity of the dispersion $E(k_{f,\perp})$ [67]. During an optical transition, photon absorption provides the electron only with the energy needed to get to the final state while the additional momentum required to reach the final state is offered by the crystal: $\boldsymbol{k}_f - \boldsymbol{k}_i = \boldsymbol{G}$, where $\boldsymbol{k}_i$ is the wavevector of the electron inside the solid before the absorption of a photon and $\boldsymbol{G}$ is the reciprocal lattice vector.

1.3 Ultrafast pump-probe spectroscopy

Pump-probe spectroscopy in the ultrafast time domain is an experimental technique used in the study of the dynamical properties of a material by employing ultrashort pulses. This section gives an introduction to the advent of this technique, followed by a description of the pump-probe method and the technique of time-resolved photoemission, which is the chosen experimental tool for the non-equilibrium studies in the thesis work.

1.3.1 Introduction

The observed electronic and optical properties of a material, such as, resistivity, dielectric constant, refractive index, etc. take origin from a complex

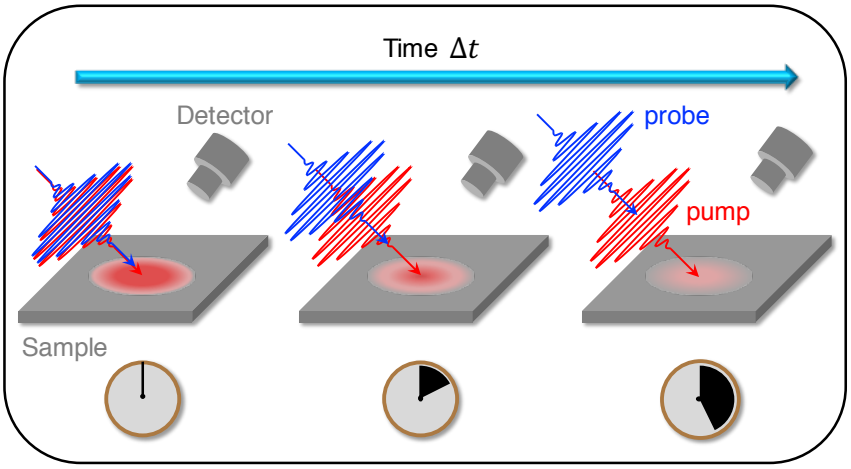

Figure 1.13: Principle of the pump-probe method for ultrafast spectroscopies: The pump and probe pulses are incident on the sample at $\Delta t = 0$ and the response of the system after photoexcitation ($\Delta t > 0$) is studied. Δt is the time delay between the pump and probe pulses.

interplay between charge, spin, orbital and lattice degrees of freedom that generally occurs on timescales ranging from 10^{-18} - 10^{-9} seconds, or longer. Standard electrical characterization techniques can be used to determine the complex dielectric function of the material. However, these electrical measurements are limited to a maximum bandwidth that is determined by the inverse of the system response time, i.e., the time constant ($\tau = RC$, for a first-order RC circuit) of the electrical components used. Electronic signals faster than this response time cannot be detected. Therefore, using the current electrical techniques, it is possible to perform measurements which are limited to timescales $>$ 0.1 nanoseconds (1 nanosecond = 10^{-9} secs). To overcome this limitation on the material response time and access relevant ultrafast timescales, alternative *non-electrical* methods are needed.

Experimental methods to measure the dynamical properties of materials on a femtosecond timescale have transformed our understanding of their electronic and optical properties. Pump–probe spectroscopies are perhaps the simplest experimental techniques that have enabled us to study different ultrafast phenomena inside matter under nonequilibrium conditions, which include dynamics of electron–electron interactions [77], coupling between electron, phonon, and spin subsystems [77, 78], photoinduced phase transitions [79, 80, 81, 82, 83, 84], and explaining the underlying electronic structure of complex materials [85, 86]. The advancement made in the generation of ultrashort pulses over the past two decades [87, 88] have made it possible to observe these fundamental processes. These developments have taken us from the picosecond (1 picosecond = 10^{-12} secs) timescale [89, 90, 91, 92] to the femtosecond (1 femtosecond = 10^{-15} secs) timescale [93, 94, 95, 96, 97] in the past decade and recently into the attosecond (1 attosecond = 10^{-18} secs) regime [98, 99, 100].

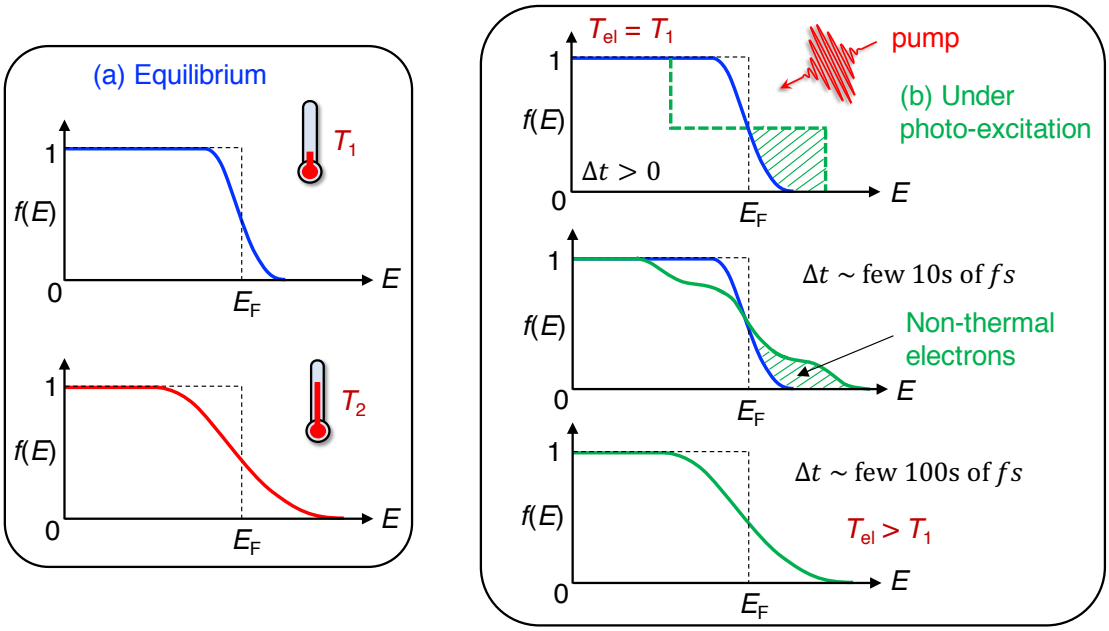

Figure 1.14: (a) Response of the electronic subsystem to a thermal change in equilibrium ($T_2 > T_1$). (b) Modified from Ref. [101]. Under photoexcitation of the sample, a non-thermal distribution of electrons is created. T_1 is the initial sample temperature, T_{el} is the Fermi-Dirac temperature of the thermalized electron population.

1.3.2 The pump-probe method

Pump-probe spectroscopy has the capability to provide distinct snapshots of an obervable that is evolving with time in a system under nonequilibrium, as shown by a schematic in Figure 1.13. In this method, matter (the sample) is perturbed from its equilibrium state by an ultrashort pump pulse and a probe pulse, subsequently incident on the sample at a certain time delay Δt, measures the photoinduced change in the measured observable of the material. From an experimental point of view, pump-probe technique necessitates a high temporal resolution [102] comparable to the fundamental timescales of the dynamics to be observed and an appropriate detection system to measure the intensity variation of the studied observable. This technique also takes advantage of the possibility of tuning the wavelengths of pump and probe pulses independently. The tunability of pump wavelength enables selective excitation of different energy states [103] while the variation of probe wavelength provides access to the system dynamics over different energy ranges.

The response of the system to the perturbation induced by the pump pulse is significantly different from its response towards an external stimulus, such as change in temperature in equilibrium. The differences appear in the Fermi-Dirac distribution of the electrons $f(E)$ and the Maxwell-Boltzmann distribution of the phonons $n(E)$ of the system. Upon ultrafast photoexcitation, a sudden injection of electrons into high-energy states destroys the thermodynamic equilibrium of the electron population with the lattice. Since $f(E)$ does not take into account such out-of-equilibrium electron distribution, an electronic

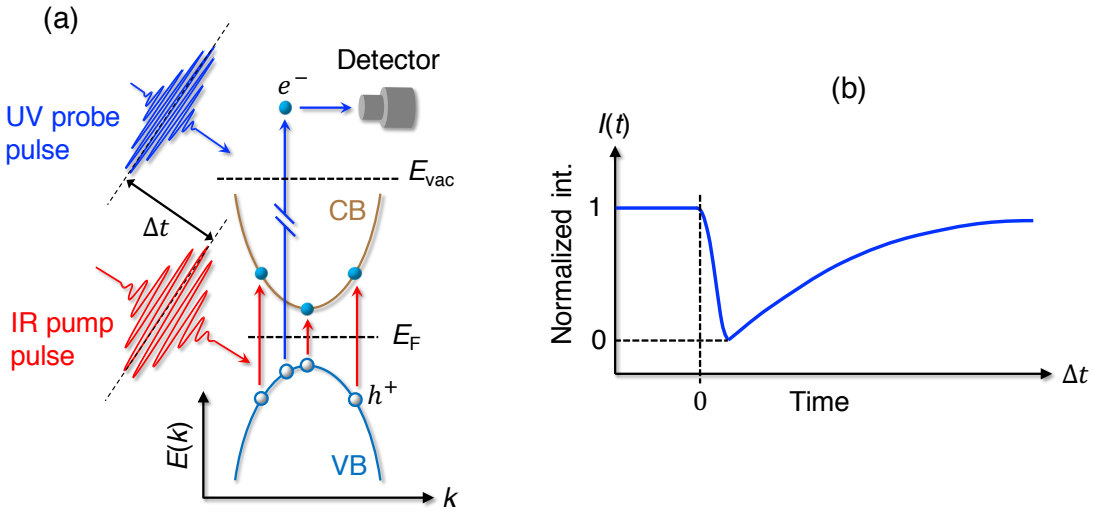

Figure 1.15: (a) Schematic illustration of trARPES technique: A low energy infrared (IR) pump pulse excites the electrons from the (occupied) valence band to the (unoccupied) conduction band and a higher energy ultra-violet (UV) probe pulse, arriving on the sample after time delay Δt, photoemits electrons from different energy levels inside the solid. (b) Normalized spectral intensity $I(t)$ of the valence band as a function of Δt. VB and CB are the valence and conduction bands while e^- and h^+ indicate electrons and holes, respectively.

temperature T_{el} cannot be precisely defined immediately after photoexcitation. However, as the electrons start thermalizing, the energy distribution of electrons around Fermi level E_F starts to resemble a Fermi-Dirac function at $\Delta t > 100$ fs [104] with T_{el} higher than the initial sample temperature. A sketch of the electron distribution and of the thermalization process in equilibrium and out-of-equilibrium conditions is shown in Figure 1.14. Understanding the evolution of the electronic subsystem during its thermalization provides information on the lifetime of excited states, and the fundamental coupling between different microscopic degrees of freedom. Under a critical photoexcitation strength, a dramatic change may be induced in the system properties [103], and consequently, the relaxation dynamics can follow completely new pathways giving rise to different scenarios. The system can undergo a photo-induced phase transition to its high temperature phase or/and it might evolve in a new phase which is inaccessible under equilibrium.

There are a number of pump-probe techniques in the field of microscopy and spectroscopy that are used according to the information they can provide and this depends on the observable that is being measured [103]. Some of the pump-probe techniques include time-resolved X-ray absorption spectroscopy, time-resolved photoemission spectroscopy, time-resolved Raman spectroscopy, time-resolved magneto-optical spectroscopy, time-resolved photoluminiscence spectroscopy, pump-probe microscopy, etc. Time- and angle-resolved photoemission spectroscopy is the pump-probe approach that augments and complements conventional ARPES by folding in femtosecond time resolution. Fur-

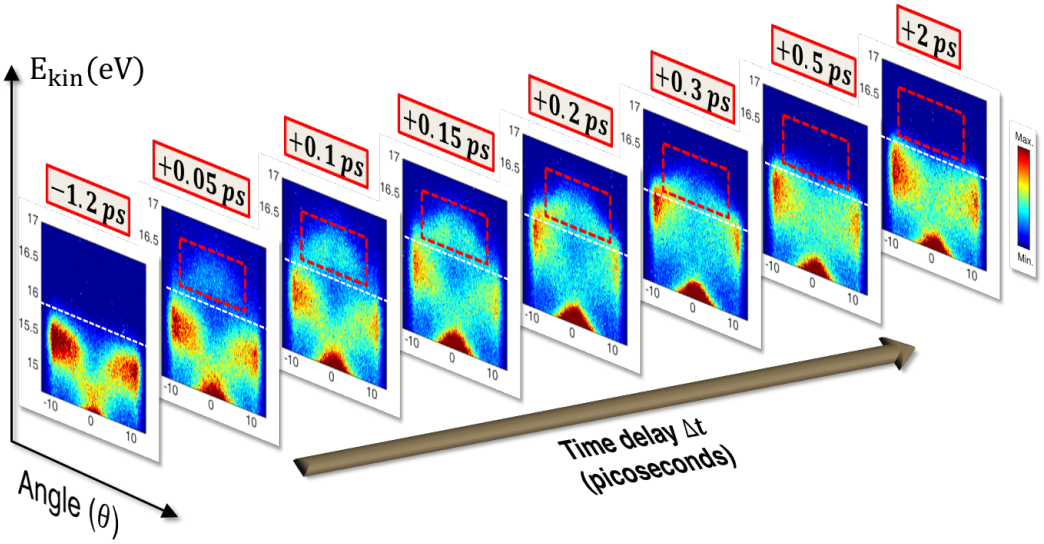

Figure 1.16: Evolution of the band structure of 1T-TaS_2 in the ultrafast time domain: ARPES snapshots at different time delays Δt. The white dashed line marks the Fermi level E_F. At $\Delta t > 0$, the transient occupation of the states above E_F (indicated by the red box) is accompanied by a depopulation of the states below E_F. At later times, there is a subsequent decay of the excited carrier population.

ther description of the trARPES technique is presented in the next section.

1.3.3 Angle-resolved photoemission spectroscopy in the ultrafast time domain: trARPES

Time- and angle-resolved photoemission spectroscopy is the most suitable pump-probe technique for investigating the photo-induced dynamics of the electronic band structure in a solid. trARPES allows the study of transient distribution of electrons and holes, following the optical perturbation of the equilibrium ground state of a material as a function of energy, momentum and time [105]. This technique is extremely useful in addressing the relaxation dynamics of excited charge carriers at selected momenta in the Brillouin zone, together with their characteristic timescales, and the observation of transient phase transitions occuring in a system far from thermal equilibrium. In trARPES, an ultra-violet (high photon energy) probe pulse photoemits electrons from valence band states. Using a probe photon energy larger than the work function allows for the spectroscopy of both occupied and unoccupied electronic states. The scheme of trARPES technique is illustrated in Figure 1.15. The detection system of a trARPES setup essentially measures the $E - k$ band structure of the photo-induced system at subsequent time delays, thereby, mapping the energy band structure in the ultrafast time domain as is clearly shown in Figure 1.16.

The pump pulse affects the ground state of the system by exciting electrons from energy states below E_F to states above E_F (below the vacuum level) at zero time delay, $\Delta t = 0$. This creats a transient population of holes in the oc-

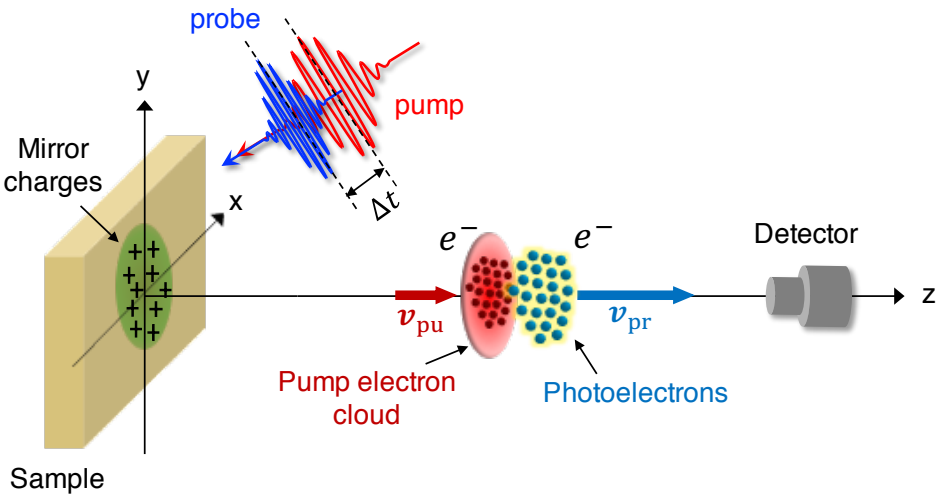

Figure 1.17: Pump-induced space-charge effects in trARPES: At $\Delta t < 0$, the electron cloud emitted by the pump pulse travels with an average velocity v_{pu} and the photoelectrons emitted by the probe pulse move with a velocity $v_{pr} > v_{pu}$ towards the detector place along z-axis. The positive charges in the green region represent pump-induced mirror charges inside the sample.

cupied energy bands and electrons in the unoccupied bands. At different time delays following the photoinduced perturbation, i.e., at $\Delta t > 0$, the photoemission intensity as a function of energy and momentum is recorded and its yield depends on the rate of decay of the transient electron population above E_F. The relaxation of photoexcited charge carriers towards equilibrium occurs through various scattering channels [see Section 1.4]. To study the variation in population of occupied/unoccupied states, the photoemission intensity acquired at time delays $\Delta t > 0$ is normalized with respect to that acquired at $\Delta t < 0$ (before photoexcitation), see Figure 1.15(b). The relative changes in the spectral intensity depend on the density of states around E_F. Typical pump fluences used in a trARPES experiment range from few tens of μJ/cm^2 to few mJ/cm^2 [106]. However, the maximum threshold of the incident pump fluence is sample dependent and is limited by the pump-induced space charge effects.

From a trARPES experiment, the quantities that can be determined are the decay times of the electron and hole populations, the time-dependent energy shifts of the band structure relative to E_F, the temperature of the thermalized hot electron population and its temporal evolution, and the shifts in the chemical potential followed by its subsequent decay as a function of time. In addition, modes of collective excitations such as phonons can be identified [107, 108] from the periodic modulations of the time-dependent photoemission spectrum. Analysis of the aforementioned quantities provides an accurate description of the relaxation dynamics in a photoexcited system. Furthermore, pump fluence-dependent studies can help us understand the differences in carrier dynamics between weak and strong photoexcitation strengths as well as determine the critical pump fluence for systems undergoing non-

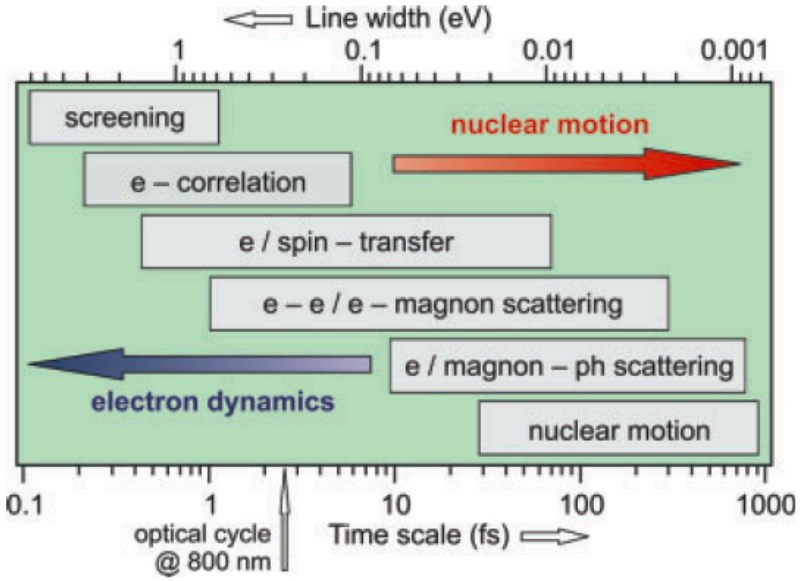

Figure 1.18: From Ref. [109] Typical timescales and respective line widths of various elementary processes in solid-state systems.

equilibrium phase transitions.

Pump laser-induced space-charge effects in trARPES

Time- and angle-resolved photoemission experiments are often limited by vacuum space-charge effects induced by the high peak intensities of ultrashort pump pulses. At sufficiently high fluences, multiphoton absorption can lead to simultaneous emission of electrons by the pump pulse. The repulsive Coulomb interaction between the photoelectrons emitted by the probe pulse and the electron cloud ejected by the pump pulse leads to pump-induced space-charge effects in trARPES experiments. Such effects are manifested as energy shifts, arising from the pump-induced accelerating electric field acting on the probe emitted photoelectrons, and momentum broadening in the time-dependent ARPES spectra. For increasing pump fluence, the valence band spectrum is increasingly broadened and shifted towards higher kinetic energies [110]. Such distortions of the energy and momentum distributions of the probe photoelectrons are detrimental when one is interested in the relaxation dynamics intrinsic to the sample. Hence, while performing trARPES experiments at high pump fluences, it is important to determine the maximum threshold of the pump fluence for a given sample in order to avoid significant contributions from space-charge in the experimental data. A schematic illustration of the pump laser-induced space-charge effects in a trARPES experiment for $\Delta t < 0$ is shown in Figure 1.17.

1.4 A microscopic picture of the various elementary interactions in solid-state systems

The theory of electron scattering in solid-state materials was first formulated within the framework of metals by Drude [111]. Such a theory explains the electrical resistivity by scattering of electrons with ion cores. The order of magnitude of the electron relaxation time τ gives an estimate of the elementary scattering timescales that typically range from $10^{-12} - 10^{-18}$ seconds. An optically excited electron can decay via interaction with other electrons, with phonons, or spin waves (magnons) with decay rates $\Gamma_{e-e}, \Gamma_{e-ph}$ and Γ_{e-mag}, respectively. Following Matthiesen's rule, the rate of individual decay processes Γ_i add up to give the total decay rate, $\Gamma_t = \Sigma_i \Gamma_i$. Figure 1.18 gives an overview of the line widths of the fundamental processes and their corresponding timescales [104], which are given by $\tau = \hbar/\Gamma_i$. The linewidth obtained from the photoemission spectum provides information on the decay rate.

Scattering of electrons or magnons with phonons is responsible for energy transfer between different degrees of freedom in a solid. Characteristic times cover a wide range from picoseconds up to a few tens of attoseconds in strongly coupled systems [112, 113, 114, 115]. Electron-electron scattering, which in ferromagnets can be accompanied by magnon excitation [116, 117, 118], represents a major energy decay channel of excited electrons. The respective relaxation times have been widely studied in experiment and theory [119, 120] and range from several fs up to several 100 fs. Transfer of an electron or its spin across interfaces is an essential relaxation process in two-dimensional systems supported by a substrate. The current state of this field is presented in [121]. In strongly correlated systems such as Mott insulators, electron correlations addressing the many-body effects related to the electron-electron interaction are described by an energy U and characterised by a time scale of $\hbar/W \approx 1$ fs, where W is the bandwidth. For systems having high electron densities, charge screening in an electron gas is built up on a time scale of the order of tenths of femtoseconds, i.e., in the attosecond range, for typical metallic densities [122]. Decay and dephasing of nuclear motion like vibrational wave packet propagation in molecules [123, 124] or coherent optical phonon dynamics in condensed matter range from few 10 fs [125] in light molecules to several ps in inorganic systems with heavier nuclei [126]. The following section deals with an overview of the energy relaxation processes in a semiconductor upon photoexcitation.

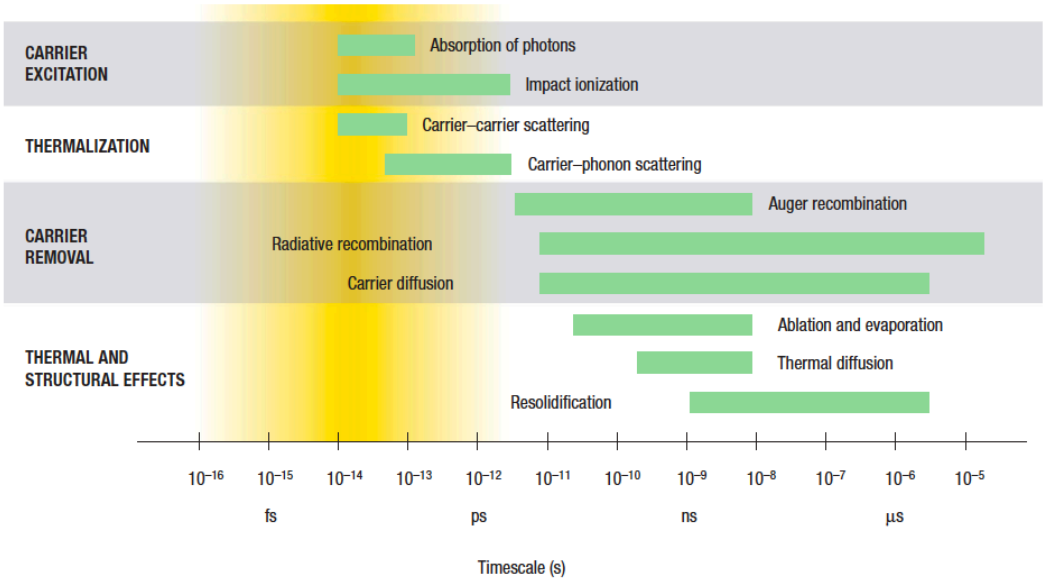

Figure 1.19: From Ref. [127]. Timescales of relaxation in a photo-excited semiconductor GaAs. Each green bar represents an approximate range of characteristic times over a range of carrier densities from 10^{17} to 10^{22} cm^{-3}.

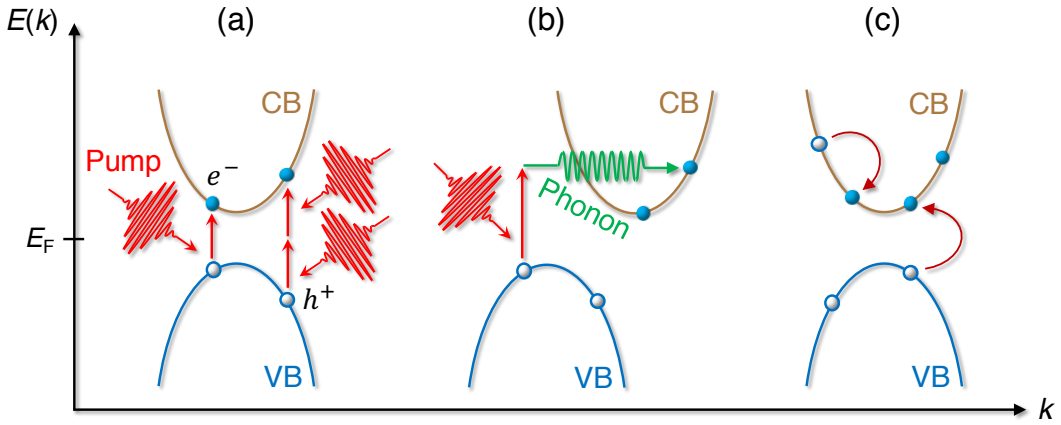

Figure 1.20: Modified from Ref. [128]. Possible mechanisms of carrier excitation: (a) Single- and multi-photon absorption. (b) Phonon-mediated absorption for an indirect band gap semiconductor. (c) Auger electrons or impact ionization. The blue filled (open) circles indicate electrons (holes), E_F is the Fermi level.

1.5 Ultrafast electron and lattice dynamics in semiconductors after photoexcitation

On excitation with femtosecond laser pulses, the electrons and the lattice are driven far out of equilibrium. A photoexcited semiconductor, therefore, undergoes different stages of relaxation before returning to its equilibrium ground state. The excess energy absorbed by an electron on photoexcitation is transferred first to the other electrons and then to the lattice. Carrier excitation and relaxation processes can be placed under the following regimes: excitation of charge carriers, thermalization of the excited carrier population, recombination of carriers and thermal/structural effects [127]. These regimes and their corresponding timescales are shown in Figure 1.19. The different processes under these regimes do not occur sequentially; instead, they overlap in time forming a continuous chain of events spanning the time range from attoseconds to microseconds.

1.5.1 Carrier excitation

Following the incidence of a pump photon on the target material, excitation of an electron can occur through various processes [128, 129]. When the photon energy is larger than the bandgap of a semiconductor, the dominant mechanism for exciting electrons from the valence band to the conduction band is single photon absorption. In case of indirect band gap semiconductors, single photon absorption process is accompanied by phonons in order to conserve momentum. If the direct bandgap is larger than the photon energy or single photon absorption is forbidden by band filling, then multiphoton absorption becomes important. The other mechanisms of excitation are free carrier absorption and impact ionization. The number density of excited carriers is not altered in free-carrier absorption while impact ionization generates additional electron-hole pairs and hence, there is an increase in the excited carrier population. Possible mechanisms of carrier excitation are represented in Figure 1.20.

1.5.2 Thermalization of the carriers

The energy relaxation process after photoexcitation involves a redistribution of electrons and holes throughout the conduction and valence bands via carrier-carrier and carrier-phonon interactions [128]. The description of energy relaxation of electrons and holes is very similar, though the scattering times may vary due to differences in their effective masses. Carrier-carrier scattering, shown in Figure 1.21(a), occurs in less than 10 fs, but it takes hundreds of femtoseconds for the non-thermal carrier distribution to reach a Fermi-Dirac distribution. In carrier-phonon scattering, free carriers exchange energy and momentum by emission or absorption of a phonon. Phonon absorption can occur only at lattice temperatures $T > 0$ K. After scattering with phonons, the carrier may be found in the same valley of the conduction

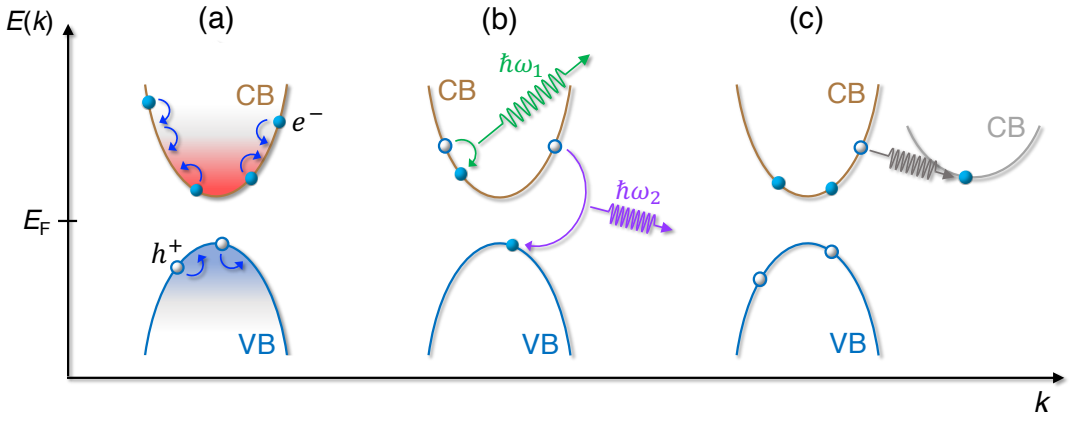

Figure 1.21: Modified from Ref. [128]. Thermalization of the carriers: (a) Carrier-carrier scattering. (b) Carrier-phonon scattering. (c) Intervalley carrier-scattering. ω_1 and ω_2 are low and high frequency phonons, respectively.

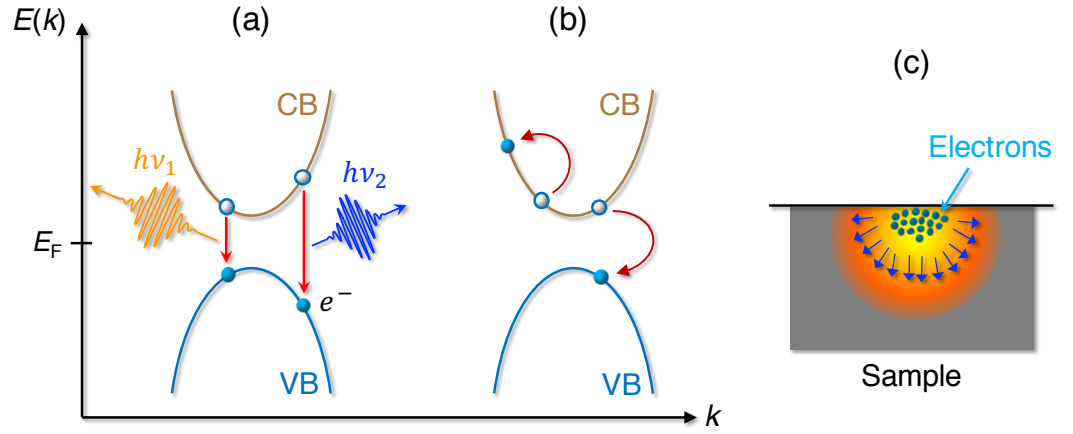

Figure 1.22: Modified from Ref. [128]. Recombination of the charge carriers: (a) Radiative recombination. (b) Auger recombination. (c) Diffusion of excited carriers. ν_1 and ν_2 are low and high frequency photons, respectively.

or valence band (intravalley scattering) or in a different valley (intervalley scattering), as represented in Figure 1.21(b) and 1.21(c), respectively. In this way, the carriers transfer their excess energy to the lattice. Since the phonon modes carry less energy, it takes many carrier-phonon scattering processes and hence, several picoseconds before the carriers and lattice reach thermal equilibrium.

1.5.3 Carrier recombination

The material is at a well defined temperature once an equilibrium has been established between the carriers and the lattice. Although the carrier distribution has the same temperature as the lattice, the number of free carriers is still higher than that in the non-excited equilibrium state. These excess

carriers are removed through the recombination of electrons and holes. The recombination process can be radiative or non-radiative [128]. In radiative recombination, as illustrated Figure 1.22(a), a photon is emitted when an electron and hole recombine with (indirect bandgap semiconductors) or without (direct bandgap semiconductors) phonon-assisted processes. Non-radiative recombination channels include Auger recombination where an electron recombines with a hole and the energy released in this process excites another electron in the conduction band, shown in Figure 1.22(b). The free carriers can also be removed by carrier diffusion, see Figure 1.22(c), but only from the region of the sample where they were originally excited and so, in contrast to recombination process, this does not decrease the total number of free carriers in the material.

If the photoexcitation density is below the threshold of inducing any irreversible changes in the material, the main relaxation mechanism is thermal diffusion. If melting or vaporization has occurred, then resolidification or condensation follows as the lattice cools down to temperatures lower than the melting or boiling point of the sample, respectively; however, the material does not necessarily revert back to its original structure or phase [130, 131].

References

[1] N.F. Mott, "Metal-insulator transition." *Reviews of Modern Physics* **40**, 677 (1968).

[2] N.F. Mott, "The transition to the metallic state." *Philosophical Magazine* **6**, 287 (1961).

[3] R. E. Peierls, "Quantum theory of Solids." Oxford University Press Inc., 1955.

[4] M. Z. Hasan and C. L. Kane, "Topological insulators." *Reviews of Modern Physics* **82**, 3045 (2010).

[5] R. S. Knox, "Theory of excitons." Solid State Physics, Academic Press, New York (1963).

[6] D. Jerome, T. M. Rice and W. Kohn, "Excitonic insulator." *Physical Review* **158**, 462 (1967).

[7] X. L. Wang, S. X. Dou and C. Zhang, "Zero-gap materials for future spintronics, electronics and optics." *NPG Asia Materials* **2**, 31 (2010).

[8] Y. F. Lu, H. Kono1, T. I. Larkin, A. W. Rost, T. Takayama, A. V. Boris, B. Keimer and H. Takagi, "Zero-gap semiconductor to excitonic insulator transition in Ta_2NiSe_5." *Nature Communications* **8**, 14408 (2017).

[9] Z. Li, M. Nadeem, Z. Yue, D. Cortie, M. Fuhrer and X. Wang, "Possible Excitonic Insulating Phase in Quantum-Confined Sb Nanoflakes." *Nano Letters* **19**, 4960 (2019).

[10] M. Kumagai and T. Takagahara, "Excitonic and nonlinear-optical properties of dielectric quantum-well structures." *Physical Review B: Condensed Matter Materials Physics* **40**, 12359 (1989).

[11] J. A. Wilson, "Concerning the semimetallic characters of TiS_2 and $TiSe_2$." *Solid State Communications* **22**, 551 (1977).

[12] H. Cercellier, C. Monney, F. Clerc, C. Battaglia, L. Despont, M. G. Garnier, H. Beck, P. Aebi, L. Patthey, H. Berger, and L. Forró, "Evidence for an Excitonic Insulator Phase in 1T-$TiSe_2$." *Physical Review Letters* **99**, 146403 (2007).

[13] Y.Wakisaka, T. Sudayama, K. Takudo, T.Mizokawa, M. Arita, H. Namatame, M. Taniguchi, N. Katayama, M. Nohara and H. Takagi, "Excitonic insulator state in Ta_2NiSe_5 probed by photoemission spectroscopy." *Physical Review Letters* **103**, 026402 (2009).

[14] B. Bucher, P. Steiner, and P. Wachter, "Excitonic insulator phase in $TmSe_{0.45}Te_{0.55}$." *Physical Review Letters* **67**, 2717 (1991).

[15] L. Du, X. Li, W. Lou, G. Sullivan, K. Chang, J. Kono and R. R. Du, "Evidence for a topological excitonic insulator in InAs/GaSb bilayers." *Nature Communications* **8**, 1971 (2017).

[16] R. A. Craven, F. J. Di Salvo and F. S. L. Hsu, "Mechanisms for the 200 K transition in TiSe2: A measurement of the specific heat." *Solid State Communications* **25**, 39 (1978).

[17] B. Bucher, T. Park, J. D. Thompson and P. Wachter, "Thermodynamical Signatures of an Excitonic Insulator." Preprint at https://arxiv.org/abs/0802.3354 (2008).

[18] K. Rossnagel, "On the origin of charge-density waves in select layered transition-metal dichalcogenides." *Journal of Physics: Condensed Matter* **23**, 213001 (2011).

[19] M. Porer, U. Leierseder, J. M. Ménard, H. Dachraoui, L. Mouchliadis, I. E. Perakis, U. Heinzmann, J. Demsar, K. Rossnagel and R. Huber, "Non-thermal separation of electronic and structural orders in a persisting charge density wave." *Nature Materials* **13**, 857 (2014).

[20] J. R. Manson, G. Benedek and S. Miret-Artes, "The electron-phonon coupling strength at metal surfaces directly determined from the helium atom scattering Debye-Waller factor." *Journal of Physical Chemistry Letters* **7**, 1016 (2016).

[21] A. Kogar, M. S. Rak, S. Vig, A. A. Husain, F. Flicker, Y. Il Joe, L. Venema, G. J. MacDougall, T. C. Chiang, E. Fradkin, J. V. Wezel and P. Abbamonte, "Signatures of exciton condensation in a transition metal dichalcogenide." *Science* **358**, 1314 (2017).

[22] B. I. Halperin and T. M. Rice, "Possible anomalies at a semimetal-semiconductor transition." *Reviews of Modern Physics* **40**, 755 (1968).

[23] F. X. Bronold and H. Fehske, "Possibility of an excitonic insulator at the semiconductor-semimetal transition." *Physical Review B* **74**, 165107 (2006).

[24] K. Seki, Y. Wakisaka, T. Kaneko, T. Toriyama, T. Konishi, T. Sudayama, N. L. Saini, M. Arita, H. Namatame, M. Taniguchi, N. Katayama, M. Nohara, H. Takagi, T. Mizokawa, and Y. Ohta, "Excitonic Bose-Einstein condensation in Ta_2NiSe_5 above room temperature." *Physical Review B* **90**, 155116 (2014).

[25] Y. F. Lu, H. Kono, T. I. Larkin, A. W. Rost, T. Takayama, A. V. Boris, B. Keimer and H. Takagi, "Zero-gap semiconductor to excitonic insulator transition in Ta_2NiSe_5." *Nature Communications* **8**, 14408 (2017).

[26] T. I. Larkin, A. N. Yaresko, D. Pröpper, K. A. Kikoin, Y. F. Lu, T. Takayama, Y.-L. Mathis, A. W. Rost, H. Takagi, B. Keimer, and A. V. Boris, "Giant exciton Fano resonance in quasi-one-dimensional Ta_2NiSe_5." *Physical Review B* **95**, 195144 (2017).

[27] H. Bethe, "Theorie der Beugung von Elektronen an Kristallen." *Annalen der Physik* **87**, 55 (1928).

[28] A. Sommerfield, "Zur Elektronentheorie der Metalle auf Grund der Fermischen Statistik." *Zeitschrift für Physik* **47**, 1 (1928).

[29] F. Bloch, "Bemerkung zur Elektronentheorie des Ferromagnetismus und der elektrischen Leitfähigkeit." *Zeitschrift für Physik* **57**, 545 (1929).

[30] J. H. de Boer and E. J. W. Verwey, "Semi-conductors with partially and with completely filled 3*d*-lattice bands". *Proceedings of the Physical Society* **49**, 59 (1937).

[31] N. F. Mott and R. Peierls, "Discussion of the paper by de Boer and Verwey." *Proceedings of the Physical Society* **49**, 72 (1937).

[32] N. F. Mott, "The Basis of the Electron Theory of Metals, with Special Reference to the Transition Metals." *Proceedings of the Physical Society. Section A* **62**, 416 (1949).

[33] N. F. Mott, "On the transition to metallic conduction in semiconductors." *Canadian Journal of Physics* **34**, 1356 (1956).

[34] N. F. Mott, "The transition to the metallic state." *Philosophical Magazine* **6**, 287 (1961).

[35] N. F. Mott, "Metal-Insulator Transition." Taylor and Francis, London/Philadelphia (1990).

[36] G. Kotliar and D. Vollhardt, "Correlated materials: Insights from dynamical mean-field theory." *Physics Today* **57**, 53 (2004).

[37] S. B. Roy, "Mott Insulators: Physics and applications." IOP Publishing Ltd. (2019).

[38] J. Hubbard, "Electron Correlations in Narrow Energy Bands." *Proceedings of the Royal Society of London. Series A, Mathematical and Physical Sciences* **276**, 238 (1963).

[39] J. Hubbard, "Electron correlations in narrow energy bands III. An improved solution." *Proceedings of the Royal Society of London. Series A. Mathematical and Physical Sciences* **281**, 401 (1964).

[40] T. Lancaster and S. J. Blundell, "Quantum Field Theory for the Gifted Amateur." Oxford: Oxford University Press (2014).

[41] F. Gebhard, "The Mott Metal-insulator Transition." Springer, Berlin (1997).

[42] O. Madelung, "Introduction to Solid State Theory." Springer Berlin, Heidelberg (1978).

[43] P. P. Edwards and C. N. R. Rao (eds.), "Metal-insulator Transitions Revisited." London: Taylor and Francis (1995).

[44] M. Imada, A. Fujimori and Y. Tokura, "Metal-insulator transitions." *Reviews of Modern Physics* **70**, 1040 (1998).

[45] P. P. Edwards, R. L. Johnston, F. Henstell, C. N. R. Rao and D. P. Tunstall, "Solid State Physics." vol 52, F. Seitz and D. Turnbull (eds.) p 229 (1999).

[46] P. Fazekas and E. Tosatti, "Electrical, structural and magnetic properties of pure and doped 1T-TaS_2." *Philosophical Magazine B* **39**, 229 (1979).

[47] L. Perfetti, P. A. Loukakos, M. Lisowski, U. Bovensiepen, H. Berger, S. Biermann, P. S. Cornaglia, A. Georges, and M. Wolf, "Time Evolution of the Electronic Structure of 1T-TaS_2 through the Insulator-Metal Transition." *Physical Review Letters* **97**, 067402 (2006).

[48] H. Fröhlich, "On the theory of superconductivity: the one dimensional case." *Proceedings of The Royal Society of London* **A223**, 296 (1954).

[49] C. G. Kuper, "On the Thermal Properties of Fröhlich's One-Dimensional Superconductor." *Proceedings of the Royal Society of London* **A227**, 214 (1955).

[50] A. W. Overhauser, "Giant Spin Density Waves." *Physical Review Letters* **4**, 462 (1960).

[51] A. W. Overhauser, "Spin Density Waves in an Electron Gas." *Physical Review* **128**, 1437 (1962).

[52] C. Kittel, "Quantum Theory of Solids." John Wiley and Sons, New York (1963).

[53] J. Lindhard, "On the properties of a gas of charged particles." *Dan. Vid. Selsk Mat.-Fys. Medd.* **28**, 8 (1954).

[54] G. Grüner, "Density Waves In Solids." Frontiers in physics, volume 89, Cambridge, Massachusettes : Perseus Publishing (2000).

[55] W. Kohn, "Image of the Fermi Surface in the Vibration Spectrum of a Metal." *Physical Review Letters* **2**, 393 (1959).

[56] E. J. Woll, Jr. and W. Kohn, "Images of the Fermi Surface in Phonon Spectra of Metals." *Physical Review* **126**, 1693 (1962).

[57] M. Suzuki and I. Suzuki, “Lecture Note on Charge density wave Solid State Physics“ (2015).

[58] L. B. Coleman, M. J. Cohen, D. J. Sandman, F. G. Yamagishi, A. F. Garito and A. J. Heeger, “Superconducting fluctuations and the peierls instability in an organic solid.“ *Solid State Communications* **12**, 1125 (1973).

[59] H. A. Mook and Charles R. Watson, Jr., “Neutron Inelastic Scattering Study of Tetrathiafulvalene Tetracyanoquinodimethane (TTF-TCNQ).“ *Physical Review Letters* **36**, 801 (1976).

[60] X. Zhu, Y. Cao, J. Zhang, E. W. Plummer and J. Guo, “Classification of charge density waves based on their nature.“ *Proceedings of the National Academy of Sciences* **112**, 2367 (2015).

[61] R. Comin, A. Frano, M. M. Yee, Y. Yoshida, H. Eisaki, E. Schierle, E. Weschke, R. Sutarto, F. He, A. Soumyanarayanan, Y. He, M. L. Tacon, I. S. Elfimov, J. E. Hoffman, G. A. Sawatzky, B. Keimer and A. Damascelli, “Charge Order Driven by Fermi-Arc Instability in $Bi_2Sr_{2-x}La_xCuO_{6+\delta}$.“ *Science* **343**, 390 (2014).

[62] C. -W. Chen, J. Choe and E. Morosan, “Charge density waves in strongly correlated electron systems.“ *Reports on Progress in Physics* **79**, 084505 (2016).

[63] K. Bechgaard, C. S. Jacobsen, K. Mortensen, H. J. Pedersen, and N. Thorup, “The properties of five highly conducting salts: $(TMTSF)_2X$, X = PF_6^-, AsF_6^-, SbF_6^-, BF_6^- and NO_6^-, derived from tetramethyltetraselenafulvalene (TMTSF).“ *Solid State Communications* **33**, 1119 (1980).

[64] H. Hertz, ”On the influence of ultraviolet light on the electric discharge.” *Annalen der Physik* **267**, 983 (1887).

[65] A. Einstein, *Annalen der Physik* **322**, 1521–3889 (1905).

[66] C. Nordling, K. Siegbahn, E. Sokolowski and A. H. Wapstra, ”Possible finite nuclear size effect on the 279 keV transition in $T1^{203}$.” *Nuclear Physics* **1**, 326 (1956).

[67] A. Damascelli, “Probing the electronic structure of complex systems by ARPES." *Physica Scripta* **2004**, 61 (2004).

[68] S. Hüfner, ”Photoelectron Spectroscopy: Principles and Applications.” Springer, Third Revised and Enlarged Edition.

[69] H. P. Bonzel and C. Kleint, “On the history of photoemission." *Progress in Surface Science* **49**, 107 (1995).

[70] C. N. Berglund and W. E. Spicer, “Photoemission studies of copper and silver: theory." *Physical Review* **136**, A1030–44 (1964).

[71] P. J. Feibelman and D. E. Eastman, “Photoemission spectroscopy—Correspondence between quantum theory and experimental phenomenology.” *Physical Review B***10**, 4932 (1974).

[72] A. Damascelli, Z. Hussain, and Z.-X. Shen, “Angle-resolved photoemission studies of the cuprate superconductors.” *Reviews of Modern Physics* **75**, 473 (2003).

[73] G. A. Somorjai, “Chemistry in two dimensions: surfaces." Ithaca : Cornell University Press, 1981.

[74] M. P. Seah and W. A. Dench, “Quantitative electron spectroscopy of surfaces: A standard data base for electron inelastic mean free paths in solids." *Surface and Interface Analysis* **1**, 2 (1979).

[75] G. D. Mahan, “Theory of Photoemission in Simple Metals." *Physical Review B* **2**, 4334 (1970).

[76] A. Pramanik, “Anomalies in the Dirac States - a high-resolution photoemission spectroscopic study“ PhD thesis, Tata Institute of Fundamental Research (2021).

[77] R. H. M. Groeneveld, R. Sprik, and A. Lagendijk, “Femtosecond spectroscopy of electron-electron and electron-phonon energy relaxation in Ag and Au.” *Physical Review B* **51**, 11433 (1995).

[78] E. Beaurepaire, *et al.*, “Ultrafast spin dynamics in ferromagnetic nickel.” *Physical Review Letters* **76**, 4250 (1996).

[79] Y. Ogawa, *et al.*, “Dynamical aspects of the photoinduced phase transition in spin-crossover complexes.” *Physical Review Letters* **84**, 3181 (2000).

[80] A. Cavalleri, *et al.*, “Femtosecond structural dynamics in VO_2 during an ultrafast solid-solid phase transition.” *Physical Review Letters* **87**, 237401 (2001).

[81] A. Cavalleri, *et al.*, “Evidence for a structurally-driven insulator-to-metal transition in VO_2: A view from the ultrafast timescale.” *Physical Review B* **70**, 161102 (2004).

[82] K. Nasu, “Photoinduced Phase Transitions.” World Scientific, Hackensack, NJ, p. 345 (2004).

[83] M. Rini, “Photoinduced phase transition in VO_2 nanocrystals: Ultrafast control of surface-plasmon resonance.” *Optics Letters* **30**, 558 (2005).

[84] K. Yonemitsu, and K. Nasu,“ Theory of photoinduced phase transitions in itinerant electron systems.” *Physics Reports* **465**, 1 (2008).

[85] J. Demsar, *et al.*, “Femtosecond snapshots of gapforming charge-density-wave correlations in quasi-two-dimensional dichalcogenides $1T$-TaS_2 and $2H$-$TaSe_2$.” *Physical Review B* **66**, 041101 (2002).

[86] J. Demsar, *et al.*,“Quasiparticle relaxation dynamics in heavy fermion compounds." *Physical Review Letters* **91**, 027401 (2003).

[87] C. V. Shank, “Ultrashort Laser Pulses – Generation and Applications (ed. W. Kaiser)" 5–34 (Springer, Berlin and New York, 1993).

[88] C. Hirlimann, “Femtosecond Laser Pulses – Principles and Experiments (ed. C. Rullière)" 83–110 (Springer, Berlin, 1998).

[89] C. Rose-Petruck, *et al.*, “Picosecond-milliångström lattice dynamics measured by ultrafast X-ray diffraction." *Nature* **398**, 310 (1999).

[90] H. M. van Driel, “Kinetics of high-density plasmas generated in Si by 1.06- and 0.53-μm picosecond laser pulses." *Physical Review B* **35**, 8166 (1987).

[91] P. L. Liu, R. Yen and N. Bloembergen, “Picosecond laser-induced melting and resolidification morphology on Si." *Applied Physics Letters* **34**, 864 (1979).

[92] J.-K. Wang, *et al.*, “Ultrafast Phenomena VI" 236–239 (Springer, Berlin, 1989).

[93] M. L. M. Balistreri, *et al.*, “Tracking femtosecond laser pulses in space and time." *Science* 295, 1080 (2001).

[94] A. H. Zewail, “Femtochemistry: Atomic-scale dynamics of the chemical bond." *Journal of Physical Chemistry A* **104**, 5660 (2000).

[95] J. P. Callan, *et al.*, “Ultrafast dynamics and phase changes in highly excited GaAs." *Semiconductors and Semimetals* **67**, 151 (2001).

[96] P. C. Becker, *et al.*, “Femtosecond photon echoes from band-to-band transitions in GaAs." *Physical Review Letters* **61**, 1647 (1988).

[97] J.-K. Wang, “Femtosecond Nonlinear Optics In Gases And Solids." Thesis, Harvard Univ., Cambridge (1992).

[98] H. Stapelfeldt, E. Constant and P. B. Corkum, “Femtoscience: from femtoseconds to attoseconds." *Progress in Crystal Growth and Characterization of Materials* **33**, 209 (1996).

[99] P. B. Corkum, “Attosecond pulses at last.“ *Nature* **403**, 845 (2000).

[100] P. M. Paul, *et al.*, "Observation of a train of attosecond pulses from high harmonic generation." *Science* **292**, 1689 (2001).

[101] L. Rettig, "Ultrafast Dynamics of Correlated Electrons." PhD thesis, Freien Universität Berlin, 2012.

[102] T. Hertel, E. Knoesel, A. Hotzel, M. Wolf and G. Ertl, "Femtosecond time-resolved photoemission of electron dynamics in surface Rydberg states." *Journal of Vacuum Science and Technology A* **15**, 1503 (1997).

[103] D. J. Hilton, "Ultrafast Pump–Probe Spectroscopy: Optical techniques for solid state materials characterization" edited by R. P. Prasankumar A. J. Taylor. CRC Press - Taylor and Francis Group (2012).

[104] H. Petek and S. Ogawa, "Femtosecond time-resolved two-photon photoemission studies of electron dynamics in metals." *Progress in Surface Science* **56**, 239 (1997).

[105] S. Mor, "Fundamental interactions governing the (non-)equilibrium electronic structure in low dimensions." PhD thesis (2019).

[106] P. S. Kirchmann."Ultrafast Electron Dynamics in Low-Dimensional Materials." PhD thesis (2018).

[107] J. A. Sobota, S.-L. Yang, D. Leuenberger, A. F. Kemper, J. G. Analytis, I. R. Fisher, P. S. Kirchmann, T. P. Devereaux and Z.-X. Shen, "Distinguishing Bulk and Surface Electron-Phonon Coupling in the Topological Insulator Bi_2Se_3 Using Time-Resolved Photoemission Spectroscopy." *Physical Review Letters* **113**, 157401 (2014).

[108] S. Gerber, *et al.*, "Femtosecond electron-phonon lock-in by photoemission and x-ray free-electron laser." *Science* **357**, 71 (2017).

[109] U. Bovensiepen and P. S. Kirchmann, "Elementary relaxation processes investigated by femtosecond photoelectron spectroscopy of two-dimensional materials." *Laser and Photonics Reviews* **6**, 1 (2012).

[110] L.-P. Oloffa, K. Hanff, A. Stange, G. Rohde, F. Diekmann, M. Bauer and K. Rossnagel, "Pump laser-induced space-charge effects in HHG-driven time- and angle-resolved photoelectron spectroscopy." *Journal of Applied Physics* **119**, 225106 (2016).

[111] P. Drude, "Zur Elektronentheorie der Metalle." *Annalen der Physik* **1**, 566 (1900).

[112] J. Shah, "Ultrafast Spectroscopy of Semiconductors and Semiconductor Nanostructures." 2nd edition, Springer, Berlin (1983).

[113] T. Kampfrath, L. Perfetti, F. Schapper, C. Frischkorn and M. Wolf, "Strongly Coupled Optical Phonons in the Ultrafast Dynamics of the Electronic Energy and Current Relaxation in Graphite." *Physical Review Letters* **95**, 187403 (2005).

[114] D. Song, F. Wang, G. Dukovic, M. Zheng, E. D. Semke, L. E. Brus and T. F. Heinz, "Direct Measurement of the Lifetime of Optical Phonons in Single-Walled Carbon Nanotubes." *Physical Review Letters* **100**, 225503 (2008).

[115] S. Wall, D. Prabhakaran, A. T. Boothroyd, and A. Cavalleri, "Ultrafast Coupling between Light, Coherent Lattice Vibrations, and the Magnetic Structure of Semicovalent $LaMnO_3$." *Physical Review Letters* **103**, 097402 (2009).

[116] J. Hong and D. L. Mills, "Spin dependence of the inelastic electron mean free path in Fe and Ni: Explicit calculations and implications." *Physical Review B* **62**, 5589 (2000).

[117] R. Vollmer, M. Etzkorn, P. S. Anil Kumar, H. Ibach and J. Kirschner, "Spin-Polarized Electron Energy Loss Spectroscopy of High Energy, Large Wave Vector Spin Waves in Ultrathin fcc Co Films on Cu(001)." *Physical Review Letters* **91**, 147201 (2003).

[118] M. Weinelt, A. B. Schmidt, M. Pickel and M. Donath, "Spin-polarized image-potential-state electrons as ultrafast magnetic sensors in front of ferromagnetic surfaces." *Progress in Surface Science* **82**, 388 (2007).

[119] E.V. Chulkov, A.G. Borisov, J. P. Gauyacq, D. Sanchez-Portal, V. M. Silkin, V. P. Zhukov, and P. M. Echenique, "Electronic excitations in metals and at metal surfaces." *Chemical Reviews* **106**, 4160 (2006).

[120] A. Mönnich, J. Lange, M. Bauer, M. Aeschlimann, I. A. Nechaev, V. P. Zhukov, P.M. Echenique and E.V. Chulkov, "Experimental time-resolved photoemission and ab initio study of lifetimes of excited electrons in Mo and Rh." *Physical Review B* **74**, 035102 (2006).

[121] U. Bovensiepen, H. Petek and M. Wolf, "Dynamics in Solid States Surfaces and Interfaces." Volume 1, Current Developments, Wiley-VCH, Weinheim (2010).

[122] A. Borisov, S. Sánchez-Portal, R. Díez Muiño and P. M. Echenique, "Building up the screening below the femtosecond scale." *Chemical Physics Letters* **387**, 95 (2004).

[123] A. Mokhari, P. Cong, J. L. Herek and A. H. Zewail, "Direct femtosecond mapping of trajectories in a chemical reaction." *Nature* **348**, 225 (1990).

[124] A. Assion, M. Geisler, J. Helbing, V. Seyfried and T. Baumert, "Femtosecond pump-probe photoelectron spectroscopy: Mapping of vibrational wave-packet motion." *Physical Review A* **54**, R4605 (1996).

[125] M. F. Emde, A. Baltuska, A. Kummrow, M. S. Pshenichnikov and D. A. Wiersma, "Ultrafast Librational Dynamics of the Hydrated Electron." *Physical Review Letters* **80**, 4645 (1998).

[126] K. Ishioka and O.V. Misochko, in: "Coherent lattice oscillations in solids and their optical control." edited by K. Yamanouchi, A. Giulietti, and K. Ledingham, Progress in Ultrafast Intense Laser Science Volume 5, Springer, Berlin, pp. 23–63 (2010).

[127] J. P. Callan, in: "Ultrafast Dynamics And Phase Changes In Solids Excited By Femtosecond Laser Pulses." (59–104) Thesis, Harvard Univ., Cambridge, (2000).

[128] S. K. Sundaram and E. Mazur, "Inducing and probing non-thermal transitions in semiconductors using femtosecond laser pulses." *Nature Materials* **1** 217, (2002).

[129] J. Demsar and T. Dekorsy, "Carrier dynamics in bulk semiconductors and metals: Optical techniques for solid state materials characterization." edited by R. P. Prasankumar A. J. Taylor. CRC Press - Taylor and Francis Group (2012).

[130] E. N. Glezer, Y. Siegal, L. Huang and E. Mazur, "Behavior of $\chi^{(2)}$ during a laser-induced phase transition in GaAs." *Physical Review B* **51**, 9589 (1995).

[131] J. Solis, C. N. Afonso, J. F. Trull and M. C. Morilla, "Fast crystallizing GeSb alloys for optical data storage." *Journal of Applied Physics* **75**, 7788 (1994).

2 Experimental framework for time-resolved ARPES

Time- and angle-resolved photoemission spectroscopy is a unique method for getting access to the microscopic processes occuring inside a solid by directly probing the electronic band structure. The time-resolved photoemission experiments were carried out in the CITIUS laboratory. This chapter begins with a short description of ultrashort light pulses and the process of high harmonic generation, followed by an overview of the relevant experimental setup and a brief discussion about the preparation of a pump-probe experiment.

2.1 The laser system

Light pulses with a duration of less than one picosecond are commonly referred to as *ultrashort pulses* (Section 2.1.1). The pulse duration is one of the most important parameters when dealing with time-resolved spectroscopies, such as trARPES. The temporal resolution of a pump-probe experimental setup is the cross-correlation between the durations of the pump and the probe pulses, and must be shorter than or comparable to the timescales of the microscopic phenomena that are under investigation. Today, the state-of-the-art laser technology has entered into the femtosecond regime: the well-established Ti:Sapphire chirped pulse laser amplifiers reliably provide femtosecond pulses centered at a photon energy close to 1.5 eV. While this photon energy is bound to the laser gain medium, different photon energies are needed for various spectroscopic experiments, including trARPES. A route to overcome this limitation and produce femtosecond pulses at different wavelengths is the use of nonlinear optical interactions such as the process of high harmonic generation (HHG), which make a wider photon energy range accessible for spectroscopies. Photoelectron spectroscopy relies on the availability of femtosecond extreme ultraviolet (XUV) pulses for probing the core energy levels and the valence band of an electron inside a solid. Pulses in the XUV regime can be generated from the infrared (IR) pulses using HHG (Section 2.1.2).

2.1.1 Ultrashort laser pulses

Ultrashort pulses are generated using mode-locked lasers. De Maria *et al.* [1] produced the first ultrashort pulses just six years after Maiman's first laser was demonstrated. In addition to having such a short pulse duration, the

ultrashort pulses generated by a Ti:Sa laser are characterised by a broad spectrum, a high peak intensity and can form pulse trains at a high repetition rate.

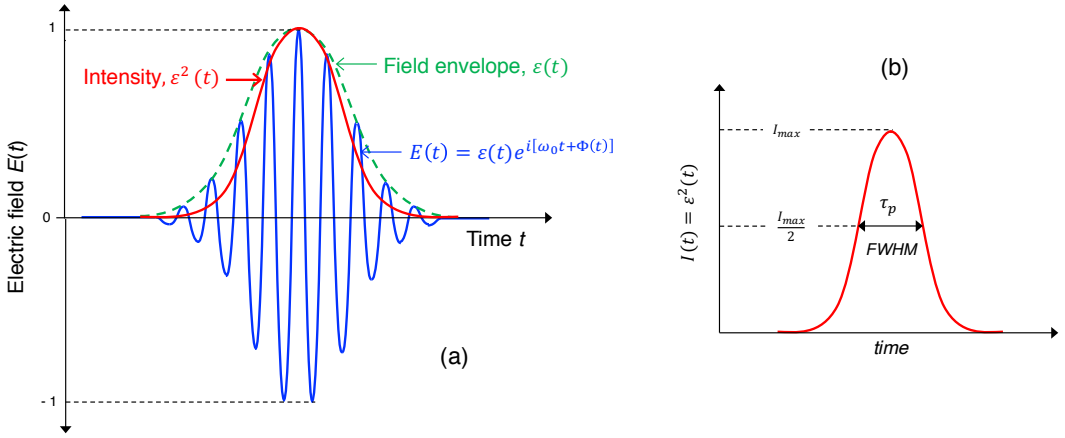

Figure 2.1: (a) Temporal profile of a Gaussian pulse carrying an electric field $\mathbf{E}(t)$ with the field envelope $\varepsilon(t)$ and (b) its intensity profile $\varepsilon^2(t)$.

Considering only the temporal dependence of the electric field $\mathbf{E}(x, y, z, t)$ of a laser pulse, one can write:

$$E(t) = \varepsilon(t)e^{i[\omega_0 t+\Phi]} \tag{2.1}$$

where $\varepsilon(t)$ is the field envelope (most commonly, a Gaussian function), ω_0 is the central frequency of the pulse and Φ is a phase constant [see Figure 2.1(a)]. In the frequency domain, one defines the spectral amplitude as the Fourier transform of $E(t)$:

$$E(\omega) = \int_{-\infty}^{\infty} E(t)e^{-i\omega t}\, dt \tag{2.2}$$

Given $E(\omega)$, the time dependent electric field is obtained through the inverse Fourier transform:

$$E(t) = \frac{1}{2\pi}\int_{-\infty}^{\infty} E(\omega)e^{i\omega t}\, d\omega \tag{2.3}$$

It is a common practice to define the pulse duration, τ_p, as the full width at half maximum (FWHM) of the intensity profile [shown in Figure 2.1(b)], $\varepsilon^2(t)$, and the spectral width, $\Delta\omega_p$, as the FWHM of the spectral intensity, $\varepsilon^2(\omega)$, where,

$$\varepsilon(\omega) = \int_{-\infty}^{\infty} \varepsilon(t)e^{-i\omega t}\, dt \tag{2.4}$$

The temporal and spectral characteristics of the field, i.e., the pulse duration τ_p and the bandwidth $\Delta\omega_p$, are not independent of each other. These quantities are related by the following inequality [2],

$$\Delta\omega_p\tau_p =\geq 2\pi c_B \tag{2.5}$$

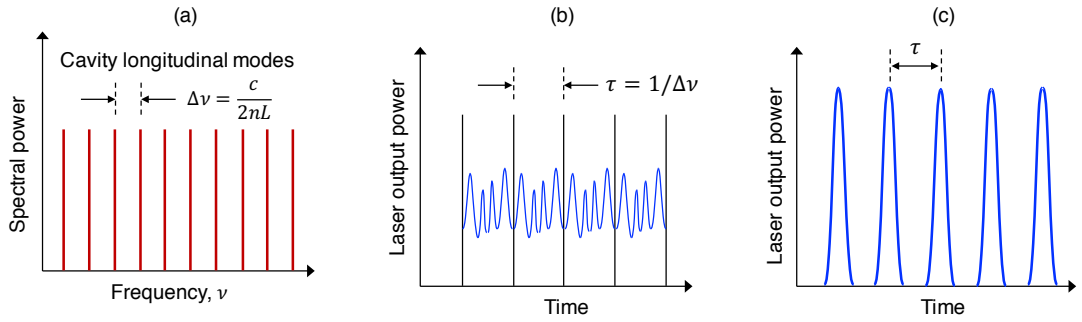

Figure 2.2: (a) Power spectrum of a set of equally spaced longitudinal modes inside a laser cavity; (b) and (c) possible output power of the laser when the modes have a random phase distribution and when all the modes are locked in the same phase, respectively.

where c_B is a numerical constant and its value depends on the shape of the pulse envelope (Gaussian, Lorentzian, sech, etc.) in the time domain. Equation 2.5 is the so-called *time-bandwidth* product. The equality holds for pulses without frequency modulation (*unchirped*) and are called *bandwidth limited* or *Fourier limited* pulses. Such pulses exhibit the shortest time duration for a given spectral width and pulse shape.

Mode-locking: As mentioned in Section 2.1.1, the standard source of ultrashort pulses is a mode-locked laser. Mode-locking refers to establishing a phase relationship between the longitudinal modes (frequencies) inside an optical cavity. A typical laser cavity can support a large number of longitudinal modes provided that each of their wavelengths, λ_m, satisfy the following condition:

$$m\frac{\lambda_m}{2} = nL \tag{2.6}$$

Here, m is a positive integer, n is the refractive index for a non-dispersive medium and has a constant value, and L is the geometrical cavity length. The frequency, ν_m, of each mode is therefore given by:

$$\nu_m = \frac{mc}{2nL} \tag{2.7}$$

where, c is the speed of light. The spacing between any two consecutive cavity modes is a constant, $\Delta\nu$, defined by the following equation [see Figure 2.2(a)]:

$$\Delta\nu = \nu_{m+1} - \nu_m = \frac{c}{2nL} \tag{2.8}$$

Each of the modes oscillate independently within the cavity with a random phase difference between every mode and the variation of output power over time can be represented by Figure 2.2(b), for example. Forcing all the modes to oscillate with an equal phase is the well known procedure called mode-locking. In this way, the electric field of all the frequencies will constructively

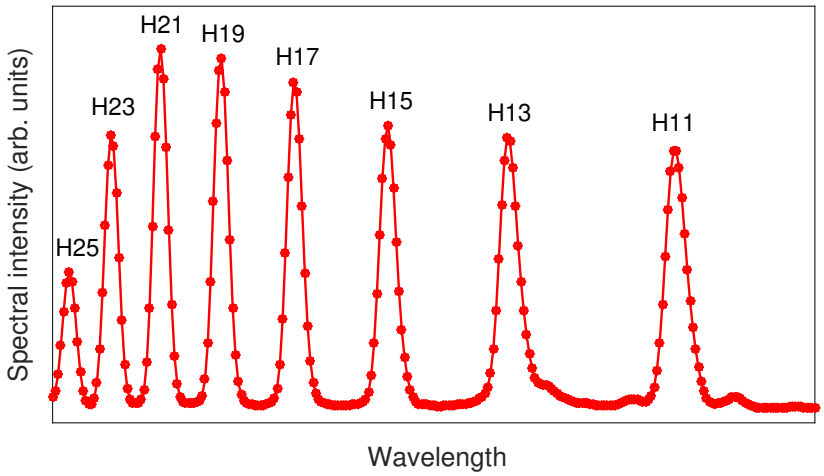

Figure 2.3: Typical spectrum produced in high harmonic generation consisting of harmonic orders that are odd integer multiples of the fundamental frequency of the laser.

interefere at one point in the time domain, resulting in an intense and short burst of light, shown in Figure. 2.2(c). The time-dependent intensity profile will appear as a train of single pulses spaced by $\tau = 1/\Delta$ [2]. The above description is the simplest case and assumes equally spaced modes.

2.1.2 Principle of harmonic generation

High harmonic generation (HHG) describes the process in which laser light at a given frequency is converted to integer multiples of this fundamental frequency. HHG occurs when an intense laser beam is focused into a conversion medium, which can be a noble gas jet or a solid. The first report of high-harmonic generation in noble gases dates back to the late 1980s [3, 4]. A typical HHG spectrum generated in gas is shown in Figure. 2.3. The HHG process is described by the so-called *three-step model* proposed by Corkum [5] and Kulander *et al* [6]. This process can be broken up into three steps: ionization of an atom, propagation of the released electron in the laser field and its recombination with the parent atom.

Step I - Ionization

If the intensity of light interacting with matter is steadily increased, the electric field of the electromagnetic wave, $E(t) = E_0\cos(\omega_0 t)$ where E_0 and ω_0 denote the field amplitude and frequency, respectively, at some point becomes comparable to the electric field strength experienced by an electron inside the atom and the electron can overcome the potential of the ion. In addition to the Coulomb potential energy of the ion, the electric field of the laser will produce a potential energy, $e\boldsymbol{E}(t) \cdot \boldsymbol{r}$. The Coulomb potential is significantly distorted for high strengths of the laser electric field and the effective potential barrier can be overcome by the bound electron through *tunnelling*, shown in Figure. 2.4. After tunnelling through the barrier, the electron can

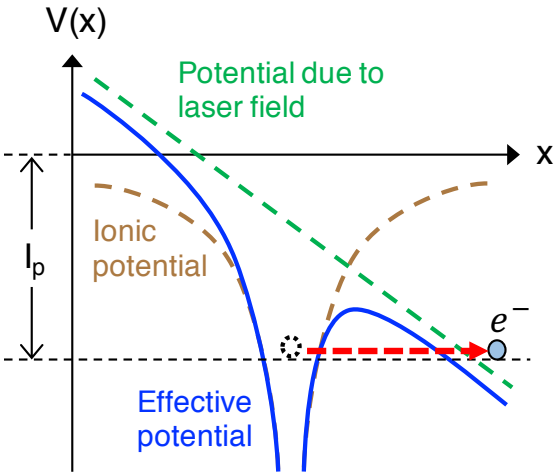

Figure 2.4: Adapted from [7]. Mechanism of tunnel ionization when an atom is exposed to an intense electric field of the laser. $V(x)$ is the electric potential as a function of x and I_p stands for the ionization potential of an electron e^-.

approximately be regarded as a free electron whose motion is just governed by the laser field. This ionization process by which an electron escapes from its parent atom into the laser electric field is known as tunnel ionization.

Step II - Propagation

To understand the subsequent motion of an electron after ionization, let us treat it as a classical particle interacting with the laser electric field. Let t_0 and $z(t)$ be the time at which the atom is ionized and the position of the electron at time, t, respectively. We assume $z(t_0) = 0$ and $\dot{z}(t_0) = 0$. Solving the differential equation of motion, the velocity can be written as

$$\begin{aligned} \dot{z}(t) &= \int_{t_0}^{t} -\frac{e}{m} E(t)\, dt \\ &= -\frac{eE_0}{m\omega_0} \left[\sin(\omega_0 t) - \sin(\omega_0 t_0)\right] \end{aligned} \tag{2.9}$$

where, e and m are the charge and mass of the electron. The position of the electron at time t is,

$$\begin{aligned} z(t) &= \int_{t_0}^{t} \dot{z}(t)\, dt \\ &= -\frac{eE_0}{m\omega_0^2} \left[\cos(\omega_0 t) - \cos(\omega_0 t_0) + \ \omega_0 (t - t_0) \sin(\omega_0 t_0)\right] \end{aligned} \tag{2.10}$$

Expressing z as a function of the phase, $\theta \equiv \omega_0 t$, we get,

$$z(\theta) = -\frac{eE_0}{m\omega_0^2} \left[\cos\theta - \cos\theta_0 + \ (\theta - \theta_0) \sin\theta_0\right] \tag{2.11}$$

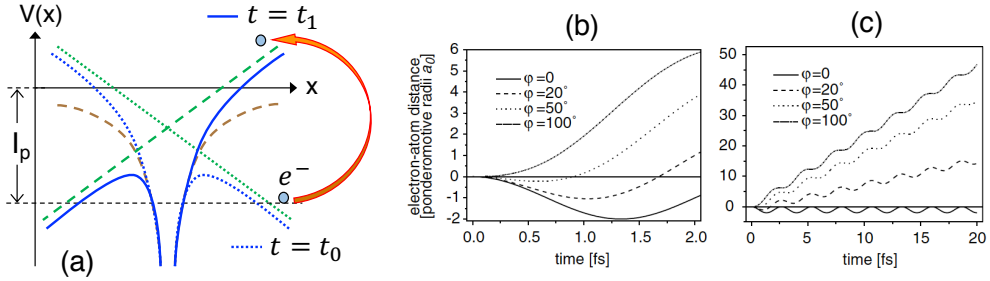

Figure 2.5: Adapted from [7]. (a) The atom is ionized at time t_0 (at some particular phase of the laser field). The electron accelerates and is driven away from the parent atom in the presence of the laser field. This occurs until time t_1 after which it starts returning to the parent atom. Electron trajectories outside its parent atom in a laser electric field (b) at early times and (c) for longer times. Taken from [7]. The amplitude of the oscillatory position is referred to as the ponderomotive radius, a_0, and is equal to $E_0 e/m\omega_0^2$.

The kinetic energy of the electron, E_{kin}, in terms of θ is,

$$\begin{aligned} E_{kin}(\theta) &= \frac{1}{2} m \dot{z}^2(\theta) \\ &= \frac{1}{2} m \left[-\frac{eE_0}{m\omega_0} (\sin\theta - \sin\theta_0) \right]^2 \\ &= 2U_p \left(\sin\theta - \sin\theta_0\right)^2 \end{aligned} \tag{2.12}$$

where $U_p = \frac{e^2 E_0^2}{4m\omega^2}$ is defined as the time-averaged kinetic energy of the electron over a complete cycle of the driving laser field. Figure 2.5(a) picturizes the propagation process and the possible electron trajectories in the laser field are shown in Figures 2.5(b) and 2.5(c).

Step III - Recombination

The electron recombines with an ion at time t_r (phase θ_r) and a photon is emitted upon recombination, as it is shown in Figure 2.6(a). The energy of the emitted photon is given by

$$\hbar\omega = E_{kin}(\theta = \theta_r) + I_p \tag{2.13}$$

where $E_{kin}(\theta = \theta_r)$ is the kinetic energy of an electron at the time of recombination. The time (phase) of recombination can be obtained from the roots of the following equation,

$$z(t) = 0 \Rightarrow z(\theta) = 0 \tag{2.14}$$

The phase of ionization θ_0 and recombination θ_r can be, hence, obtained from the following equations:

$$(\cos\theta_r - \cos\theta_0) + (\theta_r - \theta_0)\sin\theta_0 = 0 \tag{2.15}$$

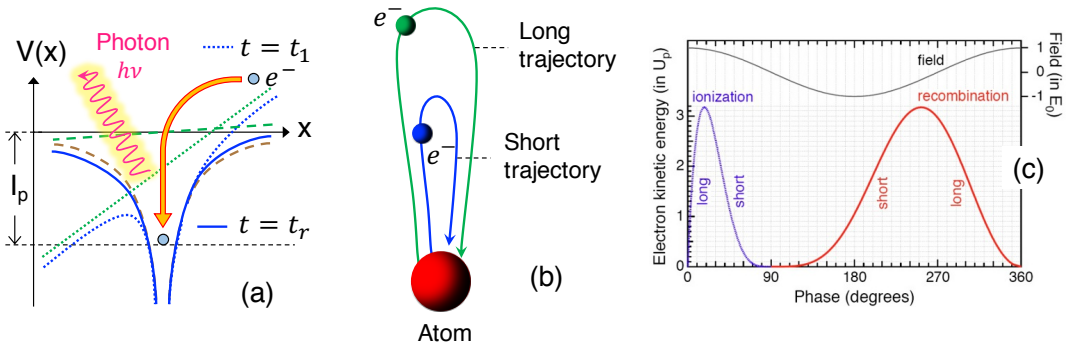

Figure 2.6: Adapted from [7]. (a) The electron recombines with its parent atom at time t_r emitting a photon carrying the kinetic energy of the electron plus its ionization potential. (b) Types of electron trajectories after ionization until it recombines with the atom. (c) Taken from [8]. E_{kin}/U_p as a function of ionization and recombination phases, θ_0 and θ_r, respectively.

$$(\sin\theta_r - \sin\theta_0)^2 = \frac{E_{kin}}{2U_p} \tag{2.16}$$

Figure 2.6(c) shows the variation of E_{kin}/U_p as a function of θ_0 and θ_r. For θ_0 = 17° and θ_r = 255°, E_{kin} attains the maximum value of $3.17U_p$ and the highest energy cutoff for the harmonics is, thus, given by $3.17U_p + I_p$. The path $z(\theta)$ that the electron follows from $\theta = \theta_0$ to θ_r is called its *trajectory*. Depending on the phase at which the electron is ionized and its subsequent phase of recombination, there are two possible types of trajectory [see Figure 2.6(b)] for a given kinetic energy below $3.17U_p$ — the *short* trajectory for $17° < \theta_0 < 90°$, $90° < \theta_r < 255°$ and the *long* trajectory for $0° < \theta_0 < 17°$, $255° < \theta_r < 360°$. If $[\theta_0, \theta_r]$ are the solutions of Equations 2.15 and 2.16, then $[\theta_0 + m\pi, \theta_r + m\pi]$ are also solutions, where m is an integer. This implies that the three step process repeats every half-cycle T/2 of the driving laser field (having time period T). This corresponds to a separation of $1/(T/2) = 2\nu$ in the frequency domain where ν is the fundamental laser frequency and to a harmonic spectrum that is composed of frequency components that are odd integer multiples of the fundamental frequency: $\nu_m = (2m+1)\nu$.

Phase-matching: High-harmonic generation is not a process involving a single atom but many of them which are coherently stimulated by the electric field of the laser. To generate a bright output beam, the emission of a large number of atoms over an extended region of the conversion medium must add in phase. For this reason, propagation effects such as phase-matching become important. This phase-matching condition is met when the fundamental frequency of the driving laser and the generated harmonic frequencies travel at the same phase velocity in the medium. A phase mismatch between the propagation of the fundamental and harmonic frequencies can, therefore, significantly affect the HHG conversion efficiency. The phase mismatch is defined as the difference between the wavevector of the fundamental laser

frequency, multiplied by the harmonic number m, and the m^{th} harmonic field,

$$\Delta k_m = mk_0 - k_m \tag{2.17}$$

where k_0 and k_m are the wavevectors of the driving laser field and the m^{th} harmonic, respectively. Any conversion medium (a noble gas, in our case) used for high-harmonic generation is dispersive, i.e., the refractive index of the medium, $n(\omega)$, depends on the frequency of light, ω. This causes the fundamental and harmonic frequencies to propagate at different phase velocities through the medium, $v_p = c/n$, where v_p is the phase velocity and c is the speed of light in vacuum. Since the wavevector in turn depends on the refractive index, there is a finite phase mismatch, $\Delta k_{m,disp}$, arising due to the material's dispersive property. At intense laser fields, the electrons that are ionized but do not recombine with their parent atoms are free and form a plasma. The latter behaves as a dielectric whose refractive index is given by, $n_{plasma}(\omega) = \sqrt{1 - (\omega_p/\omega)^2}$ where ω_p is the plasma frequency and this gives rise to an additional phase mismatch of $\Delta k_{m,plasma}$. In addition to the above, the focussing and propagation of the laser beam also contribute to the total phase mismatch by the amount, $\Delta k_{m,geom}$. The total phase mismatch between the fundamental frequency and its m^{th} harmonic is, therefore, given by:

$$\Delta k_m = \Delta k_{m,disp} + \Delta k_{m,plasma} + \Delta k_{m,geom} \tag{2.18}$$

with any of the Δk_m given by $mk_0 - k_m$. For a particular harmonic, the HHG efficiency is maximum only when the phase-matching condition, $\Delta k_m = 0$, is satisfied. From an experimental point of view, it is generally not possible to achieve a perfect phase matching over the entire volume of the conversion medium. To maximize the generation efficiency at the m^{th} harmonic, optimal phase matching ($\Delta k_m \approx 0$) can be obtained by tuning the experimental parameters, such as (i) the gas pressure in the interaction region, (ii) distance of the target medium from the focus of the laser beam, (iii) intensity of the driving laser field.

2.1.3 CITIUS beamline

The various elements of the laser system, together with a scheme of the beamline [9], is shown in Figure 2.7 and will be briefly described in this section. The laser system comprises a commercial amplifier Legend Elite Duo and an optical parametric amplifier OPerA (OPA), both manufactured by Coherent, Inc. The amplifier is seeded by a Micra oscillator (wavelength: 800 nm, spectral bandwidth about 100 nm, power about 380 mW) and includes two amplification stages: a regenerative amplifier (EVO 30), pumped by an Evolution 30 laser (frequency-doubled Q-switched Nd:YLF laser), and a single-pass amplifier (EVO HE), pumped by an Evolution HE laser (frequency-doubled Q-switched Nd:YLF laser). The system can be operated at four different repetition rates: 100 Hz, 1 kHz, 5 kHz, and 10 kHz. At 5 kHz, which is the repetition rate utilized for the studies reported in the thesis, it generates pulses

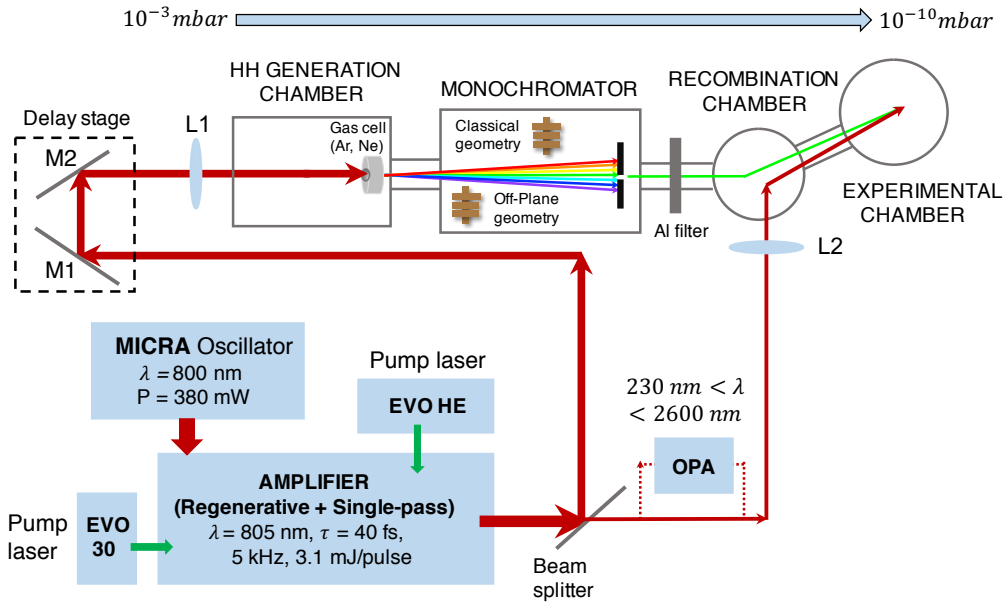

Figure 2.7: Layout of the CITIUS source, including the laser system, the high harmonic (HH) generation chamber, the monochromator, the recombination chamber, the delay line, and the experimental chamber. OPA stands for Optical Parametric Amplifier, M for mirrors and L for lenses.

carrying about 3.1 mJ, with a duration of about 40 fs, centered at 805 nm. Two third of the energy is used for generating extreme ultraviolet pulses through HHG and one third either as a pump for the OPA, or directly in combination with the HHG beam, for pump-probe experiments. The OPA produces tunable radiation in the range between 0.4 eV and 5.6 eV, with variable energy per pulse (from few to hundreds of microjoules). The beamline includes a high-vacuum section, through which the XUV beam propagates, and a section in air, used to transport the fundamental infra-red beam or the UV light generated by OPA. The XUV branch comprises an HHG chamber and a vacuum chamber hosting the monochromator grating.

- **The HHG chamber:** The spot size of the fundamental laser beam is adjusted by means of a variable diameter iris and focused by a lens (L1 in Figure 2.7) which allows the control of the intensity distribution at the focus. Directly after the focussing optics, the beam enters the generation chamber through a silica window. The focussed beam interacts with a noble gas of choice (Argon or Neon) confined in a cell, generating harmonics. The gas cell is mounted on an XYZ stage and in order to optimize the position of the cell relative to the laser focus, the gas cell is given a translational motion along the direction of propagation of the incoming beam. The high-harmonic generation efficiency for the chosen harmonic will be maximum at the best phase-matching conditions as already discussed in Section 2.1.2. Typical harmonic spectra obtained using different noble gases is shown in Figure 2.8.

- **The monochromator:** The monochromator grating has been designed to select one single harmonic, or a sub-band of it, in the spectral range be-

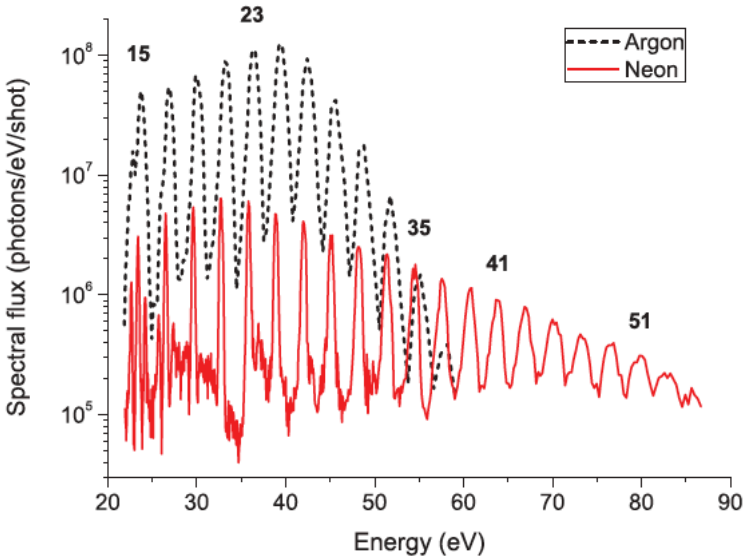

Figure 2.8: Taken from [9]. Harmonic spectra generated in two different noble gases, Argon and Neon, at CITIUS. Some of the harmonic orders are labelled.

tween 250 and 12 nm (5-100 eV) [9]. The CITIUS monochromator differs from other systems for the spectral selection of high-order harmonics [10, 11, 12] in that it adopts a single-grating design, with a double-stage configuration [13, 14]. Based on the experimental requirements, one can use either a grating stage in the off-plane geometry (OPG) with minimum pulse-front tilt for ultrafast response (i.e., few tens of femtoseconds) at the expense of energy resolution, or a grating stage in the classical geometry (CG) for high-energy resolution, albeit with long temporal response (i.e., several hundreds of femtoseconds). The characteristics of the OPG and CG gratings are reported in [9]. Figure 2.9 shows a comparison of the spectra acquired with the two different geometries of the grating.

The branch transporting the XUV beam includes a delay line, allowing one to control the optical path difference between the pump and probe beams impinging on the sample in the experimental chamber (see Figure 2.7), with sub-fs time precision. The OPA/IR beam is refocused by a lens (L2 in Figure 2.7) and intercepted by a flat mirror (high-reflectivity, replaceable according to the specific wavelength in use) hosted in the recombination chamber. At the exit of the monochromator, the XUV beam passes through a 200 nm thick Al filter (to stop the residual IR seed laser) and enters the recombination chamber. The chamber hosts a toroidal mirror (Si:Au coated; 1200 mm focal length) to refocus the monochromatized XUV light at the sample position. The mirror sits in a two-axes motorized mount, to guarantee (with micrometric precision) a perfect spatial overlap between the pump and probe beams onto the sample. The pump and probe beams impinge on the sample in an almost collinear geometry in order to minimize the temporal resolution spread due to the lateral spots' dimensions. Each chamber of the beamline is pumped by a turbo pump and a connected fore-vacuum scroll pump and can be isolated in sec-

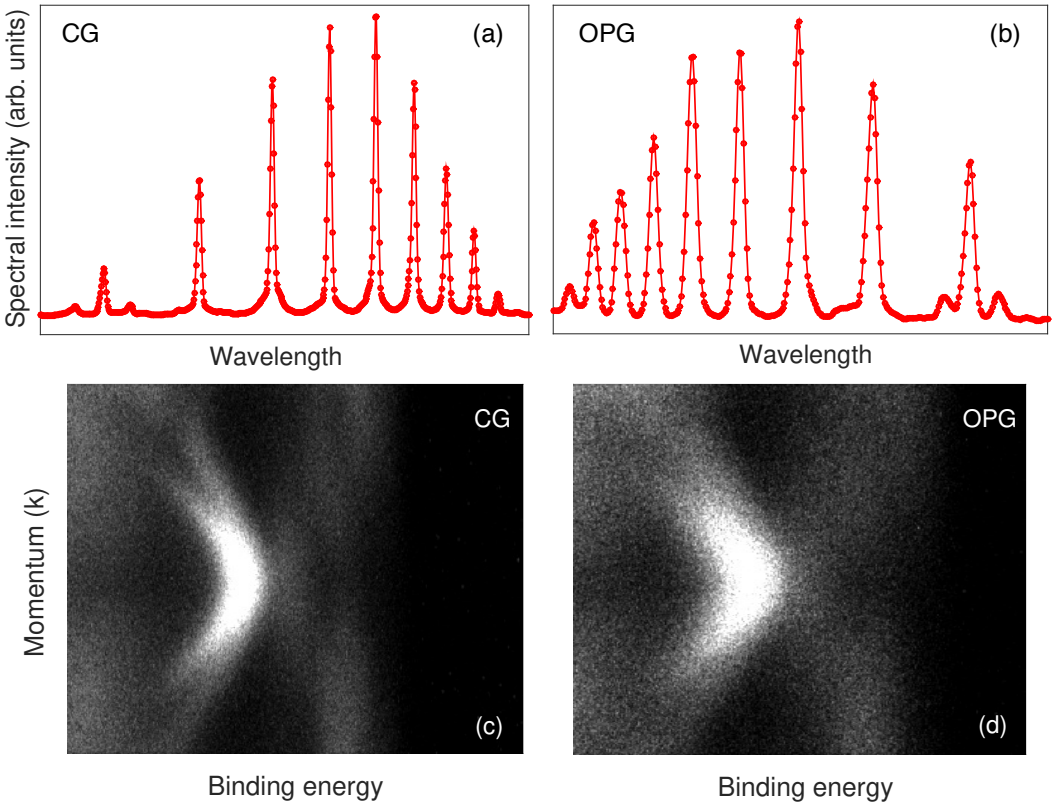

Figure 2.9: Harmonic spectra generated in Argon gas for (a) classical geometry (CG) and (b) off-plane geometry (OPG) of the monochromator grating stage. (c), (d) Angle-resolved photoemission spectra of $1T$-TaS_2, acquired at photon energy of 20 eV, using the two different grating geometries.

tions by means of manual valves. The pressure in the HHG chamber during generation is typically in the range of 10^{-3} mbar; however, a suitable set of pinholes allows to preserve the vacuum in the beamline. Typical pressures in the monochromator and in the refocusing chambers are, respectively, in the range of 10^{-7} mbar and 10^{-9} mbar. A further set of pinholes, placed after the refocusing section, preserves UHV vacuum in the experimental chambers, when needed. For ensuring beam stability while performing experiments, the laboratory floor has been isolated so to damp environmental vibrations. In order to preserve the ultrafast response, the best energy resolution that could be achieved for our trARPES setup was about 150 meV. This allowed us to achieve a temporal resolution of around 50 fs [9]. For all the reported pump-probe data in the following chapters, the pump fluence refers to the incident peak energy density (in mJ/cm^2), determined from the expression $2E_p/(\pi w^2)$, where E_p is the energy per pulse and w is the beam waist at the sample position.

2.2 The ultra high vacuum equipment for photoemission

Since photoemission spectroscopy is a surface-sensitive technique, conditions for clean sample surfaces must be achieved in UHV environment. The other fundamental reason for ensuring ultra high vacuum condition inside the experimental chamber is the following: Because of the negligible amount of gas molecules inside a UHV chamber, the probability that the photoemitted electrons suffered any collisions with other molecules during their travel towards the analyser slit is minimized. If the vacuum is poor, then the scattering probability is enhanced and this will alter the energy and the momentum of the photoemitted electrons. If this happens, the acquired photoemission spectrum provides a distorted information about the actual energy states occupied by the electrons.

2.2.1 The UHV experimental chamber

The employed UHV system is shown in Figure 2.10 and consists of two main parts, the preparation chamber and the spectrometer chamber, which are connected by a manual gate valve. There are two sample transfer lines kept in UHV and they interface with the preparation chamber by manual gate valve. The sample is held inside the chamber by a manipulator which consists of a motorized element with five degrees of freedom (three translational and two rotational) and a sample holder. The sample holder is equipped with a thermocouple, measuring the temperature directly on the crystal. The manipulator is attached to a closed cycle cryostat operating with liquid helium, capable of cooling the sample down up to 30 K. The preparation chamber is implemented with several tools for *in-situ* preparation and characterization of the sample surface:

- An ion gun that allows removing contaminants from the sample surface via sputtering with accelerated argon (Ar+) ions. The Ar+ ion beam is produced by impact of Ar_2 with the electrons thermo-emitted from the filament of the gun under precise control of the ion kinetic energy and the pressure of Ar_2 gas.
- Annealing of the sample which helps in impurity desorption and can be used to induce a surface reorganization.
- A commercial low-energy electron diffraction detector from SPECS (Er-LEED 1000-A) for determining the structural symmetry of the surface of single crystalline samples.
- Molecular films can be deposited on the prepared substrate under controlled temperature and pressure by means of evaporation of solid molecules in a cell.
- Exfoliation of the samples is obtained by cleaving them with a Scotch tape. This method is suitable for samples that have a layered crystalline

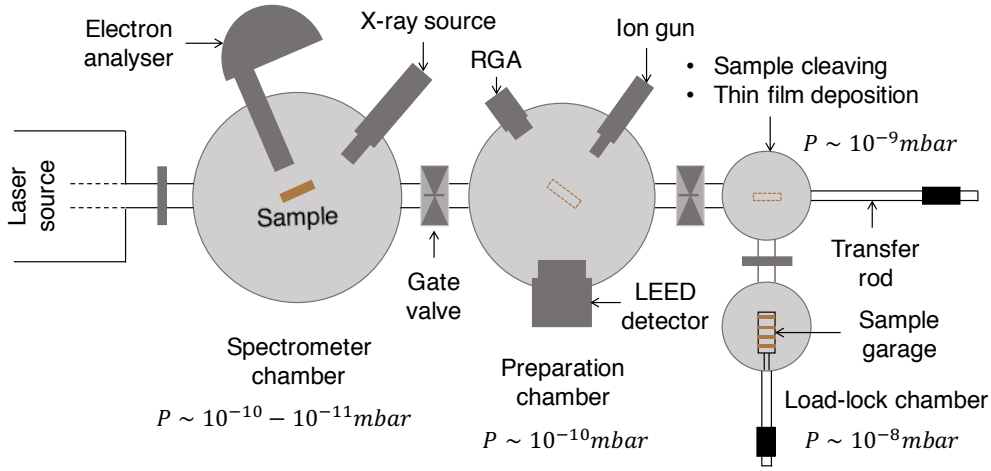

Figure 2.10: Schematic view of the ultra high vacuum experimental set-up for performing photoemission spectroscopy with all the necessary components indicated.

structure.

The spectrometer chamber is equipped with an Al K_α X-ray source (Thermo Fisher Scientific) and the hemispherical electron analyzer (VG Scienta R3000). To reach the required UHV conditions, both chambers are pumped by turbo molecular pumps. In addition, a titanium sublimation pump is used for the spectrometer chamber to improve the vacuum further and in this way, a vacuum better than 5 x 10^{-10} mbar is achieved for performing experiments.

2.2.2 The electron analyser

The electron detection system consisting of an electrostatic lens system, a hemispherical electron analyzer, and a 2D electron detector is shown in Figure 2.11. A hemispherical analyzer is made of two hemispherical plates with an applied potential diference between them. Depending on the value of the potential difference, electrons of a particular energy are allowed to pass through the center of the hemispherical plates along a circular orbit. Such an energy is called the pass energy, E_p, of the analyzer. Generally, an analyzer can be operated at different values of E_p. The electrostatic lens system is used to focus the photoemitted electrons from the sample on the entrance slit. It also accelerates or decelerates the propagating electrons to match the chosen E_p. Electrons having energy higher or lower than E_p follow elliptical orbits and move towards the outer and inner hemispheres, respectively [15]. For a chosen E_p, electrons of kinetic energies within a certain range around E_p are allowed to pass through the hemispheres. The detection system consists of a 2D micro channel plate (MCD), a phosphor screen, and a CCD camera. Once deflected towards the exit slit, electrons are multiplied by a micro-channel plate detector before impinging onto a two-dimensional phosphor screen. Finally, a CCD camera is placed behind the screen which records the kinetic energy and the angle of emission of the photoemitted electrons. The energy

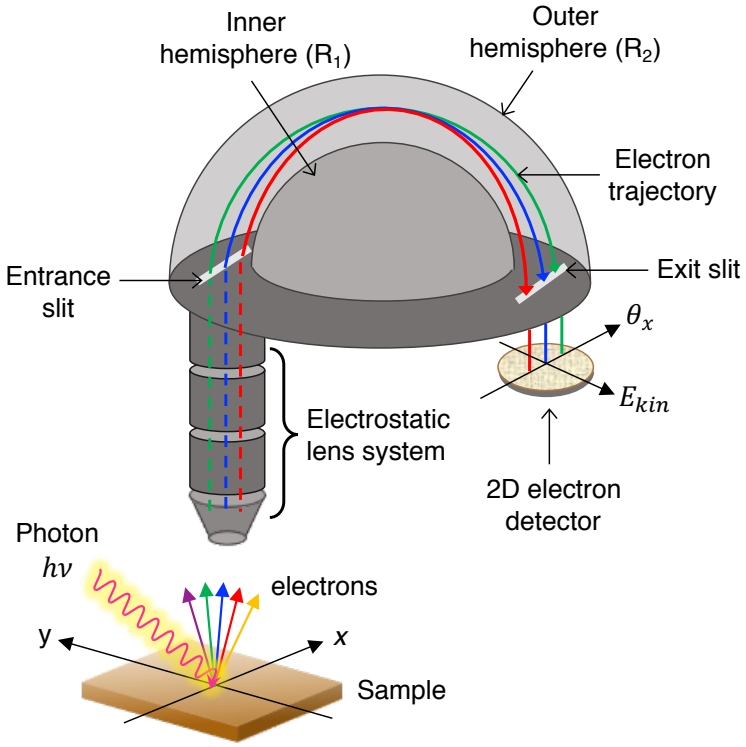

Figure 2.11: Schematics showing the main components of the photoelectron detection unit: the electrostatic lens system, the hemispherical electron analyzer, and the 2D electron detector.

resolution of the electron analyser depends on the pass energy, the radii of the hemispheres, and the width of the entrance slit s. It is given by,

$$\Delta E = \frac{sE_p}{R_1 + R_2} \tag{2.19}$$

where R_1 and R_2 are inner and outer radii of the hemispherical analyzer. The total instrumental energy resolution in a trARPES experiment includes the energy resolution given by the analyzer and finite energy width of HHG pulses. In the experimental setup at CITIUS, for a high temporal resolution (50 fs), the best achievable energy resolution ($\approx$ 150 meV) has dominant contribution from the HHG beam.

2.3 Requirements prior to measurements

This section describes the procedures for the preparation of samples and their characterisation prior to performing photoemission experiments, followed by setting up the spatial and temporal overlap of the pump and probe beams.

2.3.1 Preparation of the single crystals

Single crystals of Ta_2NiSe_5, $Ta_2Ni(Se_{1-x}S_x)_5$ and $1T$-TaS_2 having dimensions suitable for pump-probe experiments were provided by HQ Graphene. The

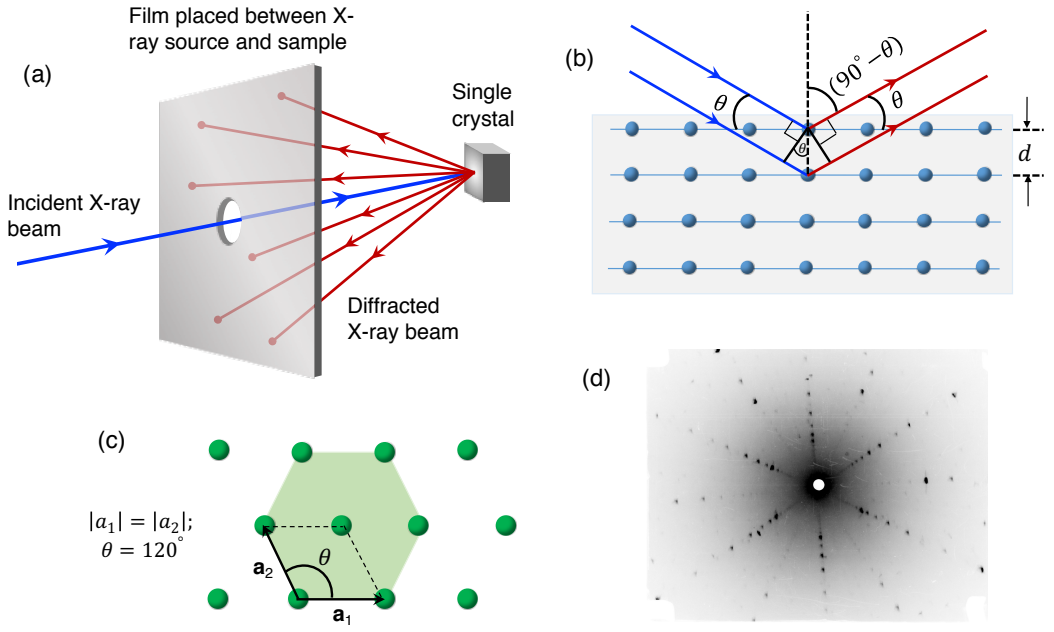

Figure 2.12: (a) Back-reflection geometry of a Laue diffraction experiment; (b) X-rays reflected from a set of lattice planes constructively interfere when Bragg's condition is satisfied: $2d \sin\theta = n\lambda$. Here, λ is the wavelength of the incident X-ray beam, n is an integer and d is the inter-planar distance. (c) A hexagonal Bravais lattice in two dimensions where $\mathbf{a}_1$ and $\mathbf{a}_2$ are the primitive lattice vectors; (d) Laue diffraction pattern obtained from a sample having hexagonal crystal structure.

samples were synthesised by chemical vapour transport (CVT) method [16, 17, 18]. In order to perform photoemission experiments, clean surfaces are obtained via cleaving in the direction perpendicular to the atomic planes. To achieve this, the sample is glued with a UHV-compatible, conducting epoxy glue (Epo-Tek E4110) onto a square copper plate. The epoxy glue is heated at $T = 120^\circ$C for approximately one hour. A piece of Scotch tape is pressed down firmly onto the surface of the so-prepared sample and the sample plate is then transferred to the UHV chamber for cleaving via a load-lock chamber holding a vacuum of $\leq 5 \times 10^{-8}$ mbar. The sample is cleaved by slowly peeling away the Scotch tape at a pressure better than 1×10^{-8} mbar. The sample ends up being cleaved as several layers from the top are removed, thus generating a clean surface. The thickness of the crystals is small, so the same sample piece can be cleaved four to five times, typically. Due to slow degradation of the sample surface in UHV conditions, continuous measurements on a freshly cleaved sample can be performed for approximately three days.

2.3.2 Sample orientation: Laue diffraction technique

The Laue diffraction technique [19] is used for mounting single crystals in a precisely known orientation for purposes such as polishing a surface or doing measurements. A knowledge of the orientation of the crystal surface is a must before performing ARPES experiments. This helps us in mounting the crystals along the desired k-symmetry direction with respect to the analyser

entrance slit and therefore probing the corresponding band dispersion. Laue diffraction can be performed in two experimental geometries: transmission geometry and back-reflection geometry. For aligning the samples related to the thesis work, back-reflection geometry has been used, as shown in Figure 2.12(a). The crystal to be aligned is mounted on a goniometer, which serves to keep the crystal in the beam of X-rays and also rotates the sample to precise degrees. The film on which the diffraction pattern forms is placed between the X-ray source and the sample. The pattern of the diffraction spots on the film provides information about the orientation of the crystal.

Laue diffraction method is based on the theory of scattering of X-rays by the atomic planes inside a solid [20]. In this method, the constituent atoms or ions of a solid from different atomic planes scatter the x-rays in all directions and sharp peaks in intensity are seen in the directions and at wavelengths at which the condition for constructive interference, $2d \sin\theta = n\lambda$ (Bragg's law), is satisfied [see Figure 2.12(b)], for each set of planes. The constructive interference of the scattered X-rays produces a spot on the film. Indeed, the path difference between the light rays reflected from two neighbouring planes is $2d \sin\theta$ and for constructive interference, this must be equal to an integer multiple of the wavelength of the light. The X-ray source produces all wavelengths roughly in the range of 0.3 Åto 4 Å. Hence for a set of planes the condition is satisfied for a correct wavelength and a diffraction spot forms on the film. In such a manner each set of planes produces one or multiple spots on the film and thus a diffraction pattern forms on the film. The experimentally obtained pattern can be compared with the simulated one to find the orientation of the crystal. An example of Laue diffraction pattern is shown in Figure. 2.12(d), for a hexagonal lattice [Figure. 2.12(c)] .

2.3.3 Overlap of pump/probe beam in space and time

Now that we have presented an overview of the technicalities of a pump-probe photoemission experiment, a brief description will be given on how the spatio-temporal overlap of the two beams is obtained in our trARPES setup. An optimal and reproducible pump/probe overlap is essential for ensuring an effective response from the sample after photoexcitation. Experimentally, this means detecting a significant number of electrons at the energy states above Fermi level E_F. However, even with an optimum overlap of the two beams, the number of detected electrons above E_F is very much dependent on the density of states of the investigated material as well as on its absorption coefficient and (non-) homogeneity of the sample surface after cleaving. The pump/probe overlap is usually set for the sample plane which is at the right focus of the analyser. Having set the analyser focal distance with respect to the sample, the spatial overlap of the pump and probe beams is established through a motorized translational movement of the mirror mount (for the pump) inside the recombination chamber. After ensuring the spatial overlap of the two beams, the temporal overlap between them is determined in the following way. The pump and probe beams pass through a non-linear crystal,

after which they impinge on a screen outside the experimental chamber, in air. The delay line placed in the path transporting the probe beam controls the optical path difference between the propagation of two beams. The delay line is first scanned over a wide range to establish a coarse temporal overlap in the range of picoseconds, followed by its fine tuning to precisely determine *time-zero* in the range of a few tens of femtoseconds.

References

[1] A. J. Maria, *et al.*, "Self mode-locking of lasers with saturable absorbers." *Applied Physics Letters* **8**, 174 (1966).

[2] J. C. Diels and W. Rudolph, "Ultrashort laser pulse phenomena : fundamentals, techniques, and applications on a femtosecond time scale." Elsevier/Academic Press, Amsterdam London (2006).

[3] A. McPherson, *et al.*, "Studies of multiphoton production of vacuum-ultraviolet radiation in the rare gases." *Journal of the Optical Society of America B* **4**, 595 (1987).

[4] M. Ferray, *et al.*, "Multiple-harmonic conversion of 1064 nm radiation in rare gases." *Journal of Physics B: Atomic, Molecular and Optical Physics* **21**, L31 (1988).

[5] P. B. Corkum, "Plasma perspective on strong field multiphoton ionization." *Physical Review Letters* **71** 1994 (1993).

[6] K. C. Kulander, K. J. Schafer and J. L. Krause, *Proc.Workshop on Super-Intense Laser Atom Physics (SILAP) III* ed B Piraux (New York: Plenum) pp 95–110 (1993).

[7] T. Pfeifer, C. Spielmann and G. Gerber, "Femtosecond x-ray science." *Reports on Progress in Physics* **69**, 443 (2006).

[8] Kenichi Ishikawa, "Chapter: High-Harmonic Generation in the book: Advances in Solid State Lasers Development and Applications" Intech Open Book Series (2010).

[9] C. Grazioli *et al.*, "CITIUS: An infrared-extreme ultraviolet light source for fundamental and applied ultrafast science." *Review of Scientific Instruments* **85**, 023104 (2014).

[10] L. Poletto, *et al.*, "Time-delay compensated monochromator for the spectral selection of extreme-ultraviolet high-order laser harmonics." *Review of Scientific Instruments* **80**, 123109 (2009).

[11] F. Frassetto, *et al.*, "Single-grating monochromator for extreme-ultraviolet ultrashort pulses." *Optics Express* **19**, 19169 (2011).

[12] H. Igarashi, *et al.*, "Pulse compression of phase-matched high harmonic pulses from a time-delay compensated monochromator." *Optics Express* **20**, 3725 (2012).

[13] L. Poletto and F. Frassetto, "Time-preserving grating monochromators for ultrafast extreme-ultraviolet pulses." *Applied Optics* **49**, 5465 (2010).

[14] L. Poletto and F. Frassetto, “Single-Grating Monochromators for Extreme-Ultraviolet Ultrashort Pulses.“ *Applied Sciences* **3**, 1 (2013).

[15] F. Hadjarab and J. L. Erskine, “Image properties of the hemispherical analyzer applied to multichannel energy detection.“ *Journal of Electron Spectroscopy and Related Phenomena* **36**, 227 (1985).

[16] S. A. Sunshine and J. A. Ibers, “Structure and physical properties of the new layered ternary chalcogenides tantalum nickel sulfide (Ta2NiS5) and tantalum nickel selenide (Ta2NiSe5).“ *Inorganic Chemistry* **24**, 3611 (1985).

[17] A. H. Thomson, F. R. Gamble and J. F. Revelli, “Transitions between semiconducting and metallic phases in 1T-TaS_2.“ *Solid State Communications* **9**, 981 (1971).

[18] For a review of transport reactions see: Harald Schafer, “Chemical Transport Reactions“ Academic Press, New York, (1964).

[19] B. D. Cullity and S. R. Stock, “Elements of X-Ray Diffraction“ Third Edition, Prentice-Hall (2001).

[20] N. W. Ashcroft and N. D. Mermin, “Solid State Physics.“ CENGAGE Learning (1976).

3 Electronic band structure in pristine and S-doped Ta_2NiSe_5

In this chapter, we present an angle-resolved photoemission study of the electronic band structure of Ta_2NiSe_5, as well as its evolution upon Sulfur doping. Our experimental data show that while the excitonic insulating phase is still preserved at a S-doping level of 25%, such phase is heavily suppressed, at liquid nitrogen temperatures, when there is a substantial amount, $\sim$ 50%, of S-doping. Moreover, our photon energy-dependent measurements reveal a clear three dimensionality of the electronic structure, both in Ta_2NiSe_5 and $Ta_2Ni(Se_{1-x}S_x)_5$ (x = 0.25, 0.50) compounds.

3.1 Introduction

The dimensionality and degree of anisotropy in electronic transport and optical properties of layered materials, such as, MoS_2 [1, 2], ReS_2 [3] and other transition-metal dichalcogenides [4], make them potentially suitable for the fabrication of new electronic and optoelectronic devices. A recent addition to the family of such materials are the ternary chalcogenides, Ta_2NiX_5 (X = Se/S), which have attracted attention due to their layered crystalline structure and in-plane anisotropic properties [5, 6, 7]. In both materials, the transition metal atoms and the chalcogen atoms are arranged forming a chain pattern in each layer and the layers are stacked by van der Waals forces [8]. While the ground state of Ta_2NiSe_5 is known to be an excitonic insulator (EI) [9, 10, 11], Ta_2NiS_5 does not show any evidence of hosting an excitonic insulating phase and is a normal semiconductor in its ground state [12].

The EI phase has been identified in a number of materials, such as $TiSe_2$ [13, 14], Ta_2NiSe_5 [15], $TmSe_{1-x}Te_x$ [16], InAs/GaSb quantum wells [17], etc. However, the phase transition in some of these materials is strongly influenced by lattice and spin degrees of freedom [18, 19], for example, a charge density wave (CDW) effect put forward for 1T-$TiSe_2$ [20, 21]. In this respect, Ta_2NiSe_5 has emerged as a promising candidate for hosting a canonical excitonic insulator phase, excluding such scenarios where lattice distortion-mediated CDW mechanism leads to the phase transformation. However, Ta_2NiSe_5 also undergoes an orthorhombic to monoclinic structural phase transition [8, 22] in addition to EI transition which raises a question on the dominant origin of the order parameter in this material. This triggered numerous experimental and theoretical [23, 24, 25] studies that used either equilibrium [10, 26, 27, 28] or non-equilibrium [29, 30] approaches trying to resolve the issue. The question on the dominant origin of the order parameter in Ta_2NiSe_5

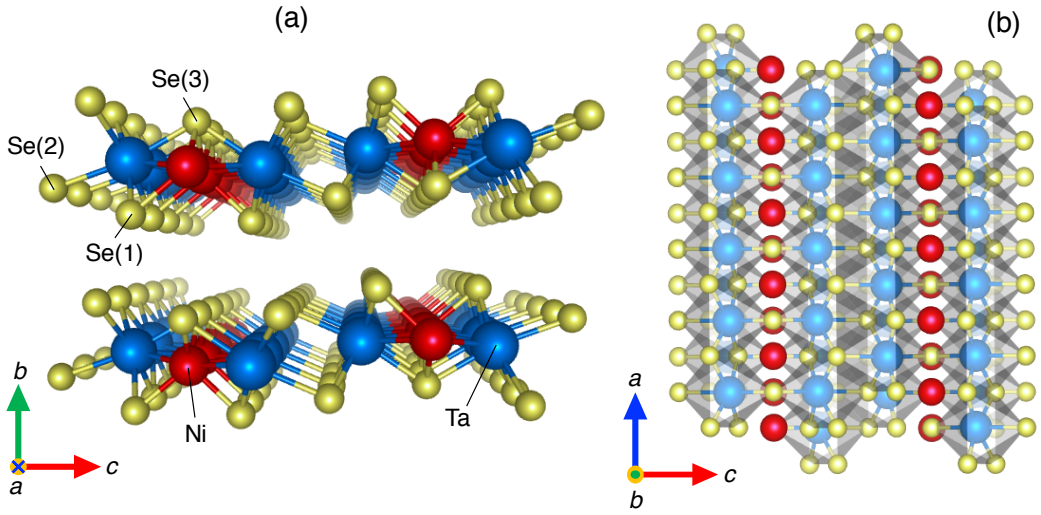

Figure 3.1: (a) Crystal structure of Ta_2NiSe_5 in the low-temperature monoclinic phase, emphasizing the layered nature in the *a*-*c* plane. (b) Top-view of the *a*-*c* plane showing the $TaSe_6$ and $NiSe_4$ chains along the *a*-axis. Here, *a*, *b*, *c* define the crystal axes and Tantalum (Ta), Nickel (Ni) and Selenium (Se) atoms are represented by blue, red and yellow spheres, respectively. The structural model was generated using VESTA [31].

has been addressed in Chapter 4. The scope of this chapter is to study the effect of increasing energy gap E_G on the electronic band structure of Ta_2NiSe_5 and the dimensionality in pure and doped compounds. The increase of E_G is obtained by introducing Sulfur atoms at Selenium sites.

In the present work, we utilize angle-resolved photoemission spectroscopy to investigate the effect of increasing S-doping level (x) on the electronic band structure of $Ta_2Ni(Se_{1-x}S_x)_5$, notably the changes in E versus k dispersion of the valence band, along different symmetry directions in k-space. While extensive equilibrium and non-equilibrium studies have been done on pristine Ta_2NiSe_5, the T_C (EI transition temperature) versus x phase diagram [15] has not been explored through ARPES so far. Although the parent compounds are known to possess strongly two-dimensional properties of the electronic structures, which is consistent with the layered structure of Ta_2NiSe_5 and Ta_2NiS_5, our photon-energy dependent ARPES data show a possible three dimensionality of the electronic structure in $Ta_2Ni(Se_{1-x}S_x)_5$ compounds.

3.2 Material description

Structural properties: Ta_2NiSe_5, first reported in Ref. [32], has a layered crystalline structure, where each layer consists of double chains of Tantalum (Ta) atoms with single chains of Nickel (Ni) atoms in-between. The crystal structure of Ta_2NiSe_5 in its low temperature monoclinic phase is shown in Figure 3.1. The Ta-Ni-Ta trichains are parallel to the crystallographic *a*-axis and repeat themselves along *c*-axis, exhibiting a quasi-one dimensional struc-

ture, see Figure 3.1(a). Selenium atoms are tetrahedrally and octahedrally coordinated around the Ni atoms ($NiSe_4$) and Ta atoms ($TaSe_6$), respectively, see Figure 3.1(b). The layers are stacked along b-axis and are held together through van der Waals forces. This compound crystallizes in an orthorhombic structure of space group *Cmcm* above T_C, where it is a narrow direct band gap semiconductor. A semiconductor-to-insulator transition is observed at $T_C \approx$ 328 K, accompanied by a structural transition to monoclinic phase (of space group *C2/c*) with lattice constants a = 3.496 Å, b = 12.829 Å and c = 15.641 Å, $\alpha = 90°$, $\beta = 90.53°$, $\gamma = 90°$ [22]. The primitive unit cell contains four Tantalum atoms, two Nickel atoms, and ten Selenium atoms. All the Tantalum sites and Nickel sites are crystallographically equivalent but there are three inequivalent Selenium sites, Se(1), Se(2), Se(3), see Figure 3.1(a).

Physical properties: For the electronic properties of Ta_2NiSe_5 in equilibrium, electrical resistivity [22, 33, 34], heat capacity [34], and optical conductivity [5, 34] measurements have reported an anomalous change in the respective observables at T_C. The resistivity shows a metal-like behavior above 550 K, while it becomes semiconductor-like below 500 K with an anomaly at T_C, where it increases by approximately one order of magnitude and the system becomes an insulator. Magnetic susceptibility exhibits diamagnetism with an anomaly at the same T_C, found in resistivity measurements [22]. The heat capacity decreases upon cooling as predicted by the Debye model [35]. However, an anomalous peak appears around T_C, which is reminiscent of the discontinuity in the specific heat function of BCS superconductors at the transition temperature [36]. This feature is assigned to a change of the electronic entropy of the system and the appearance of a new ground state. Optical conductivity measurements reveal the opening of an excitation gap of $E_{op} \sim 0.16$ eV below T_C. The excitation gap is comparable to the expected exciton binding energy and is reasonably ascribed to the excitonic gap. The above anomaly is associated to a second-order phase transition from a semiconducting state to an excitonic insulator ground state.

The tight-binding band structure calculation suggests that the system is a semiconductor and has a direct band gap at the Γ-point of the Brillouin zone [37]. Along the ΓX direction, the dispersion of the valence and conduction bands close to Fermi level follows a one-dimensional (1D) cosine function, consistent with the predictions of a 1D two-band semiconductor model [11, 38]. This k-direction corresponds to the crystallographic a-axis of the Ta and Ni atomic chains in real space. A schematic of the bulk Brillouin zone of Ta_2NiSe_5 for the monoclinic phase, along with its projection on the k_xk_y plane is shown in Figure 3.2(a). X-ray photoemission spectroscopy (XPS) and cluster-model calculation for Ta_2NiSe_5 [39] reveal that although the formal valency of the Ni site can be viewed as +2, the actual electronic configuration of the Ni site has the d^9L character, where L denotes a Se $4p$ hole. The valence band top is composed of Ni $3d$ t_{2g} and Se $4p$ orbitals while the conduction band bottom is mainly constructed from the Ta $5d$ t_{2g} orbitals. The flat dispersion of the topmost valence band around Γ-point, observed

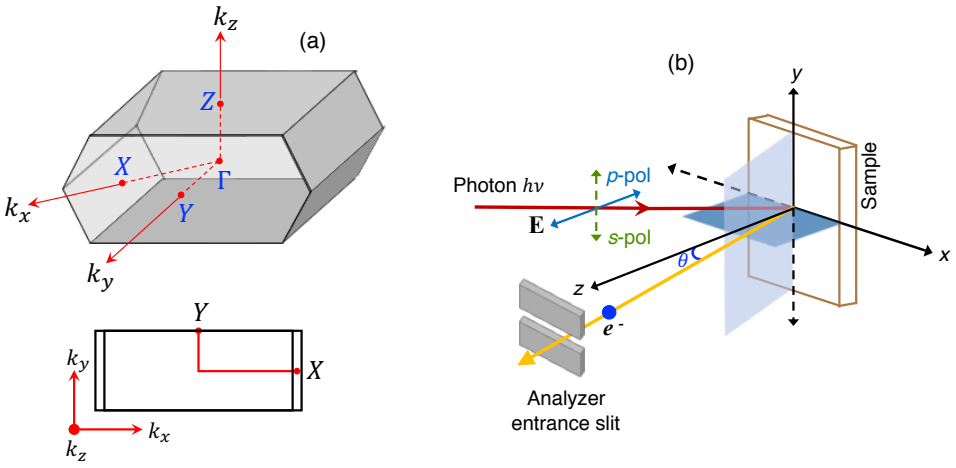

Figure 3.2: (a) (Top) BZ of a monoclinic lattice where Γ, X, Y, Z are the high symmetry k-points, (bottom) projection of the BZ on k_xk_y plane. (b) Schematic representation of the experimental geometry showing the horizontal (p-pol, blue arrow) and vertical (s-pol, green arrow) polarizations of electric field **E** of the incident photon with respect to the sample.

in angle-resolved photoemission spectroscopy experiments [39], suggests that an excitonic insulator ground state is realized in Ta_2NiSe_5, where the excitons are formed by the Ni $3d$–Se $4p$ holes and the Ta $5d$ electrons. The evolution of valence band along ΓX direction upon cooling below T_C is characterized by a shift towards higher binding energies as well as narrowing of the spectral width [33]. Lately, a semi-metallic picture of the normal phase of Ta_2NiSe_5 has been suggested based on the two-peak structure of the valence band dispersion below Fermi level, which is a characteristic of the so-called BCS regime [28, 40, 41, 42].

3.3 Experimental conditions

For the purchased samples, the stoichiometry of the elements was confirmed using Energy-Dispersive X-ray analysis (EDAX) by the company. The ARPES experiments were carried out at the BaDElPh beamline [43] of the Elettra synchrotron in Trieste, Italy. It offers both horizontal (p-pol) and vertical (s-pol) light polarizations, a maximum angular resolution of 0.1° and energy resolution of 5.4 meV. A photon energy range from $h\nu$ = 16 eV to $h\nu$ = 34 eV was used for this study and all the data presented in the paper were acquired at sample temperature T = 80 K. Prior to ARPES measurements, clean sample surfaces were obtained via cleaving in the direction perpendicular to the atomic planes. The samples were cleaved under UHV pressure better than 5 x 10^{-10} mbar and the measurements were performed at a base pressure $<$ 1 x 10^{-10} mbar. The experimental geometry of the sample plane with respect to the analyser slit and direction of light polarization is schematically represented in Figure 3.2(b).

3.4 Results

3.4.1 Light polarization dependent ARPES

Figure 3.3 shows an overview of the band structure in Ta_2NiSe_5 for the low temperature phase along ΓX direction, using light with different linear polarizations. The ARPES spectra in Figures 3.3(a)-(b) show that the top part of the valence band centered at Γ ($k_x = 0$) is characterised by a flat band dispersion [9], which is known to be a charactersistic of the EI phase. The stacked energy distribution curves (EDCs) along k_x extracted from the (a)-(b) ARPES intensity plots are shown in Figures 3.3(c)-(d), respectively, to give a better perspective of the band dispersions, especially the valence band below Fermi level, E_F (referenced as 0 eV). To give a clear picture of the characteristic band flatness close to E_F, the peak energy positions of the topmost valence band determined from the EDCs in (c) and (d) are plotted as a function of k_x in Figures 3.3(e) and 3.3(f), respectively. We observe that the top valence band lies at $\sim$ 0.2 eV below E_F and its dispersion around Γ is hole-like with a flattened top, giving an overall shallow M-shaped dispersion. The parts away from Γ and more towards X are strongly dispersive. A characteristic M-shaped dispersion which becomes sharper on lowering the temperature has been previously reported from ARPES studies done using different light polarization geometries [28]. Moving to the polarization dependence of the ARPES spectra, we note from Figures 3.3(a) and 3.3(b) that the photoemission spectra acquired using two different polarization geometries, namely, p-pol [**E** lying in xz plane in Figure 3.2(b)] and s-pol [**E** along y-direction in Figure 3.2(b)], exhibit strong differences. The spectral weight of the flat top part of the valence band centered at Γ is relatively strong for s-pol. For the dispersive parts of the valence band which are away from Γ and along the ΓX line, the spectral weight is stronger when probed with p-pol light. This polarization-dependent contrast is attributed to the symmetry selection rules of the photoemission process [44, 45]. Similar symmetry contrasts are also observed in 25% and 50% S-doped Ta_2NiSe_5, as shown in Figure 3.4. Such drastic changes in the spectral intensity of polarization-dependent ARPES data can help us identify the mirror symmetries associated with different atomic orbitals. From now on, we will only show the data acquired using s-pol light due to the better visibility of the top part of the valence band, which is relevant for the excitonic insulator phase.

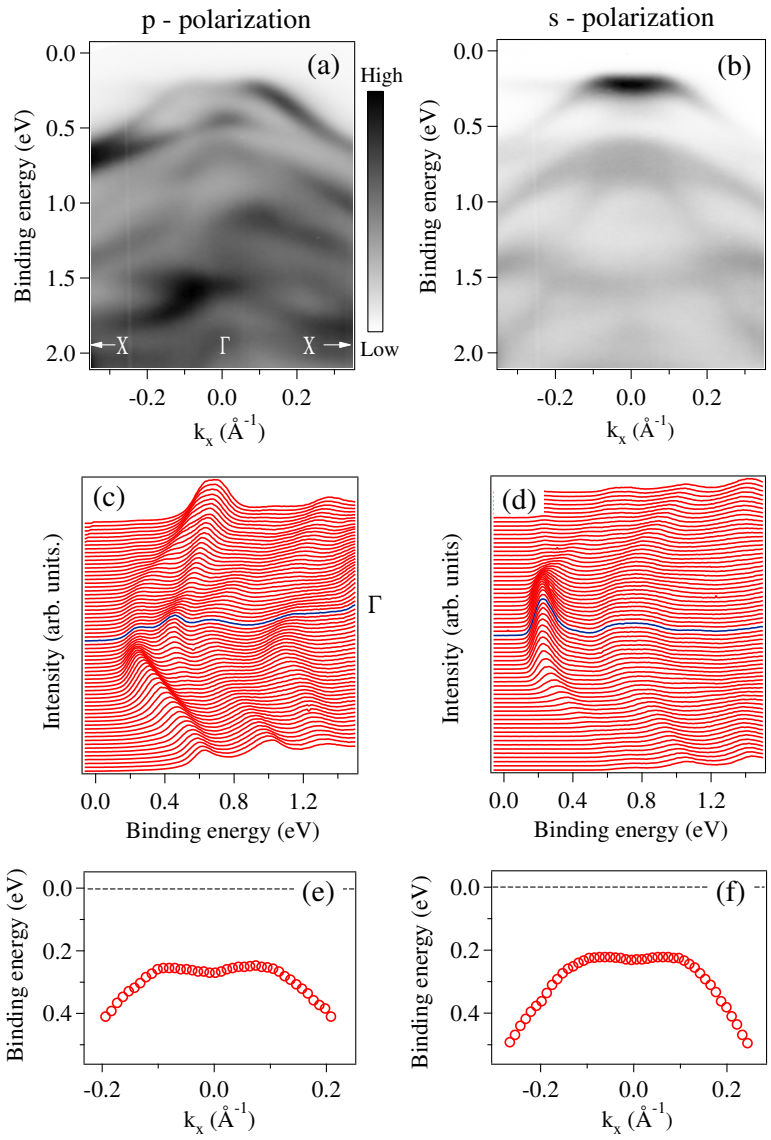

Figure 3.3: ARPES intensity maps of Ta_2NiSe_5 along ΓX direction acquired at T = 80 K using (a) p-pol and (b) s-pol light, with photon energy $h\nu$ = 19 eV. The extracted energy distribution curves (EDCs) stacked along k_x-axis for p-pol (c) and s-pol (d). The blue curve corresponds to the EDC at Γ ($k_x = 0$). A zoomed view of the valence band dispersion showing the band flatness near Fermi level, E_F, where the peak positions of the band obtained from the EDCs in (c) and (d) are plotted as a function of k_x in (e) for p-pol and (f) s-pol. The dashed lines denote E_F.

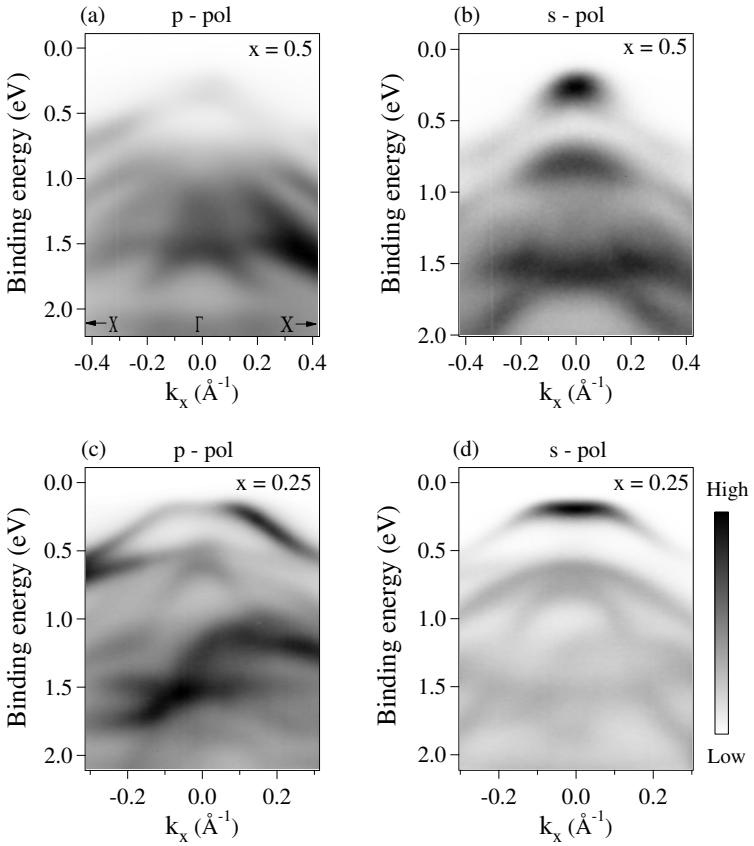

Figure 3.4: ARPES intensity maps of $Ta_2Ni(Se_{0.5}S_{0.5})_5$ acquired along ΓX direction at T = 80 K and at photon energy 26 eV using (a) p-pol light and (b) s-pol light. The same for $Ta_2Ni(Se_{0.75}S_{0.25})_5$ in (c) and (d), respectively at photon energy 20 eV.

3.4.2 Anisotropic band dispersions

Although Ta_2NiSe_5 is believed to form a quasi-one-dimensional structure, the hopping of mobile carriers along c-axis gives rise to a two-dimensional (2D) character of the electronic band structure. There exists an anisotropy in the band dispersions of Ta_2NiSe_5 [28, 46, 47] and Ta_2NiS_5 [12] along ΓX and ΓY directions. Our ARPES data reveal similar anisotropic properties of the electronic structure in S-doped Ta_2NiSe_5 as well. The ARPES intensity maps along ΓX and ΓY (refer to Figure 3.2(a) for the k-space symmetry points) of $Ta_2Ni(Se_{1-x}S_x)_5$ for $x = 0.25$ are shown in Figures 3.5(a) and 3.5(b), respectively. We observe that the dispersion around Γ point along k_x-axis (ΓX direction) is characterized by a flat feature of the valence band top while the dispersion of the valence band at Γ along k_y-axis (ΓY direction) does not exhibit the hybridized flattened band dispersion. The periodicity of the band dispersion along k_y in Figure 3.5(b) could be easily captured with the photon energy range used in this study, due to its small periodicity along ΓY direction. In order to better illustrate the band dispersion along both directions, the corresponding stacked EDC plots are displayed in Figures 3.5(c) and 3.5(d). A zoomed view of the dispersion for the top part of the valence band centered

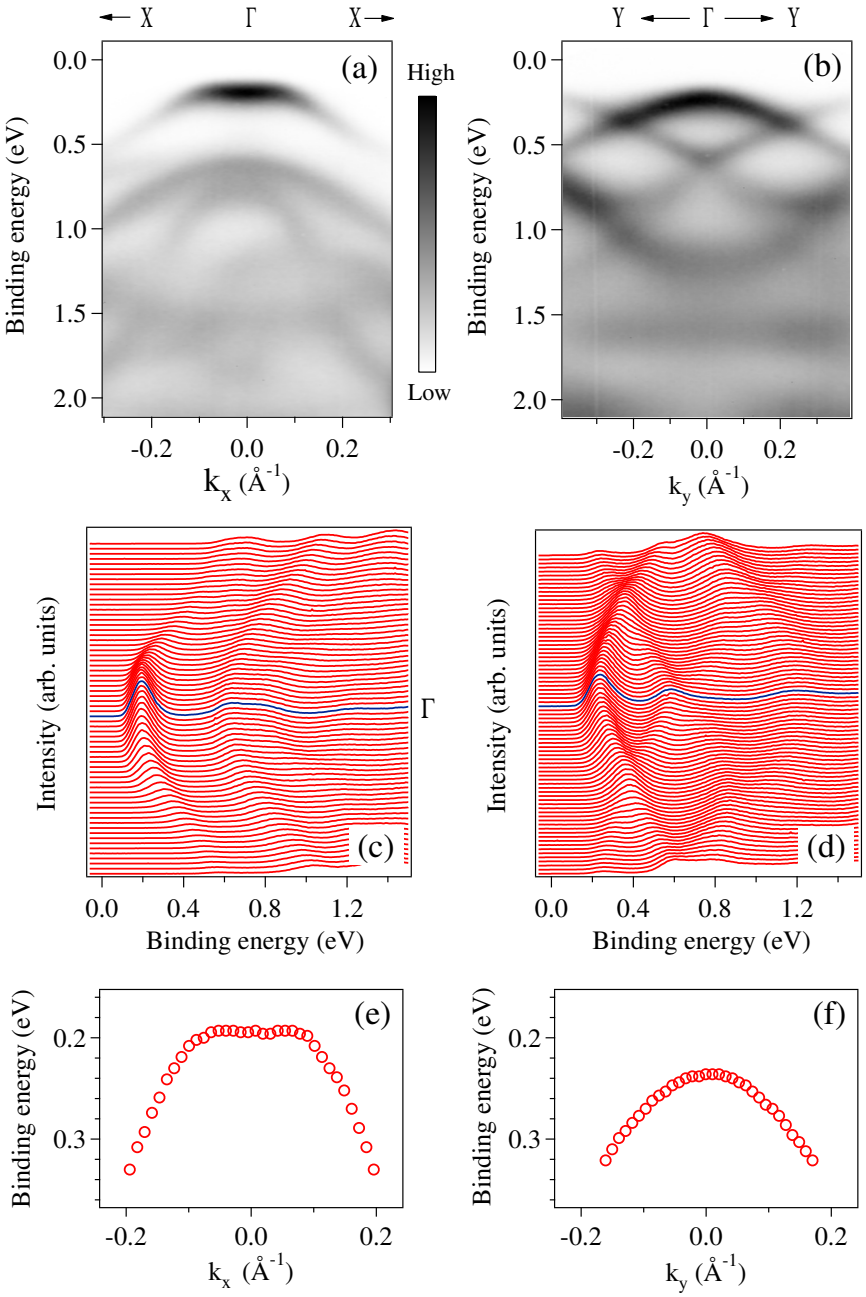

Figure 3.5: ARPES intensity maps of 25% S-doped Ta_2NiSe_5 along (a) ΓX and (b) ΓY directions acquired at T = 80 K and photon energy $h\nu$ = 20 eV using s-pol photons. The extracted energy distribution curves (EDCs) stacked along k_x-axis in (c) and k_y-axis in (d). The blue curve corresponds to the EDC at Γ [$k_x = 0$ in (a), $k_y = 0$ in (b)]. A zoomed view of the valence band dispersion near Fermi level, E_F, where the peak positions of the EDCs in (c) and (d) are plotted as a function of k_x and k_y in (e) and (f), respectively.

at Γ along k_x and k_y directions is presented in Figures 3.5(e) and 3.5(f), respectively. The dispersion has been obtained from the peak energy positions of the corresponding EDCs [in Figures 3.5(c) and 3.5(d)] for the valence band top below E_F. The flat band feature around Γ along k_x is clearly seen while the dispersion of the valence band top along k_y seems to be parabolic. The difference in the binding energy at Γ-point along ΓX and ΓY directions is not a property of the material but is due to the geometry of the sample alignment (see Appendix). For completeness, the anisotropic dispersion for pristine Ta_2NiSe_5 and $Ta_2Ni(Se_{1-x}S_x)_5$ ($x = 0.5$) is shown in Figure 3.6. Because the bands also show a dispersion in the (in-plane) direction perpendicular to the Ta-Ni-Ta chains, the quasi-1D structure often assumed for this family of compounds does not fully describe the electronic structure in these materials.

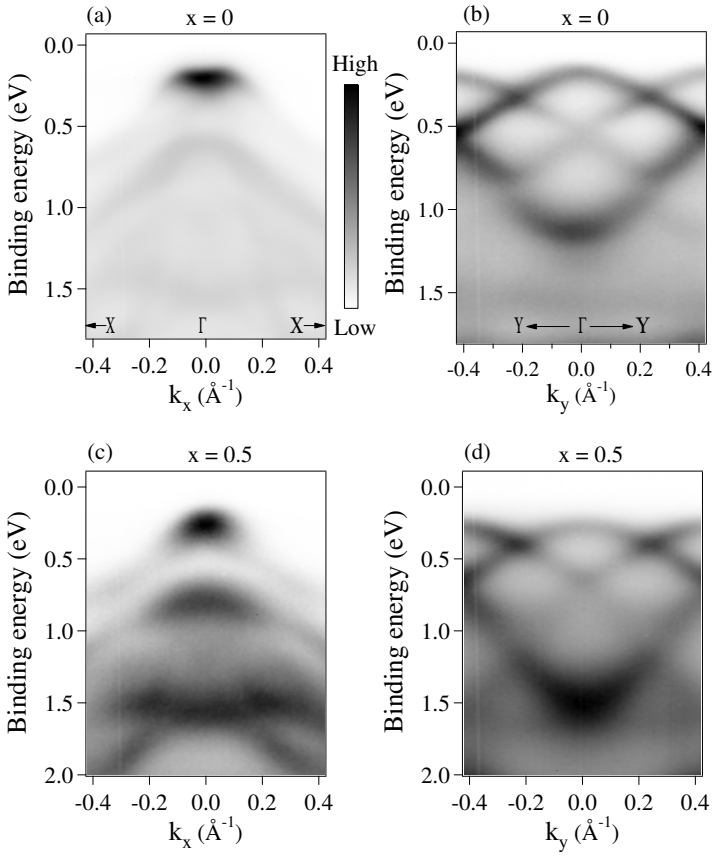

Figure 3.6: (a) and (b) Anisotropic band dispersions along ΓX and ΓY directions in Ta_2NiSe_5. Band dispersions along ΓX and ΓY in $Ta_2Ni(Se_{0.5}S_{0.5})_5$ in (c) and (d), respectively. A photon energy of 26 eV and s-pol light is used.

3.4.3 Suppression of the excitonic insulating phase at a high S-doping level

We now study the effect of S-doping on the electronic structure of Ta_2NiSe_5, i.e., the band dispersion in $Ta_2Ni(Se_{1-x}S_x)_5$, with increasing values of x. Fig-

ure 3.7 shows the evolution of the band dispersion along ΓX direction in $Ta_2Ni(Se_{1-x}S_x)_5$ with x changing from 0 to 0.5. We observe that for S-doping levels of $x = 0, 0.25$ and 0.5, the band structure retains the main dispersive features down to approximately 2 eV below E_F, except for the top-part of the valence band at Γ. What is interesting to note here is that while the band flatness with the shallow M-shape is present for pristine Ta_2NiSe_5 [0% S-doping in Figures 3.7(a), (d)] and remains almost unaffected under 25% S-doping [see Figures 3.7(b), (e)], it is significantly distorted for a substantial S-doping level of 50% [see Figures 3.7(c), (f)]. Considering Ta_2NiSe_5 to be a semi-metal in its normal state, we find that the band gap first decreases [in Figure 3.7(h)] and then increases [in Figure 3.7(i)] upon S-doping. Since the flat dispersion of the valence band top is an indicator of the excitonic insulator phase, the observed deviation suggests the suppression of an excitonic insulator phase under heavy S-doping. For better clarity, the valence band dispersion around Γ extracted from respective EDC plots are displayed in Figures 3.7(g)–(i). The flat band distortion can be understood considering the size of the band gap E_G in the high temperature phase of $Ta_2Ni(Se_{1-x}S_x)_5$. Indeed, at high levels of S-doping, there is a substantial increase of the band gap E_G, which suppresses the spontaneous formation of excitons. Hence, the excitonic insulating state becomes unstable against the semi-metallic ground state. This emphasizes that although an excitonic insulator phase in Ta_2NiSe_5 can be realized with 25% of S-doping at 80 K, the excitonic ground state is destroyed when the doping level is $\approx$ 50%.

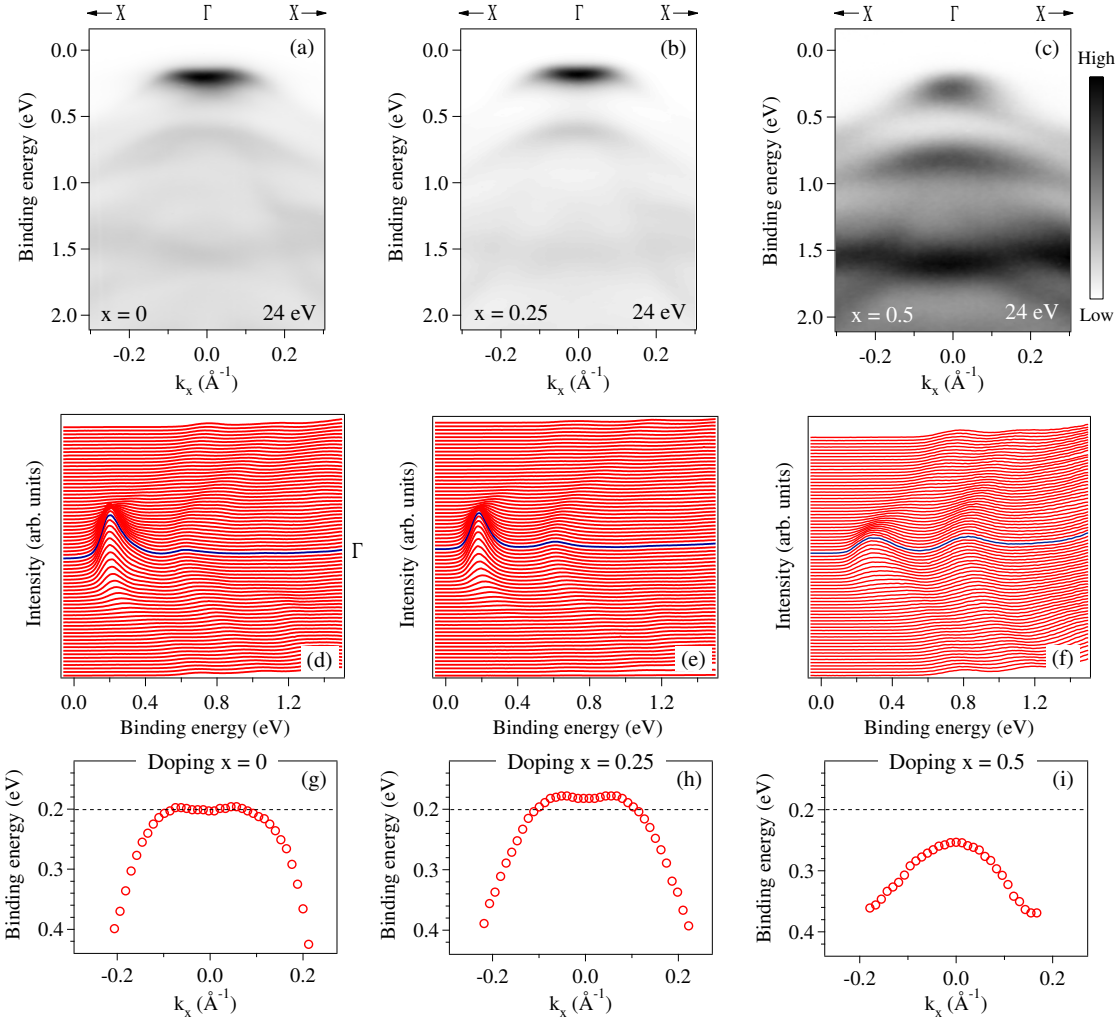

Figure 3.7: (a)-(c) ARPES intensity plots of Ta_2NiSe_5, $Ta_2Ni(Se_{0.75}S_{0.25})_5$ and $Ta_2Ni(Se_{0.5}S_{0.5})_5$, respectively, along ΓX direction acquired at photon energy $h\nu$ = 24 eV (s-pol) and T = 80 K. (d)-(f) Stacked energy distribution curves (EDCs) extracted from their respective ARPES plots in (a)-(c); the blue curve corresponds to the EDC at Γ in each case. (g)-(i) Band dispersion of the top part of the valence band near E_F for x = 0, 0.25, 0.5, respectively, obtained from the peak positions of the corresponding EDCs. The dashed line denotes the flat band binding energy at Γ-point for x = 0.

3.4.4 Enhancement of the effective mass

We now turn to the evolution of the band structure along ΓY direction as a function of S-doping. Figures 3.8(a)-(c) shows the band structure of $Ta_2Ni(Se_{1-x}S_x)_5$ for x = 0, 0.25, 0.5 and the corresponding stacked EDCs are plotted in Figures 3.8(d)-(f) for better visualization of the band dispersion. As already shown in Figures 3.5(b), (d) and (f), the valence band near E_F is characterized by a hole-like parabolic dispersion along k_y centered at Γ-point. From the ARPES intensity maps [Figures 3.8(a)-(c)], we see that the band dispersions along k_y-direction show small changes in the binding energy of different states for 25% S-doping [Figure 3.8(e)] but pronounced changes for 50% S-doping [Figure 3.8(f)], when compared to the energy states in pristine Ta_2NiSe_5 [Figure 3.8(d)]. The dispersion of the valence band around Γ near E_F for the three doping levels are compared in Figures 3.8(g)-(i). While the observed trend with S-doping should be similar to Figure 3.7(g)-(i), the deviation of the trend in binding energy along ΓY direction is attributed to sample misalignment issues (see Appendix). Since the valence band is composed of Ni 3d and Se 4p (S 3p) orbitals, increasing substitution by S atoms at the Se atom sites brings the states at the top of the valence band to higher binding energies.

Another interesting fact that can be noted from the band dispersions is the change in effective mass ratio, m^*/m_e (where, m_e is the rest mass of an electron), in $Ta_2Ni(Se_{1-x}S_x)_5$ at different S-doping levels. The valence band dispersions along ΓY have been fitted with quadratic functions, $E_0 - \hbar^2k^2/2m^*$ (h is the Planck's constant), with two fitting parameters E_0 and m^*. The experimental data in Figures 3.8(g)-(i) are well reproduced by the fits, an example of which is shown in Figure 3.9(a). The values of m^* obtained from the fits are plotted in units of m_e as a function of S-doping level in Figure 3.9(b). We observe that while the difference in the values of m^*/m_e between $x = 0$ and $x = 0.25$ is relatively small, it is significantly larger for $x = 0.5$. This is expected due to stronger carrier localization at high S-doping levels which arises from hybridized Ni 3d and S 3p orbitals, leading to higher effective masses. It is to be noted that even though the E versus k cuts along $Y\Gamma Y$ may not exactly be at the Γ-point (due to sample misalignment) but at $k_x \neq 0$, this will not affect the conclusions derived above due to the following. Since the sample inclination with respect to the sample plate is not more than a few degrees and due to low photon energies used in the experiment, the values of k_x at which the cuts have been taken are quite close to Γ-point. Based on the above, we can safely say that the deviation from an ideal high symmetry ΓY cut in k-space is very small. Therefore, in spite of the uncontrolled misalignment leading to small offsets in the binding energy, demonstration of a significant increase in the effective mass ratio with S-doping level is appropriate as long as the offset in k_x is small enough. Ref. [15] reports a decrease in the lattice constant b with an increase in the S-doping level, x, in $Ta_2Ni(Se_{1-x}S_x)_5$ compounds. The values of b at different doping levels from Ref. [15] are the following (these are estimated values): 12.83 Å, $x = 0$; 12.7 Å, $x = 0.25$; and 12.55 Å, $x = 0.5$. This does introduce a change in the value of k_z but is limited to $\sim 2\%$. Such a small variation in k_z is hardly able to change the correspon-

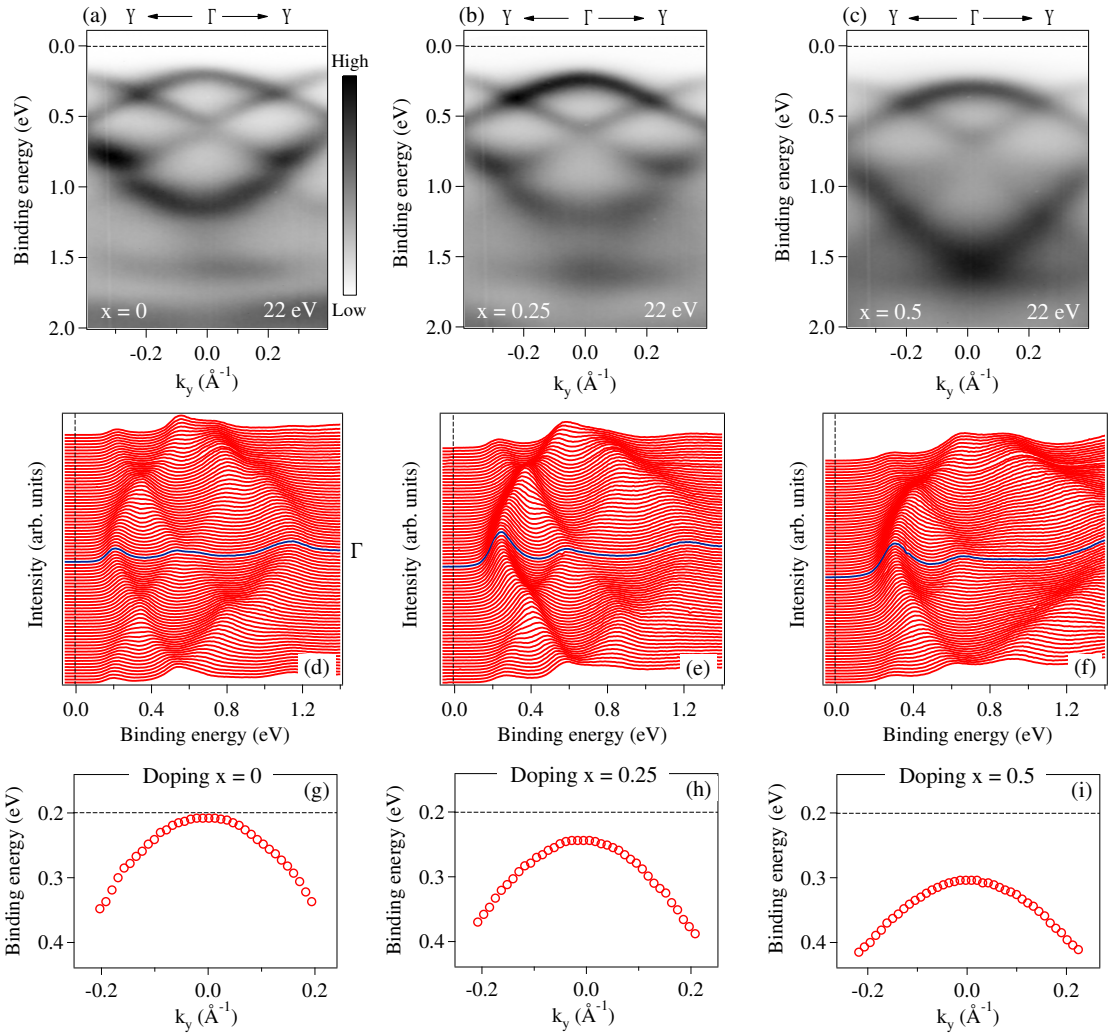

Figure 3.8: (a)-(c) ARPES intensity plots of Ta_2NiSe_5, $Ta_2Ni(Se_{0.75}S_{0.25})_5$ and $Ta_2Ni(Se_{0.5}S_{0.5})_5$, respectively, along ΓY direction acquired at photon energy $h\nu$ = 22 eV (s-pol) and at T = 80 K. (d)-(f) Stacked energy distribution curves (EDCs) extracted from their respective ARPES plots in (a)-(c); the blue curve corresponds to the EDC at Γ in each case. The dashed lines in (a)-(f) denote the Fermi level, E_F. (g)-(i) Band dispersion of the top part of the valence band near E_F for x = 0, 0.25, 0.5 respectively obtained from the peak position of the corresponding EDCs. The dashed line denotes the peak position at Γ-point for x = 0.

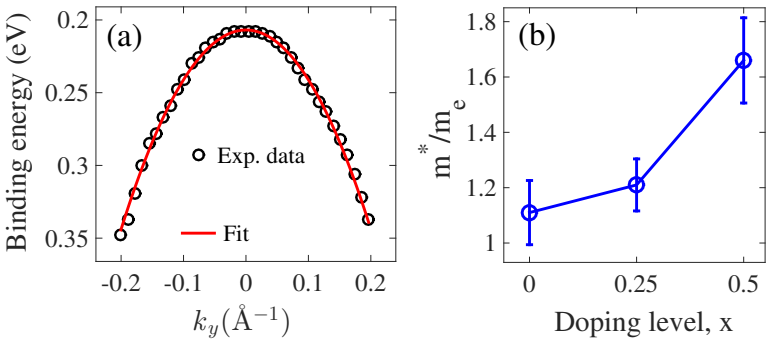

Figure 3.9: (a) Fit (red curve) to the E versus k dispersion (black circles) around Γ in pristine Ta_2NiSe_5. (b) Effective mass m^* (in units of electron rest mass, m_e) at different doping levels, x.

dence between photon energy and k_z among different Sulfur concentrations, allowing us to compare the effect of doping on the electronic band structure at the same photon energy in Figure 3.7 and Figure 3.8.

3.4.5 Three dimensional band structure of $Ta_2Ni(Se_{1-x}S_x)_5$ compounds (x = 0, 0.25, 0.5)

Next, we investigate whether the band dispersion in $Ta_2Ni(Se_{1-x}S_x)_5$ compounds exhibits a three-dimensional character. The three dimensionality of the electronic structure can be determined by probing the out-of-plane ΓZ direction which corresponds to $k_\perp$ in our experimental geometry. A photon-energy-dependent ARPES study is required to obtain such an information. A first indication of three-dimensionality in pristine Ta_2NiSe_5 comes from Ref. [28]. We provide a broader and detailed picture of the dispersion along $k_\perp$ (or k_z) direction in the pristine as well as the S-doped Ta_2NiSe_5 compounds. Figures 3.10(a)-(e) shows the E versus k maps of $Ta_2Ni(Se_{1-x}S_x)_5$, $x = 0.25$, along ΓX direction acquired at different photon energies. Due to low photoionization cross section at photon energies below 15 eV and above 35 eV, a photon energy range from 16 eV to 34 eV was chosen. Looking at ARPES intensity maps, one can notice a photon energy-dependent cross sectional contrast, as well as a considerable variation of the binding energies of different bands, especially for bands lying between 0.5 eV and 1 eV below E_F and the flat band near E_F. We will mainly concentrate on the evolution of the 'flat band', with variations in photon energy. The EDCs at Γ-point [along the red dotted line in Figure 3.10(a)] within 0.3 eV below E_F, capturing the spectral intensity of the flat band, are plotted for different photon energies in Figure 3.10(f). From the ARPES images and the EDC plots, we observe that there is a binding energy shift of the flat band relative to E_F as a function of photon energy. This is clearly seen if one notes the energy separation between 0 eV binding energy (horizontal dashed line) and the flat band below it in Figures 3.10(a)-(e). The dispersion of the flat band along $k_\perp$ can be visualized from the red dashed line denoting the peak position of the EDCs at

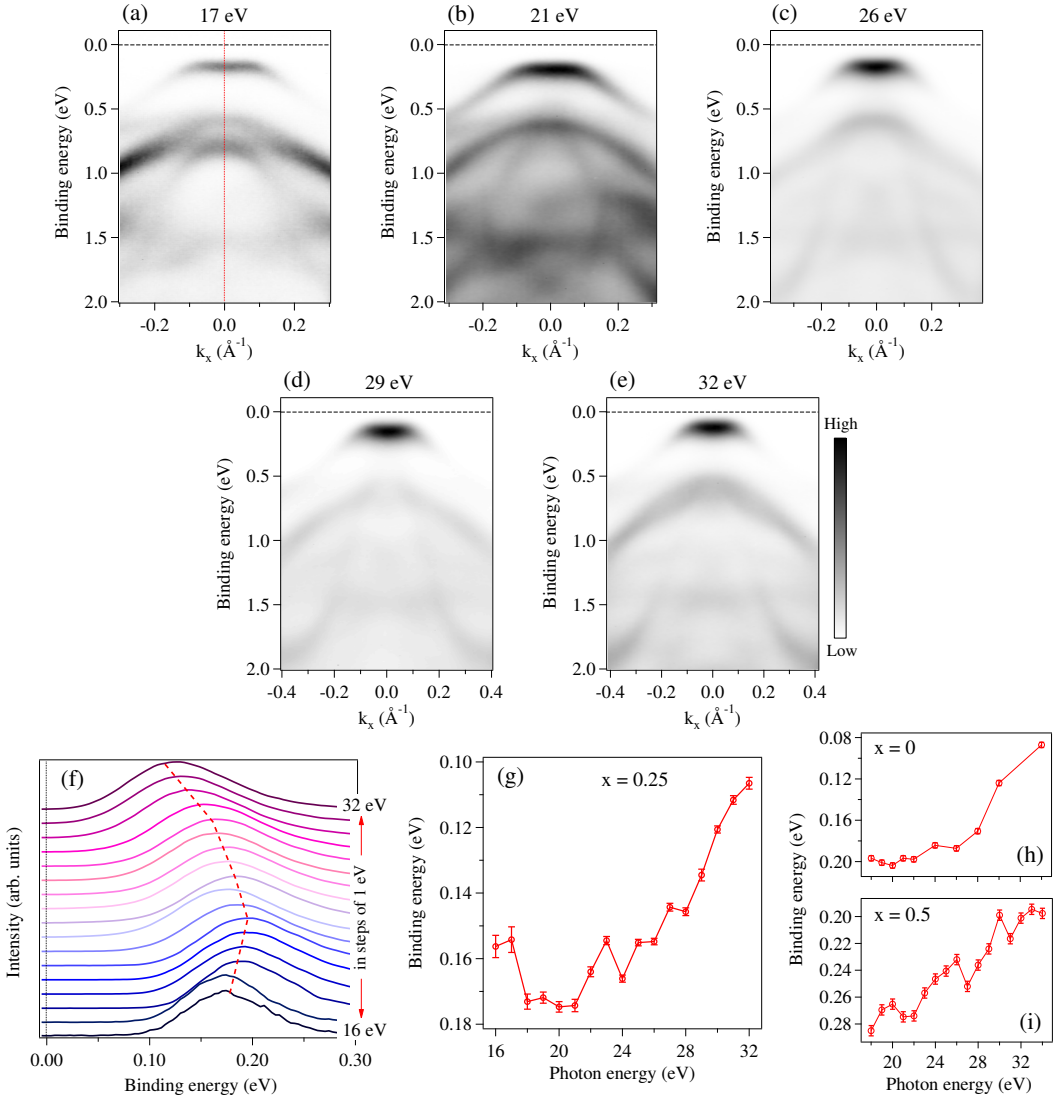

Figure 3.10: (a)-(e) ARPES intensity plots of $Ta_2Ni(Se_{0.75}S_{0.25})_5$ (T = 80 K) along ΓX direction for s-pol light at photon energies, $h\nu$ =17 eV, 21 eV, 26 eV, 29 eV, 32 eV respectively. The Γ-point is denoted by the vertical line in (a) and the horizontal lines in (a)-(e) at 0 eV binding energy denote E_F. (f) EDCs at Γ for different photon energies covering a range from $h\nu$ =16 eV to 32 eV with a step size of 1 eV. The red dashed line is a guide to the eye following the peak position of the valence band with increasing photon energy. (g) Peak position of the valence band obtained by fitting the EDCs with a Lorentzian-Gaussian line shape at Γ as a function of photon energy. (h), (i) Dependence of the valence band peak position on photon energy in pristine and 50% S-doped Ta_2NiSe_5, respectively.

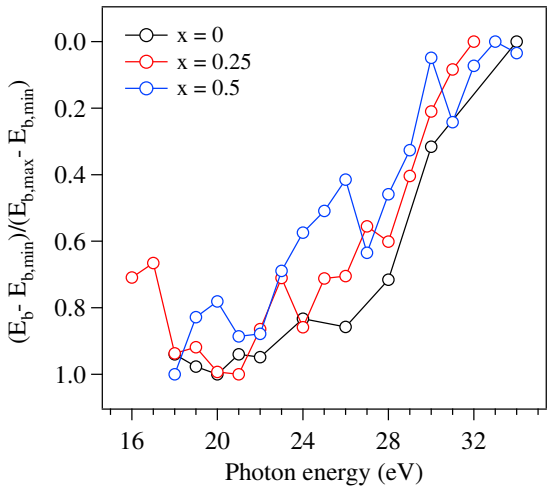

Figure 3.11: Peak position of the valence band at Γ [shown in Figure 3.10] as a function of incident photon energy for pure and S-doped Ta_2NiSe_5, plotted on the same relative scale for comparison. E_b stands for the binding energy.

different photon energies in Figure 3.10(f). The peak position of the flat band relative to E_F at different photon energies has been obtained by fitting each of the EDCs with a Gaussian-Lorentzian distribution function after Shirley background subtraction. Figure 3.10(g) shows that the peak position of the flat band at Γ in $Ta_2Ni(Se_{0.75}S_{0.25})_5$ initially moves away from E_F and then moves towards E_F with increasing photon energy. Such a trend with photon energy is also present for the flat band in Ta_2NiSe_5 [see Figure 3.10(h)]. For the distorted flat band in $Ta_2Ni(Se_{0.5}S_{0.5})_5$, though the shift of the valence band away from E_F is not evident, an overall movement of the valence band towards E_F with increasing photon energy is present [see Figure 3.10(i)]. A comparison in the trend of binding energy vs photon energy curves amongst the three compounds is shown in Figure 3.11. For a perfectly two-dimensional electronic structure often used for Ta_2NiSe_5 and Ta_2NiS_5, the band dispersions should be independent of k_z ($k_\perp$ in our experimental geometry) but the above observations clearly show a dispersion along k_z. This demonstrates the three-dimensionality of electronic band structure in this family of compounds.

For completeness, we also present the photon energy dependence of the band structure along ΓY direction. Figures 3.12(a)-(d) show the ARPES intensity plots at different photon energies for pristine Ta_2NiSe_5. Again, an energy shift of the valence band relative to E_F is observed as a function of photon energy. The EDCs containing only the top-part of the valence band at Γ are plotted for various photon energies in Figure 3.12(e). A similar trend in the peak position of the valence band as that in Figure 3.10(f) can be noted here (follow the red curve). The photon energy-dependent peak positions are plotted in Figure 3.12(f), where an initially small increase, followed by a decrease in binding energy is observed, thereby demonstrating a clear dispersion along ΓZ direction. The above results of the photon energy dependent ARPES measurements in all the three compounds do emphasize that in spite of the well

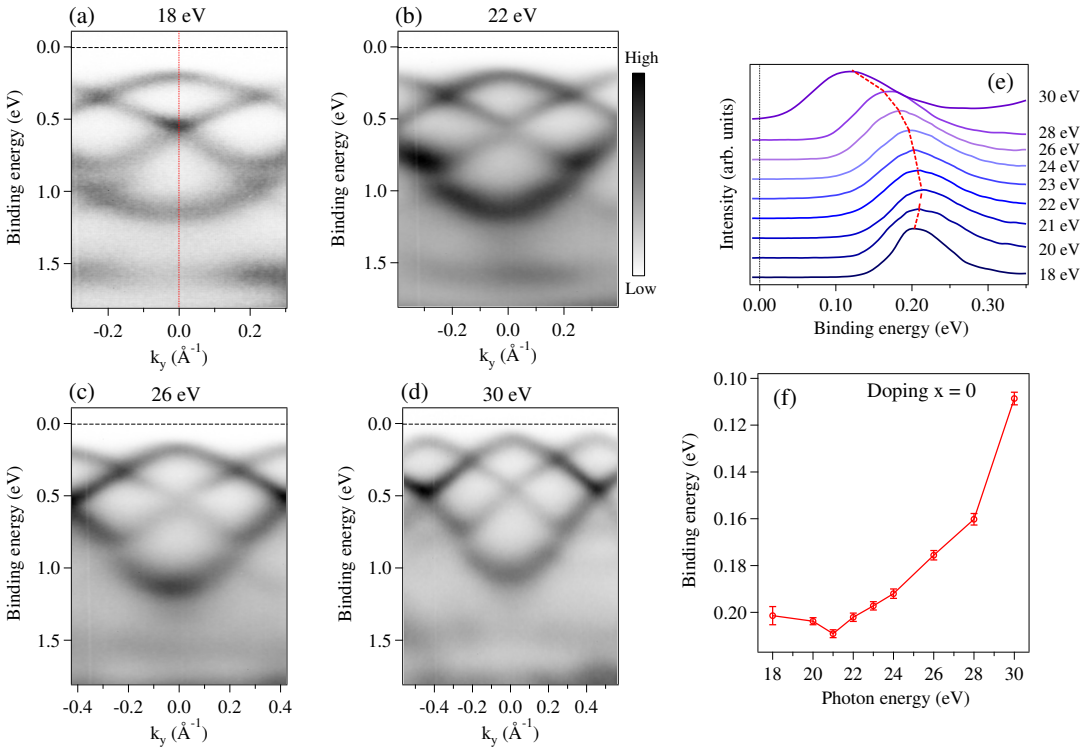

Figure 3.12: (a)-(d) ARPES intensity plots of pristine Ta_2NiSe_5 (T = 80 K) along ΓY direction for s-pol light at photon energies, $h\nu$ =18 eV, 22 eV, 26 eV, 30 eV respectively. The Γ-point is denoted by the vertical line in (a) and the horizontal lines in (a)-(d) at 0 eV binding energy denote E_F. (e) EDCs at Γ for various photon energies. The red dashed line is a guide to the eye following the peak position of the valence band with increasing photon energy. (f) Peak position of the valence band obtained by fitting the EDCs at Γ as a function of photon energy.

known layered structure characteristing the $Ta_2Ni(Se_{1-x}S_x)_5$ compounds, the electronic structure is not strictly two-dimensional.

3.5 Summary

To summarize, we investigated the evolution of the band structure in Ta_2NiSe_5, as a function of Sulfur concentration and the three-dimensionality of the band dispersion using ARPES. The anisotropy of the in-plane band dispersions along ΓX and ΓY directions in the doped compounds is clearly revealed. A substantial amount of S-doping $\sim$ 50% is able to suppress the excitonic ground state in S-doped Ta_2NiSe_5. This can be claimed due to the observed deviation of the dispersion of valence band top from its flattened E versus k feature along ΓX at $x = 0.5$ but not at $x = 0.25$. The suppression of the excitonic insulator state is accompanied by a pronounced increase in the effective mass m^* for the highest doping level, indicating stronger localization of the charge carriers, which is in agreement with the weakening of hybridization between Ni $3d$ and Se $4p$ (S $3p$) orbitals that also leads to large values of E_G. Photon-energy dependent ARPES data show considerable shifts in the

binding energy of states near Fermi level on increasing the photon energy (increasing k_z). This emphasizes that the two-dimensional picture often used for Ta_2NiSe_5 (and Ta_2NiS_5, not studied in this work) does not fully represent the entire electronic structure and that three-dimensionality must be taken into account when studying $Ta_2Ni(Se_{1-x}S_x)_5$ compounds. Dimensionality of the underlying electronic structure in a material is an important parameter while choosing potential candidates for electronic applications. Low-dimensional systems have surpassed their bulk counterparts in this field due to their high electrical and thermal conductivity. Our results therefore suggest that the three-dimensional nature of $Ta_2Ni(Se_{1-x}S_x)_5$ needs to be taken into account when considering these compounds for applications in the field of electronics and optoelectronics.

References

[1] B. W. H. Baugher, H. O. H. Churchill, Y. Yang, and P. J.-Herrero, "Intrinsic Electronic Transport Properties of High-Quality Monolayer and Bilayer MoS_2." *Nano Letters* **13**, 4212 (2013).

[2] X. Cui *et al.*, "Multi-terminal transport measurements of MoS2 using a van der Waals heterostructure device platform." *Nature Nanotechnology* **10**, 534 (2015).

[3] J. L. Webb, L. S. Hart, D. Wolverson, C. Chen, J. Avila, and M. C. Asensio, "Electronic band structure of ReS_2 by high-resolution angle-resolved photoemission spectroscopy." *Physical Review B* **96**, 115205 (2017).

[4] J. N. Coleman *et al.*, "Two-Dimensional Nanosheets Produced by Liquid Exfoliation of Layered Materials." *Science* **331**, 568 (2011).

[5] T. I. Larkin *et al.*, "Giant exciton Fano resonance in quasi-one-dimensional Ta_2NiSe_5." *Physical Review B* **95**, 195144 (2017).

[6] L. Li, P. Gong, W. Wang, B. Deng, L. Pi, J. Yu, X. Zhou, X. Shi, H. L. Orcid and T. Zhai, "Strong In-Plane Anisotropies of Optical and Electrical Response in Layered Dimetal Chalcogenide." *ACS Nano* **11**, 10264 (2017).

[7] S. Y. Kim *et al.*, "Layer-Confined Excitonic Insulating Phase in Ultrathin Ta_2NiSe_5 Crystals." *ACS Nano* **10**, 8888 (2016).

[8] S. A. Sunshine and J. A. Ibers, "Structure and physical properties of the new layered ternary chalcogenides tantalum nickel sulfide (Ta_2NiS_5) and tantalum nickel selenide (Ta_2NiSe_5)." *Inorganic Chemistry*, **24**, 3611 (1985).

[9] Y.Wakisaka, T. Sudayama, K. Takudo, T.Mizokawa, M. Arita, H. Namatame, M. Taniguchi, N. Katayama, M. Nohara and H. Takagi, "Excitonic Insulator State in Ta_2NiSe_5 Probed by Photoemission Spectroscopy." *Physical Review Letters* **103**, 026402 (2009).

[10] K. Seki *et al.*, "Excitonic Bose-Einstein condensation in Ta_2NiSe_5 above room temperature." *Physical Review B* **90**, 155116 (2014).

[11] T. Kaneko, T. Toriyama, T. Konishi and Y. Ohta, "Orthorhombic-to-monoclinic phase transition of Ta_2NiSe_5 induced by the Bose-Einstein condensation of excitons." *Physical Review B* **87**, 035121 (2013).

[12] K. Mu, H. Chen, Y. Li, Y. Zhang, P. Wang, B. Zhang, Y. Liu, G. Zhang, L. Song and Z. Sun, "Electronic structures of layered Ta_2NiSe_5 single crystals revealed by high-resolution angle-resolved photoemission spectroscopy." *Journal of Materials Chemistry C* **6**, 3976 (2018).

[13] J. A. Wilson, "Concerning the semi-metallic characters of TiS_2 and $TiSe_2$."Solid State Commun. **22**, 551 (1977).

[14] H. Cercellier *et al.*,"Evidence for an Excitonic Insulator Phase in 1*T*-$TiSe_2$." *Physical Review Letters* **99**, 146403 (2007).

[15] Y. F. Lu, H. Kono, T. I. Larkin, A. W. Rost, T. Takayama, A.V. Boris, B. Keimer and H. Takagi, "Zero-gap semiconductor to excitonic insulator transition in Ta_2NiSe_5."*Nature Communications* **8**, 14408 (2017).

[16] B. Bucher, P. Steiner, and P. Wachter, "Excitonic insulator phase in $TmSe_{0.45}Te_{0.55}$." *Physical Review Letters* **67**, 2717 (1991).

[17] L. Du, X. Li, W. Lou, G. Sullivan, K. Chang, J. Kono and R. R. Du, "Evidence for a topological excitonic insulator in InAs/GaSb bilayers." *Nature Communications* **8**, 1971 (2017).

[18] R. A. Craven, F. J. Di Salvo and F. S. L. Hsu, "Mechanisms for the 200 K transition in $TiSe_2$: A measurement of the specific heat." *Solid State Communications* **25**, 39 (1978).

[19] B. Bucher, T. Park, J. D. Thompson and P. Wachter, Preprint at https://arxiv.org/abs/0802.3354 (2008).

[20] H. P. Hughes, "Structural distortion in $TiSe_2$ and related materials-a possible Jahn-Teller effect?" *Journal of Physics C: Solid State Physics* **10**, L319 (1977).

[21] J. Ishioka, Y. H. Liu, K. Shimatake, T. Kurosawa, K. Ichimura, Y. Toda, M. Oda, and S. Tanda, "Chiral Charge-Density Waves." *Physical Review Letters* **105**, 176401 (2010).

[22] F. J. Di Salvo, C. H. Chen, R. M. Fleming, J. V. Waszczak, R. G. Dunn, S. A. Sunshine and J. A. Ibers, "Physical and structural properties of the new layered compounds Ta_2NiS_5 and Ta_2NiSe_5." *Journal of the Less Common Metals* **116**, 51 (1986).

[23] D. Golež, P. Werner and M. Eckstein, "Photoinduced gap closure in an excitonic insulator." *Physical Review B* **94**, 035121 (2016).

[24] M. Babadi, E. Demler and M. Knap, "Far-from-Equilibrium Field Theory of Many-Body Quantum Spin Systems: Prethermalization and Relaxation of Spin Spiral States in Three Dimensions." *Physical Review X* **5**, 041005 (2015).

[25] M. Babadi, M. Knap, I. Martin, G. Refael and E. Demler, "Theory of parametrically amplified electron-phonon superconductivity." *Physical Review B* **96**, 014512 (2017).

[26] K. Kim, H. Kim, J. Kim, C. Kwon, J. S. Kim, and B. J. Kim, "Direct observation of excitonic instability in Ta_2NiSe_5." *Nature Communications* **12**, 1969 (2021).

[27] T. I. Larkin, R. D. Dawson, M. Höppner, T. Takayama, M. Isobe, Y.-L. Mathis, H. Takagi, B. Keimer, and A. V. Boris, "Infrared phonon spectra of quasi-one-dimensional Ta_2NiSe_5 and Ta_2NiS_5." *Physical Review B* **98**, 125113 (2018).

[28] M. D. Watson, I. Marković, E. A. Morales, P. Le Fèvre, M. Merz, A. A. Haghighirad and P. D. C. King, "Band hybridization at the semi-metal-semiconductor transition of Ta_2NiSe_5 enabled by mirror-symmetry breaking." *Physical Review Research* **2**, 013236 (2020).

[29] S. Mor *et al.*, "Ultrafast Electronic Band Gap Control in an Excitonic Insulator." *Physical Review Letters* **119**, 086401 (2017).

[30] E. Baldini *et al.*, "The spontaneous symmetry breaking in Ta_2NiSe_5 is structural in nature." https://doi.org/10.48550/arXiv.2007.02909

[31] K. Momma and F. Izumi, "VESTA 3 for three-dimensional visualization of crystal, volumetric and morphology data." *Journal of Applied Crystallography*, **44**, 1272 (2011).

[32] S. A. Sunshine and J. A. Ibers, "Structure and physical Properties of the new layered ternary chalcogenides Ta_2NiS_5 and Ta_2NiSe_5." *Inorganic Chemistry* **24**, 3611 (1985).

[33] K. Seki, Y. Wakisaka, T. Kaneko, T. Toriyama, T. Konishi, T. Sudayama, N. L. Saini, M. Arita, H. Namatame, M. Taniguchi, N. Katayama, M. Nohara, H. Takagi, T. Mizokawa and Y. Ohta, "Excitonic Bose-Einstein condensation in Ta_2NiSe_5 above room temperature." *Physical Review B* **90**, 155116 (2014).

[34] Y. F. Lu, H. Kono, T. I. Larkin, A. W. Rost, T. Takayama, A. V. Boris, B. Keimer and H. Takagi, "Zero-gap semiconductor to excitonic insulator transition in Ta_2NiSe_5." *Nature Communications* **8**, 14408 (2017).

[35] P. Debye, "Zur Theorie der spezifischen Wärmen." *Annalen der Physik* **344**, 789 (1912).

[36] J. F. Annett, "Superconductivity, Superfluids and Condensates." Oxford University Press Inc. (2004).

[37] E. Canadell and M. H. Whangbo, "Metallic versus nonmetallic properties of ternary chalcogenides: tantalum metal selenide, Ta_2MSe_7

(M = nickel, platinum), and tantalum nickel chalcogenide, Ta_2NiX_5 (X = sulfide, selenide).“ *Inorganic Chemistry* **26**, 3974 (1987).

[38] T. Kaneko, T. Toriyama, T. Konishi and Y. Ohta, “Electronic structure of Ta_2NiSe_5 as a candidate for excitonic insulators.“ *Journal of Physics: Conference Series* **400**, 032035 (2012).

[39] Y. Wakisaka, T. Sudayama, K. Takubo, T. Mizokawa, M. Arita, H. Namatame, M. Taniguchi, N. Katayama, M. Nohara and H. Takagi, “Excitonic Insulator State in Ta_2NiSe_5 Probed by Photoemission Spectroscopy.“ *Physical Review Letters* **103**, 026402 (2009).

[40] K. Okazaki *et al.*, “Photo-induced semimetallic states realised in electron–hole coupled insulators.“ *Nature Communications* **9**, 4322 (2018).

[41] B. Zenker, D. Ihle, F. X. Bronold and H. Fehske, “Electron-hole pair condensation at the semimetal-semiconductor transition: A BCS-BEC crossover scenario.“ *Physical Review B* **85**, 121102(R) (2012).

[42] T. Kaneko, S. Ejima, H. Fehske and Y. Ohta, “Excitonic BCS-BEC Crossover in Double-Layer Systems.“ *JPS Conference Proceedings* **3**, 017006 (2014).

[43] L. Petaccia, P. Vilmercati, S. Gorovikov, M. Barnaba, A. Bianco, D. Cocco, C. Masciovecchio and A.Goldoni, “BaDElPh: A 4 m normal-incidence monochromator beamline at Elettra.“ *Nuclear Instruments and Methods in Physics Research A* **606**, 780 (2009).

[44] J. Harmanson, “Final-state symmetry and polarization effects in angle-resolved photoemission spectroscopy.“ *Solid State Communications* **22**, 9 (1977).

[45] A. Damascelli, Z. Hussain and Z. X. Shen, “Angle-resolved photoemission studies of the cuprate superconductors.“ *Reviews of Modern Physics* **75**, 473 (2003).

[46] K. Fukutani, R. Stania, C. II Kwon, J. S. Kim, K. J. Kong, J. Kim and H. W. Yeom, “Detecting photoelectrons from spontaneously formed excitons.“ *Nature Physics* **17**, 1024 (2021).

[47] Y. Wakisaka *et al.*, “Photoemission spectroscopy of Ta_2NiSe_5.“ *Journal of Superconductivity and Novel Magnetism* **25**, 1231 (2012).

4 Photoinduced phase transition and associated timescales in Ta_2NiSe_5

In this chapter, we investigate the nonequilibrium electronic structure and characteristic timescales in a candidate excitonic insulator, Ta_2NiSe_5, using time- and angle-resolved photoemission spectroscopy. Following a strong photoexcitation, the band gap closes transiently within 100 fs, i.e., on a timescale faster than the typical lattice vibrational period. Furthermore, we find that the characteristic time associated with the rise of the photoemission intensity above the Fermi level decreases with increasing excitation strength, while the relaxation time of the electron population towards equilibrium shows an opposite behavior. We argue that these experimental observations can be consistently explained by an excitonic origin of the band gap in the material. The excitonic picture is supported by microscopic calculations based on the non-equilibrium Green's function formalism for an interacting two-band system.

4.1 Introduction

Excitonic insulators were originally proposed as materials where a spontaneous condensation of excitons takes place in the vicinity of the semiconductor–semi-metal transition [1, 2]. Such a condensation is associated with the breaking of internal $U(1)$ gauge symmetry related to charge conservation. While this phase has been unambiguously identified for heterostructures in the quantized Hall regime [3, 4, 5], only a few single-material systems have been suggested to exhibit a ground-state excitonic insulator phase, the most prominent ones being Ta_2NiSe_5 [6, 7] and 1T-$TiSe_2$ [8]. However, in real materials, there are always effects that may break the $U(1)$ symmetry [9]. In addition, the presence of electron-phonon coupling [10, 11, 12] can lead to a structurally ordered phase with properties similar to those of an excitonic insulator. Indeed, Ta_2NiSe_5 shows a structural phase transition from an orthorhombic to a monoclinic lattice at $T_C = 328$ K [10, 13]. This raises an important long-standing question: What is the dominant origin of the order in Ta_2NiSe_5? A number of experiments have been performed, employing different methods such as Raman spectroscopy [14, 15, 16], optical techniques [17, 18], and angle-resolved photoemission spectroscopy (ARPES) [19, 20], to answer this question. However, the results were interpreted in either the excitonic or phononic picture, and no consensus has been reached so far.

Tracking the system as it evolves through a non-equilibrium phase transition triggered by a short optical pulse can provide further clues as to the origin of the symmetry breaking in Ta_2NiSe_5. However, also in this case, the

situation is controversial, as groups performing time-resolved ARPES experiments have reported rather contradictory results [21, 22, 23, 24, 25]. Some studies [21, 23] found a short-lived increase in the gap, which was interpreted as a transient enhancement of the excitonic order [21], stimulating further theoretical studies [11, 26, 27, 28]. On the other hand, some recent experimental works have observed a decrease in the gap [21, 22, 24], albeit marginal in recent high-resolution data [23], that is naturally expected, as the excited electrons can scatter with condensed excitons [29]. Differences have also been observed in the measured characteristic timescales of the photoemission signal after photoexcitation. Ref. [22] reports a characteristic timescale of around 100 fs, which is faster than the typical lattice oscillation period in Ta_2NiSe_5. On the other hand, the authors of Ref. [23] argue that this timescale is comparable to the lattice distortion period (characteristic time > 250 fs) and consider this as an evidence of a lattice-driven transition. More generally, the behavior of the timescales versus the excitation fluence is also controversial. In particular, this concerns the apparent disagreement between the dynamical slowing down, observed in both experimental [30, 31] and some theoretical studies focused on symmetry-broken states [29, 32, 33, 34, 35, 36, 37], and the measured rise time of the photoemission intensity above the Fermi level, which becomes shorter for increasing photoexcitation strengths [22]. Summing up the above contrasting results, the question about the dominant driving force of the order in Ta_2NiSe_5 still remains open.

Here, we study the non-equilibrium electron dynamics of Ta_2NiSe_5 in a high photoexcitation regime, which was not explored before on this material. A similar photoexcitation regime was previously used to study the destruction of long-range charge order in $TiSe_2$ [38, 39]. Using trARPES, we show that a strong photoexcitation induces a phase transition from an insulating to a semi-metallic phase and that the melting of the band gap occurs on a timescale faster than the period of a phonon oscillation. Next, we show that the dependence of different characteristic timescales on the photoexcitation strength shows contrasting behaviours. On one hand, the rise time of the photoemission intensity above the Fermi level becomes shorter with increasing excitation strength. On the other hand, the relaxation time of the electron population towards equilibrium becomes longer with increasing fluence, reaching saturation above a critical value. The experimental findings have been corroborated by numerical simulations, performed by **D. Golež and J. Mravlje** which accounts for the non-equilibrium response of a two-band tight-binding system, with interband Coulomb repulsion and an excitonic ground state (Section 4.3.4). The calculations confirm closing of the band gap for high excitation strengths and the speed up of the photoemission signal in the conduction band with increasing fluence. Our combined experimental/theoretical study supports a pre-eminently excitonic origin of the band gap in Ta_2NiSe_5.

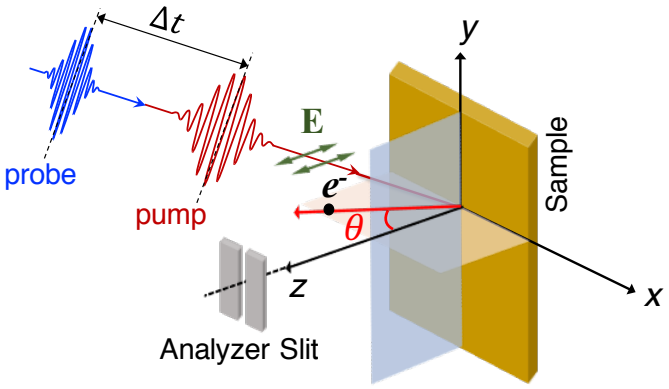

Figure 4.1: Schematic representation of the pump-probe experimental geometry. Δt is the time delay between the pump and probe pulses, the electric field **E** of the both the pulses lies in the xz plane, θ is the emission angle of the photoemitted electrons with respect to the z-axis.

4.2 Experimental conditions

The time-resolved ARPES measurements were performed at the CITIUS high-harmonic generation (HHG) light source. A schematic representation of the pump-probe experimental geometry is shown in Figure 4.1. The fundamental frequency of the laser, $h\nu$ = 1.55 eV, was used as the pump beam and its intensity on the sample was controlled with a variable attenuator. For this study, the maximum fluence that could be used is $\sim$ 6 mJ/cm^2, since pump-induced space-charge effects begin to dominate at higher fluences. The photon energy of the probe was selected using the off-plane geometry of the monochromator grating, which preserved the pulse duration. Because Ni 3*d* and Se 4*p* electron orbitals have a high photoionization cross-section at photon energies close to 26 eV, a probe energy of 26.35 eV (harmonic 17 of the seed laser) was used in the experiments. The electric field, **E**, of both the pump and the probe pulse lies in the xz plane, see Figure 4.1. All the presented data were acquired at sample temperature T = 100 K. The samples were cleaved *in situ* under UHV pressure better than 6x10^{-9} mbar to generate a clean mirror-like surface, prior to each measurement. The trARPES experiments were performed at a base pressure < 1x10^{-10} mbar. The Fermi level E_F, is determined with respect to the valence band spectrum of a clean gold sample.

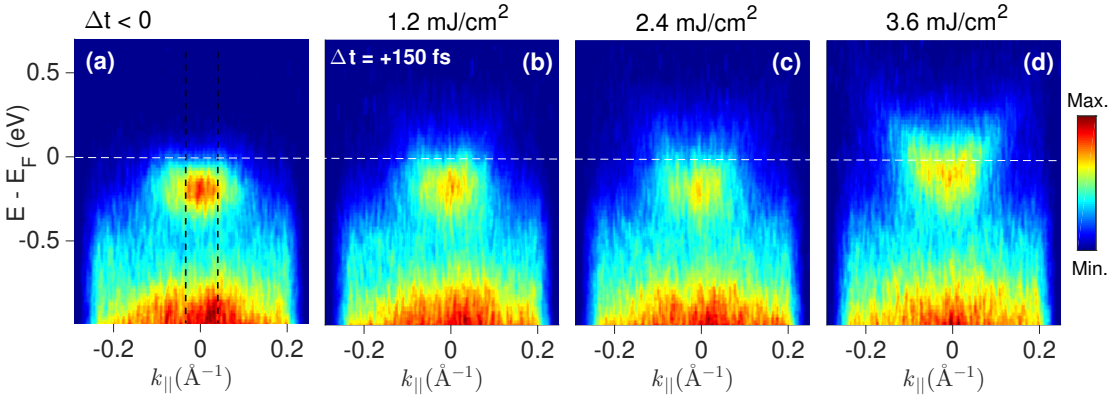

Figure 4.2: (a) Static (no pump) ARPES spectrum of Ta_2NiSe_5 along $X\Gamma X$ direction acquired using photon energy $h\nu = 26.35$ eV and at $T = 100$ K. (b), (c) and (d) trARPES snapshots at $\Delta t = 150$ fs after photoexcitation at pump fluences 1.2 mJ/cm^2, 2.4 mJ/cm^2 and 3.6 mJ/cm^2, respectively. The Fermi level, E_F, is indicated by the (white) horizontal line and integrated k-range is marked in (a) by the vertical dashed lines.

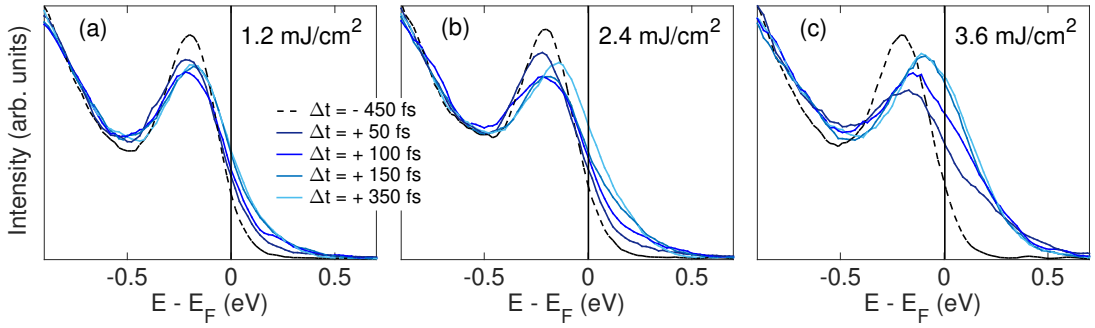

Figure 4.3: Momentum-integrated EDCs at different time delays (Δt) showing the temporal evolution of the gap dynamics at pump fluences (a) 1.2 mJ/cm^2, (b) 2.4 mJ/cm^2 (c) 3.6 mJ/cm^2. The vertical dashed lines in Figure 4.2(a) indicate the considered region for momentum integration.

4.3 Results

4.3.1 Signature of a photoinduced phase transition

We investigated the evolution of the valence band, composed of Ni 3d and Se 4p orbitals, as a function of the incident pump fluence. The equilibrium (no pump) ARPES spectrum of Ta_2NiSe_5 along $X\Gamma X$ direction is shown in Figure 4.2(a). E_F, represented by the horizontal dashed line in Figure 4.2, lies at about 0.2 eV above the valence band. After photoexcitation of the system with an infrared pump pulse, the spectral weight of the valence band decreases and is transferred to unoccupied energy levels above E_F. In Figure 4.2(b), one can observe that, at a pump fluence of 1.2 mJ/cm^2, the amount of spectral weight transfer to the conduction band is relatively small. Increasing the pump fluence results in an increase of the spectral weight transfer. While this increase is modest at 2.4 mJ/cm^2, see Figure 4.2(c), it is considerably enhanced for a

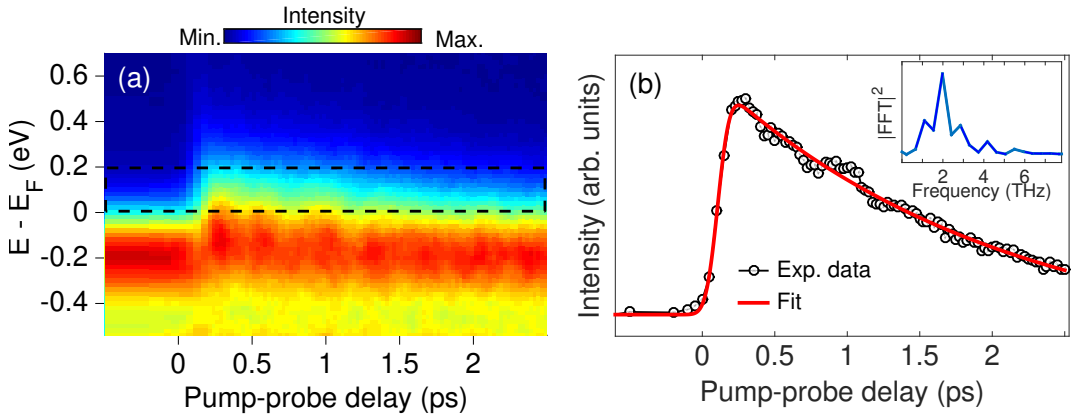

Figure 4.4: (a) trARPES spectrum around the Γ-point for the integrated $k_{||}$ range indicated by the vertical dashed lines in Figure 4.2(a). (b) Temporal evolution of the integrated photoemission intensity (empty circles) in the energy interval [0.0, 0.2] eV, shown by the horizontal dashed lines in (a). The red curve represents a fit (see text for details) to the experimental data. The measurements were acquired at a pump fluence of 3.6 mJ/cm^2. Inset: Fourier analysis of the oscillatory part of the photoemission signal. FFT: fast fourier transform.

pump fluence of 3.6 mJ/cm^2 in Figure 4.2(d). These observations are made more evident in Figure 4.3, where we show the momentum-integrated energy distribution curves (EDCs) before the arrival of the pump pulse (Δt = -450 fs) and at different delays after photoexcitation, with different pump fluences. The integrated angular range for all the EDCs is indicated by the black vertical lines in the ARPES spectrum shown in Figure 4.2(a). Comparing the EDCs before and after photoexcitation, we observe that for the lowest fluence of 1.2 mJ/cm^2 in Figure 4.3(a), the dynamics of the valence band shows a depopulation and broadening, accompanied by a small energy shift towards the Fermi level at subsequent delay times. At an intermediate pump fluence of 2.4 mJ/cm^2, which is above the value reported in previous studies [21, 22], the spectral weight transfer to the conduction band is increased, while the energy shift of the valence band towards the Fermi level remains relatively small, as shown in Figure 4.3(b). Finally, at a pump fluence of 3.6 mJ/cm^2, the energy shift of the valence band towards E_F is pronounced and there is a significant increase of the photoemission intensity up to several hundreds of meV above the Fermi level, see Figure 4.3(c). These observations suggest that a strong pump fluence can induce a phase transition in which the energy gap closes and the system is driven from an insulating to a semi-metallic state [22, 24].

The key information that can be extracted from the above results is the timescale (after photoexcitation) within which the band gap closes. This provides details on the origin of the band gap [40], i.e., whether the dominant interaction governing the band dynamics is electronic or phononic. Figure 4.3(c) shows that at a pump fluence of 3.6 mJ/cm^2, the band gap closes within ∼ 100 fs, a time interval that is shorter compared with the relevant vibrational time, which is about 500 fs for the 2-THz phonon mode [12, 14, 15, 16, 41]. An even faster response is observed at the highest pump fluence used in this study (see

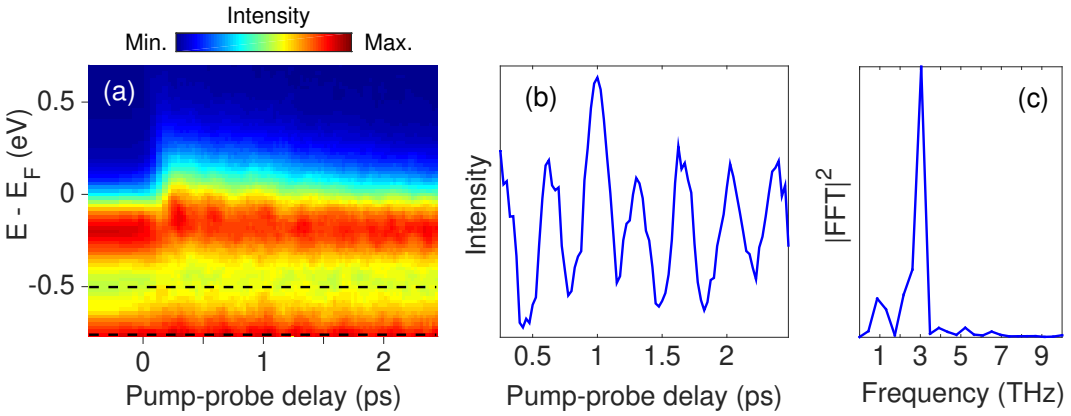

Figure 4.5: (a) trARPES spectrum at a pump fluence of 3.6 mJ/cm^2 around Γ-point for the integrated $k_{||}$ range indicated by the vertical dashed lines in Figure 4.2(a). (b) Oscillatory part of the photoemission signal. The energy integration window is shown by the horizonal dashed lines in (a). (c) Fourier analysis of (b) showing the 3 THz phonon mode.

Figure 4.6). This observation suggests that the induced phase transition has a strong electronic character. Notice that the gap closing is seen only for the highest fluence in Figure 4.3, while for the two lower fluences, only marginal energy shifts are observed. This suggests the existence of a critical fluence and might also help to explain the relatively small energy shifts observed in some of the previous trARPES experiments [21, 23].

4.3.2 Coupling to coherent phonon modes

An electronic origin of the band gap inferred from the timescale of gap closure is, however, not fully conclusive. For example, one could argue that the relevant timescale for a pure structural phase transition is a quarter of the phononic oscillation only [42], which is comparable to the observed timescale in Figure 4.3. In addition, the structural and electronic dynamics are coupled: The structural monoclinic displacement and the excitonic order act in a similar way on the electronic dispersion [9, 12]. Coherent oscillations in the photoemission spectrum with the relevant phonon frequency are therefore expected. Indeed, our data show a modulation of the integrated photoemission intensity in the energy range from 0.0 to 0.2 eV, see Figure 4.4. We find that the periodic temporal modulation of the intensity has dominant contribution from the 2 THz phonon mode [see inset of Figure 4.4(b)]. **The presence of the 2 THz mode at temperatures below T_C = 328 K is related to the symmetry of the underlying lattice. Since Ta_2NiSe_5 also undergoes a second-order structural phase transition at T_C, the reduced crystal symmetry in the low-temperature monoclinic phase, in comparison to the high-temperature orthorhombic phase, increases the number of coherent phonon modes. While the other modes (3 THz and 3.7 THz) are insensitive to the changes in crystal symmetry, the 2 THz mode is present only in the monoclinic phase and disappears upon lattice heating above T_C.** Since this mode is a fingerprint of

the monoclinic phase [14, 41, 43, 44], our results suggest that the underlying lattice remains in its low-temperature phase even under photoexcitation with relatively high fluences used in our experiment. The observation of a significant shift of the valence band towards the Fermi level in Figure 4.3(c) with the lattice remaining in the low-temperature phase supports an electronic rather than a structural origin [23] of the bandgap. **We have also observed a 3 THz phonon mode for the band lying at (-0.7,-0.5) eV relative to E_F, as shown in Figure 4.5 (the energy integration window is shown by the horizonal dashed lines). The analysis of the 3 THz phonon mode shows that the electronic states at -0.6 $\pm$ 0.1 eV are strongly coupled to this mode (Ref. [24]). This is not the case with Ni 3d - Se 4p valence band (2 THz mode is dominant) that undergoes strong band renormalization around Γ-point in the excitonic insulator phase, suggesting that the coupling of the valence band electrons to the 3 THz phonon mode is extremely weak.** An excitonic origin of the band gap is further discussed in Section 4.4.3, where we investigate the fluence dependence of the characteristic timescales observed in the photoemission signal.

4.3.3 Characteristic timescales and their dependence on pump fluence

Figure 4.4(a) shows the momentum-integrated photoemission spectral intensity as a function of electron binding energy and time delay between the pump and probe pulses for a pump fluence of 3.6 mJ/cm^2. The temporal evolution of the integrated intensity in the energy interval [0.0, 0.2] eV is plotted in Figure 4.4(b). We observed two characteristic timescales: a fast rise time, τ_r, of the momentum- and energy-integrated photoemission signal above E_F and a slow relaxation time, τ_d, of the electron population towards equilibrium. The intensity profile is fitted using the following function:

$$I(t) = H(t)[Ae^{(-t/\tau_d)} + B], \tag{4.1}$$

where $H(t)$ describes the finite rise time of the intensity which is modeled by an error function, given by

$$H(t) = 1 + \mathrm{erf}(t/\tau_c); \tag{4.2}$$

A and τ_d are the amplitude and the decay time of the electronic response, respectively, and B is a constant. Here, τ_c is the convolution of the natural electron-intensity rise time τ_r and the pump-probe cross-correlation, which represents the finite temporal resolution of our system.

The energy-integrated, time-resolved photoemission intensity at different pump fluences is shown in Figure 4.6(a). The rise time shows obvious shortening with increased excitation strengths, as emphasized by the dashed line marking the peak position. In Figure 4.6(b), we plot the rise time τ_r, determined from fits shown in Figure 4.6(a), as a function of pump fluence. The rise time has a maximum value of about 120 fs for the lowest pump fluence

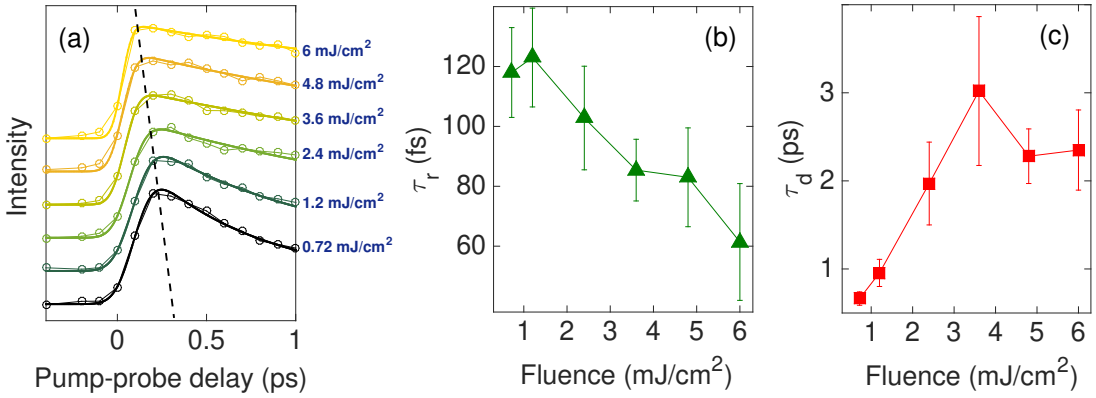

Figure 4.6: (a) Energy-integrated photoemission intensity for different pump fluences, where the smooth curves are fits to the experimental data. The shortening of the rise time for increasing pump fluence is indicated by the black dashed line. (b) Rise time τ_r as a function of pump fluence. (c) Dependence of the electron decay time τ_d on pump fluence.

and decreases down to around 60 fs at the highest pump fluence used in the experiment. **A fluence dependence of the rise time for any photoexcited system can be expected if a given scattering channel becomes more and more probable with increasing photoexcitation strength. Besides the intraband and interband electron-electron scattering processes, the photoexcited electrons in an excitonic insulator might also relax towards a quasi-equilibrium distribution by breaking an exciton pair, leaving behind a bare electron and a bare hole. Such an electron-exciton scattering process has an increased probability if the excitons can be easily decomposed, which demands a smaller electron-hole binding energy of the exciton. Since one of the factors affecting the exciton binding energy is carrier screening, increasing excitation strengths lead to smaller values of the binding energy. This increases the scattering probability between the photoexcited electrons and the excitons, and hence, to a faster rise time as a function of the pump fluence.** On the other hand, some degree of fluence dependence of the rise time might also occur in the purely phononic scenario but the phonon modes are expected to soften upon photoexcitation [45], which would result in a trend opposite to the one observed in the experiment. We also examined the fluence dependence of the electron relaxation time τ_d towards equilibrium, see Figure 4.6(c). Contrary to the behaviour of τ_r, the relaxation time τ_d shows a monotonic increase up to the critical fluence, after which saturation is observed. This trend is consistent with previous experiments [22] and can be attributed to the scattering of phonons with excitons: at high excitation fluences a substantial population of excited vibrational modes can transfer energy back to the perturbed excitonic condensate and suppress its reestablishment [46].

4.3.4 Theoretical analysis

We now turn to the theoretical discussion, which will help us understand the early stages of the photoinduced dynamics in Ta_2NiSe_5. The theoretical description considers a two-band tight-binding model in one-dimension where the electrons in the two bands are coupled by a local interband repulsion, appropriate for Ta_2NiSe_5 [19, 47]. The total Hamiltonian for the excitonic insulator phase is composed of:

(a) a kinetic energy term H_{kin};
(b) a local interband density-density interaction term H_{int};
(c) coupling of the electromagnetic field to the electrons given by H_{dip};
(d) a phonon interaction term H_{ph}.

In the second quantization formalism, the above terms are:

$$H_{\text{kin}} = \sum_{\substack{k \\ \alpha\in\{0,1\}}} h_{k,\alpha} c^{\dagger}_{k,\alpha} c_{k,\alpha} \tag{4.3}$$

where $h_{k,\alpha} = -2J_\alpha \cos(k) - \mu + (-1)^\alpha \Delta\epsilon$ is the single-particle dispersion relation, $\Delta\epsilon$ is the band-level splitting, $J_0 = -J_1$ is the hopping integral, $c^{\dagger}_{k,\alpha}$ and $c_{k,\alpha}$ are, respectively, the creation and annihilation operators of an electron with momentum k in the orbital α. The chemical potential μ is chosen such that the system is at half filling.

$$H_{\text{int}} = V \sum_i n_{i,0} n_{i,1} \tag{4.4}$$

Here, V is the Coulomb interaction strength, and $n_{i,\alpha} = c^{\dagger}_{i,\alpha} c_{i,\alpha}$ is the electronic density at site i and band α.

$$H_{\text{dip}} = E(t) \sum_i c^{\dagger}_{i,1} c_{i,0} + \text{H.c.} \tag{4.5}$$

where the index i runs over all sites, H.c. is the Hermitian conjugate of the first term and $E(t) = \varepsilon(t)\sin[\omega(t - t_0)]$, with $\varepsilon(t)$ as the Gaussian field envelope and amplitude E_0, is the time-dependent electric field responsible for the optical excitation between the conduction and valence bands ($\hbar\omega = 1.5$ eV is chosen such that it is consistent with the experimental value).

$$H_{\text{ph}} = g \sum_i (b_i + b^{\dagger}_i)(c^{\dagger}_{i,1} c_{i,0} + c^{\dagger}_{i,0} c_{i,1}) + \omega_0 \sum_i b^{\dagger}_i b_i \tag{4.6}$$

Here $b^{\dagger}_i$ and b_i are, respectively, the phonon creation and annihilation operators, g is the electron-phonon interaction strength and ω_0 is the phonon frequency. Under the photodoping regime used in this study, the second Born approximation is employed for describing the non-equilibrium dynamics within the Keldysh formalism [48, 49, 50, 51].

The results of the calculations are reported in Figure 4.7 and Figure 4.8. At equilibrium, the valence band dispersion shows a two-peak structure, see

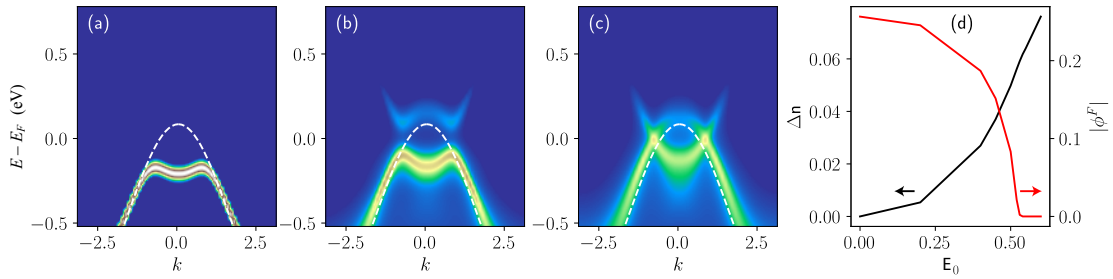

Figure 4.7: Snapshots of the simulated photoemission spectrum (a) at equilibrium; (b) at a fixed pump-probe delay of 70 fs and for an electric field strength E_0, which is less than the critical value E_C corresponding to the dynamical phase transition; and (c) at 70 fs and $E_0 > E_C$. The Fermi level corresponds to 0 eV. The white dashed lines represent the valence band dispersion in the absence of the excitonic phase. (d) Dependence of the order parameter $|\phi_F|$ (red curve) and the polarization Δn (black curve) on the excitation strength E_0 in the long-time limit.

Figure 4.7(a), which is a characteristic of the so-called BCS regime and the corresponding disordered phase is semi-metallic [20, 22, 52, 53]. After photoexcitation, the valence band broadens and moves towards E_F, see Figure 4.7(b). Above a critical value E_C, the gap is suppressed, see Figure 4.7(c), and one observes a semi-metallic dispersion, which is consistent with the experimental results corresponding to the largest excitation strength in Figure 4.2. The reduction of the gap is driven by the suppression of excitonic order. The value of the order parameter $|\phi_F|$ and the photoinduced polarization, Δn, in the long-time limit, are displayed in Figure 4.7(d). With increase in fluence, one observes a progressive suppression of the order parameter while the occupancy of the conduction band increases, corresponding to higher Δn values.

Figure 4.8(a) shows momentum-integrated photoemission spectra at different time delays, indicating a reduction of the gap size. The evolution of the electronic population above the Fermi level shows a fast (order of 100 fs) dynamics. The number of photoexcited electrons, $\Delta n(t)$, increases even after the photoexcitation (not shown) suggesting the scattering of electrons of excess kinetic energy with excitons. The dissociation of the excitons leads to an increase in the number of conduction electrons, previously observed in Ref. [29]. The energy-integrated photoemission spectra for different photoexcitation strengths and their corresponding rise times, $\tilde{\tau}_r$, are shown in Figure 4.8(b) and Figure 4.8(c), respectively. We note that the functional dependence of $\tilde{\tau}_r$ on the excitation strength (polarization) is in good qualitative agreement with the experimental results in Figure 4.6(b) (for $\lambda = 0$ where $\lambda = 2g^2/\omega_0$). Although the critical excitation strength increases with λ, the rise time shows a speed-up with increasing photoexcitation also for $\lambda \neq 0$ and the shape of the curve is similar to that found experimentally. The fluence dependence of the rise time is relatively weak for low fluences and becomes stronger at larger ones, showing a very weak trend in the region around the critical fluence (indicated by the dashed lines for different strengths of the

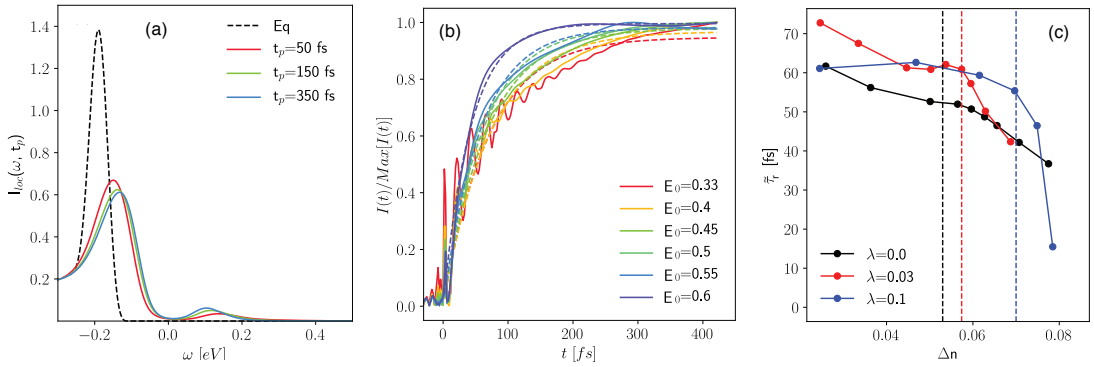

Figure 4.8: (a) Time evolution of the momentum-integrated photoemission spectra, after photoexcitation with a strength of $E_0 < E_C$. The dashed line corresponds to the equilibrium (Eq) spectrum (i.e., no pump). (b) Time evolution of the photoemission integral integrated over the energy range [0.0, 0.2] eV, for different photoexcitation strengths. (c) Rise time $\tilde{\tau}_r$ of the energy-integrated photoemission spectrum versus the excitation strength, for the purely electronic theory ($\lambda = 0$) and in the presence of a finite electron-phonon coupling ($\lambda = 0.03$ and $\lambda = 0.1$). The vertical lines mark the critical excitation strength, E_C, for each value of λ.

electron-phonon coupling λ). The general trend of a faster rise time with increasing fluence is surprising due to the expected slowdown of the dynamics close to the critical point [29, 32, 37, 54]. The rise-time of the photoemission signal is related to the early-stages of the dynamics of the order parameter, where no critical slowing down is observed [55]. The increase of the intensity in the momentum- and energy-integrated spectrum can originate from two processes; i) relaxation of the excited electrons to lower energies due to scattering and ii) shift of the conduction band bottom into the integrated energy range. In i), if scattering of the high-energy electrons with condensed excitons is the dominant relaxation process, this relaxation stops when the excitons are completely consumed. Therefore, under strong photoexcitation, $|\phi_F|$ initially decays faster, and as the exciton bath is depleted, the relaxation also stops rapidly. In ii), because the order parameter is proportional to the band gap, the increase of the signal in the integrated region is directly proportional to the early-stages of the evolution of $|\phi_F|$. These two processes are therefore cooperating to shorten $\tilde{\tau}_r$ at high fluences.

4.4 Summary

In summary, we investigated the non-equilibrium electronic structure and characteristic timescales in a candidate excitonic insulator, Ta_2NiSe_5, using time- and angle-resolved photoemission spectroscopy with a temporal resolution of 50 fs. Our experimental results demonstrate that a phase transition from an insulating to a semi-metallic state can be induced in Ta_2NiSe_5 under strong photoexcitation, which belongs to a fluence regime that has not been explored before [22, 41]. We observe that the closing of the band gap occurs

on a timescale faster than the typical phonon oscillation period in the material. Furthermore, we find that the (fast) rise time of photoemission intensity above the Fermi level and the (slow) relaxation time of the electron population towards equilibrium show contrasting behaviours as a function of the excitation strength: while the rise time becomes shorter with increasing fluence, the relaxation time towards the equilibrium becomes longer, reaching saturation above the critical fluence. The observed speed up of the photoemission signal is confirmed by the results provided by a theoretical two-band tight-binding model, which allowed us to interpret the experimental trends in terms of scattering of the photoexcited electrons with the excitonic condensate. We found that the inclusion of a phonon mode in the model does not modify the physics qualitatively. However, it makes the model system more robust towards photoexcitation. This might explain the apparent discrepancies between different trARPES studies reported in the literature [21, 22, 23, 24, 25]. Finally, the above results point to a predominately electronic origin of the order parameter in Ta_2NiSe_5.

References

[1] N.F. Mott, "The transition to the metallic state." *Philosophical Magazine* **6**, 287 (1961).

[2] R. Knox, "Theory of Excitons" New York : Academic Press, 1963.

[3] L. V. Butov, A. C. Gossard and D. S. Chemla, "Macroscopically ordered state in an exciton system." *Nature* **418**, 751 (2002).

[4] J. P. Eisenstein and A. H. MacDonald, "Bose–Einstein condensation of excitons in bilayer electron systems." *Nature* **432**, 691 (2004).

[5] Z. Wang, D. A. Rhodes, K. Watanabe, T. Taniguchi, J. C. Hone, J. Shan and K. F. Mak, "Evidence of high-temperature exciton condensation in two-dimensional atomic double layers." *Nature* **574**, 76 (2019).

[6] Y. Wakisaka, T. Sudayama, K. Takubo, T. Mizokawa, M. Arita, H. Namatame, M. Taniguchi, N. Katayama, M. Nohara and H. Takagi, "Excitonic Insulator State in Ta_2NiSe_5 Probed by Photoemission Spectroscopy." *Physical Review Letters* **103**, 026402 (2009).

[7] Y. Wakisaka, T. Sudayama, K. Takubo, T. Mizokawa, N. L. Saini, M. Arita, H. Namatame, M. Taniguchi, N. Katayama, M. Nohara and H. Takagi, "Photoemission Spectroscopy of Ta_2NiSe_5." *Journal of Superconductivity and Novel Magnetism* **25**, 1231 (2012).

[8] H. Cercellier, C. Monney, F. Clerc, C. Battaglia, L. Despont, M. G. Garnier, H. Beck, P. Aebi, L. Patthey, H. Berger and L. Forró, "Evidence for an Excitonic Insulator Phase in $1T$-$TiSe_2$." *Physical Review Letters* **99**, 146403 (2007).

[9] G. Mazza, M. Rösner, L. Windgätter, S, Latini, H. Hübener, A. J. Millis, A. Rubio and A. Georges, "Nature of Symmetry Breaking at the Excitonic Insulator Transition: Ta_2NiSe_5." *Physical Review Letters* **124**, 197601 (2020).

[10] T. Kaneko, T. Toriyama, T. Konishi and Y. Ohta, "Orthorhombic-to-monoclinic phase transition of Ta_2NiSe_5 induced by the Bose-Einstein condensation of excitons." *Physical Review B* **87**, 035121 (2013).

[11] Y. Murakami, D. Golež, M. Eckstein and P. Werner, "Photoinduced Enhancement of Excitonic Order." *Physical Review Letters* **119**, 247601 (2017).

[12] A. Subedi, "Orthorhombic-to-monoclinic transition in Ta_2NiSe_5 due to a zone-center optical phonon instability." *Physical Review Materials* **4**, 083601 (2020).

[13] F. J. Di Salvo, C. H. Chen, R. M. Fleming, J. V. Waszczak, R. G. Dunn, S. A. Sunshine and J. A. Ibers, "Physical and structural properties of the new layered compounds Ta_2NiS_5 and Ta_2NiSe_5." *Journal of the Less Common Metals* **116**, 51 (1986).

[14] K. Kim, H. Kim, J. Kim, C. Kwon, J. S. Kim and B. J. Kim, "Direct observation of excitonic instability in Ta_2NiSe_5." *Nature Communications* **12**, 1969 (2021).

[15] M.-J. Kim, A. Schulz, T. Takayama, M. Isobe, H. Takagi and S. Kaiser, "Phononic soft mode behavior and a strong electronic background across the structural phase transition in the excitonic insulator Ta_2NiSe_5." *Physical Review Research* **2**, 042039(R) (2020).

[16] P. A. Volkov, M. Ye, H. Lohani, I. Feldman, A. Kanigel and G. Blumberg, "Critical charge fluctuations and emergent coherence in a strongly correlated excitonic insulator." *npj Quantum Materials* **6**, 52 (2021).

[17] T. I. Larkin *et al.*, "Giant exciton Fano resonance in quasi-one-dimensional Ta_2NiSe_5." *Physical Review B* **95**, 195144 (2017).

[18] T. I. Larkin, R. D. Dawson, M. Höppner, T. Takayama, M. Isobe, Y.-L. Mathis, H. Takagi, B. Keimer and A. V. Boris, "Infrared phonon spectra of quasi-one-dimensional Ta_2NiSe_5 and Ta_2NiS_5." *Physical Review B* **98**, 125113 (2018).

[19] K. Seki, Y. Wakisaka, T. Kaneko, T. Toriyama, T. Konishi, T. Sudayama, N. L. Saini, M. Arita, H. Namatame, M. Taniguchi, N. Katayama, M. Nohara, H. Takagi, T. Mizokawa and Y. Ohta, "Excitonic Bose-Einstein condensation in Ta_2NiSe_5 above room temperature." *Physical Review B* **90**, 155116 (2014).

[20] M. D. Watson, I. Marković, E. A. Morales, P. L. Fèvre, M. Merz, A. A. Haghighirad and P. D. C. King, "Band hybridization at the semimetal-semiconductor transition of Ta_2NiSe_5 enabled by mirror-symmetry breaking." *Physical Review Research* **2**, 013236 (2020).

[21] S. Mor, M. Herzog, D. Golež, P. Werner, M. Eckstein, N. Katayama, M. Nohara, H. Takagi, T. Mizokawa, C. Monney and Julia Stähler, "Ultrafast Electronic Band Gap Control in an Excitonic Insulator." *Physical Review Letters* **119**, 086401 (2017).

[22] K. Okazaki *et al.*, "Photo-induced semimetallic states realised in electron–hole coupled insulators." *Nature Communications* **9**, 4322 (2018).

[23] E. Baldini, A. Zong, D. Choi, C. Lee, M. H. Michael, L. Windgaetter, I. I. Mazin, S. Latini, D. Azoury, B. Lv, A. Kogar, Y. Wang, Y. Lu, T. Takayama, H. Takagi, A. J. Millis, A. Rubio, E. Demler and N. Gedik, "The spontaneous symmetry breaking in Ta_2NiSe_5 is structural in nature." arXiv:2007.02909

[24] T. Tang, H. Wang, S. Duan, Y. Yang, C. Huang, Y. Guo, D. Qian and W. Zhang, "Non-Coulomb strong electron-hole binding in Ta_2NiSe_5 revealed by time- and angle-resolved photoemission spectroscopy." *Physical Review B* **101**, 235148 (2020).

[25] T. Suzuki, Y. Shinohara, Y. Lu, M. Watanabe, J. Xu, K. L. Ishikawa, H. Takagi, M. Nohara, N. Katayama, H. Sawa, M. Fujisawa, T. Kanai, J. Itatani, T. Mizokawa, S. Shin and K. Okazaki, "Detecting electron-phonon coupling during photoinduced phase transition." *Physical Review B* **103**, L121105 (2021).

[26] Y. Tanaka, M. Daira and K. Yonemitsu, "Photoinduced enhancement of excitonic order in the two-orbital Hubbard model." *Physical Review B* **97**, 115105 (2018).

[27] T. Tanabe, K. Sugimoto and Y. Ohta, "Nonequilibrium dynamics in the pump-probe spectroscopy of excitonic insulators." *Physical Review B* **98**, 235127 (2018).

[28] R. Fujiuchi, T. Kaneko, Y. Ohta and S. Yunoki, "Photoinduced electron-electron pairing in the extended Falicov-Kimball model." *Physical Review B* **100**, 045121 (2019).

[29] D. Golež, P. Werner and M. Eckstein, "Photoinduced gap closure in an excitonic insulator." *Physical Review B* **94**, 035121 (2016).

[30] A. Zong, *et al.*, "Dynamical Slowing-Down in an Ultrafast Photoinduced Phase Transition." *Physical Review Letters* **123**, 097601 (2019).

[31] A. Tomeljak, H. Schäfer, D. Städter, M. Beyer, K. Biljakovic and J. Demsar, "Dynamics of Photoinduced Charge-Density-Wave to Metal Phase Transition in $K_{0.3}MoO_3$." *Physical Review Letters* **102**, 066404 (2009).

[32] N. Tsuji, M. Eckstein and P. Werner, "Nonthermal Antiferromagnetic Order and Nonequilibrium Criticality in the Hubbard Model." *Physical Review Letters* **110**, 136404 (2013).

[33] N. Tsuji, P. Barmettler, H. Aoki and P. Werner, "Nonequilibrium dynamical cluster theory." *Physical Review B* **90**, 075117 (2014).

[34] M. Babadi, E. Demler and M. Knap, "Far-from-Equilibrium Field Theory of Many-Body Quantum Spin Systems: Prethermalization and Relaxation of Spin Spiral States in Three Dimensions." *Physical Review X* **5**, 041005 (2015).

[35] M. Babadi, M. Knap, I. Martin, G. Refael and E. Demler, "Theory of parametrically amplified electron-phonon superconductivity." *Physical Review B* **96**, 014512 (2017).

[36] A. Picano and M. Eckstein, "Accelerated gap collapse in a Slater antiferromagnet." *Physical Review B* **103**, 165118 (2021).

[37] P. E. Dolgirev, M. H. Michael, A. Zong, N. Gedik and E. Demler, "Self-similar dynamics of order parameter fluctuations in pump-probe experiments." *Physical Review B* **101**, 174306 (2020).

[38] T. Rohwer, S. Hellmann, M. Wiesenmayer, C. Sohrt, A. Stange, B. Slomski, A. Carr, Y. Liu, L. M. Avila, M. Kalläne, S. Mathias, L. Kipp, K. Rossnagel and M. Bauer, "Collapse of long-range charge order tracked by time-resolved photoemission at high momenta." *Nature* **471**, 490 (2011).

[39] S. Mathias *et al.*, "Self-amplified photo-induced gap quenching in a correlated electron material." *Nature Communications* **7**, 12902 (2016).

[40] S. Hellmann, T. Rohwer, M. Kalläne, K. Hanff, C. Sohrt, A. Stange, A. Carr, M. M. Murnane, H.C. Kapteyn, L. Kipp, M. Bauer and K. Rossnagel, "Time-domain classification of charge-density-wave insulators." *Nature Communications* **3**, 1069 (2012).

[41] S. Mor, M. Herzog, J. Noack, N. Katayama, M. Nohara, H. Takagi, A. Trunschke, T. Mizokawa, C. Monney and Julia Stähler, "Inhibition of the photoinduced structural phase transition in the excitonic insulator Ta_2NiSe_5." *Physical Review B* **97**, 115154 (2018).

[42] M. Ligges, I. Avigo, D. Golež, H. U. R. Strand, Y. Beyazit, K. Hanff, F. Diekmann, L. Stojchevska, M. Kalläne, P. Zhou, K. Rossnagel, M. Eckstein, P. Werner and U. Bovensiepen, "Ultrafast Doublon Dynamics in Photoexcited 1T-TaS_2." *Physical Review Letters* **120**, 166401 (2018).

[43] D. Werdehausen, T. Takayama, M. Höppner, G. Albrecht, A. W. Rost, Y. Lu, D. Manske, H. Takagi and S. Kaiser, "Coherent order parameter oscillations in the ground state of the excitonic insulator Ta_2NiSe_5." *Science Advances* **4**, eaap8652 (2018).

[44] H. M. Bretscher, P. Andrich, P. Telang, A. Singh, L. Harnaga, A. K. Sood and A. Rao, "Ultrafast melting and recovery of collective order in the excitonic insulator Ta_2NiSe_5." *Nature Communications* **12**, 1699 (2021).

[45] É. D. Murray, S. Fahy, D. Prendergast, T. Ogitsu, D. M. Fritz and D. A. Reis, "Phonon dispersion relations and softening in photoexcited bismuth from first principles." *Physical Review B* **75**, 184301 (2007).

[46] H. Hedayat *et ai.*, "Excitonic and lattice contributions to the charge density wave in 1T-$TiSe_2$ revealed by a phonon bottleneck." *Physical Review Research* **1**, 023029 (2019).

[47] K. Seki, R. Eder and Y. Ohta, "BCS-BEC crossover in the extended Falicov-Kimball model: Variational cluster approach." *Physical Review B* **84**, 245106 (2011).

[48] K. Balzer, S. Bauch and M. Bonitz, "Time-dependent second-order Born calculations for model atoms and molecules in strong laser fields." *Physical Review A* **82**, 033427 (2010).

[49] N. Schlünzen, S. Hermanns, M. Scharnke and M. Bonitz, "Ultrafast dynamics of strongly correlated fermions—nonequilibrium Green functions and selfenergy approximations." *Journal of Physics: Condensed Matter* **32**, 103001 (2020).

[50] R. Tuovinen, F. Covito and M. A. Sentef, "Efficient computation of the second-Born self-energy using tensor-contraction operations." *The Journal of Chemical Physics* **151**, 174110 (2019).

[51] R. Tuovinen, D. Golež, M. Eckstein and M. A. Sentef, "Comparing the generalized Kadanoff-Baym ansatz with the full Kadanoff-Baym equations for an excitonic insulator out of equilibrium." *Physical Review B* **102**, 115157 (2020).

[52] B. Zenker, D. Ihle, F. X. Bronold and H. Fehske, "Electron-hole pair condensation at the semimetal-semiconductor transition: A BCS-BEC crossover scenario." *Physical Review B* **85**, 121102(R) (2012).

[53] T. Kaneko, S. Ejima, H. Fehske and Y. Ohta, "Excitonic BCS-BEC Crossover in Double-Layer Systems." *JPS Conference Proceedings* **3**, 017006 (2014).

[54] A. Zong, A. Kogar, Y.-Q. Bie, T. Rohwer, C. Lee, E. Baldini, E. Ergeçen, M. B. Yilmaz, B. Freelon, E. J. Sie, H. Zhou, J. Straquadine, P. Walmsley, P. E. Dolgirev, A. V. Rozhkov, I. R. Fisher, P. J.-Herrero, B. V. Fine and N. Gedik, "Evidence for topological defects in a photoinduced phase transition." *Nature Physics* **15**, 27 (2019).

[55] T. Saha, D. Golež, G. D. Ninno, J. Mravlje, Y. Murakami, B. Ressel, M. Stupar and P. R. Ribič, "Photoinduced phase transition and associated timescales in the excitonic insulator Ta_2NiSe_5." *Physical Review B* **103**, 144304 (2021).

5 Uncovering the nature of out-of-equilibrium phases in 1T-TaS_2

In this chapter, we study the photoinduced transient phase and the recovery dynamics of the ground state in a complex material, the charge density wave (CDW) - Mott insulator 1T-TaS_2, employing femtosecond trARPES. We reveal striking similarities between the band structures of the transient phase and the (equilibrium) structurally undistorted metallic phase, with evidence for the coexistence of the low-temperature Mott insulating phase and high-temperature metallic phase. As the suppressed order starts to recover, we find that a long-lived metastable emerges before the material recovers the ground state. Our results demonstrate that it is the CDW lattice order that drives the material into the metastable phase. However, we find that the long-lived state emerges only under strong photoexcitation and does not show up when the photoexcitation strength is weak enough.

5.1 Introduction

The layered CDW-Mott insulator 1T-TaS_2 is a prominent example of complex systems since both electron-electron and electron-lattice interactions are simultaneously strong. It exhibits a manifold of electronic and structurally ordered phases [1, 2, 3, 4, 5, 6]: at high temperatures ($T > 550$ K), the system has an undistorted hexagonal structure while cooling results in the formation of various CDW phases. Below the critical temperature for the commensurate CDW (CCDW) phase, $T_C = 180$ K, a periodic lattice distortion gives rise to the formation of "Star-of-David"-shaped clusters consisting of thirteen Ta atoms. Figures 5.1(a) and 5.1(b) illustrate the layered crystal structure of 1T-TaS_2 and lattice reconstruction in the plane of Ta atoms as well as its Brillouin zone in CCDW phase, respectively. Previous trARPES studies have shown an instantaneous collapse of the Mott gap at E_F on timescales < 50 fs after photoexcitation [1, 5, 7, 8]. In addition, the CDW gap between the Ta 5d subbands was found to melt faster than the lattice vibrational timescale, suggesting that electron correlations might play a key role in the CDW ordering [5, 8]. A prompt collapse of charge ordering was also shown using ultrafast core-level PES [9]. Ultrafast electron diffraction studies have identified a suppression of the periodic lattice distortion in the nearly-CCDW phase from the optically induced change in the spatial distribution of the electron density [10]. Lately, single-shot time-resolved techniques were able to capture the emergence of a persistent "hidden" phase in 1T-TaS_2 [11, 12, 13, 14, 15, 16, 17, 18]. However, different characteristics of such a state may show up by tuning the experi-

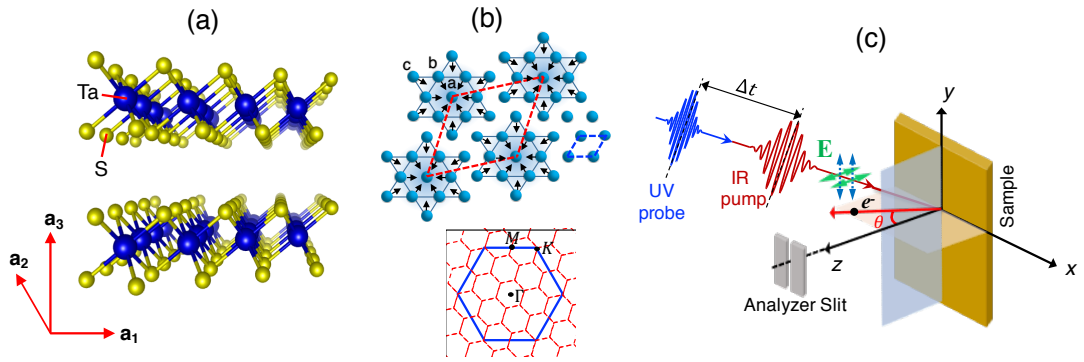

Figure 5.1: (a) Crystal structure of 1T-TaS_2 showing the layered nature in the a_1-a_2 plane. Here, $\mathbf{a}_1$, $\mathbf{a}_2$, $\mathbf{a}_3$, define the crystal axes and Tantalum (Ta) and Sulfur (S) atoms are represented by blue and yellow spheres, respectively. The structural model was generated using VESTA. (b) (Top) In-plane structural distortion in the CCDW phase of 1T-TaS_2 produces "Star-of-David" clusters having inequivalent "a", "b", and "c" Ta atoms. Red and blue dashed lines indicate the unit cells in the CCDW and unreconstructed phases, respectively. The arrows indicate the displacement of the Ta atoms from their initial positions. (Bottom) Brillouin zone in the unreconstructed (blue) and distorted phases (red) with the high-symmetry points Γ, M, K. (c) A schematic of the pump-probe experimental geometry where the electric field **E** of s- and p-polarized photons are indicated by blue (along y-axis) and green (along xz-plane) double-headed arrows, respectively.

mental conditions [19].

Even though this material has been extensively studied, there has been minimal emphasis on the state of charge and lattice ordering in the non-equilibrium transient phase. Moreover, the majority of the studies have focussed on the early stages of the dynamics, i.e., on the collapse rather than the recovery to the ground state. In the present work, we address the above scenario by studying the electronic band structure in the transient phase, as well as the recovery dynamics of electronic and lattice order in 1T-TaS_2. We choose band structure as the spectroscopic indicator since its various features, such as bandwidth, dispersion of the band and binding energy, provide information about the lattice order, which plays a prominent role in the ground state of 1T-TaS_2. ARPES in the ultrafast time domain is employed to systematically track the temporal evolution of Ta 5d subbands in the CCDW-Mott phase. Our trARPES study demonstrates that, after optical excitation, the material enters a transient phase which bears a striking correspondence with the high-temperature unreconstructed phase. Simultaneously, the early dynamics of the photoexcited system also demonstrates the coexistence of Mott-insulating and unreconstructed metallic phases. Interestingly, the recovery of the Mott and CDW dynamics, after traversing the transient phase, is observed to commence around the same time. It is important to note that although the suppression of Mott-CDW electronic order and CDW lattice order is known to occur on two distinct time scales in 1T-TaS_2 [5, 8], the same timescale observed for the re-establishment emphasizes that Mott state is indeed coupled to the CCDW ordering in this material. Moving further, we find that the lat-

tice order of the CDW drives the material to a long-lived hidden phase at high photoexcitation strengths.

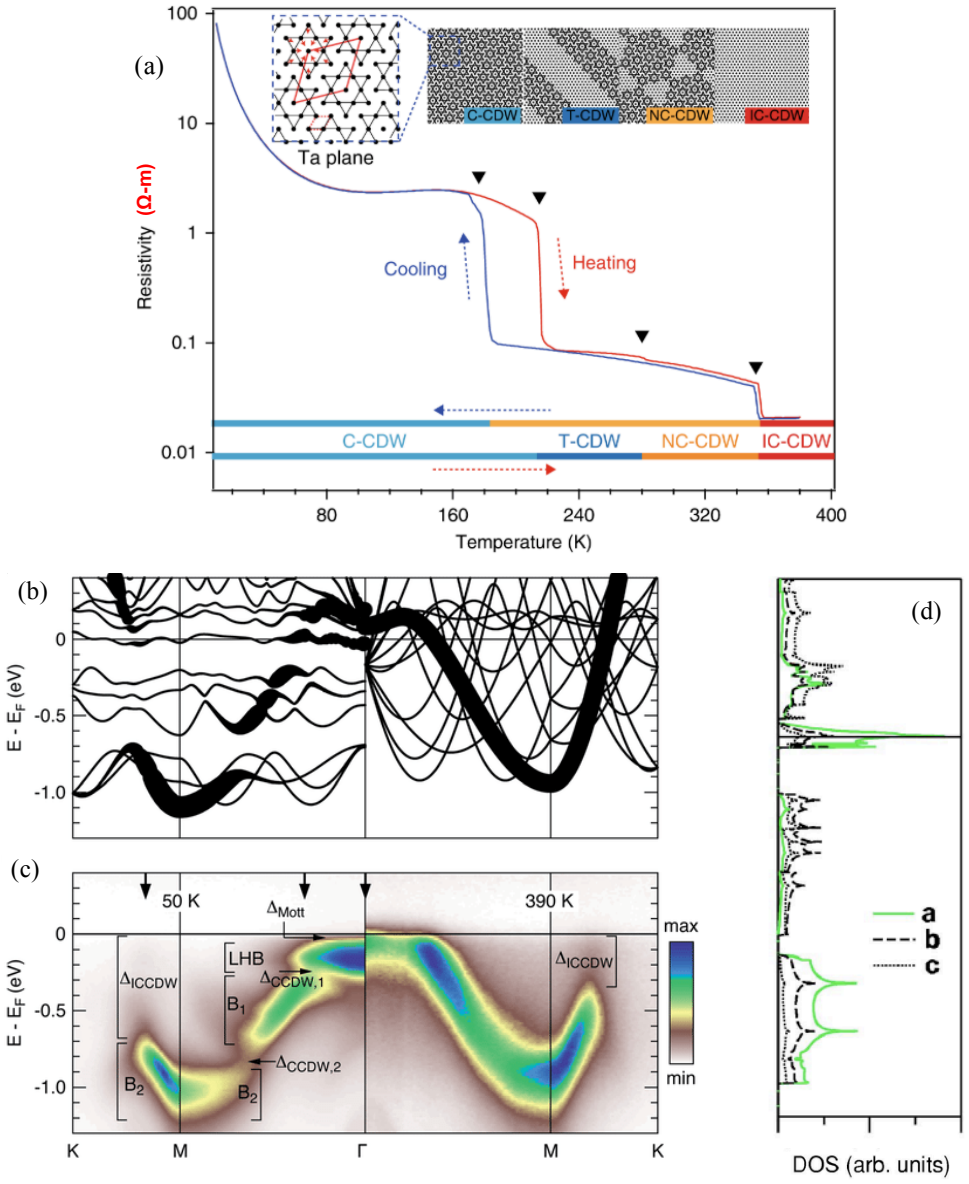

Figure 5.2: (a) Taken from Ref. [6]. Temperature dependence of in-plane resistivity taken upon heating and cooling. The black arrows mark the transition temperatures and the bars below the curves indicate temperature intervals corresponding to the different phases. Inset: Schematic illustrations for the in-plane lattice modulations in the C-CDW, NC-CDW, T-CDW, and IC-CDW phases. The SD clusters of Ta atoms (black dots) are marked with the dark outlines. (b) Taken from Ref. [5]. Simulated reconstructed band structure (left) and folded-out band structure (right) in the unreconstructed phase with Umklapp bands generated by translation through the reciprocal lattice vectors of the reconstructed phase. The spectral weight carried by the electronic states is indicated by the line thickness. (c) Taken from Ref. [5]. Measured ARPES band structure in the commensurate (left) and incommensurate (right) CDW phase. (d) Taken from Ref. [2]. Atom-projected densities of states showing that the states across E_F in reconstructed phase reside primarily on the "a" atoms at the center of the cluster.

5.2 Structural and physical properties of 1T-TaS_2

1T-TaS_2 is a quasi two-dimensional (2D) material exhibiting a number of peculiar CDW phases [20, 21, 22, 23]. The 2D compounds exhibiting CDWs have the composition MX_2, where M is a transition metal (V, Nb, Ta, etc.) and X is one of the chalcogenides (S, Se, Te) [24]. The atoms are strongly bonded into layers, with a close-packed sheet of M atoms sandwiched between two close-packed sheets of X atoms. The three atoms thick layers are weakly bonded to each other through chalcogen-**chalcogen** van-der-Waals interactions [see Figure 5.1(a)]. These compounds can be prepared in a number of polymorphs that differ from each other in the stacking arrangement of the layers and by the metal coordination within a given layer. The two observed coordinations are octahedral, in which chalcogens alternate and trigonal prismatic, in which the chalcogens are aligned above each other in each layer. The simplest polymorphs are the 1T, which have one layer per unit cell, octahedral coordination and overall trigonal symmetry, such as 1T-TaS_2; and the 2H, which have two layers per unit cell, trigonal prismatic coordination and overall hexagonal symmetry, such as 2H-TaS_2. The designations of the polymorphs come from the initial letters of the overall symmetry classes.

1T-TaS_2 undergoes successive first-order phase transitions that are accompanied by large increases in electrical resistivity. These transitions result in the formation of various CDWs with increasing degree of commensurability [22, 25, 26, 27]. On cooling, metallic 1T-TaS_2 enters an incommensurate CDW (IC-CDW) phase below 550 K, a nearly commensurate CDW (NC-CDW) phase below 350 K, and finally a commensurate CDW (C-CDW) phase below 180 K. Upon heating, there is a prominent hysterisis behaviour in the electrical resisitivity where the material enters triclinic CDW (T-CDW) phase at 220 K, and then the NC-CDW phase at 280 K. All these properties are shown in Figure 5.2(a). In the C-CDWphase, the modulation of conduction electron density leads to the displacement of the atoms, resulting in the formation of Star-of-David (SD) clusters. Each SD cluster consists of thirteen Ta atoms where twelve adjacent Ta atoms within a layer move radially towards a thirteenth central Ta atom, giving rise to $\sqrt{13} \times \sqrt{13}$ superlattice rotated by 13.9° [2, 28, 29] [see Figure 5.1(b), top panel]. In the reconstructed unit cell, there are three inequivalent types of Ta atoms designated as a, b, and c, with shrinkage of ab and bc interatomic distances by 6.4 and 3.2 %, respectively [28]. The CDW reconstruction reduces the size of the Brillouin zone [see Figure 5.1(b), bottom panel] leading to bandfolding, which splits the Ta 5d valence band into submanifolds. There are two low-lying threeband submanifolds each containing six electrons and one narrow band across E_F filled by the "13th" electron. This band has a very small width (≈80 meV) and is therefore susceptible to a Mott-Hubbard transition [2, 20]. The electronic band structure of 1T-TaS_2 in the reconstructed phase is shown in Figures 5.2(b) and 5.2(c). The electronic states in the half-filled narrow band are located preferentially on the central atom, a, of the SD cluster [see Figure 5.2(d)]. ARPES results have generally confirmed the CCDW-induced reconstruction of the band stucture and the

opening of the Mott gap ($\approx$ 440 meV) predicted by theory [27, 30, 31, 32]. The NCCDW phase equally contains SD clusters, although they are arranged in a less uniform manner [21]. Ambient-pressure X-ray studies in 1T-TaS_2 reveal that in the NCCDW phase, several tens of stars organize into roughly hexagonal domains, locally reproducing the CCDW phase [22, 33]. The domains are separated by triangular regions where the amplitude of the deformation is reduced, forming the planar structure that resembles the kagome patchwork [22, 33]. The Fermi surface of 1T-TaS_2 has elliptical electron pockets centered on the edges (M-point) of the hexagonal Brillouin zone [2, 34].

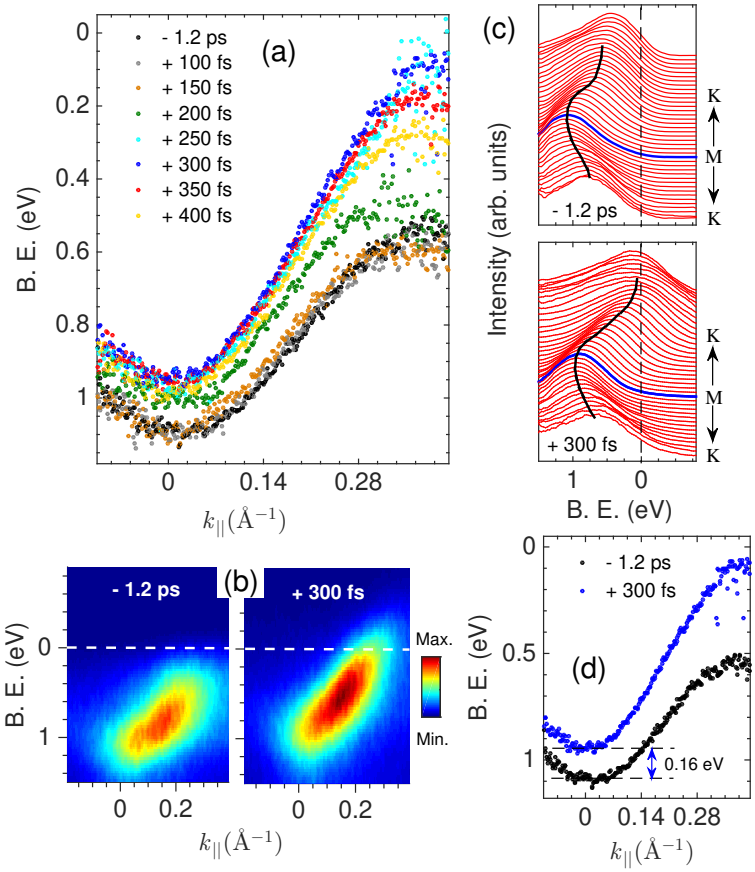

Figure 5.3: (a) Time evolution of the electronic band structure in 1T-TaS_2 about M-point (along MK direction). The peak positions of the EDCs have been plotted as a function of $k_{||}$ at each pump-probe delay Δt. (b) ARPES snapshots acquired before and after (Δt = +300 fs) photoexcitation. (c) Corresponding EDC stacking where the blue curve represents the EDC at M. The black curves are guide to the eye for the band dispersion. (d) Comparison of the band dispersion before photoexcitation and in the transient state of the system, where there is an energy shift towards E_F and the band is more dispersive. All the data correspond to a high pump fluence of 3.6 mJ/cm^2 and the dashed lines in (b) and (c) indicate E_F. Binding energy is abbreviated to B. E.

Besides the Mott physics that occurs within one TaS_2 layer, interlayer coupling has recently been emphasized as a crucial aspect to understand the insulating property of 1T-TaS_2 [35, 36, 37]. Every two adjacent TaS_2 layers

form a dimerized bilayer and these bilayers form different stacking arrangements based on the in-plane sliding configurations [36, 37]. Recent scanning tunneling microscopy and transport measurements show possible existence of the stacking order in 1T-TaS_2 [38, 39]. Band structure calculations show that, without considering the strong electronic correlation, the interlayer stacking order itself can open a band gap at E_F, yielding an insulating property of 1T-TaS_2. The CCDW-Mott phase of 1T-TaS_2 was found to be sensitive to doping [40, 41], disorder induced by irradiation [42] and pressurization [43].

5.3 Results and Discussion

Experimental conditions: A probe energy of $\sim$ 20 eV (harmonic 13 of the fundamental laser) was used in the experiments due to the higher photoionization cross-section of the Ta 5d bands and a high photon flux. A pump energy of 1.55 eV (fundamental frequency of the source) was used for photoexcitation of the sample. A schematic of the experimental geometry showing the polarization of pulses is shown in Figure 5.1(c). A closed-cycle Helium cryostat was used to control the sample temperature and the measurements were performed at $T = 100$ K ($< T_C$). Prior to trARPES measurements, clean sample surfaces were obtained via cleaving under UHV pressure better than 6x10^{-9} mbar and the measurements were performed at a base pressure $<$ 1x10^{-10} mbar. p-polarized pump and probe pulses [green arrows in Figure 5.1(c)] were used for the obtained data, unless specified.

We will refer to the (equilibrium) electronic band structure of 1T-TaS_2 reported in Ref. [5], shown in Figure 5.2(b), while presenting the trARPES results on different Ta 5d subbands.

5.3.1 Band structure along MK-direction in the photoinduced transient phase

For a high photoexcitation strength (3.6 mJ/cm^2), the time evolution of the Ta 5d subband along high symmetry MK direction (we call it B_2 band) [5] is plotted in Figure 5.3(a). We observe that a shift in binding energy towards E_F and an enhancement of the bandwidth characterize the evolution, which occurs on a 200 fs-timescale. Since the timescale corresponds to half an oscillation cycle of the CDW amplitude mode [45, 46], the temporal changes indicate the collapse of CDW lattice order after photoexcitation. Subsequent recovery of the suppressed order is observed to occur after 300 fs [red and yellow circles in Figure 5.3(a)]. The characterization of the transient phase at pump-probe delay $\Delta t = +300$ fs is presented in Figures 5.3(b)-(d). A band shift of the minima by 0.16 eV towards E_F accompanied by a substantial increase of the bandwidth [see Figure 5.3(d)] are in excellent agreement with the dispersion of the B_2 band in the unreconstructed phase [5]. According to theoretical calculations [2, 5], the dispersion crosses E_F at a $k_{||}$ value away from M, which is however, not evident in our data at 300 fs. This is because

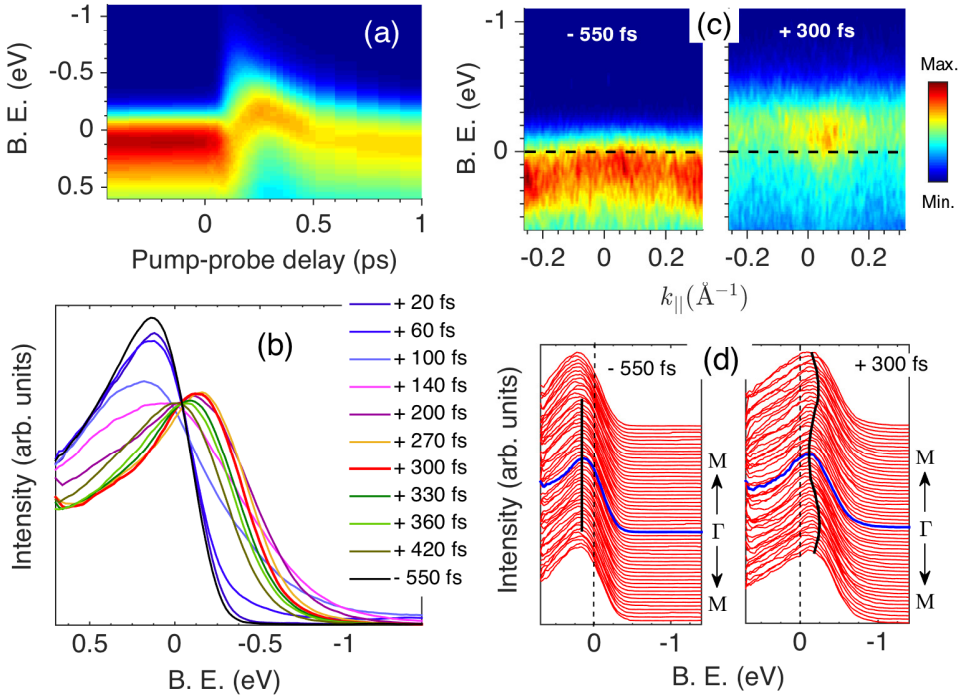

Figure 5.4: (a) trARPES spectrum for an integrated $k_{||}$ range of ± 0.1 Å^{-1} about Γ-point (along ΓM direction) at pump fluence 3.2 mJ/cm^2. (b) Temporal evolution of the EDCs obtained at different pump-probe delays from (a). (c) ARPES snapshots acquired before and after (Δt = +300 fs) photoexcitation. (d) Corresponding EDC stacking where the blue curve denotes the EDC at Γ. Smooth curves are guide to the eye to emphasize the change in the band dispersion around Γ in the transient phase. The dashed lines indicate E_F and binding energy is abbreviated to B. E.

B_2 might have traversed such a feature within a few 10s of fs before 300 fs and could not be captured due to a large time interval (50 fs) used in the experiments. This particular characteristic of the dispersion is reported in Ref. [1]. **Despite the correspondence of the transient band dispersion with that of the (equilibrium) high-temperature phase, the evolved band structure does not reflect phase transitions due to the rise in effective lattice temperature. This is because the observed changes occur much faster than the timescale needed to transfer the energy from the electronic subsystem to the lattice through phonon emission. According to the partial density of states in 1T-TaS$_2$ (Ref. [2]), photoexcitation involves a redistribution of the conduction electron density within the SD clusters. This results in a radial motion of the Ta atoms towards the outer ring of the SD clusters ["c" atom in Figure 5.1(a)] and hence, a relaxation of the periodic lattice distortion. The electrons can accommodate instantaneously to the atomic positions (Born-Oppenheimer approximation) which is evidenced by the band structures obtained at different time delays in Figure 5.3(a). Hence, the relaxation of the PLD demonstrated in our results is driven by the redistribution of charge density and is not an effect related to the increase in lattice temperature.**

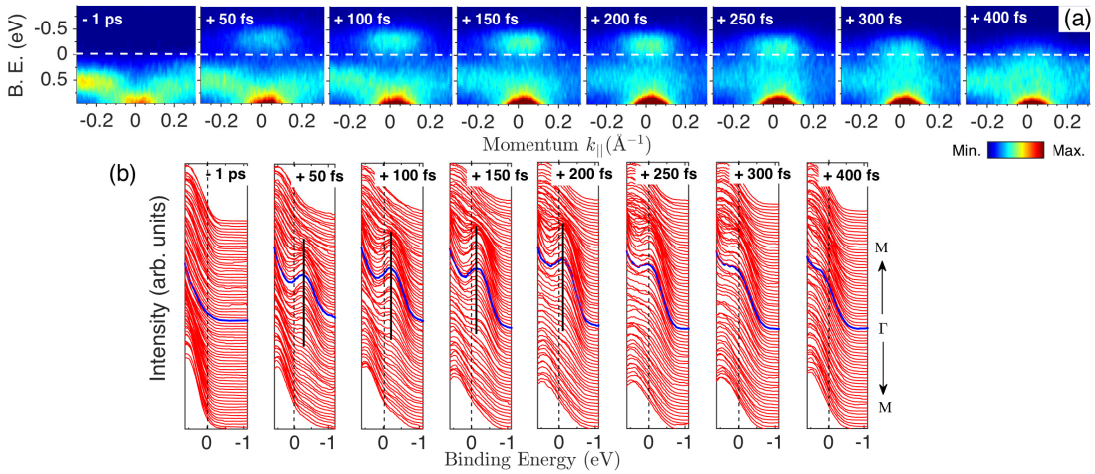

Figure 5.5: Dynamics of the upper Hubbard band (UHB) (a) Time-dependent ARPES spectra along ΓM-direction acquired using s-polarized probe pulses at pump fluence 3.6 mJ/cm^2. (b) Corresponding EDC stackings at different time delays. The black line indicates the flat UHB, the dashed lines in (a) and (b) indicate E_F and binding energy is abbreviated to B. E. The blue curve in (b) denotes the EDC at Γ-point.

5.3.2 Dynamics of the lower and upper Hubbard bands in the transient phase

We will now look at the dynamics of the lower Hubbard band (LHB) [5] along high symmetry ΓM direction at a similar photoexcitation strength (3.2 mJ/cm^2). The EDCs at various time delays extracted from the k-integrated trARPES spectrum are shown in Figure 5.4(a). The early dynamics show a collapse of the Mott phase as the spectral weight in LHB is suppressed and transferred to binding energies at and above E_F, similar to earlier studies [1, 3, 8]. The recovery of the spectral weight begins after 300 fs; it is to be noted that this is the same time at which the CDW lattice order starts to re-form in Figure 5.3(a). In the established scenario [8], the suppression of electronic and lattice order occurs on different time scales. Here, we find that the re-establishment of Mott electronic order and CDW lattice order begins at the same time. This provides evidence that the CCDW lattice reconstruction is the mechanism behind the Mott transition in this material [2, 5]. Figures 5.4(b)-(e) display the characteristics of the band structure in the transient phase at $\Delta t = +300$ fs. We find that the spectral weight from LHB has shifted to an energy band above E_F, which is (i) dispersive about Γ unlike the flatness of LHB, (ii) the band minima lies at ≈ -0.1 eV [see Figs 5.4(b) and 5.4(c)]. It is to be noted that the dispersive feature beyond ± 0.15Å^{-1} in Figures 5.4(b) and 5.4(c) (left panels) is a contribution from other Ta 5d subbands. More importantly, the dispersive band at 300 fs does not correspond to the flat upper Hubbard band (UHB). This has been verified from the UHB dynamics shown in Figure 5.5 that could be tracked at 20 eV probe energy by changing the polarization of the probe pulses [see Figure 5.1(c)] from horizontal (p-pol) to vertical (s-pol). The polarization dependence follows from the photoemission selection rules [47]. In Figures 5.5(a) and 5.5(b), the UHB lying at ∼ -0.25 eV

can be distinctly observed at $\Delta t = +50$ fs [see the black line in Figure 5.5(b)]. With time, the UHB is found to shift towards E_F and at $\Delta t = +300$ fs, the UHB lies across E_F and cannot be spectrally resolved [see Figure 5.5(b) (7th panel)]. All the above features of the dispersive band have a close resemblance to the band structure of the unreconstructed metallic phase about Γ [5]. **Therefore, the above results demonstrate two features near E_F: (i) depletion of the LHB intensity and emergence of a dispersive band above E_F and (ii) shift of the UHB towards E_F indicating a reduction of the Coulomb repulsion strength [5, 44]. The former corresponds to the relaxation of the PLD towards the undistorted high-temperature (metallic) phase, whereas the latter indicates photoinduced modification of the Mott-Hubbard gap. These provide evidence for phase coexistence in 1T-TaS_2 under non-equilibrium conditions, which might arise due to a particular lattice structure comprising hexagonal or striped SD domains separated by metallic islands. The manifestation of such a lattice configuration in the electronic band structure can be addressed through ARPES studies on the nearly commensurate and triclinic CDW phases of 1T-TaS_2. Altogether, our trARPES results at early time delays show that under the destruction of electronic and lattice order in 1T-TaS_2, it enters a transient phase that has remarkable similarities with the unreconstructed metallic phase, along with coexistence of the metallic (high-temperature) and insulating (Mott) phases.**

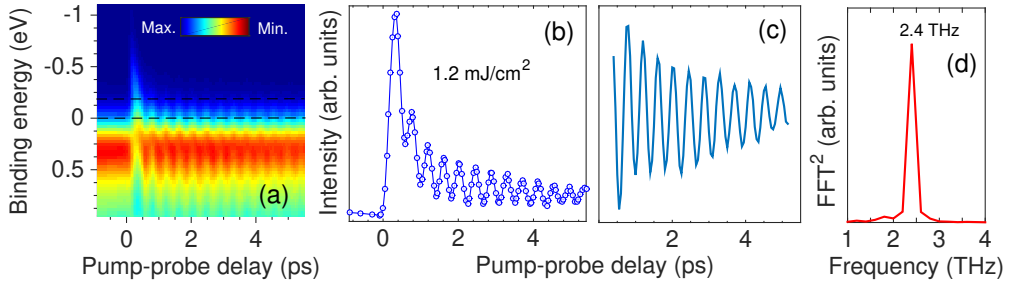

Figure 5.6: (a) trARPES spectrum about Γ-point integrated over a $k_{||}$ range of ±0.35 Å^{-1}. (b) Temporal evolution of the integrated photoemission intensity (empty circles) in the energy interval [-0.15, 0] eV, shown by the horizontal dashed lines in (a). (c) Damped oscillatory part of the photoemission signal. (d) Fourier analysis of (c) showing the 2.4 THz CDW amplitude mode. FFT stands for Fast Fourier Transform. The data corresponds to a pump fluence of 1.2 mJ/cm^2.

5.3.3 Coupling of the electrons to the CDW amplitude mode

Figure 5.6(a) shows a typical momentum-integrated time-resolved ARPES spectrum in 1T-TaS_2 (for $T < T_C$), at a low photoexcitation strength (1.2 mJ/cm^2). The spectral function shows an oscillatory response, which starts at early time delays and persists during several picoseconds. Following photoexcitation, the periodically modulated exponential decay of the hot electron population is shown by the energy-integrated spectral intensity in Figure 5.6(b). The extracted oscillatory signal and its Fourier component are displayed in Figures 5.6(c) and 5.6(d), that identifies the presence of a 2.4 THz phonon mode. These observations are in accordance with earlier trARPES studies [3, 8]. Such a frequency is ascribed to the amplitude mode of the CDW [45, 46] which corresponds to a radial displacement of the nuclear coordinate of the Ta atoms in every 13-atom SD cluster. This mode is excited due to a redistribution of the conduction electron density, leading to the relaxation of structural distortion upon photoexcitation and emphasizes the strong coupling of the electronic subsystem to the lattice.

5.3.4 Recovery dynamics and the emergence of a long-lived metastable state

Now, we will move on to the recovery dynamics and identify the nature of the phase where it settles at longer time delays. Figure 5.7 captures such dynamics under strong photoexcitation (3.6 mJ/cm^2) for the probed Ta 5d subbands (B_2 and LHB). We observe that, as the relaxed lattice structure of the transient phase starts to recover after 300 fs, there is only a partial recovery of the lattice order till $\Delta t = +600$ fs shown in Figure 5.7(a). We call it partial since B_2 band does not exhibit the dispersion corresponding to that of before photoexcitation ($\Delta t = -1.2$ ps). Any further recovery occurs on extremely long time scales which can be clearly identified from the negligible changes in the band dispersion from 600 fs to $\Delta t = +3.5$ ps. This signifies the emer-

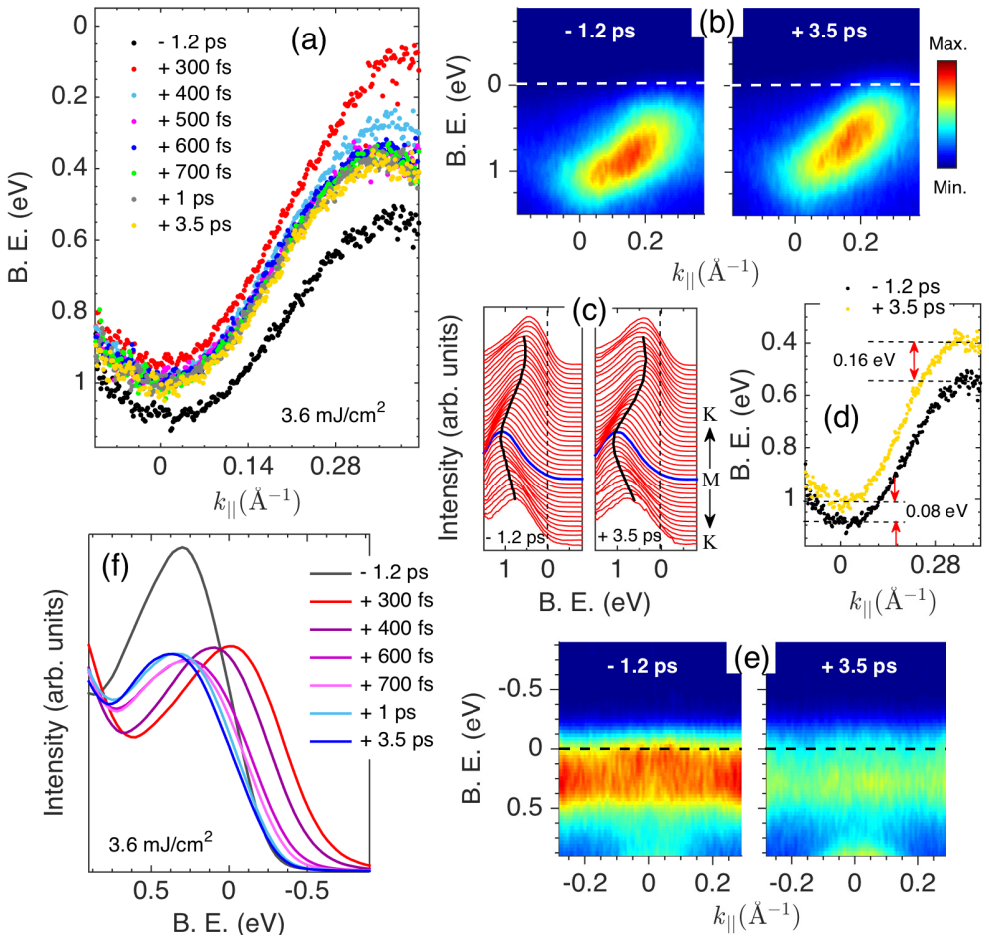

Figure 5.7: (a) Time evolution of the electronic band dispersion about M-point (along MK direction). For each pump-probe delay Δt, the peak position of the EDCs are plotted as a function of $k_{||}$. (b) ARPES snapshots acquired before and after (Δt = +3.5 ps) photoexcitation. (c) Corresponding EDC stacking where the blue curve represents the EDC at M. The black curves are guide to the eye for the band dispersion. (d) Comparison of the band dispersion before photoexcitation and in the long-lived state of the system. The energy shifts around the band minimum and maximum are indicated by arrows. (e) ARPES snapshots acquired before and after (Δt = 3.5 ps) photoexcitation about Γ-point (along ΓM direction). (f) Temporal evolution of the EDCs at longer delays integrated over a $k_{||}$ range of ± 0.1 Å^{-1} about Γ. All the data correspond to a high pump fluence of 3.6 mJ/cm^2 and the dashed lines in (b), (c), (e) denote E_F. Binding energy is abbreviated to B. E.

gence of a long-lived metastable state in photoexcited 1T-TaS_2. The ARPES snapshots taken before and after (3.5 ps) photoexcitation, and their EDCs are shown in Figure 5.7(b) and Figure 5.7(c), respectively. **In the long-lived hidden phase, B_2 exhibits a weaker band dispersion in comparison to the transient phase [compare red and yellow curves in Figure 5.7(a)]. However, the band minima is still shifted by ≈ 0.08 eV towards E_F and B_2 has a larger bandwidth with respect to the ground state dispersion [see Figure 5.7(d)]. On the other hand, the dynamics of the LHB display a complete recovery of the Mott phase. This can be claimed from the following features of LHB**

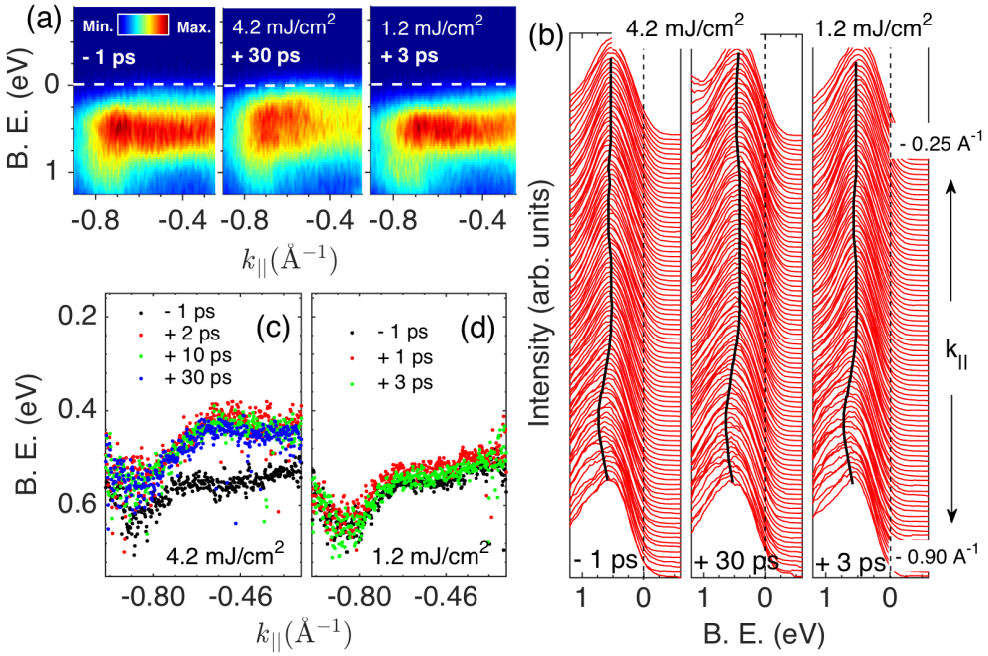

Figure 5.8: (a) ARPES snapshots of the Ta 5d subband at 0.5 eV below E_F along ΓM direction taken before and after photoexcitation: delay Δt = - 1 ps (left), Δt = + 30 ps at pump fluence 4.2 mJ/cm^2 (middle), Δt = + 3 ps at pump fluence 1.2 mJ/cm^2 (right). (b) Corresponding stacked EDCs representing the band dispersion. Smooth black curves are guide to the eye for the dispersion and dashed lines denote E_F. (c) Peak positions of the EDCs plotted as a function of $k_{||}$ at various time delays for high pump fluence, 4.2 mJ/cm^2. (d) The same for low pump fluence, 1.2 mJ/cm^2. The data at high fluence show the presence of a long-lived state. Binding energy is abbreviated to B. E.

at $\Delta t = +3.5$ ps: (i) the spectral weight recovery in LHB and no additional weight at the tail of the EDC in Figure 5.7(f), and (ii) the peak of the EDC lying at a similar binding energy as that of before photoexcitation [see Figures 5.7(e) and 5.7(f)]. However, the recovery of LHB intensity slows down after 600 fs, with no pronounced changes at longer time delays. It is not clear whether such slow dynamics of LHB can be linked to the destruction of CDW order and this will require fluence-dependent studies in the future to make any further comments.

5.3.5 Absence of the metastable state in the low photoexcitation regime

Finally, we look at the features of the metastable state under strong (4.2 mJ/cm^2) and weak (1.2 mJ/cm^2) photoexcitation, by tracking the dynamics of the Ta 5*d* subband lying at 0.5 eV below E_F (we call it B_1) [5] in Figure 5.8. For a high photoexcitation strength, the band dispersion at long time delays is stronger and shifted towards E_F while this is not the case at a low photoexcitation strength [see Figures 5.8(c) and 5.8(d)]. We show the data at $\Delta t = +30$ ps for pump fluence 4.2 mJ/cm^2 in Figures 5.8(a) and 5.8(b) to emphasize that the dispersion (CDW lattice order) has not recovered even at longer times. The quantitative changes in the band structure at $\Delta t = +2$ ps are persistent till $\Delta t = +30$ ps and longer, under strong photoexcitation in Figure 5.8(c). This, once again, provides evidence that the system is driven to a long-lived metastable state prior to the complete recovery of the CDW lattice order. On the contrary, we do not find any signatures of the metastable state under weak photoexcitation since the small bandshifts are completely recovered within $\Delta t = +3$ ps [compare black and green curves in Figure 5.8(d)]. At low photoexcitation strengths ($\sim$ 1.3 mJ/cm^2 in this study), the LHB dynamics show complete recovery of the Mott phase. Hence, the long time dynamics of the Ta 5*d* subbands (LHB, B_1, B_2) provide insights into the metastable phase in 1*T*-TaS_2, which is a hidden phase having no counterparts in equilibrium.

Discussion: The correspondence between the (photoinduced) transient and (equilibrium) structurally undistorted phases imply that the ordering in the CCDW-Mott phase is completely destroyed as the lattice order relaxes to the undistorted metallic phase. Although the recovery of both the CDW and Mott phases begin at the same time, the CDW phase undergoes only a partial recovery while the Mott phase fully recovers within one ps. The metastable state attained by the system after partial recovery does not correspond to any of the thermally accessible equilibrium phases. The signatures of the metastable phase are exhibited only by B_1 and B_2 bands, while LHB shows no evidence of such a long-lived state. Since the LHB is derived from electron-electron interactions and B_1 and B_2 have dominant contribution from electron-lattice interactions [2], it can be inferred that it is primarily the interaction of the electrons with the lattice that pushes the material towards a long-lived state. Such a state could be mediated by mode-selective electron-phonon coupling due to the destruction of CDW order, as it has been shown for a similar compound, i.e., 1*T*-$TaSe_2$ [48].

It is the electronic and lattice configuration in the low-temperature CCDW phase, which makes it susceptible to a Mott-Hubbard transition. Even though the CDW phase is not observed to reform completely, the ordering of the electronic and lattice degrees of freedom is such that the intracluster Coulomb repulsion (U) is larger than the electronic hopping strength (W), i.e., $U/W \gtrsim 1.2$ [4]. This tends to localize the electrons at the atomic sites, leading to the recovery of the Mott phase. Therefore, it can be deduced that the metastable

state is indeed a Mott insulating phase but with a reduced CDW amplitude as compared to the CCDW phase in equilibrium. A clear and direct investigation of the structural configuration in the metastable non-equilibrium phase can be obtained from time-resolved electron diffraction, which will be used in future studies to probe the long-lived hidden phases in this compound. It is also important to identify the critical fluence above which such a long-lived hidden phase emerges. Further time-resolved studies in this direction would involve a deeper investigation of how the microscopic interactions evolve as the material changes its state under non-equilibrium.

5.4 Summary

In summary, we demonstrated the characteristics of the non-equilibrium phases in photoexcited 1T-TaS_2 using time-resolved ARPES. In the transient phase, the Mott-CDW order is suppressed and the band structure has excellent resemblance with that of the unreconstructed metallic phase. Together with the complete relaxation of the PLD driven by charge redistribution, the dynamics at early time delays also exhibit signatures of phase coexistence in photoexcited 1T-TaS_2. The Mott and CDW orders begin recovering around the same time, but only to settle in a long-lived metastable phase. In this "hidden" phase, 1T-TaS_2 is a CCDW-Mott insulator but with a reduced CDW amplitude and the emergence of this phase is driven by the lattice order. In addition, the metastable state emerges only under strong photoexcitation of the system. A distinct characterization of these phases provides deeper insights into the state of charge and lattice order under non-equilibrium conditions and the prominent role played by the different degrees of freedom in governing these phases in a complex system.

References

[1] S. Hellmann *et al.*, "Time-domain classification of charge-density-wave insulators." *Nature Communications* **3**, 1069 (2012).

[2] K. Rossnagel and N. V. Smith, "Spin-orbit coupling in the band structure of reconstructed 1T-TaS_2." *Physical Review B* **73**, 073106 (2006).

[3] L. Perfetti, P. A. Loukakos, M. Lisowski, U. Bovensiepen, H. Berger, S. Biermann, P. S. Cornaglia, A. Georges, and M. Wolf, "Time Evolution of the Electronic Structure of 1T-TaS_2 through the Insulator-Metal Transition." *Physical Review Letters* **97**, 067402 (2006).

[4] L. Perfetti, P. A. Loukakos, M. Lisowski, U. Bovensiepen, M. Wolf, H. Berger, S. Biermann, and A. Georges, "Femtosecond dynamics of electronic states in the Mott insulator 1T-TaS2 by time resolved photoelectron spectroscopy." *New Journal of Physics* **10**, 053019 (2008).

[5] C. Sohrt, A. Stange, M. Bauer, and K. Rossnagel, "How fast can a Peierls–Mott insulator be melted?" *Faraday Discussions* **171**, 243 (2014).

[6] Y. D. Wang, W. L. Yao, Z. M. Xin, T. T. Han, Z. G. Wang, L. Chen, C. Cai, Yuan Li, and Y. Zhang, "Band insulator to Mott insulator transition in 1T-TaS_2." *Nature Communications* **11**, 4215 (2020).

[7] M. Ligges *et al.*, "Ultrafast Doublon Dynamics in Photoexcited in 1T-TaS_2." *Physical Review Letters* **120**, 166401 (2018).

[8] J. C. Petersen *et al.*, "Clocking the Melting Transition of Charge and Lattice Order in 1T-TaS_2 with Ultrafast Extreme-Ultraviolet Angle-Resolved Photoemission Spectroscopy." *Physical Review Letters* **107**, 177402 (2011).

[9] S. Hellmann *et al.*, "Ultrafast Melting of a Charge-Density Wave in the Mott Insulator 1T-TaS_2." *Physical Review Letters* **105**, 187401 (2010).

[10] M. Eichberger, H. Schäfer, M. Krumova, M. Beyer, J. Demsar, H. Berger, G. Moriena, G. Sciaini, and R. J. Dwayne Miller, "Snapshots of cooperative atomic motions in the optical suppression of charge density waves." *Nature* **468**, 799 (2010).

[11] I. Vaskivskyi, I. A. Mihailovic, S. Brazovskii, J. Gospodaric, T. Mertelj, D. Svetin, P. Sutar, and D. Mihailovic, "Fast electronic resistance switching involving hidden charge density wave states." *Nature Communications* **7**, 11442 (2016).

[12] Y. A. Gerasimenko, P. Karpov, I. Vaskivskyi, S. Brazovskii, and D. Mihailovic, "Intertwined chiral charge orders and topological stabilization of the light-induced state of a prototypical transition metal dichalcogenide." *npj Quantum Materials* **4**, 32 (2019).

[13] Q. Stahl, M. Kusch, F. Heinsch, G. Garbarino, N. Kretzschmar, K. Hanff, K. Rossnagel, J. Geck, and T. Ritschel, "Collapse of layer dimerization in the photo-induced hidden state of 1T-TaS_2." *Nature Communications* **11**, 1247 (2020).

[14] J. Ravnik, M. Diego, Y. Gerasimenko, Y. Vaskivskyi, I. Vaskivskyi, T. Mertelj, J. Vodeb, and D. Mihailovic, "A time-domain phase diagram of metastable states in a charge ordered quantum material." *Nature Communications* **12**, 2323 (2021).

[15] F. Y. Gao, Z. Zhang1, Z. Sun, L. Ye, Y.-H. Cheng, Z.-J. Liu, J. G. Checkelsky, E. Baldini, and K. A. Nelson, "Snapshots of a light-induced metastable hidden phase driven by the collapse of charge order." *Science Advances* **8**, eabp9076 (2022).

[16] L. Stojchevska, I. Vaskivskyi, T. Mertelj, P. Kusar, D. Svetin, S. Brazovskii, and D. Mihailovic, "Ultrafast switching to a stable hidden quantum state in an electronic crystal." *Science* **344**, 177 (2014).

[17] I. Vaskivskyi, J. Gospodaric, S. Brazovskii, D. Svetin, P. Sutar, E. Goreshnik, I. A. Mihailovic, T. Mertelj, and D. Mihailovic, "Controlling the metal-to-insulator relaxation of the metastable hidden quantum state in 1T-TaS_2." *Science Advances* **1**, e1500168 (2015).

[18] K. Sun, S. Sun, C. Zhu, H. Tian, H. Yang, and J. Li, "Hidden CDW states and insulator-to-metal transition after a pulsed femtosecond laser excitation in layered chalcogenide 1T-$TaS_{2-x}Se_x$." *Science Advances* **4**, eaas9660 (2018).

[19] I. Avigo, I. Vaskivskyi, M. Ligges, M. Kalläne, K. Rossnagel, L. Stojchevska, D. Mihailović, and U. Bovensiepen, "Accessing and probing of the photo-induced hidden state in 1T-TaS2 with time- and angle-resolved photoemission spectroscopy." Proceedings Volume SPIE 9931, *Spintronics IX*, 99313V (2016).

[20] P. Fazekas and E. Tosatti, "Electrical, structural and magnetic-properties of pure and doped 1T-TaS_2." *Philosophical Magazine B* **39**, 229 (1979).

[21] J. A. Wilson, F. J. Di Salvo, and S. Mahajan, "Charge density waves and superlattices in metallic layered transition-metal dichalcogenides." *Advances in Physics* **24**, 117 (1975).

[22] R. E. Thomson, B. Burk, A. Zettl, and J. Clarke, "Scanning tunneling microscopy of the charge-density-wave structure in 1T-TaS_2." *Physical Review B* **49** 16899 (1994).

[23] P. Fazekas and E. Tosatti, "Charge carrier localization in pure and doped 1T-TaS_2." *Physica B and C* **99**, 183 (1980).

[24] F. J. Di Salvo and T. M. Rice, "Charge-density waves in transition-metal compounds." *Physics Today* **32**, 32 (1979).

[25] E. Tosatti and P. Fazekas, "On the nature of the low temperature phase of 1T-TaS_2." *Journal de Physique Colloques* **37**, C4-165-C164-168 (1976).

[26] B. Sipos, A. F. Kusmartseva, A. Akrap, H. Berger, L. Forró, and E. Tutiš, "From Mott state to superconductivity in 1T-TaS_2." *Nature Materials* **7**, 960 (2008).

[27] K. Rossnagel, "On the origin of charge-density waves in select layered transition-metal dichalcogenides." *Journal of Physics: Condensed Matter* **23**, 213001 (2011).

[28] R. Brouwer and F. Jellinek, "The low-temperature superstructures of 1T-$TaSe_2$ and 2H-$TaSe_2$." *Physica B and C* **99**, 51 (1980).

[29] N. V. Smith, S. D. Kevan and F. J. DiSalvo, "Band structures of the layer compounds 1T-TaS_2, and 2H-$TaSe_2$, in the presence of commensurate charge-density waves." *Journal of Physics C: Solid State Physics* **18**, 3175 (1985).

[30] B. Dardel, M. Grioni, D. Malterre, P. Weibel, Y. Baer, and F. Lévy, "Temperature-dependent pseudogap and electron localization in 1T-TaS_2"*Physical Review B: Condensed Matter* **45**, 1462(R) (1992).

[31] L. Perfetti, T. A. Gloor, F. Mila, H. Berger, and M. Grioni, "Unexpected periodicity in the quasi-two-dimensional Mott insulator 1T-TaS_2 revealed by angle-resolved photoemission." *Physical Review B: Condensed Matter and Materials Physics* **71**, 153101 (2005).

[32] R. Ang, Y. Tanaka, E. Ieki, K. Nakayama, T. Sato, L. J. Li, W. J. Lu, Y. P. Sun, and T. Takahashi, "Real-Space Coexistence of the Melted Mott State and Superconductivity in Fe-Substituted 1T-TaS_2." *Physical Review Letters* **109**, 176403 (2012).

[33] A. Spijkerman, J. L. de Boer, A. Meetsma, G. A. Wiegers, and S. van Smaalen, "X-ray crystal-structure refinement of the nearly commensurate phase of 1T-TaS_2 in (3+2)-dimensional superspace." *Physical Review B* **56**, 13757 (1997).

[34] M. Bovet, D. Popović, F. Clerc, C. Koitzsch, U. Probst, E. Bucher, H. Berger, D. Naumović, and P. Aebi, "Pseudogapped Fermi surfaces of 1T-TaS_2 and 1T-$TaSe_2$: A charge density wave effect." *Physical Review B: Condensed Matter and Materials Physics* **69**, 125117 (2004).

[35] T. Ritschel, *et al.*, "Orbital textures and charge density waves in transition metal dichalcogenides." *Nature Physics* **11**, 328 (2015).

[36] T. Ritschel, H. Berger, and J. Geck, "Stacking-driven gap formation in layered 1T-$TaS_2$2." *Physical Review B* **98**, 195134 (2018).

[37] S. H. Lee, J. S. Goh, and D. Cho, "Origin of the insulating phase and first-order metal–insulator transition in 1T-$TaS_2$2." *P*hysical Review Letters **122**, 106404 (2019).

[38] C. J. Butler, M. Yoshida, T. Hanaguri, and Y. Iwasa, "Mottness versus unit-cell doubling as the driver of the insulating state in 1T-TaS_2." *Nature Communications* **11**, 2477 (2020).

[39] E. Martino *et al.*, "Preferential out-of-plane conduction and quasi-onedimensional electronic states in layered van der Waals material 1T-TaS_2." *npj 2D Materials and Applications* **4**, 7 (2020).

[40] F. Zwick, *et al.*, "Spectral consequences of broken phase coherence in 1T-TaS_2." *Physical Review Letters* **81**, 1058 (1998).

[41] F. J. Di Salvo, J. A. Wilson, B. G. Bagley, and J. V. Waszczak, "Effects of doping on charge density waves in layer compounds." *Physical Review B* **12**, 2220 (1975).

[42] H. Mutka, L. Zuppiroli, P. Molinié, and J. C. Bourgoin, "Charge-density waves and localization in electron-irradiated 1T-TaS_2." *Physical Review B* **23**, 5030 (1981).

[43] T. Tani, T. Osada, and S. Tanaka, "The pressure effect on the CDW-transition temperatures in 1T-TaS_2." *Solid State Communications* **22**, 269 (1977).

[44] S. Kaiser, S. R. Clark, D. Nicoletti, G. Cotugno, R. I. Tobey, N. Dean, S. Lupi, H. Okamoto, T. Hasegawa, D. Jaksch and A. Cavalleri, "Optical Properties of a Vibrationally Modulated Solid State Mott Insulator." *Scientific Reports* **4**, 3823 (2014).

[45] J. R. Duffey, R. D. Kirby, and R. V. Coleman, "Raman scattering from 1T-TaS_2." *Solid State Communications* **20**, 617 (1976).

[46] J. Demsar, L. Forró, H. Berger, and D. Mihailovic, "Femtosecond snapshots of gap-forming charge-density-wave correlations in quasi-two-dimensional dichalcogenides 1T-TaS_2 and 2H-$TaSe_2$." *Physical Review B* **66**, 041101(R) (2002).

[47] A. Damascelli, Z. Hussain and Z. X. Shen, "Angle-resolved photoemission studies of the cuprate superconductors." *Reviews of Modern Physics* **75**, 473 (2003).

[48] X. Shi *et al.*, "Ultrafast electron calorimetry uncovers a new long-lived metastable state in 1T-$TaSe_2$ mediated by mode-selective electron-phonon coupling." *Science Advances* **5**, eaav4449 (2019).

6 Orbital selective electron dynamics in $CaFe_2As_2$

In this chapter, we study the electron dynamics in $CaFe_2As_2$ employing time-resolved ARPES. This material is a parent compound of Fe-based superconductors and exhibits phase transition from a metallic to SDW state, accompanied by a structural transition at 170 K. The β band constituted by d_{xz}/d_{yz} orbitals develops an energy gap across the magnetic phase transition. We demonstrate that by tuning the polarization of pump pulses, one can induce orbital selective photoexcitation of electrons. More specifically, while s-polarized light excites the electronic states of all hole pockets, p-polarized light excites electrons essentially from α and β bands - which are responsible for magnetic order. In the SDW phase, the rise of the photoemission signal for p-polarized pump pulses occurs at a timescale of 50 fs (electronic process), which is significantly faster than that for s-polarized light (200 fs ∼ lattice-driven process). These results suggest that electrons belonging to orbitals with different symmetries have different scattering timescales and this method can be used to disentangle coexisting/competing interactions in the study of quantum materials.

6.1 Introduction

Fe-based compounds [1, 2, 3] often exhibit complex phase diagrams, involving magnetic order, superconductivity and structural transitions [4, 5]. The coexistence of mutually exclusive magnetic order and superconductivity is among the many outstanding puzzles observed in these materials, and questions the existing theoretical models [6, 7, 8, 9]. Numerous investigations allowed scientists to shed light on the fundamental properties of Fe-based systems: the parent compounds exhibit spin density wave state at low temperature, accompanied by a structural transition from tetragonal to orthorhombic phase [3, 5]. Since multiple bands contribute to the formation of Fermi surfaces, it is difficult to disentangle the role of different orbitals/electronic states in determining the electronic properties of the material.

In order to investigate the possibility of inducing orbital selective electron dynamics, we studied the photoexcitation of electrons in an archetypical Fe-based compound $CaFe_2As_2$, a parent Fe-pnictide superconductor. $CaFe_2As_2$ undergoes a concomitant magnetic transition to SDW ground state and a structural transition at about T_C = 170 K [10]. ARPES and band structure calculations [11, 12, 13] show that the electronic structure of this material consists of three hole pockets around the Brillouin zone center, Γ and two electron pockets around the zone corner, X (π,π). Our calculated [14] en-

ergy band structure in the tetragonal phase is shown in Figure 6.1(a). The α and β bands possess d_{xz}/d_{yz} orbital symmetry while the γ band has primary contribution from d_{xy} orbital. The structural transition at T_C often leads to a symmetry breaking in the Fe-based superconductors [15, 16, 17]. In $CaFe_2As_2$, this leads to a lifting of d_{xz}/d_{yz} orbital degeneracy, which is about 43 meV [see Figure 6.1(b)]. In the SDW phase, the spin magnetic moments of Fe arrange antiferromagnetically [18], leading to an energy gap in the β band at the Fermi level, E_F [11, 12]. Thus, the magnetic/spin order involves primarily d_{xz}/d_{yz} orbitals. The Fermi surface nesting of the β band with the electron pocket around X-point and formation of the SDW gap below T_C are illustrated in Figure 6.1(c). It was reported that the energy bands shift towards higher binding energies on cooling due to the formation of a collapsed tetragonal phase, which does not exhibit magnetic ordering [11, 12]. In this study, we attempted to selectively photoexcite electrons of different orbital symmetries by varying the polarization of pump pulses. This allowed us to identify the role played by different orbitals in the ground state properties of the system, based on their respective timescales.

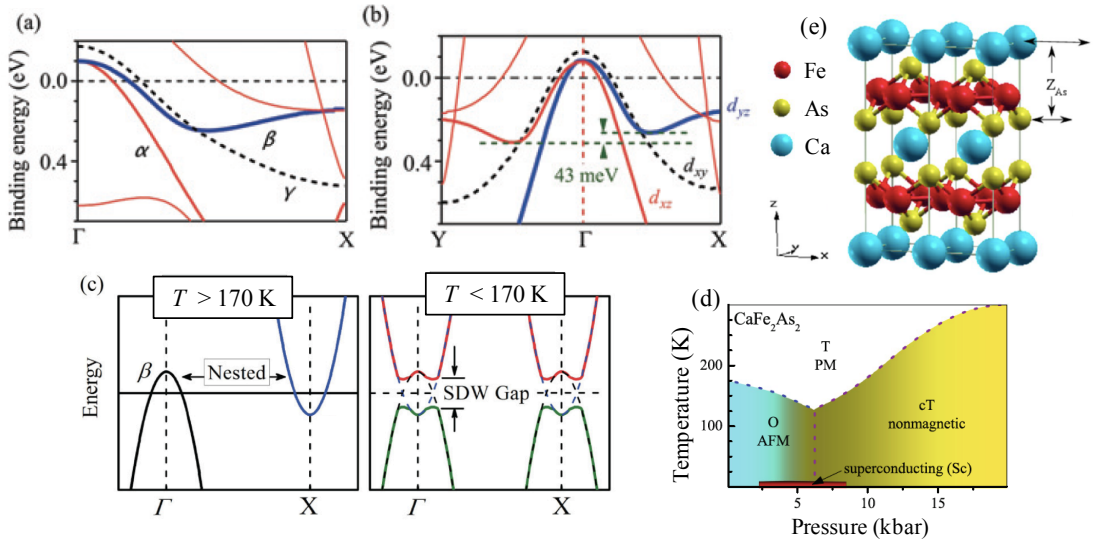

Figure 6.1: Calculated band structure in (a) tetragonal phase along ΓX direction and (b) orthorhombic phase along $Y\Gamma X$ direction. In the orthorhombic phase, the degeneracy of d_{xz} and d_{yz} bands is lifted. The d_{xy} band also shows different dispersions along ΓX and ΓY. (c) Taken from [19]. A schematic of the nesting between β band at Γ and electron pocket at X as well as the formation of SDW gap at $T < 170$ K. (d) Taken from [13]. Temperature-Pressure phase diagram of $CaFe_2As_2$. The dotted line represents the phase boundary between various structural and magnetic phases. O: orthorhombic; AFM: antiferromagnetic; T: tetragonal; PM: paramagnetic; cT: collapsed tetragonal. (e) Taken from [13]. Crystal structure of $CaFe_2As_2$ in the tetragonal phase; z_{As} is the *pnictogen height* (distance of As atoms from the Fe plane).

6.2 Material description

The $A Fe_2As_2$ (A = Ca, Ba, Sr) based compounds display a rich temperature-pressure phase diagram. Superconductivity in $BaFe_2As_2$ and $SrFe_2As_2$, having alkaline earth elements larger than Ca, was found at a reasonably high pressure ($P \sim 4$ GPa and 3.2 GPa, respectively [20]) with T_C of about 29 K and 27 K [21, 22, 23, 24, 25, 26], respectively. On the other hand, $CaFe_2As_2$ shows superconductivity with T_C upto 12 K in a low pressure range from 2.5 kbar to 8 kbar [27]. A typical temperature-pressure phase diagram, shown in Figure 6.1(d) shows the experimental results obtained by Torikachvili *et al*. [27], consistently with the results obtained by others [28]. In Figure 6.1(d), we observe that the transition to orthorhombic antiferromagnetic (AFM) phase is suppressed upon increasing pressure and disappears above a critical pressure with the emergence of the collapsed tetragonal (cT) phase, possessing no long range magnetic order. The critical temperature for structural transition from tetragonal (T) to cT phase gradually increases with pressure. In fact, superconductivity with $T_C \approx 10$ K at 6.9 kbar pressure has been detected by several groups [29, 30]. Subsequent experiments, however, did not find superconductivity although cT phase could be reached on the application of pressure. The observance/non-observance of superconductivity under pressure, non-observance of other structural phases under pressure, absence of superconductivity in ambient conditions, etc., are examples of challenging topics in this field. The crystal structure of $CaFe_2As_2$ at room temperature and ambient pressure is tetragonal possessing $I4/mmm$ space group with lattice parameters a = 3.8915 Å, c = 11.690 Å, and z_{As} = 0.372 [31, 32, 33]. The orthorhombic crystal structure in SDW phase ($T \leq 170$ K) belongs to the space group $Fmmm$ with lattice parameters, a = 5.506 Å, b = 5.45 Å, c = 11.664 Å, and z_{As} = 0.36642. The crystal structure in ambient conditions is shown in Fig. 6.1(e). The electronic structure is very sensitive to the distance of As sites from the Fe plane, which is termed as '*pnictogen height*'. Electronic structure calculations based on first principle approaches were employed extensively to address the ground state properties, Fermi surface and pressure induced effects [8, 32, 34, 35, 36]. These systems are more complex than cuprates due to the contribution of multiple bands at the Fermi level E_F and drastic changes in the Fermi surface topology arising from magnetic and structural transitions.

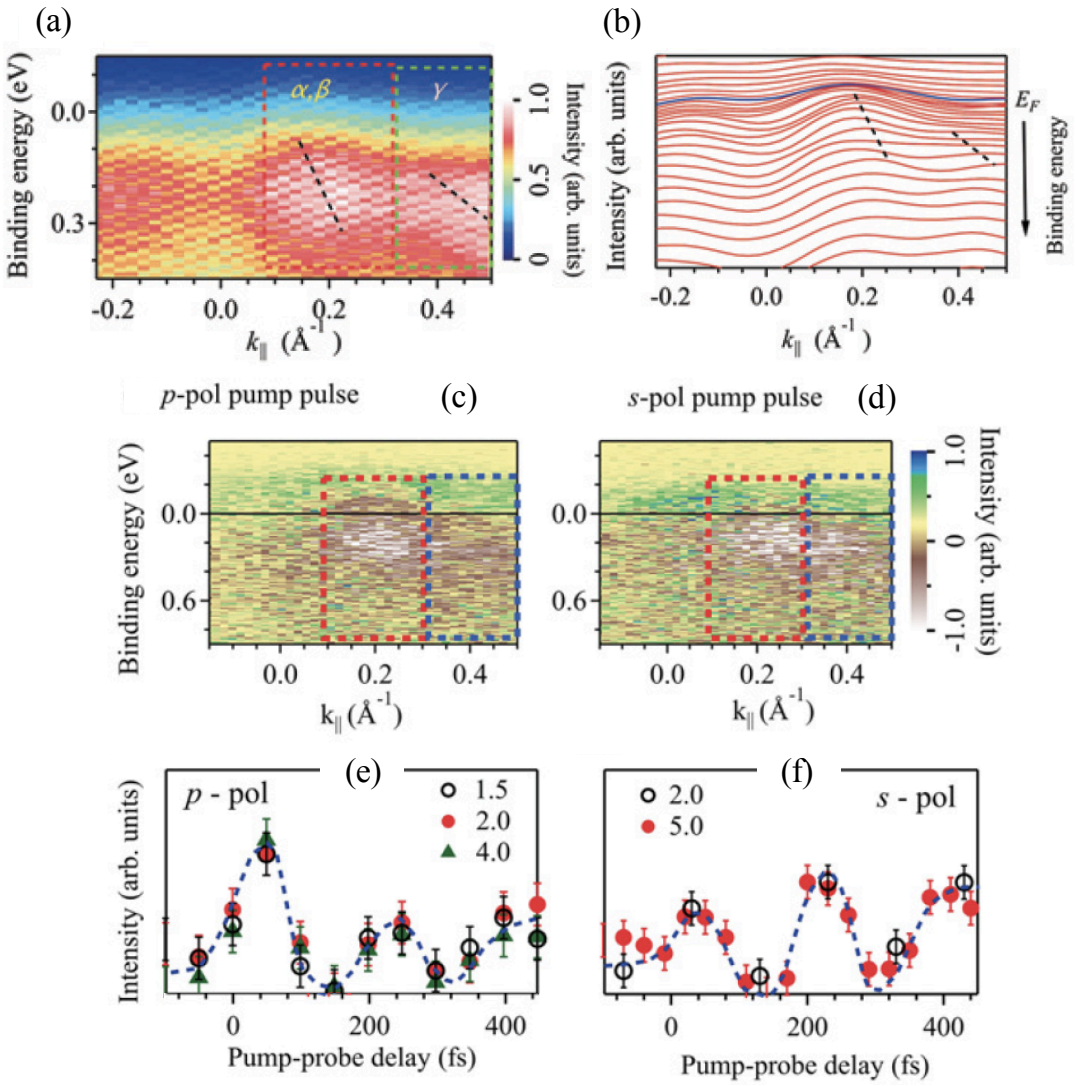

Figure 6.2: (a) Static ARPES spectrum at 120 K collected using s-polarized pulses of photon energy ≈ 29 eV. (b) Corresponding momentum distribution curves (MDCs). The difference ARPES spectra at pump-probe delay Δt = +200 fs with respect to Δt = -300 fs for (c) p-pol and (d) s-pol pump pulses. Initial sample temperature is 30 K and the probe photon energy is ≈ 20 eV. The boxed regions in red and blue correspond to the α, β bands and the γ band, respectively [see Figure 6.1(a)]. **Energy-integrated (0.1-0.2 eV above E_F) photoemission intensity for (e) p-pol** and (f) s-pol pump pulses as a function of pump-probe delay at different pump fluences. Hand-drawn dashed lines are guide to the eye.

6.3 Results and discussion

Experimental conditions: A probe energy of $\sim$ 20 eV (harmonic 17 of the fundamental laser) was used in the experiments, unless specified, due to high photoionization cross-section of Fe 3*d* and As 4*p* states. Pump pulses of wavelength 800 nm (1.55 eV) were used for photoexcitation of the sample. Single crystals of $CaFe_2As_2$ were provided by our collaborators, **Prof. Arumugum Thamizhavel and his team** [37]. The samples were cleaved *in situ* under UHV pressure better than $6x10^{-9}$ mbar to generate clean mirror-like surfaces, prior to each measurement. The trARPES experiments were performed at a base pressure < $1x10^{-10}$ mbar.

The measured (static) ARPES spectrum of $CaFe_2As_2$ along high symmetry ΓX-direction at T = 120 K is shown in Figure 6.2(a). The ARPES data exhibits distinct signatures of the α/β bands separated from the γ band. For better clarity of the bands [11, 12], we show the momentum distribution curves (MDCs) in Figure 6.2(b). After identifying the required E versus k regime and its consistency with literature, pump-probe measurements were carried out to study the electron dynamics. The pump fluence was fixed to 2 mJ/cm^2, which is much below the energy required to drive the system into anharmonic regime [38].

6.3.1 Pump-polarization dependent electron dynamics above and below the SDW transition temperature

In Figures 6.2(c) and 6.2(d), we show the difference of the spectra acquired at pump-probe delay Δt = + 200 fs (after photoexcitation) and Δt = -300 fs (before photoexcitation) for p-polarized (p-pol) and s-polarized (s-pol) pump pulses, respectively (initial sample temperature, 30 K). This provides information on the depleted intensity in the occupied part and enhanced intensity in the unoccupied part of the electronic band structure, remaining 200 fs after the pump-induced excitations. The experimental data collected with different pump polarizations reveal that the relative changes in intensity for the energy bands [indicated by the boxes in Figures 6.2(c) and 6.2(d)] are polarization dependent. In order to investigate if such a behavior can be linked to the pump fluence, we have carried out a number of pump-probe measurements by varying the fluence of both p-pol and s-pol pump pulses. The momentum- and energy-integrated intensity as a function of pump-probe delay is shown in Figures 6.2(e) and 6.2(f) for both polarizations. We observe that there are no marked differences of the electron dynamics with fluence for a given pump polarization, therefore, establishing the absence of fluence dependence, upto 5 mJ/cm^2.

We define the sample surface as xy plane, photoemission occurs in the xz plane and detector's slit is placed on the z-axis. In our setup, since the incident beam defines an angle of 36° with the z-axis, the electric field vector of p-pol light is aligned with d_{xz} orbitals and, hence, primarily excites d_{xz} (α,

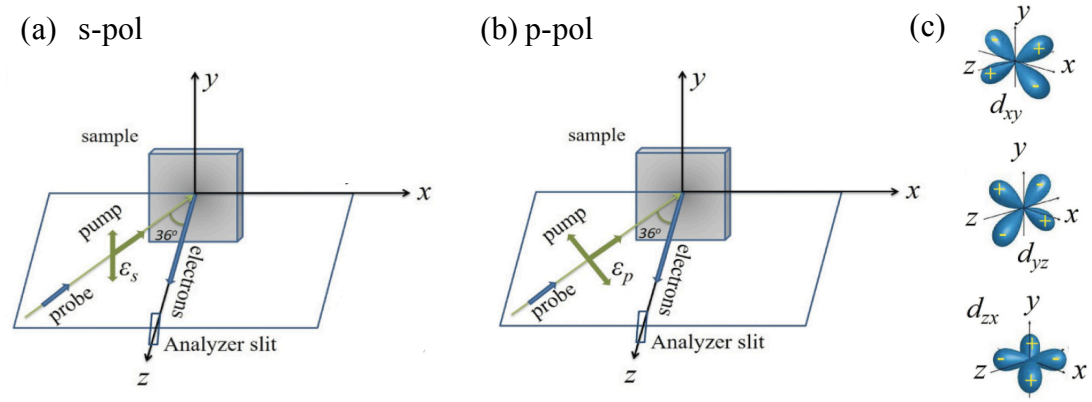

Figure 6.3: Schematics of the experimental geometry for photoexcitation by (a) s-polarized and (b) p-polarized pump pulses. (c) The orientation of d_{xy}, d_{yz}, d_{xz} orbitals with respect to the electric field vector of pump and probe pulses.

β bands) electrons [19]. The polarization vector of the s-pol pump pulse lies in the xy plane (along y-axis), which has a finite component along d_{xy} and d_{yz} electrons for photoexcitation. The d_{xz} orbital plane is orthogonal to the polarization direction (y-axis) of the s-pol pulse and hence will be essentially insensitive to s-pol excitations. A schematic of the experimental geometry for photoexcitation by s-pol and p-pol pump pulses is shown in Figure 6.3. In the experimental results shown in Fig. 6.2, it is evident that the p-pol pump pulse excites primarily the red boxed region (α, β bands) as expected from the symmetry selection rules discussed above, while the s-pol pump pulse excites all the three (α, β and γ) bands. This establishes experimentally that the signal corresponding to the p-pol pump excitations, even if integrated over k along the ΓX-direction, represents the dynamics of (α, β) bands. The s-pol case, on the other hand, provides information on the dynamics of all the three bands with the caveat that it is less sensitive to d_{xz} symmetry.

After photoexcitation, the excited electrons start interacting with the electronic and lattice subsytems, leading to different collective excitations involving magnons, phonons, etc. and this may affect the ground state properties. In general, the response related to electron-phonon coupling is a relatively slower process due to the lattice inertia [39], while the electronic phenomena like SDW order will respond relatively fast to the pump-induced excitation [40]. The spectral response of the excited electronic states gets modulated by the coherent phonon mode ($A1_g$ phonon mode in the present case) [41]. The normalized intensity of the hot electrons for the paramagnetic phase (initial sample temperature = 200 K) are shown in Figures 6.4(a), 6.4(b) and 6.5(a). The results exhibit similar electron dynamics for both p-pol and s-pol pump excitations. In the SDW phase (initial sample temperature = 150 K), when the system is excited with p-pol light, the maximum yield of intensity occurs at Δt = +50 fs, as shown in Figures 6.4(c) and 6.5(b). However, a maximum is observed at about Δt = +170 fs for photoexcitation with s-pol pump pulse, as shown in Figures 6.4(d) and 6.5(b). In order to understand the origin of this difference, we analyze the energy distribution curves (EDC) around Γ-point

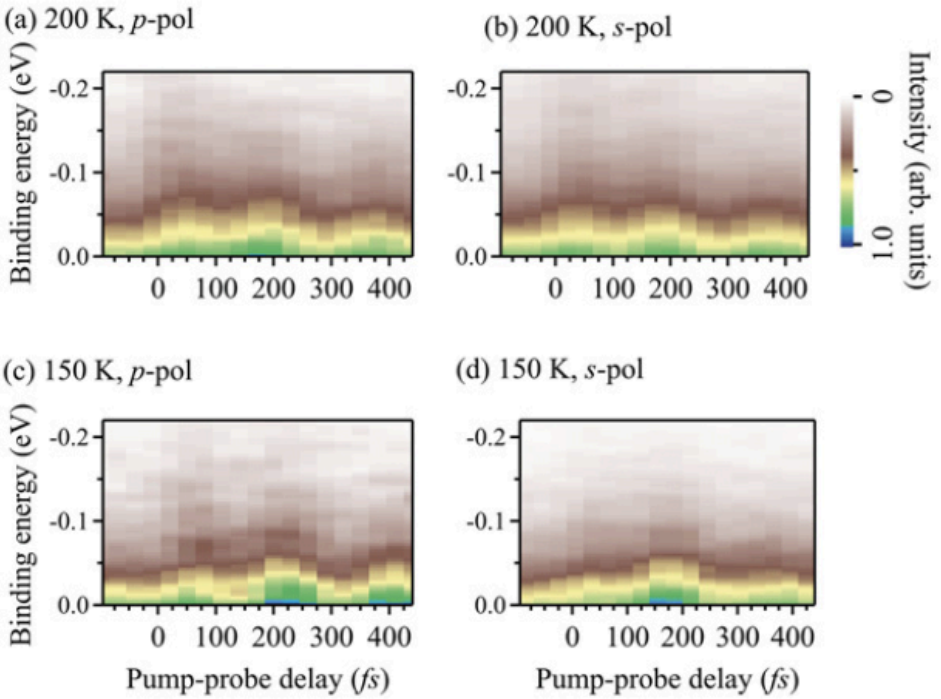

Figure 6.4: Momentum-integrated photoemission spectra (probe energy $\approx$ 20 eV) as a function of pump-probe delay for (a) p-pol and (b) s-pol pump pulses, with initial sample temperature of 200 K. The same at an initial sample temperature of 150 K, for (c) p-pol and (d) s-pol pump pulses.

($\Delta k = 0.0 \pm 0.035$ Å^{-1}), collected at a pump-probe delay of +50 fs. It is evident from Figure 6.5(c) that for the s-pol pump excitations, the leading-edge midpoint (LEM) at T = 30 K is shifted by 35 meV below the LEM of the spectra at T = 200 K, suggesting survival of the SDW gap. Interestingly, the p-pol case shown in Figure 6.5(d) exhibits LEM at the same energy at 200 K and 30 K data providing evidence of the melting of the SDW order. These results demonstrate the survival of the SDW order in the s-pol case while the SDW phase is melted in the p-pol case. The time scale of the melting of the SDW order is manifested by an intense peak at +50 fs delay in the p-pol case, as shown in Figure 6.5(b).

The electron yield above E_F can be associated, via the FD distribution function, to the increase of the transient electronic temperature, T_e, which is responsible for the melting of the magnetic and structural long-range order [42]. Thus, a maximum of the spectral intensity at 50 fs time delay for the p-pol excitation and its absence for the s-pol case (intensity at 50 fs is significantly small with the peak appearing at 170 fs) reveal an interesting scenario: the changes in magnetic and structural orders may be triggered on different time scales. An earlier study [43] suggested nematic processes in Fe-based materials to happen instantaneously, after excitation within the time resolution (170 fs for pump pulse and 250 fs for probe pulse) used in those measurements. Employment of 40 fs time resolution reveals a difference between the timescales for the melting of magnetic and structural order. While

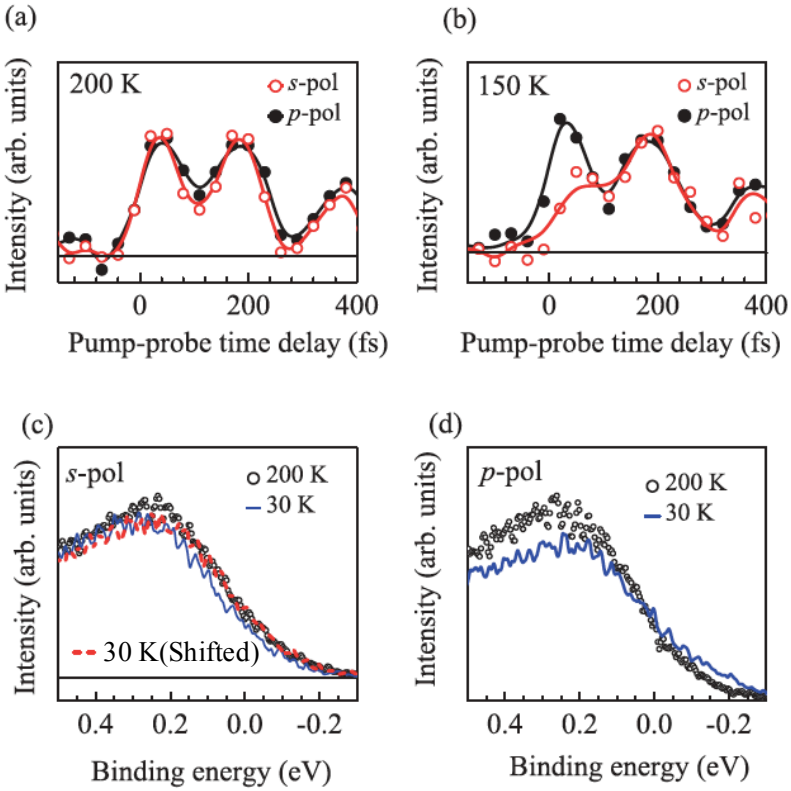

Figure 6.5: Time resolved photoemission intensity for p-pol (filled circles) and s-pol (empty circles) pump pulses at temperatures (a) 200 K (above T_C) and (b) 150 K (below T_C). EDC at Γ-point at $\Delta t = +50$ fs for (c) s-pol and (d) p-pol pump pulses at temperatures above and below T_C. The dashed line in (c) is the 30 K data shifted by 35 meV.

this separation of timescales has interesting implications in the study of electronic properties of complex quantum materials, this also suggests that one can reveal orbital selective dynamics using polarized pump pulse excitations. In order to further support the above scenario, we carried out some additional experiments. In Figure 6.6(a), we show the photoelectron yield extracted from trARPES spectra at 30 K for p-pol and s-pol pump pulses with a photon energy of 20 eV. We observe that the photoelectron intensity rises very fast when the system is excited with p-pol light. When the system is excited with s-pol light, the yield of intensity rises slowly and the maximum intensity appears at a delay time of Δt = +200 fs.

In order to verify the transient dynamics at another k_z-point, we used probe photon energy of 29 eV, which is close to the Γ-point on the k_z axis, ($k_z \approx 12\pi/c$) at an initial sample temperature of T = 150 K. Once again, the experimental results shown in Figure 6.6(b) exhibit a maximum yield of intensity at $\sim$ +50 fs, when the system is photoexcited with p-pol light, while the yield of intensity is maximum at about $\sim$ +200 fs when the system is excited with s-pol light. ARPES results [11, 12] exhibit back folding of the β band occurring around 0.2 $Å^{-1}$ below 170 K due to the SDW order, which extends till the Γ-point [see Figure 6.1(c)]. In Figures 6.6(c) and 6.6(d), we

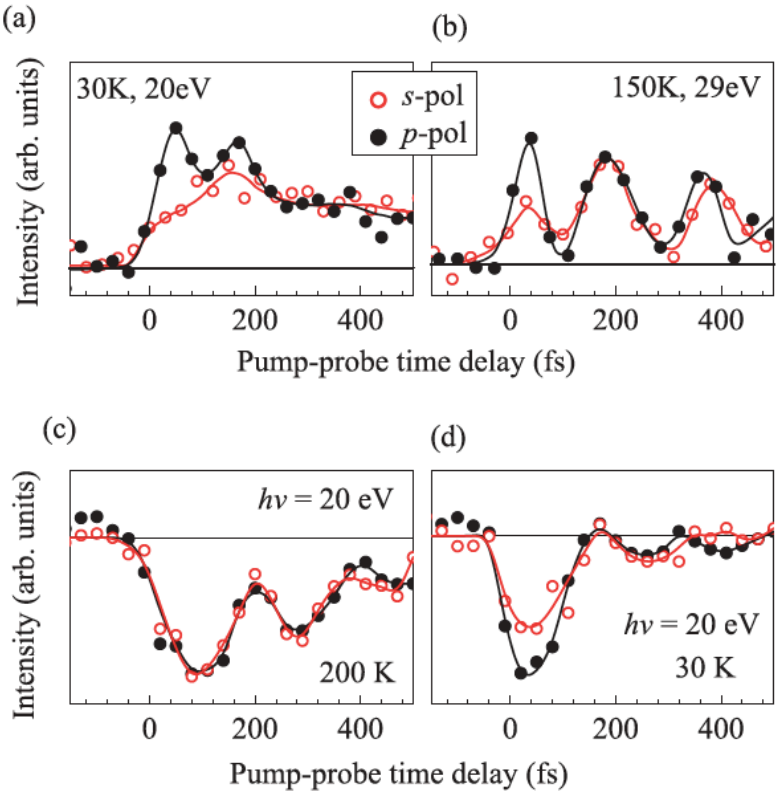

Figure 6.6: (a) Time-resolved photoemission intensity as a function of pump-probe delay for s-pol (empty circles) and p-pol (filled circles) pump pulses with probe energy $\approx$ 20 eV and initial sample temperature of 30 K. (b) The same with probe energy $\approx$ 29 eV and initial sample temperature of 150 K. Time-resolved spectral intensity at 0.2 eV binding energy for p-pol (filled circles) and s-pol (empty circles) pump pulses at the same probe photon energy at (c) 200 K and (d) 30 K.

plot the k-integrated spectral intensity at binding energy 0.2 eV, which, below the critical temperature T_C (e.g., at 30 K), reflects the yield of the folded band due to SDW order; the probe pulse energy is 20 eV. At 200 K ($> T_C$), we do not observe any discernible differences between the p-pol and s-pol case, see Figure 6.6(c). However, at 30 K, we observe a significantly more intense dip in the p-pol case, compared to the s-pol case, as shown in Figure 6.6(d). This confirms that the folded band formed due to the SDW order is more efficiently depopulated in the p-pol case. Note that the relaxation of the hole states at 30 K is much faster compared to 200 K, which is in agreement with the other measurements [41].

For $T > T_C$, the α and β bands have both d_{xz} and d_{yz} characters as the crystal structure is tetragonal. Therefore, both p- and s-polarized pump pulses are able to excite such bands; the difference in intensity of excitations might be related to the cross-section due to the component of light polarization vector along the orbital lobes. In the magnetically ordered phase, the structure becomes orthorhombic and the degeneracy of d_{xz} and d_{yz} electrons is lifted. Evidently, the p-polarized light is able to excite d_{xz} electrons which are coupled via electron-magnon coupling and the response occurs at a fast time scale. On

the other hand, s-polarized light is not able to excite the electrons participating in the magnetic order and the slower electron temperature rise might be related to the relatively slower electron-phonon response. It is to note here that Rettig *et al.*, [41] have studied the perturbation dynamics for optically excited $EuFe_2As_2$ to investigate different coupling phenomena and reported different time scales for magnetic ordering ($\sim$ 50 fs) and structural orientation ($\sim$ 100 fs). While our results are consistent with those findings, we discover that electrons corresponding to different symmetries can be selectively excited by using suitably polarized pump pulses. In this study, we utilize the polarization tunability of the pump pulses instead of the probe pulse, unlike earlier studies [19, 44]. Phtotoexcitation with an ultrafast pump pulse allows one to disentangle symmetries associated to varied excitations. This implies that a pump pulse may in principle excite electrons of selective symmetry without affecting electrons of the other symmetry. While this description explains the experimental results qualitatively, we hope that these results will trigger theoretical activities in this direction. These results also indicate that the magnetic and structural orders may not be linked. This is in agreement with various observations of structural and magnetic orders occurring at two different temperatures. For example, Co-doping in $Ba(Fe_{1-x}Co_x)_2As_2$ shows that the structural transition precedes the magnetic transition [45]. On the other hand, with the application of external pressure on $BaFe_2As_2$, the magnetic transition precedes the structural one [46].

6.4 Summary

In summary, we studied the electron dynamics in a parent compound of Fe-pnictide superconductors using time-resolved and angle-resolved photoemission spectroscopy. Our results suggest that light polarization of the pump pulse in a pump-probe measurement can be used to study orbital selective excitation dynamics in complex quantum materials. Employing this method, we show that the excitation dynamics in $CaFe_2As_2$ corresponding to s-pol of the pump pulse is relatively slower ($\sim$ 200 fs) than the dynamics of electrons probed by p-pol pump pulses ($\sim$ 50 fs). Clearly, the electronic properties linked to the corresponding orbital symmetries are occurring at different time scales. This is in line with the discoveries of orbital selective behavior, such as β bands showing the emergence of a band gap across the SDW transition, while the Fermi surfaces corresponding to other bands survive [11], orbital selective Mottness [47], etc. These results demonstrate an experimental method to probe such orbital selective behavior which might have significant implications in the study of the physics of complex quantum materials.

References

[1] Y. Kamihara, H. Hiramatsu, M. Hirano, R. Kawamura, H. Yanagi, T. Kamiya, and H. Hosono, "Iron-Based Layered Superconductor: LaOFeP." *Journal of the American Chemical Society* **128**, 10012 (2006).

[2] Y. Kamihara, T. Watanabe, M. Hirano, and H. Hosono, "Iron-Based Layered Superconductor La($O_{1-x}F_x$)FeAs (x = 0.05-0.12) with T_C = 26 K." *Journal of the American Chemical Society*, **130** 3296 (2008).

[3] K. Ishida, Y. Nakai, and H. Hosono, "To What Extent Iron-Pnictide New Superconductors Have Been Clarified: A Progress Report." *Journal of the Physical Society of Japan*, **78** 062001 (2009).

[4] K. Maiti, "Electronic structure of Fe-based superconductors." *Pramana - Journal of Physics*, **84**, 947 (2015).

[5] G. R. Stewart, "Superconductivity in iron compounds." *Reviews of Modern Physics*, **83**, 1589 (2011).

[6] J. A. Sobota, Y. He, and Z. X. Shen, "Angle-resolved photoemission studies of quantum materials." *Reviews of Modern Physics* **93**, 025006 (2021).

[7] N. Kurita, M. Kimata, K. Kodama, A. Harada, M. Tomita, H. S. Suzuki, T. Matsumoto, K. Murata, S. Uji, and T. Terashima, "Phase diagram of pressure-induced superconductivity in $EuFe_2As_2$ probed by high-pressure resistivity up to 3.2 GPa." *Physical Review B*, **83** 214513 (2011).

[8] G. Adhikary, N. Sahadev, D. Biswas, R. Bindu, N. Kumar, A. Thamizhavel, S. K. Dhar, and K. Maiti, "Electronic structure of $EuFe_2As_2$." *Journal of Physics: Condensed Matter*, **25**, 225701 (2013).

[9] P. Dai, J. Hu, and E. Dagotto, "Magnetism and its microscopic origin in iron-based high-temperature superconductors." *Nature Physics*, **8**, 709 (2012).

[10] A. Chubukov and P. J. Hirschfeld, "Iron-based superconductors, seven years later." *Physics Today* **68**, 46 (2015).

[11] K. Ali *et al.*, "Hidden phase in parent Fe-pnictide superconductors." *Physical Review B*, **97**, 054505 (2018).

[12] G. Adhikary, D. Biswas, N. Sahadev, R. Bindu, N. Kumar, S. K. Dhar, A. Thamizhavel, and K. Maiti, "Complex temperature evolution of the electronic structure of $CaFe_2As_2$." *Journal of Applied Physics* **115**, 123901 (2014).

[13] K. Ali and K. Maiti, "Emergent electronic structure of $CaFe_2As_2$." *Scientific Reports* **7**, 6298 (2017).

[14] P. Blaha, K. Schwarz, G. K. H. Madsen, D. Kvasnicka, and J. Luitz, "WIEN2k: An Augmented Plane Wave Plus Local Orbitals Program for Calculating Crystal Properties." (Karlheinz Schwarz, Technische Universität Wien, Austria) 2001.

[15] R. M. Fernandes, A. V. Chubukov, and J. Schmalian, "What drives nematic order in iron-based superconductors? " Nature Physics, **10**, 97 (2014).

[16] H. Pfau *et al.*, "Momentum Dependence of the Nematic Order Parameter in Iron-Based Superconductors." *Physical Review Letters*, **123** 066402 (2019).

[17] F. Yang, S. F. Taylor, S. D. Edkins, J. C. Palmstrom, I. R. Fisher, and B. L. Lev, "Nematic transitions in iron pnictide superconductors imaged with a quantum gas." *Nature Physics* **16**, 514 (2020).

[18] A. I. Goldman, D. N. Argyriou, B. Ouladdiaf, T. Chatterji, A. Kreyssig, S. Nandi, N. Ni, S. L. Bud'ko, P. C. Canfield, and R. J. McQueeney, "Lattice and magnetic instabilities in $CaFe_2As_2$: A single-crystal neutron diffraction study." *Physical Review B* **78**, 100506(R) (2008).

[19] G. Adhikary, B. Ressel, M. Stupar, P. R. Ribič, J. Urbančič, G. D. Ninno, D. Krizmancic, A. Thamizhavel, and K. Maiti, "Orbital-dependent electron dynamics in Fe-pnictide superconductors." *Physical Review B* **98**, 205142 (2018).

[20] P. L. Alireza1, Y. T. Chris Ko, J. Gillett, C. M. Petrone, J. M. Cole, G. G. Lonzarich, and S. E Sebastian, "Superconductivity up to 29 K in $SrFe_2As_2$ and $BaFe_2As_2$ at high pressures." *Journal of Physics: Condensed Matter* **21**, 012208 (2009).

[21] M. Kumar, M. Nicklas, A. Jesche, N. Caroca-Canales, M. Schmitt, M. Hanfland, D. Kasinathan, U. Schwarz, H. Rosner, and C. Geibel, "Effect of pressure on the magnetostructural transition in $SrFe_2As_2$." *Physical Review B* **78**, 184516 (2008).

[22] A. Mani, N. Ghosh, S. Paulraj, A. Bharathi and C. S. Sundar, "Pressure-induced superconductivity in $BaFe_2As_2$ single crystal." *Europhysics Letters* **87**, 17004 (2009).

[23] H. Kotegawa, T. Kawazoe, H. Sugawara, K. Murata, and H. Tou, "Effect of Uniaxial Stress for Pressure-Induced Superconductor $SrFe_2As_2$." *Journal of the Physical Society of Japan* **78**, 083702 (2009).

[24] E. Colombier, S. L. Bud'ko, N. Ni, and P.C. Canfield, "Complete pressure-dependent phase diagrams for $SrFe_2As_2$ and $BaFe_2As_2$." *Physical Review B* **79**, 224518 (2009).

[25] H. Kotegawa, H. Sugawara, and H. Tou, " Abrupt Emergence of Pressure-Induced Superconductivity of 34 K in $SrFe_2As_2$: A Resistivity Study under Pressure." *Journal of the Physical Society of Japan* **78**, 013709 (2009).

[26] K.Igawa, H. Okada, H. Takahashi, S. Matsuishi, Y. Kamihara, M. Hirano, H. Hosono, K. Matsubayashi, and Y. Uwatoko, "Pressure-Induced Superconductivity in Iron Pnictide Compound $SrFe_2As_2$." *Journal of the Physical Society of Japan* **78**, 025001 (2009).

[27] M. S. Torikachvili, S. L. Bud'ko, N. Ni, and P. C. Canfield, "Pressure Induced Superconductivity in $CaFe_2As_2$." *Physical Review Letters* **101**, 057006 (2008).

[28] M. S. Torikachvili, S. L. Bud'ko, N. Ni, P. C. Canfield, and S. T. Hannahs, "Effect of pressure on transport and magnetotransport properties in $CaFe_2As_2$ single crystals." *Physical Review B* **80**, 014521 (2009).

[29] T. Park, E. Park, H. Lee, T. Klimczuk, E. D. Bauer, F. Ronning, and J. D. Thompson, "Pressure-induced superconductivity in $CaFe_2As_2$." *Journal of Physics: Condensed Matter* **20**, 322204 (2018).

[30] H. Lee, E. Park, T. Park, V. A. Sidorov, F. Ronning, E. D. Bauer, and J. D. Thompson, "Pressure-induced superconducting state of antiferromagnetic $CaFe_2As_2$." *Physical Review B* **80**, 024519 (2009).

[31] N. Ni, S. Nandi, A. Kreyssig, A. I. Goldman, E. D. Mun, S. L. Bud'ko, and P. C. Canfield, "First-order structural phase transition in $CaFe_2As_2$." *Physical Review B* **78**, 014523 (2008).

[32] D. A. Tompsett and G. G. Lonzarich, "Dimensionality and magnetic interactions in $CaFe_2As_2$: An ab initio study." *Physica B: Condensed Matter* **405**, 2440 (2010).

[33] A. Kreyssig *et al.*, "Pressure-induced volume-collapsed tetragonal phase of $CaFe_2As_2$ as seen via neutron scattering." *Physical Review B* **78**, 184517 (2008).

[34] T. Yildirim, "Strong Coupling of the Fe-Spin State and the As-As Hybridization in Iron-Pnictide Superconductors from First-Principle Calculations." *Physical Review Letters* **102**, 037003 (2009).

[35] N. Colonna, G. Profeta, A. Continenza, and S. Massidda, "Structural and magnetic properties of $CaFe_2As_2$ and $BaFe_2As_2$ from first-principles density functional theory." *Physical Review B* **83**, 094529 (2011).

[36] Y.-Z. Zhang, H. C. Kandpal, I. Opahle, H. O. Jeschke, and R. Valentí, "Microscopic origin of pressure-induced phase transitions in the iron pnictide superconductors AFe_2As_2: An ab initio molecular dynamics study." *Physical Review B* **80**, 094530 (2009).

[37] N. Kumar, R. Nagalakshmi, R. Kulkarni, P. L. Paulose, A. K. Nigam, S. K. Dhar, and A. Thamizhavel, "Anisotropic magnetic and superconducting properties of $CaFe_{2-x}Co_xAs_2$ ($x = 0.0, 0.6$) single crystals." *Physical Review B* **79**, 012504 (2009).

[38] B. Mansart, D. Boschetto, A. Savoia, F. Rullier-Albenque, A. Forget, D. Colson, A. Rousse, and M. Marsi, "Observation of a coherent optical phonon in the iron pnictide superconductor $Ba(Fe_{1-x}Co_x)_2As_2$ ($x = 0.06, 0.08$)." *Physical Review B* **80**, 172504 (2009).

[39] F. Schmitt *et al.*, "Transient Electronic Structure and Melting of a Charge Density Wave in $TbTe_3$." *Science* **321**, 1649 (2008).

[40] J. C. Petersen et al., "Clocking the Melting Transition of Charge and Lattice Order in 1T-TaS_2 with Ultrafast Extreme-Ultraviolet Angle-Resolved Photoemission Spectroscopy." *Physical Review Letters* **107**, 177402 (2011).

[41] L. Rettig, R. Cortés, S. Thirupathaiah, P. Gegenwart, H. S. Jeevan, M. Wolf, J. Fink, and U. Bovensiepen, "Ultrafast Momentum-Dependent Response of Electrons in Antiferromagnetic $EuFe_2As_2$ Driven by Optical Excitation."*Physical Review Letters* **108**, 097002 (2012).

[42] C. W. Nicholson, C. Monney, R. Carley, B. Frietsch, J. Bowlan, M. Weinelt, and M. Wolf, "Ultrafast Spin Density Wave Transition in Chromium Governed by Thermalized Electron Gas." *Physical Review Letters* **117**, 136801 (2016)

[43] T. Shimojima, Y. Suzuki, A. Nakamura, N. Mitsuishi, S. Kasahara, T. Shibauchi, Y. Matsuda, Y. Ishida, S. Shin, and K. Ishizaka, "Ultrafast nematic-orbital excitation in FeSe." *Nature Communications* **10**, 1946 (2019)

[44] L. X. Yang *et al.*, "Ultrafast Modulation of the Chemical Potential in $BaFe_2As_2$ by Coherent Phonons." *Physical Review Letters* **112**, 207001 (2014).

[45] S. Nandi *et al.*, "Anomalous Suppression of the Orthorhombic Lattice Distortion in Superconducting $Ba(Fe_{1-x}Co_x)_2As_2$ Single Crystals." *Physical Review Letters* **104**, 057006 (2010).

[46] J. J. Wu, J.-F. Lin, X. C. Wang, Q. Q. Liu, J. L. Zhu, Y. M. Xiao, P. Chow, and C. Jin, "Pressure-decoupled magnetic and structural transitions of the parent compound of iron-based 122 superconductors $BaFe_2As_2$." *The Proceedings of the National Academy of Sciences U.S.A.* **110**, 17263 (2013).

[47] L. de' Medici, G. Giovannetti, and M. Capone, "Selective Mott Physics as a Key to Iron Superconductors."*Physical Review Letters* **112**, 177001 (2014).

7 Conclusions

7.1 Summary of the thesis

The thesis addresses the study of ultrafast timescales associated with the fundamental interactions between various degrees of freedom, such as charge, spin and lattice, constituting a solid. The characteristic timescales help to identify the predominant interactions governing the equilibrium ground phases. A knowledge of these timescales is of paramount importance in the investigation of systems that are described by many-body physics. We also highlight how photodoping can induce non-equilibrium phase transitions from an insulating ground state of a solid to either known equilibrium phases or long-lived metastable phases. In parallel, we signify the role of chemical doping in inducing equilibrium phase transitions in many-body systems. For the intended study, we choose prominent examples of well-known models (excitonic insulators, Mott insulators, charge and spin density wave systems) as target materials. Time- and angle-resolved photoemission spectroscopy and synchrotron-based (static) ARPES have been exploited as work tools for the experimental findings of the thesis. Numerical simulations in collaboration with theoreticians corroborate some of the experimental findings. In the following, the key results of the thesis work are summarized.

An investigation of the evolution of the band structure in $Ta_2Ni(Se_{1-x}S_x)_5$ as a function of Sulfur concentration x was performed using static ARPES. A substantial amount of Sulfur doping $\sim$ 50% is able to suppress the excitonic ground state of Ta_2NiSe_5. This can be claimed due to the observed deviation from the flattened E versus k dispersion of the valence band top at $x = 0.5$ but not at $x = 0.25$. The suppression of the excitonic phase is followed by a marked increase in the effective mass ratio for $x = 0.5$ as compared to $x = 0$ and $x = 0.25$. This indicates higher localization of the electrons, which is in agreement with the weakening of hybridization between Ni $3d$ and Se $4p$ (S $3p$) orbitals that also leads to large values of the band gap. In addition, the photon-energy dependent measurements show considerable shifts in the binding energy of states near E_F with increasing photon energy (increasing k_z). This emphasizes that the two-dimensional picture often used for Ta_2NiSe_5 does not fully represent the entire electronic structure and that three-dimensionality must be taken into account when studying $Ta_2Ni(Se_{1-x}S_x)_5$ compounds. The dimensionality of the underlying electronic structure in a material is an important parameter while choosing potential candidates for electronic applications.

For the candidate excitonic insulator Ta_2NiSe_5, the non-equilibrium electron dynamics in a high photoexcitation regime have been studied. We observed that strong photoexcitation induces a non-equilibrium phase transition

from an insulating to a semimetallic phase. Moreover, the melting of the energy gap occurs on a timescale faster than the oscillation period associated with the characteristic phonon mode. Next, we demonstrated that the dependence of different timescales on the photoexcitation strength shows contrasting trends. On one hand, the (fast) rise time of photoemission spectral intensity above E_F becomes shorter with increasing excitation strength, while, on the other hand, the (slow) relaxation time of the hot electron population towards equilibrium becomes longer with increasing excitation strength, and saturates above a critical strength. The experimental results are supported by theoretical calculations based on the tight-binding model. The speedup of the rise time is interpreted in terms of an enhanced probability of scattering between photoexcited electrons and excitons, and the inclusion of electron-phonon coupling does not modify the physics qualitatively. The obtained results point to a predominantly electronic i.e., excitonic origin of the order parameter in Ta_2NiSe_5.

The characteristics of the non-equilibrium phases in photoexcited CDW-Mott insulator 1T-TaS_2 were studied using time-resolved ARPES. We observe that in the transient phase occurring after photoexcitation, the Mott-CDW order is suppressed and the electronic band structure has strong resemblance with that of the unreconstructed (equilibrium) metallic phase. The Mott and CDW ordering begins to recover around the same time, but the CDW phase undergoes only a partial recovery, while the Mott phase fully recovers within 1 ps and the material settles in a long-lived metastable phase. The metastable "hidden" phase does not correspond to any of the thermally accessible equilibrium phases. Our results suggest that it is primarily the interaction of the electrons with the lattice that pushes the material towards such a long-lived state where 1T-TaS_2 is a commensurate CDW-Mott insulator but with a reduced CDW amplitude. In addition, we find that the metastable state emerges only under strong photoexcitation of the system. The coexistence of multiple phases and the complex phase diagram of 1T-TaS_2 give rise to some intriguing phenomena, such as the role played by electron-electron interactions in the CDW ordering, modulation of the Mott gap occurring on structural timescales, etc. Hence, a detailed characterization of the photoinduced non-equilibrium phases in this system is crucial to gain deeper insights into the interactions governing these phases, possibly triggering future studies on other complex materials.

The electron dynamics in $CaFe_2As_2$, a parent compound of Fe-based superconductors and exhibiting SDW ground state, have been studied using time-resolved ARPES. The results suggest that the polarization of the electric field of pump pulses in a pump-probe experiment can be exploited to study orbital selective photoexcitation dynamics in complex materials. Using this method, we showed that the electron dynamics in $CaFe_2As_2$ corresponding to s-polarization of the pump pulses are slower ($\sim$ 200 fs) than the dynamics of electrons excited by p-polarized pump pulses ($\sim$ 50 fs). This indicates that the microscopic phenomena associated with the corresponding orbital symmetries are occurring on different time scales, allowing us to disentangle the

dominant interactions linked to the specific orbitals. Such a decoupled behavior helps identify the role played by different orbitals in the ordered ground phases, where multiple bands constitute the Fermi surfaces. These findings are in line with the discovery of orbital selective behavior, such as β bands showing the emergence of a band gap across the SDW transition, while the Fermi surfaces corresponding to other bands survive. Therefore, the obtained results demonstrate an experimental method to probe such orbital selective behavior, which might have significant implications in the study of complex systems.

7.2 Future perspectives

Even though the thesis provides significant insights into the elementary microscopic processes governing the complex ground phases in condensed-matter systems, some of the emerging questions remain to be answered. Concerning the long-lived metastable state in 1T-TaS_2, we provide an indirect scenario of the lattice configuration in this hidden phase from the time-dependent evolution of the electronic band structure. However, direct characterization of the lattice deformation as the system enters the (non-equilibrium) metastable phase from the (equilibrium) CCDW phase is crucial. This is because the rich physics of the hidden phase(s) occurring in this CDW system is predominantly governed by the interaction of the electronic subsytem with the underlying lattice. Interestingly, the configuration of the lattice in the hidden phase does not correspond to any of the high-temperature equilibrium phases and therefore, suggests the presence of an ordered phase. It is therefore necessary to study the lattice dynamics of the metastable phase, in order to understand: (i) on which timescales does the lattice recover its ground state; (ii) if the recovery of electron dynamics follows the same timescale. A clear and direct information of the structural dynamics can be achieved through Ultrafast Electron Diffraction (UED) studies. Furthermore, it would be necessary to perform (pump) fluence-dependent studies employing time-resolved ARPES to understand whether mode-selective electron-phonon coupling plays a role in the emergence of the metastable phase. More importantly, a bottleneck in the recovery dynamics of the lower Hubbard band is quite intriguing, therefore, necessitating fluence-dependent trARPES studies and theoretical work in the future. Coming to the problem of excitonic insulators, our results indicate an electronic origin of the band gap in Ta_2NiSe_5. However, ruling out the contribution of lattice degrees of freedom in the gap formation demands an investigation of the timescales associated with the structural dynamics. This may be accomplished by means of UED. For solid-state systems where the Fermi surfaces comprise multiple energy bands, we show that polarization of the pump pulses can be utilized to disentangle the timescales associated with various orbital symmetries and hence identify the dominant interactions in different cases. While the employed method is able to untwine the magnetic and structural transitions, active theoretical input is required in this direction. We believe that our findings will provide impetus to the investigation

of ordered phases in solids and trigger further research on a diverse range of many-body systems.

Appendix

Sample misalignment

Figure I(a) shows the experimental geometry involving the sample orientation and the photoemission plane. The changes in the measured ARPES spectrum due to a finite sample misalignment δ in the yz plane are shown in Figure I(b). In our case, the misalignment arises because the sample is not mounted perfectly flat on the sample plate. δ is the tilt angle which cannot be corrected by the manipulator setup – the latter having only two rotational degrees of freedom, θ (defined in the xz plane) and ϕ (defined in the xy plane), see Figure I(a). For simplicity, we consider that the dispersions are parabolic along both k_x and k_y directions. For $\delta \neq 0$, the sample surface normal is not perfectly coinciding with the slit axis. The shape of the E versus k dispersion depends on the intersection of the vertical plane (in blue) with the parabolas (representing the band structure around Fermi energy E_F in 3D). For perfect alignment $\delta = 0$ (normal emission geometry), the intersection is exactly at the center of the 3D parabolas and the measured spectrum in this case is represented in the left panel of Figure I(b) by the red curves. But when the sample is misaligned, i.e., for a tilt angle δ ($\neq 0$), the intersection plane lies away from the center and the detected spectra (red curves) in this case are shown in the right panel of Figure I(b). As one can see, a finite misalignment manifests itself as two parabolas separated by a larger energy gap at Γ-point in comparison to the case for $\delta = 0$.

Now, we will briefly explain why the misalignment is an issue only for the measurements along ΓY direction and not along ΓX direction. Firstly, a higher binding energy at Γ-point along ΓY, see Figure 3.5(f), clearly indicates that the sample normal has an offset of δ (in the yz plane) with respect to the axis of the analyser slit (z-axis) and this misalignment cannot be corrected, as stated earlier. Coming to the deviation of the trend in binding energy with Sulfur-doping along ΓY direction, this is because the ARPES spectra in Figure 3.8(a)-(c) are cuts at slightly different values of k_x. However, it is worth stressing that the purpose of the results reported in Figure 3.8 and Figure 3.9 is to demonstrate a significant increase of the effective mass ratio with doping level. Such a trend, which is clearly shown by the experimental data, is not affected by the possible presence of a small offset of the binding energy, due to sample misalignment. Secondly, according to the experimental geometry shown in Figure I(a), on rotating the sample by 90° (through the azimuthal angle ϕ) in the xy plane for measurements along ΓX direction, one is left with a misalignment α in the xz plane. It is important to note that this misalignment can be corrected by changing the polar angle, θ, of the manipulator. This

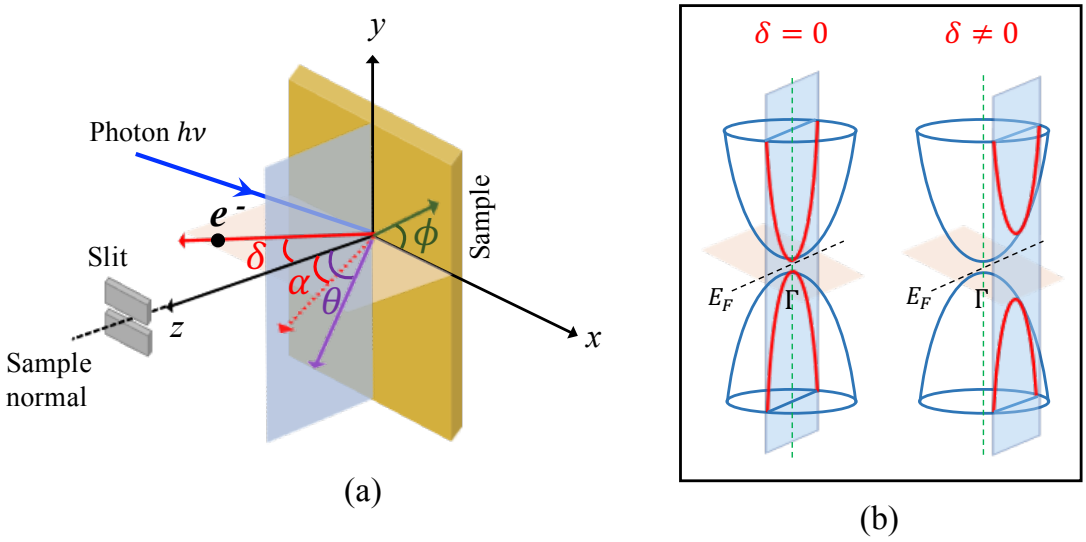

Figure I: (a) Schematic of the experimental geometry. Here, θ (rotation in the xz plane) and ϕ (rotation in the xy plane) are the available rotational degrees of freedom. The angle δ represents the residual misalignment in the yz plane, which could be corrected by rotating the sample around the x-axis (degree of freedom not available). The angle α is the misalignment angle in the xz plane, which can be corrected by changing the angle θ. (b) Left panel: Measured dispersion along k_y-direction under perfect alignment $\delta = 0$ (normal emission); Right panel: Band dispersion when there is a misalignment $\delta \neq 0$ (off-normal emission geometry). The misalignment leads to a larger energy gap and binding energy at Γ in the measured spectrum. The Γ-point is indicated by the green dashed lines and the black dashed lines denote the Fermi level E_F.

allows one to perfectly align the sample along the ΓX direction. Therefore, we can safely state that a quantitative comparison of the electronic structure as a function of Sulfur-doping is indeed possible along ΓX direction as the ARPES spectra in Figure 3.7(a)-(c) correspond to the cuts at $k_y = 0$. Based on the above, we can confirm that the trend of the binding energy at Γ-point as a function of Sulfur doping shown in Figure 3.7(g)-(i) and Figure 3.10(g)-(i) correctly fits into the semi-metallic picture of Ta_2NiSe_5. We note that the misalignment in the yz plane could be corrected by rotating the sample by 90° in the xy plane after perfectly aligning the sample along the ΓX direction. However, this could not be ensured due to extremely thin sample dimensions along the in-plane c-axis of the lattice, i.e., for measurements along ΓY direction. For mapping a constant energy contour, the high symmetry point was determined by locating the tilt angle at which Γ-point energy would be the highest by placing the horizontal slit along $X\Gamma X$ direction.